SLAC-R-505
UC-414

Production Rates of Strange Vector Mesons at the Z^0 Resonance*

Mihai O. Dima

Stanford Linear Accelerator Center
Stanford University
Stanford, CA 94309

SLAC-Report-505
May 1997

Prepared for the Department of Energy
under contract number DE-AC03-76SF00515

*Ph.D. thesis, Colorado State University

Abstract

Production of Strange Vector Mesons at the Z^0 Resonance

This dissertation presents a study of strange vector meson production, "leading particle" effect and a first direct measurement of the strangeness suppression parameter in hadronic decays of the neutral electroweak boson, Z^0. The measurements were performed in e^+e^-collisions at the Stanford Linear Accelerator Center (SLAC) with the SLC Large Detector (SLD) experiment. A new generation particle ID system, the SLD Čerenkov Ring Imaging Detector (CRID) is used to discriminate kaons from pions, enabling the reconstruction of the vector mesons over a wide momentum range. The inclusive production rates of ϕ and K^{*0} and the differential rates versus momentum were measured and are compared with those of other experiments and theoretical predictions. The high longitudinal polarisation of the SLC electron beam is used in conjunction with the electroweak quark production asymmetries to separate quark jets from antiquark jets. K^{*0} production is studied separately in these samples, and the results show evidence for the "leading particle" effect. The difference between K^{*0} production rates at high momentum in quark and antiquark jets yields a first direct measurement of strangeness suppression in jet fragmentation.

Acknowledgements

I would like to thank the SLD Collaboration of the Stanford Linear Accelerator and the HEP Group at Colorado State University for the opportunity of engaging in this research, in particular my adviser, Dr. R. Wilson who made it all possible.

I would also like to thank the SLD CRID Group for the experience I gained in hardware and the QCD Group for physics. My special thanks go to Dr. D. Muller of the SLD CRID Group for the help with numerous details of the CRID system both in hardware and physics analysis.

Last but not least, I would like to thank my parents, Ioan and Ana, for their encouragement.

This work was supported in part by grants from the Department of Energy.

Contents

List of Figures

LIST OF FIGURES

LIST OF FIGURES

List of Tables

LIST OF TABLES

Chapter 1

Introduction

The "Standard Model" successfully predicts a large and diverse number of high-energy physics phenomena that have been observed experimentally. However there still are areas in which experimental evidence is crucial to the formulation of the correct mechanisms.

One such area is the process of hadronisation, where the understanding is incomplete about the way in which hadrons are formed from jets. The fragmentation of the Z^0 boson is interpreted to proceed in four stages:

- e^+e^- *annihilation*, Z^0 production and primary $q\bar{q}$ pair formation. This process is well understood at the tree level Quantum Chromodynamics (QCD) calculations and the associated radiative corrections.

- *parton shower*, in which the primary partons radiate highly energetic gluons that in turn pair-produce $q\bar{q}$, or further radiate gluons. This sequence terminates

when the energy of the secondary partons approaches the hadron mass scale. The parton shower is understood at the level of perturbative QCD calculations.

- *hadron formation*, in which the soft partons form the observable hadrons. This stage is not understood quantitatively and it is described by various models such as the Lund string model, Webber cluster model, *etc.* An accurate description of the final state of this process could, combined with the calculations of stages one and two, validate the model that best fits the experimental results.

- *decay of short lived hadrons*, during which the unstable primary hadrons produced in fragmentation decay to lighter, stable particles. Their decay daughters smear the distributions of particles originating directly in fragmentation. However, for the more massive particles, such as ϕ and K^{*0}, it is less less likely that they are decay products of a heavier parent and more likely that they originated directly in fragmentation. Further more, selection of light flavor (*uds*) events allows to eliminate heavy hadrons and the associated decay products that smear the distributions of the particles of interest. Likewise, the study of particles with more than 22 GeV/c momentum probes closer to the actual hadronisation process.

In this respect the study of ϕ and K^{*0} production in hadronic Z^0 decays is a strong way of probing hadronisation. This dissertation presents both the traditional inclusive sample measurement, as well the first production measurement of ϕ and K^{*0}

in light and heavy flavor events. These measurements are compared to predictions of fragmentation models such as JETSET and HERWIG and give indications of how these models need to be changed in order to describe the real data. K^{*0} production is further studied in quark and antiquark jets, which are separated using the electroweak quark production asymmetry and the unique SLC capability of delivering highly polarised electron beams with longitudinal polarisation. This study yields a new, direct method for measuring strangeness suppression, a fundamental parameter of fragmentation that enters all models.

The dissertation is organised in three parts, the first part giving an overview of the Standard Model and the SLD experiment, the second part describing the particle identification system at SLD and the author's contribution to the alignment of this system, and the third part describing the author's research topic, the ϕ and K^{*0} analyses and the physics derived from these studies.

Chapter 2 gives a brief overview of the "Standard Model", describing the electroweak and strong interactions. The QCD approach to hadronisation is discussed in the context of particle production, and a general overview is given of the main fragmentation models. Chapter 3 gives a general description of the SLC Collider and the SLD Detector.

The SLD Particle ID System is discussed in detail in Chapter 4. Emphasis is given to the system's alignment with respect to the tracking chambers. This feature allows

very good identification efficiencies at momenta above 10 GeV/c, which is essential to the strangeness suppression measurement in the K^{*0} system. Calibration of the End Cap subsystem is also discussed together with a study of End Cap sub-system alignment.

Chapter 5 describes general aspects related to standard hadronic event selection and flavor and quark/antiquark jet tagging. The inclusive sample analysis is shown in detail in Chapter 6 for both ϕ and K^{*0}. Comparisons with other experiments are shown and the data is related to QCD and fragmentation model predictions. The analysis is repeated in the three flavor enriched samples in Chapter 7 and the method for unfolding the pure sample rates is described. K^{*0} production in quark and anti-quark jets is also described in Chapter 7, together with the extraction of the strangeness suppression parameter from these results, comparisons with other experiments and impact on the theory.

Chapter 8 gives a summary of the results presented in this dissertation.

Chapter 2

The Standard Model

This chapter gives an overview of two parts of the Standard Model related to the K^{*0} and ϕ analysis: the Electroweak Interaction and the Strong Interaction in the Standard Model.

2.1. The Standard Model of the Electroweak Interaction (EW)

The theory of electroweak interactions developed by Glashow, Weinberg and Salam successfully unified electromagnetic and weak interactions in the framework of a $SU(2)_L \otimes U(1)_R$ gauge invariant theory. In this model left handed fermions form isospin doublets, while right handed fermions are treated as isospin singlet states. The gauge bosons of the theory are introduced in a similar way as the A^μ fields in electromagnetism in order to insure local gauge invariance of the fermionic expectation probabilities. The difference in the electroweak model is that there are three

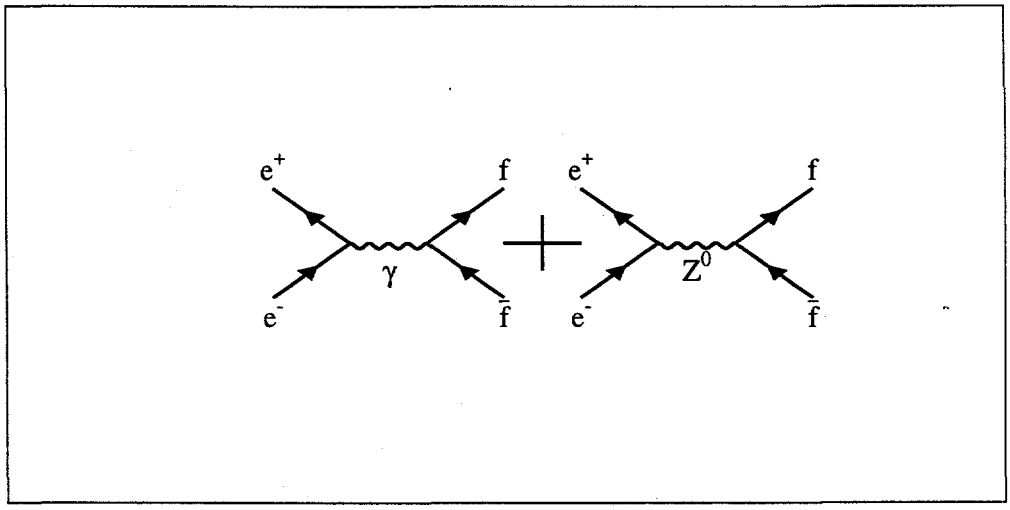

Figure 2.1: The tree level Feynman diagrams representing $e^+e^- \rightarrow f\bar{f}$

such fields that are arranged into $W^{\pm\mu}$, B^μ and A^μ fields via a linear combination[1]. At this stage the electroweak vector bosons are massless in the theory. To acquire mass an extra field is introduced, the Higgs field, with the property that by spontaneous breaking of the $SU(2)_L \otimes U(1)_R$ symmetry it gives masses to the $W^{\pm\mu}$, B^μ fields (the $W^\pm$, Z^0 bosons), but leaves the A^μ fields (the photon, γ) massless. The $W^\pm$, Z^0 bosons have been successfully observed in e^+e^-collisions at UA-1, LEP and SLD, while the Higgs boson has not yet been observed.

At SLD e^+e^-collisions are studied at the center of mass energy $\sqrt{s} = 91\text{GeV}$ corresponding to the Z^0 resonance. In these collisions the initial state annihilates producing the Z^0 boson which in turn decays to the final state fermions. The process $e^+e^- \rightarrow f\bar{f}$ is illustrated to first order in figure 2.1 as the sum of the photon

[1]Similar transformations are used in other quantum field theories, for instance the Bogoliubov transformation in superfluidity combines pairs of fermion operators to form boson operators.

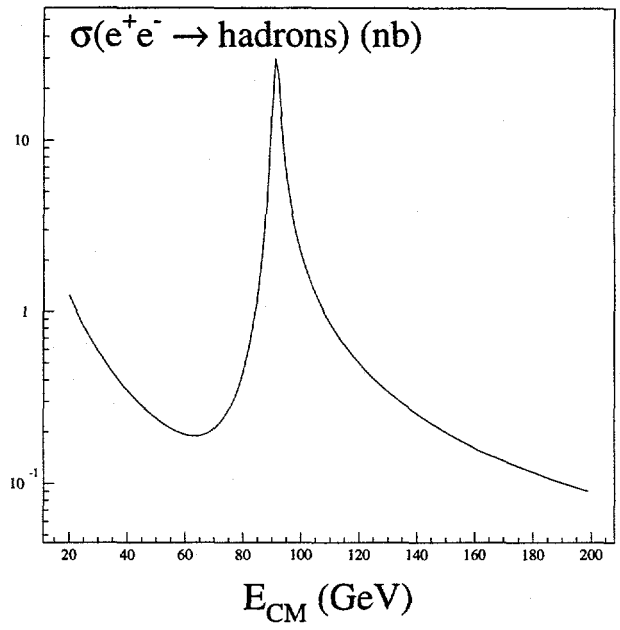

Figure 2.2: The $e^+e^- \rightarrow$ *hadrons* cross-section as a function of the center of mass energy.

and Z^0 boson exchange diagrams. The cross section of the process is proportional to the modulus square of the matrix elements and gives three terms: a negligible electromagnetic term, a large weak interaction term, and an interference term.

Figure 2.2 shows the total cross section for $e^+e^- \rightarrow$ *hadrons* as a function of the center of mass energy, $\sqrt{s}$. The cross section follows the "point-like particle" behaviour up to the Z^0 resonance, with a $1/s$ dependence. The Z^0 rises clearly above the "point cross section" by a factor of approximately 800 as a 2.5 GeV/c^2 wide asymmetric resonance.

At $\sqrt{s} = 91\text{GeV}$ the electron and final state fermion masses can be neglected and the helicity of the electron approximated with its spin. Under these assumptions the cross section for $e^+e^- \rightarrow f\bar{f}$ can be expressed as:

$$\frac{d\sigma}{d\Omega} = K(v_e^2 + a_e^2)(v_f^2 + a_f^2)[(1 + cos^2\theta) + 2A_f(A_e - P_e)cos\theta] \qquad (2.1)$$

Table 2.1: Properties of the Z^0 Boson.

Z^0 Mass (M_Z)	91.187 ± 0.007 GeV/c^2
Z^0 Decay Width (Γ_Z)	2.490 ± 0.007 GeV
Z^0 decay branching fractions	
e^+e^-	$(3.366 \pm 0.008)\%$
$\mu^+\mu^-$	$(3.367 \pm 0.013)\%$
$\tau^+\tau^-$	$(3.360 \pm 0.015)\%$
invisible	$(20.01 \pm 0.16)\%$
hadrons	$(69.90 \pm 0.15)\%$
$(u\bar{u} + c\bar{c})/2$	$(9.6 \pm 1.3)\%$
$(d\bar{d} + s\bar{s} + b\bar{b})/3$	$(16.9 \pm 0.9)\%$
$c\bar{c}$	$(11.0 \pm 0.7)\%$
$b\bar{b}$	$(15.46 \pm 0.14)\%$

where v_e and v_f are the vector couplings of the initial and final state to the Z^0, a_e and a_f the axial couplings, and P_e the signed longitudinal polarisation of the electron beam. The angle θ is the angle of the final state fermion momentum with respect to

the incoming electron beam, the quantity A_f:

$$A_f = \frac{2v_f a_f}{v_f^2 + a_f^2} \tag{2.2}$$

and the coefficient K:

$$K = \frac{\alpha^2}{4sin^2\theta_w} \frac{s}{(s - M_Z^2)^2 + \Gamma_Z^2 s^2/M_Z^2} \tag{2.3}$$

where α is the electromagnetic fine structure constant, $M_Z = 91.18$ GeV/c^2 the Z^0 mass, $\Gamma_Z = 2.49$ GeV/c^2 the Z^0 width, and the angle $\theta_w^{eff} = 28.7°$ the weak mixing angle. More data related to the Z^0 boson is listed in table 2.1.

Table 2.2: The vector and axial vector couplings for fermions to the Z^0 gauge boson. Q_f is the charge of the fermion, and T_f^3 is the third component of the weak isospin for the fermion.

$a_f = T_f^3$		
$v_f = T_f^3 - 2\sin^2\theta_W Q_f$		
fermion	a_f	v_f
ν_e, ν_ν, ν_τ	$+\frac{1}{2}$	$+\frac{1}{2}$
e^-, μ^-, τ^-	$-\frac{1}{2}$	$-\frac{1}{2} + 2\sin^2\theta_W$
u, c, t	$+\frac{1}{2}$	$+\frac{1}{2} - \frac{4}{3}\sin^2\theta_W$
d, s, b	$-\frac{1}{2}$	$-\frac{1}{2} + \frac{2}{3}\sin^2\theta_W$

The A_f deviation from zero is an indication of parity violation in the fermion coupling to the Z^0 (table 2.2 gives a list of the couplings of the various fermions to

the Z^0).

2.1.1. Electroweak Asymmetries

A very important tool in testing Standard Model (SM) predictions are the normalised differences of cross-sections sensitive to space and spin inversions. These quantities are: the *Forward-Backward Asymmetry* (A_{FB}), sensitive to space inversion, the *Left-Right Asymmetry* (A_{LR}), sensitive to spin inversion, and the *Polarised Forward-Backward Asymmetry* ($\tilde{A}^f_{FB}$), sensitive to both space and spin-space inversions.

The premier SLD measured asymmetry is the A_{LR} [1] which makes use of the unique SLC capability of delivering longitudinal highly polarised electron beams:

$$A_{LR} = \frac{\sigma(e^+e^-_L \to Z^0 \to f\bar{f}) - \sigma(e^+e^-_R \to Z^0 \to f\bar{f})}{\sigma(e^+e^-_L \to Z^0 \to f\bar{f}) + \sigma(e^+e^-_R \to Z^0 \to f\bar{f})} \tag{2.4}$$

where L and R denote the polarisation of the initial state, the electrons. For the final state both left and right polarisations are accepted, as well as hadronic, or leptonic final states. The A_{LR} relates to the weak mixing angle as:

$$A^0_{LR} = A_e = \frac{2v_e a_f}{v_e^2 + a_e^2} = \frac{2[1 - 4sin^2\theta_w^{eff}(M_Z^2)]}{1 + [1 - 4sin^2\theta_w^{eff}(M_Z^2)]} \approx 0.16 \tag{2.5}$$

The $sin^2\theta_w^{eff}(s)$ dependence on energy, indicates the "running" of the coupling con-

stants with energy. Since the SLD experiment operates at the center of mass energy of $\sqrt{s} = M_Z$, the weak mixing-angle is determined for this energy, and the radiative corrections [2; 3] that enter the calculation of $sin^2\theta_w^{eff}$ distinguish it from the "bare", tree-level value, $sin^2\theta_w$.

The SLC accelerator provides highly polarised electron beams, however not 100% polarised. In this case:

$$A_{LR}^{meas} = \frac{1}{|P_e|} A_{LR}^0 = \frac{N_L^{meas} - N_R^{meas}}{N_L^{meas} + N_R^{meas}} \tag{2.6}$$

where the measured asymmetry is smaller than A_{LR}^0 by an amount equal to the polarisation's deviation from 100%. $N_{L,R}$ are the number of Z^0 decays produced in left/right handed electron beams, regardless of the final state (hadronic or leptonic). As it can be observed in equation 2.5 the A_{LR} is independent of the final state couplings to the Z^0. This is advantageous from an experimental point of view, allowing the inclusion of all final states in the sample to increase the statistical power.

The SLD measurements on A_{LR} are based on data taken during the 1992, 1993 and 1994-95 run periods, the so-called "physics runs". The combined result [4] comprising of the hadronic left-right asymmetry, hadronic charge-flow asymmetry and lepton final state asymmetries measurements is:

$$A_{LR}^0 = 0.1542 \pm 0.0037$$

$$sin^2\theta_{eff} = 0.23061 \pm 0.00047 \tag{2.7}$$

The Forward-Backward Asymmetries A_{FB}^f and $\tilde{A}_{FB}^f$

The Forward-Backward Asymmetry is defined as:

$$A_{FB}^f = \frac{\sigma_F^f - \sigma_B^f}{\sigma_F^f + \sigma_B^f} = \frac{3}{4} A_e A_f, \tag{2.8}$$

where:

$$\sigma_F^f = \sigma^f(\cos\theta > 0) = \int_0^1 d(\cos\theta) \frac{d\sigma}{d\cos\theta} \tag{2.9}$$

is the forward integrated cross section, σ_B^f the backward integrated cross section, and the terms *forward* and *backward* refer to the hemisphere in the same (and opposite) direction of the incident electrons.

The A_{FB} depends on both the initial and the final state couplings to the Z^0. Therefore information about the initial state's couplings to the Z^0 can be extracted from this asymmetry only under certain assumptions about the final state.

A more advantageous quantity, having the benefit of longitudinally polarized electron beams, is the polarised forward-backward asymmetry, $\tilde{A}_{FB}^f$:

$$\tilde{A}_{FB}^f = \frac{(\sigma_F^L + \sigma_B^R) - (\sigma_F^R + \sigma_B^L)}{(\sigma_F^L + \sigma_B^R) + (\sigma_F^R + \sigma_B^L)} = \frac{3}{4} |P_e| A_f. \tag{2.10}$$

where $\sigma_F^{L(R)}$ is the forward cross section for left (right) polarised electron beams. The

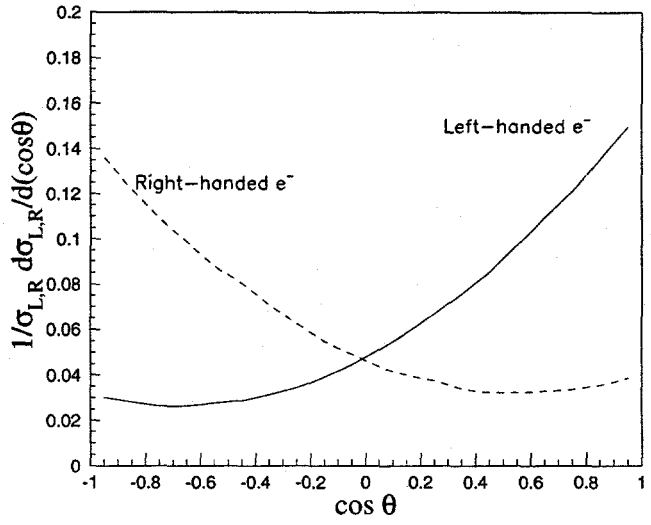

Figure 2.3: Polar angle dependence of the polarised production cross section of quarks in left and right-handed electron beams. Left-handed quarks tend to follow the direction of left-handed incident electrons.

expression of $\tilde{A}_{FB}^{f}$ is dependent only on the final state couplings to the Z^0. This unique and very interesting feature allows the SLD experiment to probe the final state couplings directly. Measurements of $\tilde{A}_{FB}^{b}$ [5] and $\tilde{A}_{FB}^{c}$ [6] have been performed at SLD using single heavy-hadron decays identified by the weak decay of the hadron. Light flavor events (uds) are considered collectively as there is no tagging technique orthogonal to the final state particle flavors.

The angular dependence [7] of $\tilde{A}_{FB}^{f}$ is:

$$\tilde{A}_{FB}^{f}(\cos\theta) = |P_e| A_f \frac{2\cos\theta}{1+\cos^2\theta}. \tag{2.11}$$

The large polar angle asymmetry observed here (figure 2.3) is useful for QCD studies in quark and anti-quark jets. This asymmetry will be discussed in more detail in Chapter 5 and will be used in Chapter 7.

2.2. The Standard Model of the Strong Interaction

The foundations for a strong interaction model were developed independently by Gell-Mann and Zweig [8] in the 1960's. The theory models hadrons as being composed of partons called quarks, and at the time explained many of the known properties of particles, such as multiplets, baryonic number conservation, conservation of strangeness in strong interactions, *etc.*

The existence of particles like Ω^- with a totally symmetric quark state (sss), however, contradicted the the Pauli exclusion principle. At the time the total wave function was written as the product of space and spin parts only. The addition of the *color* degree of freedom by Han and Nambu [9] eliminated this contradiction. Particles were required to be *colorless* states and the color part of the wave function provided the necessary symmetry such that fundamental principles not be violated.

Direct evidence of the dynamical presence of quarks came in 1968 from the SLAC-MIT deep inelastic electron scattering (DIS) experiments [10]. The DIS showed deviations from the point-like particle cross section and confirmed the Bjorken scaling properties of the structure functions, a feature characteristic to sub-nucleon structure.

On these premises the Quantum Chromodynamics (QCD) [11] theory of the strong interaction was founded. In this theory force originates from fields mediating the *color* charge. The color is of three types, conventionally called *blue*, *green* and *red* heuristically hinting at the way in which these colors combine to form white light. The sources of color are the quarks and the carriers of the force the gluons. QCD is constructed in a mathematical frame similar to that of the electroweak theory, with a non-Abelian local gauge-invariant theory based on the $SU(3)_{color}$ group. The 8 generators of the $SU(3)_{color}$ group determine the appearance of 8 gauge fields that remain massless (the gluons, g), however the six quark types (u, d, s, c, b, t) acquire masses via a Higgs mechanism. The non-Abelian gauge group determines similar features[2] to the electroweak theory, such as - in this case - the gluon-gluon coupling, however of a much more pronounced effect due to the massless force carriers. This aspect determines "anti-screening" and the negative running of the strong coupling constant α_s. The striking feature associated with this fact is the experimentally confirmed assertion that at small distances (large energies) the quarks act quasi-freely and at large distances (beyond 1 fm) they interact very strongly [12]. This behaviour has been termed as *asymptotical freedom.*

In e^+e^- experiments, jets in hadronic events were observed for the first time at

[2]This is related to the fact that in non-Abelian theories the carriers of the force can also carry themselves charge, here in the form of *bicolor* - i.e. $R\bar{B}, B\bar{G}$ *etc.* In QCD there are 9 bicolors, however the singlet state, $B\bar{B}+G\bar{G}+R\bar{R}$, carries no color and it is associated to the theory's U(1) sub-group generator, and further to the photonic gauge field.

SPEAR [13]. This observation shows that alike to leptonic events, hadronic events are also initiated by a small number of highly energetic particles. Assuming QCD to be the theory describing the dynamics of these "partons", the jet evolution can be calculated using perturbative methods that apply to this highly energetic ($\alpha_s < 1$) regime. The high collimation of jets predicted by the theory stands in good agreement with the experimental data. Furthermore, the angular distribution of the jets [14; 15] can give information related to the angular distribution of the initiating partons, which in turn is related to the spin of the parton. At SPEAR the first independent confirmation of the spin-1/2 of quarks was made.

The TASSO [16] experiment first observed events with three jets. These events have a lower momentum jet additional to the jets due to the primary quarks. The events were interpreted as evidence of "gluon radiation" from one of the primary quarks. The process is mostly longitudinally favored, but occasionally a gluon can be radiated with a high transverse-momentum to the quark direction. The high energy of the gluon permits it to initiate a separate jet that is observed in the detector. An example of such an event from SLD is shown in figure 2.4.

For the bound states where the strong coupling constant α_s is larger than unity, perturbative calculations are not valid anymore. Mean field approximations have some limited success in particles, however more complex phenomena like hadronisation, at the boundary between perturbative and non-perturbative QCD, are modeled

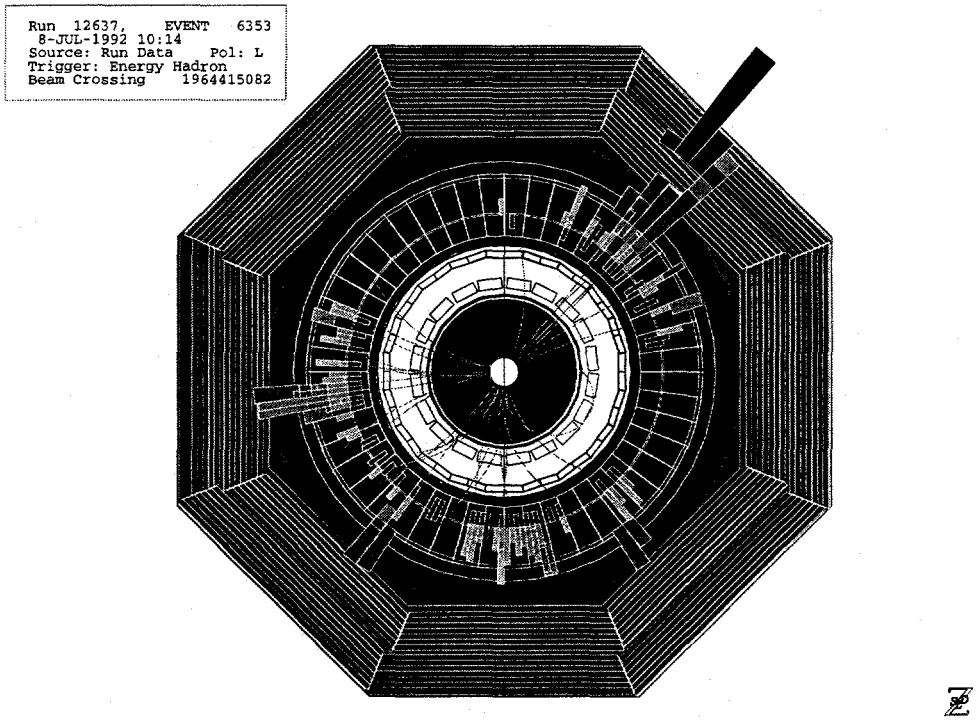

Figure 2.4: A 3-jet event recorded by SLD, viewed along electron-beam axis. The dashed lines are charged tracks measured by the tracking system (center).

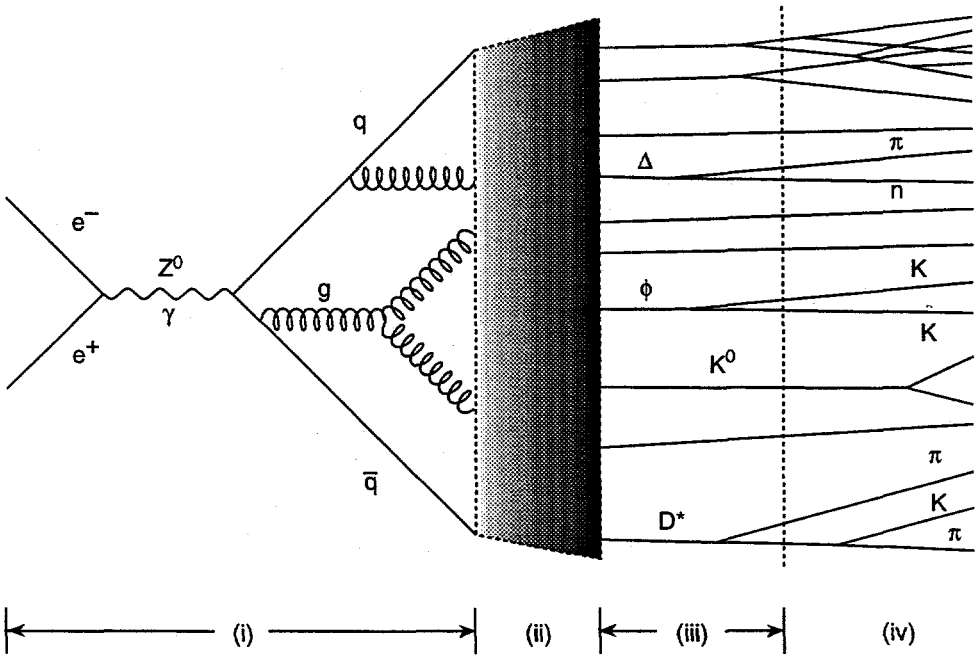

Figure 2.5: The three main phases of the $e^+e^- \rightarrow$ *hadrons* process: perturbative, hadronisation, and decay. Part (iv) is the experimentally accessible final state.

with difficulty. Several models for hadronisation that have been proposed are discussed below, however, experimental evidence remains crucial to the understanding of this process.

2.2.1. Hadro-Production in e^+e^- Collisions

From an experimental point of view the well understood initial state of e^+e^- machines is preferred due to its "clean background"[3].

The process of $e^+e^- \rightarrow$ *hadrons* is modeled [17] to proceed in three stages (figure

[3]The issue of background in this dissertation is related to particle identification where low jet multiplicities in the Čerenkov Ring Imaging Detector are preferred.

2.5):

(i) - Parton Shower Formation. This stage is understood theoretically as the creation of a $q\bar{q}$ pair and the initiation of the parton shower, calculable in perturbative QCD down to the level of $\alpha_s(\sqrt{s}) \approx 1$ where hadronisation takes place. The lowest order $e^+e^- \rightarrow q\bar{q}$ diagram (figure 2.6-a) is modified to first order QCD by the emission of a gluon (figure 2.6-b). The cross section for this process may be written [18] as:

$$\frac{d\sigma^2}{dx_1 dx_2} = \sigma_0 \frac{2\alpha_s}{3\pi} \frac{{x_1}^2 + {x_2}^2}{(1-x_1)(1-x_2)}, \tag{2.12}$$

where σ_0 is the tree-level cross section for $e^+e^- \rightarrow q\bar{q}$, and $x_i = 2E_i/\sqrt{s}$ the parton scaled energies, with $x_1 < x_2 < x_3$ and $\sum x_i = 2$. For $x_1, x_2 \rightarrow 1$ the cross section in (2.12) is divergent, however these singularities are canceled by the corresponding poles in the $e^+e^- \rightarrow q\bar{q}$ cross section from first order virtual corrections. In second order perturbative QCD, there are two additional processes: $e^+e^- \rightarrow q\bar{q}gg$ and $e^+e^- \rightarrow q\bar{q}q'\bar{q}'$ (figure 2.6-c). These cross sections have been calculated by several groups [19; 20] and the results are in good agreement with each other.

For configurations with a final state of more than 4 partons, or for virtual corrections to final states with only a few partons, the cross section calculations quickly become prohibitive due to the large number of Feynman diagrams involved. One approach to this problem is the *Parton Showers* (PS) approximation.

In the PS approach, the production of partons is viewed as successive branchings of

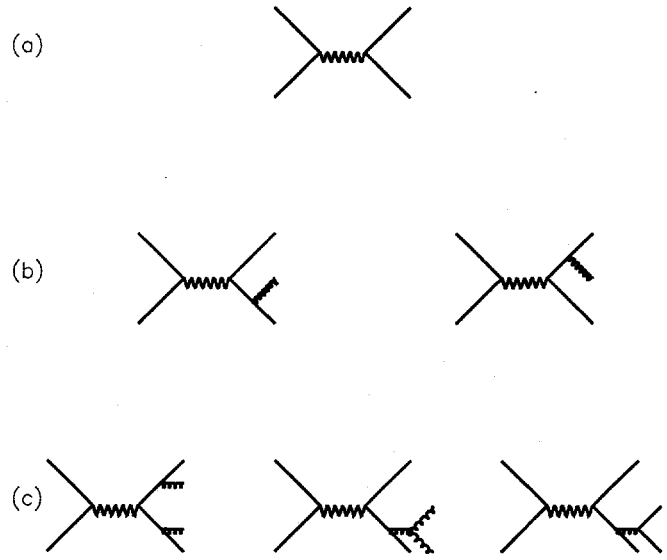

Figure 2.6: Example tree-level Feynman diagrams for (a) $q\bar{q}$ production, (b) $\mathcal{O}(\alpha_s)$ production of $q\bar{q}g$, and (c) $\mathcal{O}({\alpha_s}^2)$ production of $q\bar{q}gg$ and $q\bar{q}q'\bar{q}'$.

partons: $q \to qg$, $g \to gg$, or $g \to q\bar{q}$ (figure 2.7). A quark with 4-momentum fraction[4] z of a given parton can originate from a gluon with full fraction 1.0 4-momentum being absorbed on a quark, from a quark radiating a gluon and loosing 4-momentum, or from a gluon pair-producing $q\bar{q}$, of which q takes the fraction z of the gluon's 4-momentum. Similarly, a gluon can originate as radiation from a quark with full 4-momentum fraction 1.0, from another gluon radiating it, or from the annihilation of a $q\bar{q}$ pair, in which one of the fermions has full fraction 1.0 4-momentum. The processes are described by the Altarelli-Parisi equations [21]:

$$\frac{dq_i(z,Q^2)}{dlogQ^2} = \frac{\alpha_s}{2\pi}\int_z^1 \frac{dx}{x}\left[q_i(x,Q^2)P_{q\to qg}\left(\frac{z}{x}\right) + g(x,Q^2)P_{g\to q\bar{q}}\left(\frac{z}{x}\right)\right]$$

$$\frac{dg(z,Q^2)}{dlogQ^2} = \frac{\alpha_s}{2\pi}\int_z^1 \frac{dx}{x}\left[\sum_i q_i(x,Q^2)P_{q\to gq}\left(\frac{z}{x}\right) + g(x,Q^2)P_{g\to gg}\left(\frac{z}{x}\right)\right]$$

$$P_{q\to qg}(y) = \frac{4}{3}\frac{1+y^2}{(1-y)_+}$$

$$P_{g\to q\bar{q}}(y) = \frac{y^2+(1-y)^2}{2}$$

$$P_{q\to qg}(y) = \frac{4}{3}\frac{1+(1-y)^2}{y}$$

[4] At these energies quark masses are negligible, hence a fraction z of the momentum is equal to a fraction z of the energy, and equal to a fraction z of the 4-momentum

$$P_{g\to gg}(y) = 6\Big(\frac{1-y}{y} + \frac{y}{1-y} + y(1-y)\Big) \tag{2.13}$$

where $q_i(z, Q^2)$ is the probability that a quark q_i extract a 4-momentum fraction z from a parton at phase-space momentum transfers of Q^2 in the shower. Similarly $g(z, Q^2)$ refers to a gluon g. The phase-space parameter Q^2 has a natural cut-off scale Q_0^2 at which the shower terminates when approaching the hadron mass scale. At this stage large momentum transfers within the shower are not possible anymore as the partons become "locked" inside hadrons. The cut-off is equivalent to an effective parton mass and it is dictated by the domain of applicability of perturbative calculations ($\alpha_s < 1$, energies above hadron mass scale) that ensure convergence of the equations. By recurrently applying the Altarelli-Parisi equations in a probabilistic manner the "Parton Shower" in figure 2.7 can be calculated.

(ii) - Hadronisation. In this phase the partons of the shower have reached the hadron mass energy scale, cannot fragment further and form hadrons and resonances. Due to the non-perturbative nature of the process, several phenomenological models have been proposed to describe it. The three main "schools" of fragmentation models are: independent fragmentation, string fragmentation, and cluster fragmentation.

Independent Fragmentation (IF) dates back to the early 1970's, when it was suggested as a simple model by Field and Feynman [22]. The model was initially popular due to the availability of Monte Carlo programs [23]. It assumes that the fragmen-

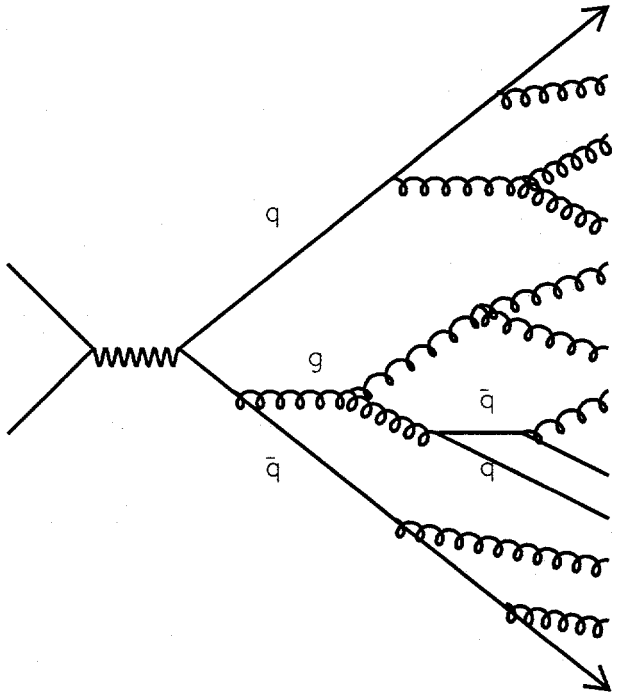

Figure 2.7: Schematic of a Parton Shower.

tation of any system of partons can be described by an incoherent sum of independent fragmentation processes. The drawback of this assumption is that neither 4-momentum is conserved, nor is the model Lorentz invariant. Although both problems have been solved, today the IF model is rarely used in e^+e^- experiments.

The first example of a *String Fragmentation (SF)* model was introduced in 1974 by Artru and Mennessier [24], with the major developments to the model being brought by the Lund group [25; 26]. The model is based on the idea that asymptotic freedom occurs as a color flux tube [27] connecting two quarks breaks. Consider the field lines connecting two color charges (figure 2.8). This is analogous to the electromagnetic field lines connecting two electrically charged objects, with the difference that for quarks the field lines are bunched together by gluon-gluon coupling. Assuming an approximately constant energy density per string unit length, estimated at approximately 1 GeV/fm, the potential energy of the string increases linearly with quark separation. Once the potential energy has grown sufficiently to produce a $q\bar{q}$ pair, the string breaks with some probability and forms two separate strings. If the invariant mass of either of the new strings is above the hadron mass scale, further splitting occurs till only hadrons remain.

Classically, massless quarks can be produced at a point. If they have mass or transverse momentum with respect to the string axis, then they are produced at some distance apart such that the energy is supplied by the string. Quantum mechanically

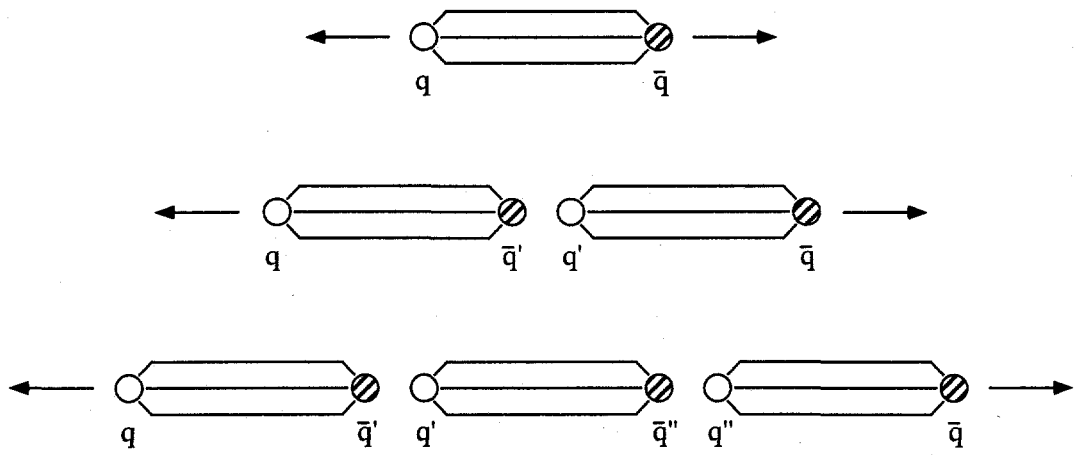

Figure 2.8: Color tube stretching between a q and $\bar{q}$. Increased separation of the q and $\bar{q}$ rises the potential energy in the string to the threshold of $q'\bar{q}'$ creation, when the string breaks.

the $q'\bar{q}'$ pair is produced at a point and it tunnels to the "allowed" region with a probability [27] that depends on the transverse momentum p_T and the quark mass:

$$P = \exp(-\frac{\pi(p_T^2 + m^2)}{\kappa}), \tag{2.14}$$

where κ is the string constant. In this model both heavy and large spin particles are suppressed. The mass term in the exponent causes heavy quarks to be extinct in light flavor events as the production ratios are $u : d : s : c : b \sim 1 : 1 : 0.3 : 10^{-11} : 10^{-73}$. The u and d quarks have similar production probabilities, while the s is suppressed by 0.3. The strangeness suppression factor is an important parameter in all fragmentation models [28] and a direct measurement of this quantity will be discussed in Chapter 7.

In the Lund model the probability for the production of a $q\bar{q}$ pair is described by:

$$f(z) = z^{-1}(1-z)^a \exp\frac{-b(p_T^2 + m^2)}{z}. \tag{2.15}$$

where z and $(1-z)$ are the energy fractions of the daughter strings. The parameters a, b are tuned to fit the experimental data [29] and are different for each quark flavor as well as for the formation of mesons versus baryons.

Cluster Fragmentation (CF) as in the Webber Model [30] is implemented in the HERWIG Monte Carlo program. A parton shower is used to form clusters with no

internal structure or color. The clusters are characterized by mass and flavor content, and are used as elementary building blocks for the hadrons. The heavy clusters fragment into lighter clusters, and ultimately these fragment into the experimentally observed hadrons. Conservation of 4-momentum is achieved by its exchange among neighboring clusters.

(iii) - Decay of Unstable Hadrons. In this phase heavy and unstable hadrons decay into the final state hadrons. The quantitative features of the decays are usually well known from experimentally determined branching fractions. By experimentally reconstructing the final state hadrons, knowledge is gained about the output of the hadronisation process.

2.2.2. MLLA/LPHD Model and Analytic Predictions

A semi-phenomenological model has been proposed for understanding hadronisation. *Local Parton-Hadron Duality* (LPHD) [31] asserts that at any stage of the Parton Shower the parton and hadron distributions bear a close correspondence. It is possible then to infer parton distributions from experimental data and reciprocally, to predict experimental *primary* hadron distributions from parton shower calculations described above.

Parton distributions have been calculated in the *Modified Leading Logarithmic Approximation* (MLLA) [32; 33]. Using the LPHD hypothesis, the distribution of

hadrons with respect to the scaled momentum $x_p = p_{hadr}/p_{beam}$ is:

$$x_p \bar{D}_i^f(x_p, Y, \lambda) = \mathcal{K} \cdot \frac{4C_F(Y+\lambda)}{bB(B+1)} \int_{\epsilon-i\infty}^{\epsilon+i\infty} \frac{d\omega}{2\pi i} x_p^{-\omega} \Phi(-A+B+1, B+2, -\omega(Y+\lambda)) \tag{2.16}$$

where the quantities in the equation are: A, B, C_F, b constants, $Y = log(E\Theta/Q_0)$ with Θ being the jet cone opening angle, Q_0 the parton evolution energy cut-off parameter, and E the center of mass energy. The quantity λ is: $\lambda = log(Q_0/\Lambda)$, where Λ is the QCD scale parameter. $\mathcal{K}$ is a function of both ω and λ as follows:

$$\mathcal{K} \equiv K(\omega, \lambda) = \frac{\Gamma(A)}{\Gamma(B)} (\omega\lambda)^B \Psi(A, B+1, \omega\lambda) \cdot C_i^f \tag{2.17}$$

In the equations above Φ and Ψ are solutions of the confluent hyper-geometric equation and the constants used are: $C_F = 4/3$, $A = 12/b\omega$, $B = 307/27b$, $b = 23/3$. The indices i and f refer to the initiating parton of the jet and the final parton spectrum, e.g. - C_q^g refers to the gluon distribution in a quark jet.

At hadron scale energies ($Q_0 \approx \Lambda$) the spectrum approximates to a gaussian in the $\xi = -ln(x_p)$ variable under the assumptions of the MLLA approximation:

$$\bar{D}(\xi, Y) \approx \mathcal{N}(Y) \left(\frac{36C_F}{\pi^2 b Y^3}\right)^{1/4} \exp\left[-\sqrt{\frac{36C_F}{b}} \frac{(\xi - \xi^*)^2}{Y^{3/2}}\right] \tag{2.18}$$

where $C_g^g = 1$, $C_q^g = \frac{4}{3}$ and the limiting parton multiplicity $\mathcal{N}$:

$$\ln \mathcal{N} \approx \frac{1}{b}\sqrt{\frac{32\pi C_F}{\alpha_s(Y)}} + \left(\frac{B}{2} - \frac{1}{4}\right)\ln \alpha_s(Y) + O(1) \tag{2.19}$$

The parton shower multiplicity increases with ξ, reaches a maximum at the cut-off scale Q_0 where hadronisation collects partons into hadrons (limiting parton multiplicity, equation 2.19) and decreases thereafter with the decrease in momentum (increase in ξ).

As the center of mass energy increases, the value of ξ corresponding to the maximum of the distribution, ξ^*, shifts to higher values:

$$\xi^* = Y\left(\frac{1}{2} + a\sqrt{\frac{\alpha_s(Y)}{32\pi C_F}} - a^2\frac{\alpha_s(Y)}{32\pi C_F} + \cdots\right) \sim log(E) \tag{2.20}$$

where

$$a = \frac{11}{3}C_F + \frac{2n_f}{3N_c^2}, \tag{2.21}$$

The predicted gaussian shape of the spectrum as well as the ξ^* energy dependence have been observed by a number of experiments operating at different center of mass energies [34]. The ξ^* dependence on the hadron mass however is not clearly understood. The stand alone meson data follows a curve similar to the expected theoretical prediction, but when combined with the baryon data, there is no immediate mass dependence that can be asserted. This behaviour could be due to the fact that heavier

hadrons originate at a higher effective cut-off Q_0, thus a lower ξ^* value. Another source that can prevent experiments from seeing the expected dependence is the "contamination" of the measured spectra by particles from secondary sources [35]. For instance experimentally observed pions may originate directly from fragmentation, but also from ρ decays, K^* decays, *etc.* Additional complications arise from the presence of heavy quarks in two ways. The heavy quarks give hard (high momenta) background distributions that contaminate the measured spectra and also, since the calculations assumed massless partons they do not apply well in heavy quark events at energies below 2-5 GeV. Using flavor tagging techniques discussed in Chapter 5, spectra in light-quark samples will be presented in Chapter 7 in addition to the conventional inclusive measurement that has contaminating sources such as the heavy hadron decays.

Chapter 3

The SLAC Linear Collider and the SLAC Large Detector

The data used for this analysis was collected with the SLC Large Detector (SLD) experiment at the Stanford Linear Accelerator Center (SLAC), California. The beams are accelerated by the SLAC Linear Collider (SLC) that consists of a 2 mile long linear accelerator (LINAC) and two separate arcs which deliver the beams to the interaction point (IP). Both electrons and positrons travel in the same vacuum pipe and are accelerated in a two phase machine cycle. The unique feature of SLC is its capability of delivering longitudinally highly polarised electrons into a very stable, highly focused, $1\mu m$ cross section interaction point (IP).

3.1. The SLAC Linear Collider (SLC)

SLAC (figure 3.1) was constructed in the 1960's to study the internal structure of the nucleon by scattering of 20 GeV electrons on fixed targets [36]. During the 1980's

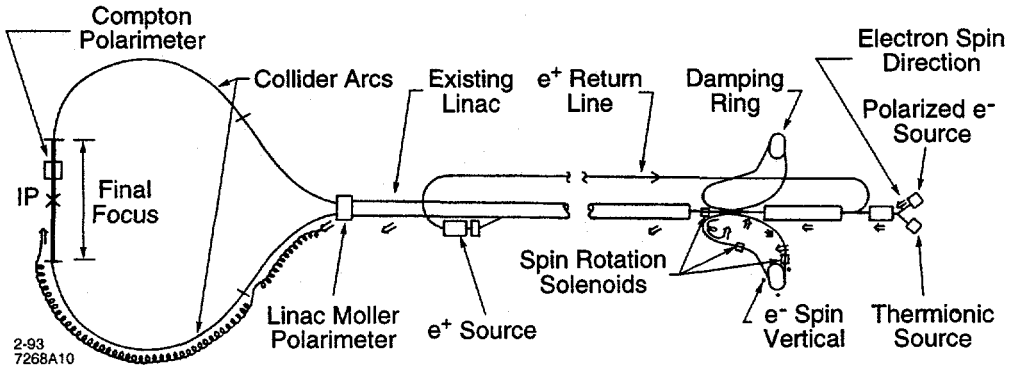

Figure 3.1: The SLC layout.

it was upgraded to a single pass electron-positron collider, the SLC, with a center of mass energy of 91 GeV (the Z^0 threshold).

The electron source of the SLC is capable of delivering polarised electrons with longitudinal polarisation of up to 80%. This feature is of very much interest for electroweak physics, as well as for QCD studies in quark and anti-quark jets as described in Chapter 7.

At the start of each 120 Hz cycle, the polarized electron source directs two 1 mm long bunches of 6×10^{10} electrons to the LINAC. They are accelerated to an energy of 1.19 GeV and stored in the north damping ring of the SLC. The role of the damping rings is to compress the phase space of the bunches as close to an ideally monochromatic energy as possible. Immediately before entering the damping ring the polarisation of the bunch is rotated from longitudinal to transverse in order to preserve it from depolarisation in the damping ring.

The two electron bunches and a positron bunch from the previous machine cycle

exit the damping rings and are further accelerated in the LINAC. The leading e^+ bunch and the first e^- bunch reach 46.7 GeV at the end of the LINAC, enter the 1km long arcs and intersect at the IP. Losses due to synchrotron radiation reduce the energy of the two bunches to 45.6 GeV each (half the Z^0 mass) at the IP. Due to depolarisation and spin precession in the arcs, the electron spins are rotated before they enter the arcs such that they reach the IP longitudinally polarised. The depolarisation in the arcs is due to the effect on the electron spin precession of the coupling between vertical betatron oscillations and dipole bending.

The trailing e^- bunch is accelerated only up to 30 GeV, after which it is extracted from the LINAC and brought into collision with a Tungsten-Rhenium alloy target to produce positrons. The result is a shower of particles, mostly electrons, positrons and photons, from which the positrons are extracted by magnets and directed back to the front end of the LINAC via a return line for use in the next machine cycle.

SLC luminosity (figure 3.2) has increased over the 1992, 1993, 1994-95 and 1996 physics runs as shown in figure 3.2. The future plans are for a 1997 run of 9 months with a goal to reach on the order of 200000 collected Z^0's.

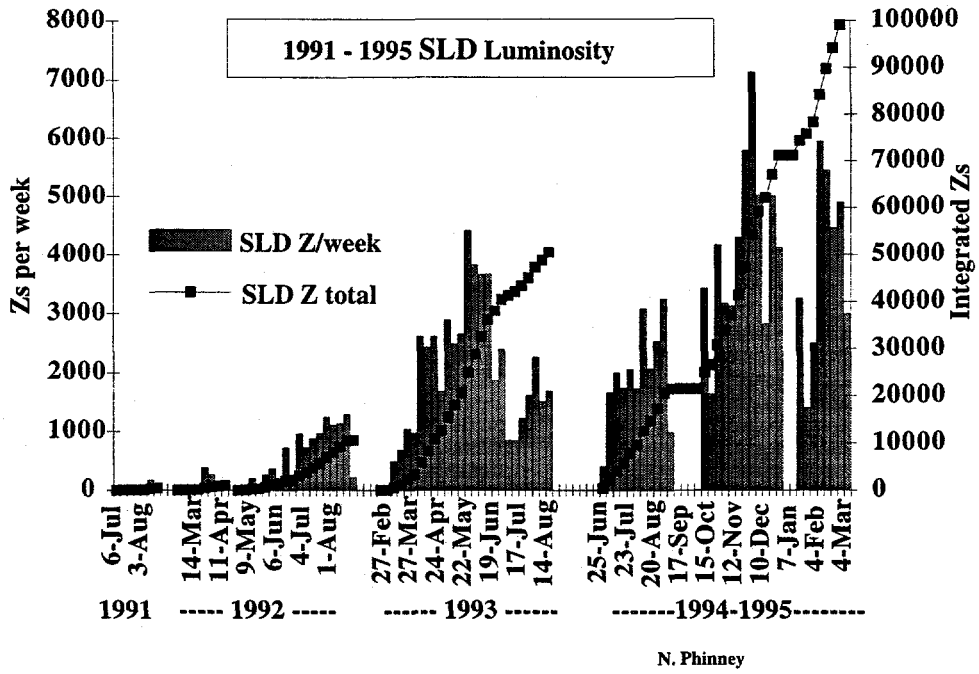

Figure 3.2: Time history of Z^0 production at SLC/SLD.

3.2. Polarisation at SLC

3.2.1. The Polarized Electron Source

Polarisation at SLC is achieved using a Gallium-Arsenide (GaAs) photo-cathode electron gun [37]. Left and right circularly polarized laser-light from a Nd:YAG-pumped Ti:sapphire laser is used to selectively excite electron transitions from the GaAs bulk to the longitudinally-polarized energy states. A thin layer of Cs is applied to the GaAs surface to lower the extraction work function and allow electrons to escape to the vacuum.

The 1992 physics run used a bulk GaAs cathode. Figure 3.3 shows the energy levels of GaAs and the corresponding transition probabilities. The transitions of interest are those marked as (3). Left or right polarisation of the laser excites the electron with the desired polarisation. However, the energy tuning of the laser excites both transitions marked (3) and (1). Their relative intensities are as labeled, so the maximum achievable polarisation is:

$$\mathcal{P} = \frac{P_{right} - P_{wrong}}{P_{right} + P_{wrong}} = \frac{3-1}{3+1} = 50\% \tag{3.1}$$

The average polarisation actually obtained [38] was 22%. The 1993 run used a strained-lattice cathode consisting of GaAs grown on a GaAsP (Gallium-Arsenide-Phosphide) substrate. In this case the levels generating the (1) transitions are energy

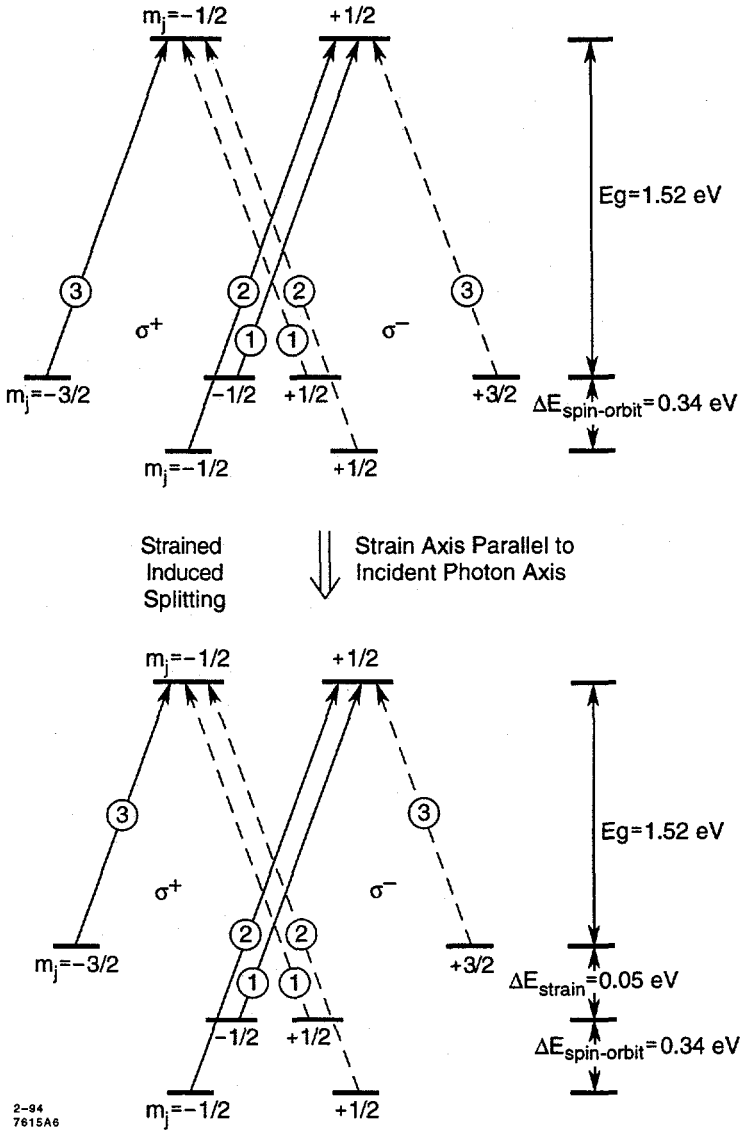

Figure 3.3: The energy state diagram for bulk GaAs (top) and the changes it undergoes when the lattice is strained (bottom). Polarisation is due to the preference of certain excitation modes; the relative sizes of the matrix elements are shown in the circles. For the bulk GaAs, the maximum theoretical polarisation is 50%, and for the strained lattice, 100%.

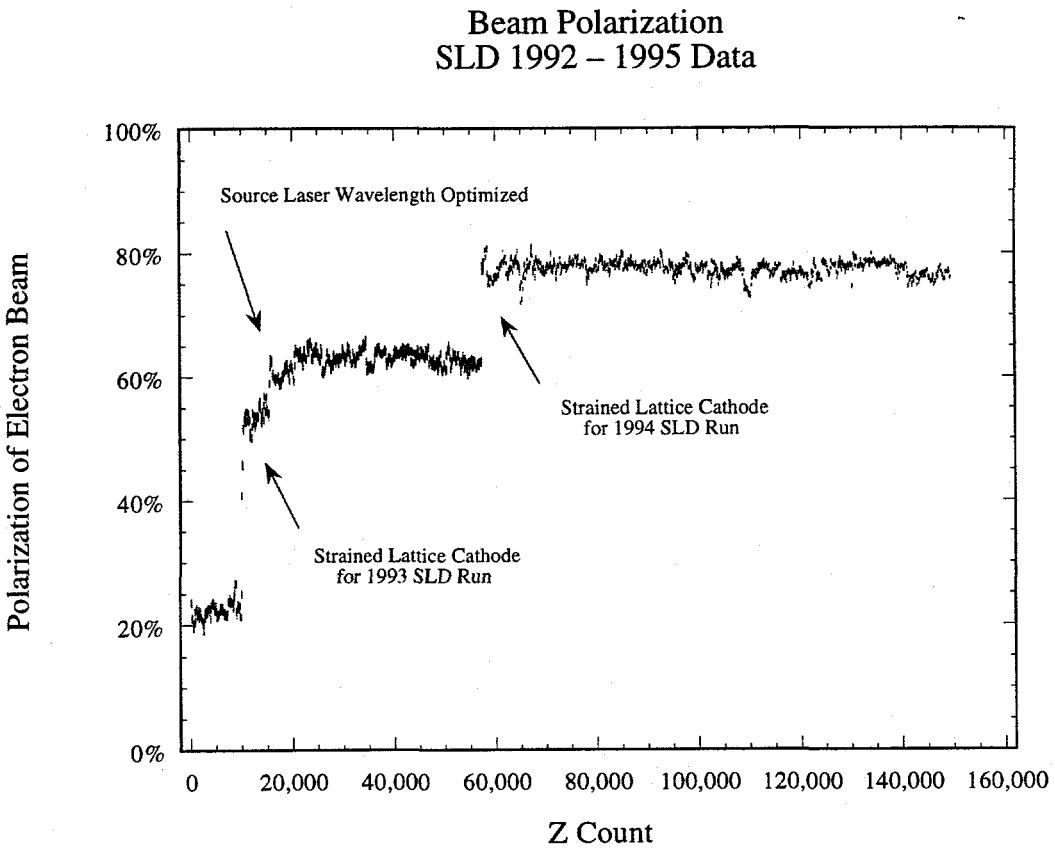

Figure 3.4: Polarisation history at SLC/SLD.

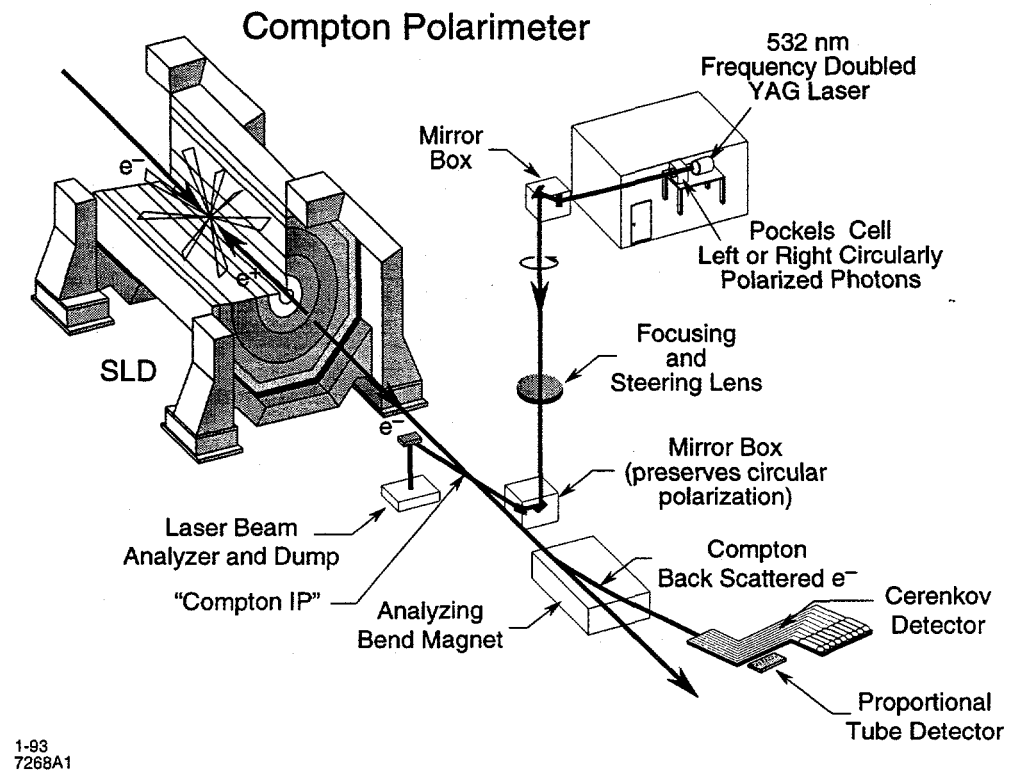

Figure 3.5: The Compton Polarimeter.

detuned and only the desired transitions (3) contribute. The maximum theoretical polarisation is in this case 100%. The polarisation achieved for the 1993 run was 65% [39]. An improvement for 1994-95 was the use of an ultra-thin GaAs cathode with the measured polarisation reaching 80% (figure 3.4).

3.2.2. The Compton Polarimeter

The polarisation of the electron beam near the IP is measured using a Compton scattering polarimeter [2]. The main components of the polarimeter are the laser,

polarizing optics and the electron spectrometer (figure 3.5). The circularly polarized laser beam is focussed onto the electron bunches at approximately 30 m away from the IP downstream. The laser beam Compton scatters on the electrons causing them to lose momentum and deviate as they pass through the precision analysing dipole magnet. The momentum spectrum of the scattered electrons is measured with Čerenkov and proportional tube chambers, into channels based on the scattering deflection angle.

The differential cross section for Compton scattering of polarised electrons and photons is:

$$\frac{d\sigma}{dE} = \frac{d\sigma_u}{dE}[1 + P_\gamma P_e A_c(E)], \tag{3.2}$$

where σ_u is the unpolarized Compton scattering cross section, P_γ the measured photon polarisation and P_e the electron polarisation. A_c is the Compton asymmetry and it depends on the energy of the scattered electron and the relative orientation of the electron and photon spins [2]. A_c can be calculated precisely, thus the precision of the Compton polarimeter is limited only by detector systematics. From equation 3.2 an asymmetry can be formed:

$$A = \frac{N^{\nearrow\nearrow} - N^{\nearrow\swarrow}}{N^{\nearrow\nearrow} + N^{\nearrow\swarrow}} = P_\gamma P_e A_c(E) \tag{3.3}$$

where $N^{\nearrow\nearrow}$ is the number of backscattered electrons accumulated during a $\sim$ 10

minute period for events with the laser and electron spins aligned, and $N^{\nearrow\swarrow}$ for spins anti-aligned. Using this asymmetry the electron polarisation can be derived.

The average longitudinal polarisation at the IP during the SLD runs was: $63.0 \pm 1.1\%$ in 1993, $77.22 \pm 0.51\%$ [40] in 1994-95, and $76.0 \pm 0.6\%$ in 1996.

3.3. The SLD

The SLD was proposed in 1984 [41] as a general purpose detector designed for nearly 4π solid angle coverage of the interaction point. Figure 3.6 shows a section through the SLD and figure 3.7 one quadrant of the detector. The SLD consists of identical subsystems for two geometric regions: the *Barrel*, a cylindrical region of 4.5 m radius and 10 m length, and the *End Caps*, regions that close the two faces of the *Barrel*. The e^+e^- beams enter along the axis of the detector, and the various detector subsystems are arranged radially within the cylinder. At small angles to the beam due to beam-pipe and related support structures there is no detector coverage. However, overall, the SLD provides 98% coverage in solid angle.

The outer support structure for the SLD inner sub-systems is a 0.6 T conventional magnetic coil. The magnetic flux return iron is the Warm-Iron Calorimeter (WIC).

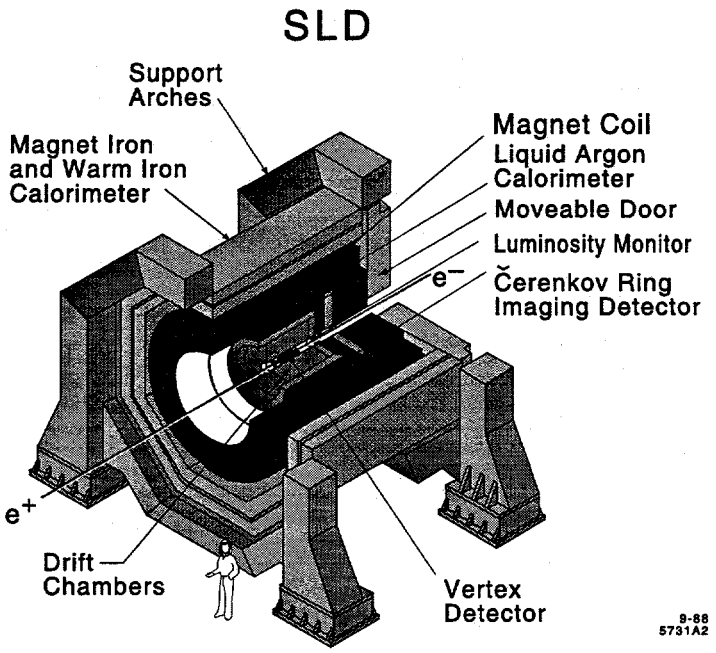

Figure 3.6: The SLD detector (isometric view). The endcaps have been removed for clarity.

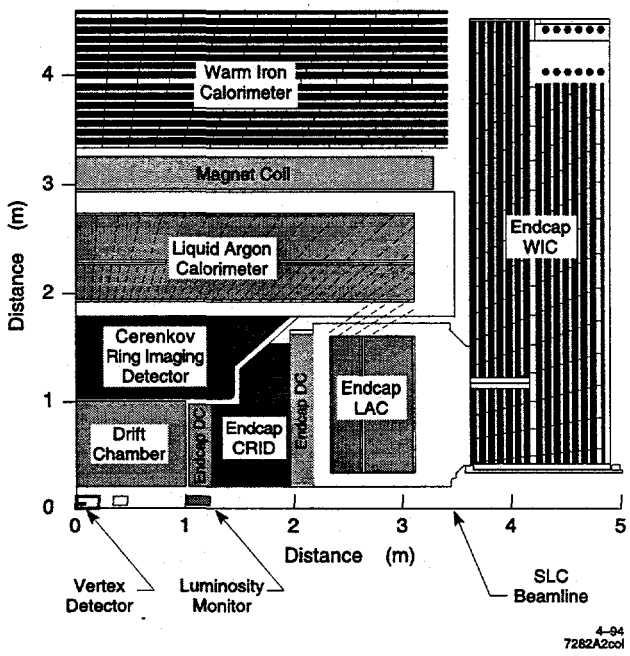

Figure 3.7: Quadrant view of the SLD detector.

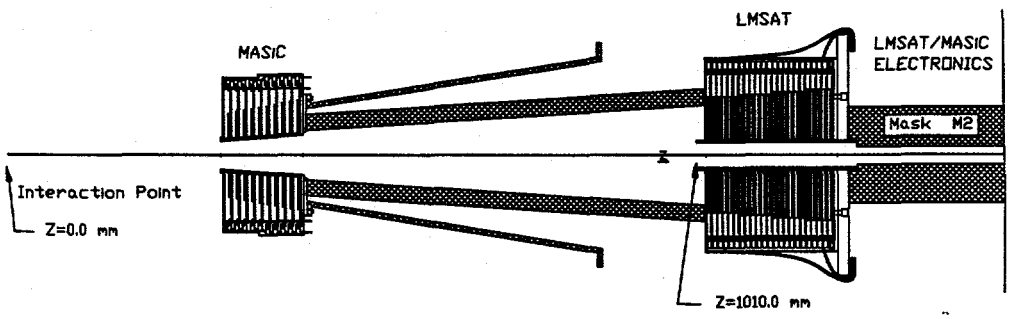

Figure 3.8: The SLD LUM, showing the LMSAT and the MASiC.

3.3.1. The Luminosity Monitor (LUM)

The Luminosity Monitor provides high-precision monitoring of the luminosity [42]. The LUM also extends electromagnetic calorimetry coverage down to very small polar angles for the Liquid Argon Calorimeter (Section 3.3.5).

The LUM (figure 3.8) is divided into two modules: the Luminosity-Monitor/Small-Angle Trigger (LMSAT) mounted on the Superconducting Final-Focus triplet and the Medium Angle Silicon Calorimeter (MASiC). The polar angle coverages are of 28-68 mrad for the LMSAT, 68-200 mrad for the MASiC and above 200 mrad for the EndCap LAC.

3.3.2. The Vertex Detector (VXD)

The VXD is composed of ladders of Charge-Coupled Devices (CCDs) arranged concentrically around the IP. Charge deposition from minimum ionizing particles traversing the active region is recorded by the 120 million pixels and is reconstructed

to point to the origin of the particle's trajectory.

There are four (figure 3.9) concentric cylinders supported by beryllium shells that house 60 ladders of 9.2 cm long. The ladders have eight CCD's each, four on each side for symmetry in polar angle, covering a range down to $cos(\theta) = 0.75$.

The CCD's contain $\sim 200K$ pixels, each $22\mu m^2$ in size. Charged particles passing through the VXD hit approximately 2.3 pixels per CCD. The inner layer of CCD's is at 29.5 mm radially from the IP, and the outer layer at 41.5 mm. Each layer is about 0.011 radiation lengths thick[1]. Inside the inner-most CCD layer is the VXD cooling jacket and a thin beryllium cylinder that forms the beampipe section around the IP. The total radiation thickness of the material between the IP and the first CCD layer is 0.0071 X_0.

Single hit resolution is determined using tracks that have three VXD hits. Figure 3.10 shows the residual between the found and expected hit positions on the VXD middle layer, where the expected position is projected using the inner and outer layer VXD hits. After correcting for the resolution of the inner and outer hits, the single hit resolution is approximately 5 μm in the $r\phi$ plane and 5-9 μm in the rz plane, the latter being dip-angle dependent. For high momentum tracks, such as muons from $Z^0 \rightarrow \mu^+\mu^-$ events, typical impact parameter resolutions are 12 μm in the $r\phi$ plane and 38 μm in the rz plane [44].

[1] A charged particle loses energy by a factor of $1/e$ over 1 radiation length (X_0) of material via bremsstrahlung [43]. The geometrical significance of $1X_0$ varies with the material.

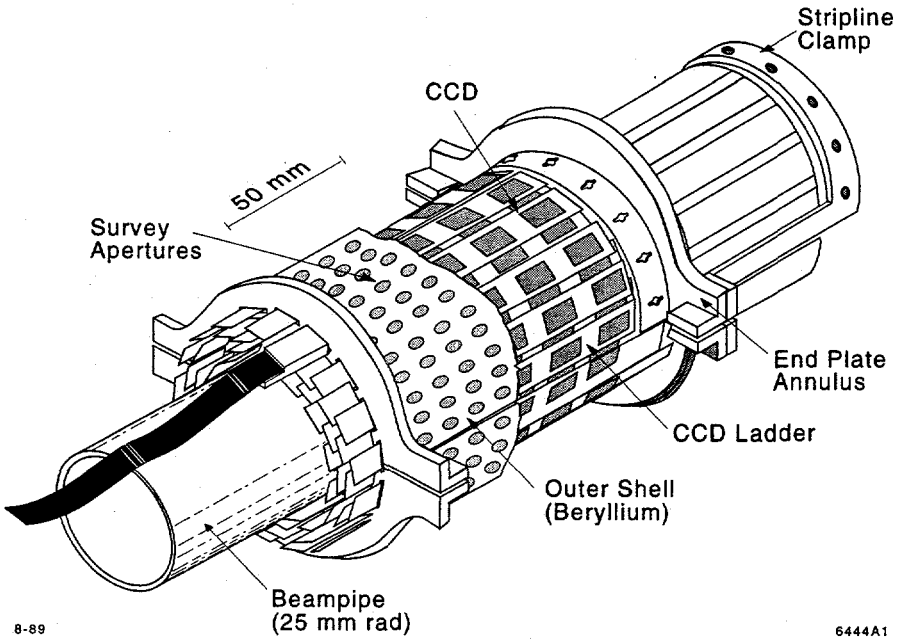

Figure 3.9: The SLD VXD vertex detector.

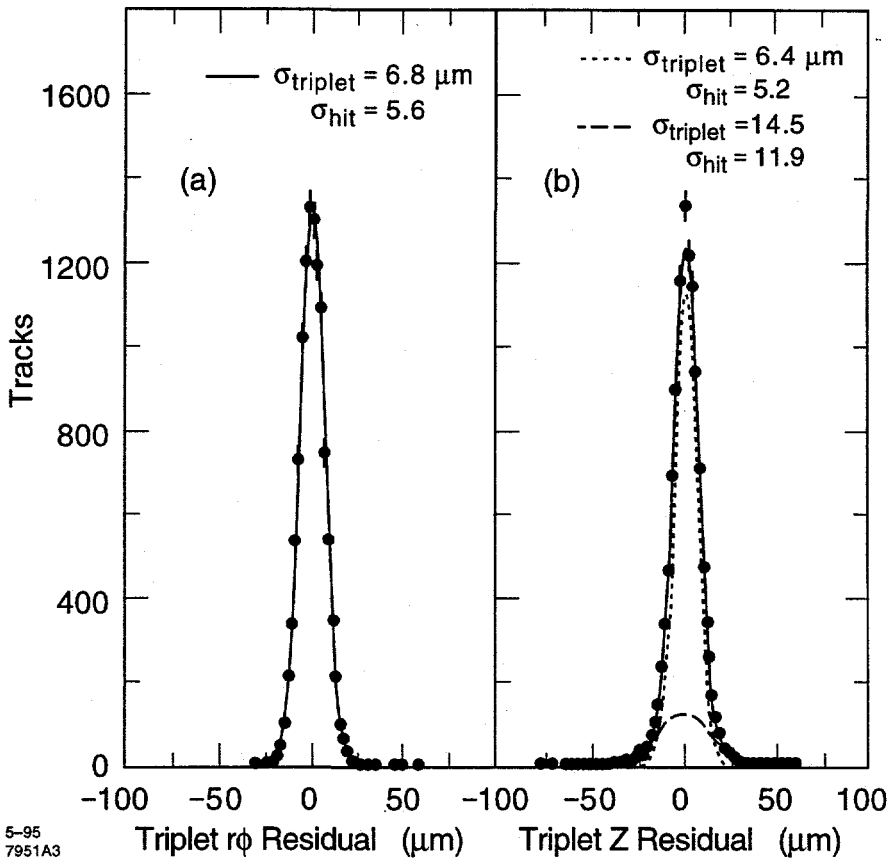

Figure 3.10: VXD single hit resolution in (a) the $r\phi$ plane and (b) the rz plane.

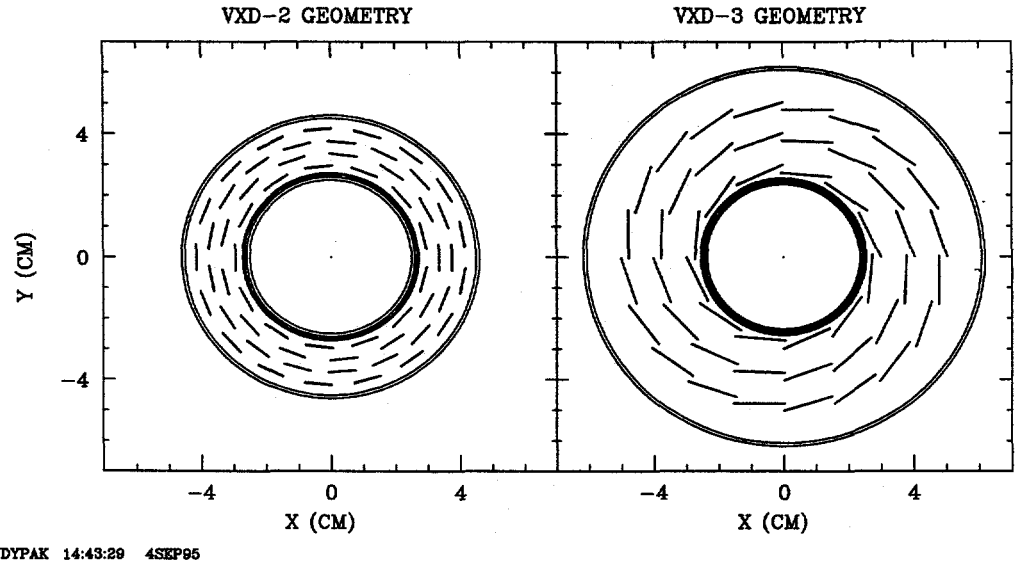

Figure 3.11: An end-view comparison of the current "VXD2" vertex detector and the new "VXD3" tracker. The overlapping CCDs insure that at least three spatial points are obtained for charged tracks that traverse all three layers.

In early 1996 the VXD detector was upgraded to the VXD3 detector. The special feature of the new vertex detector is that each track has minimum three spatial points. This allows SLD to do stand alone tracking with VXD3. Also, the VXD3 ladder length is longer and can provide coverage for up to $cos\theta = 0.9$. Figures 3.11 and 3.12 compare the end and side views of the two vertex detectors. VXD3 has taken approximately 50000 Z^0's data during the 1996 run.

3.3.3. The Drift Chambers

There are two drift chamber systems in the SLD - the Central Drift Chamber (CDC) and the EndCap Drift Chambers (EDC's). The CDC covers roughly 80%

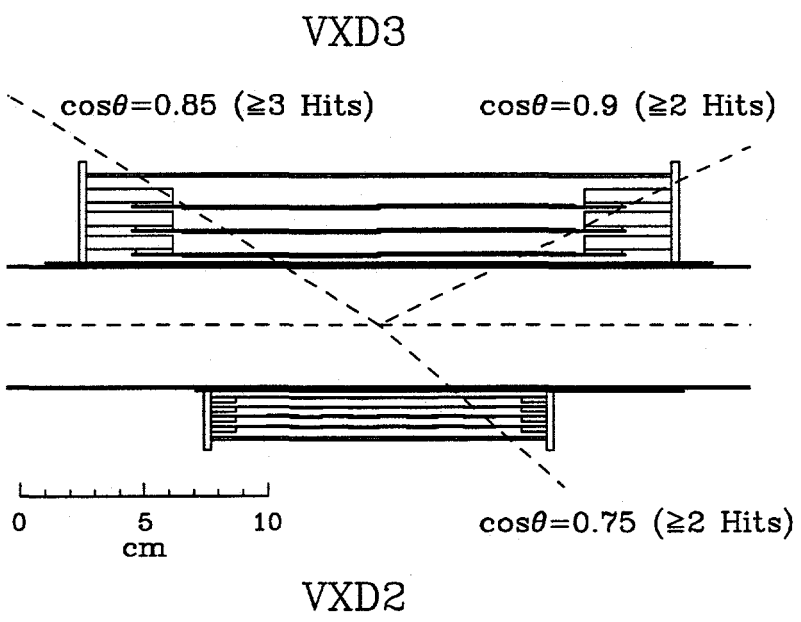

Figure 3.12: A side view comparison of VXD2 and VXD3. The new tracker provides coverage up tp 0.9 in $\cos\theta$.

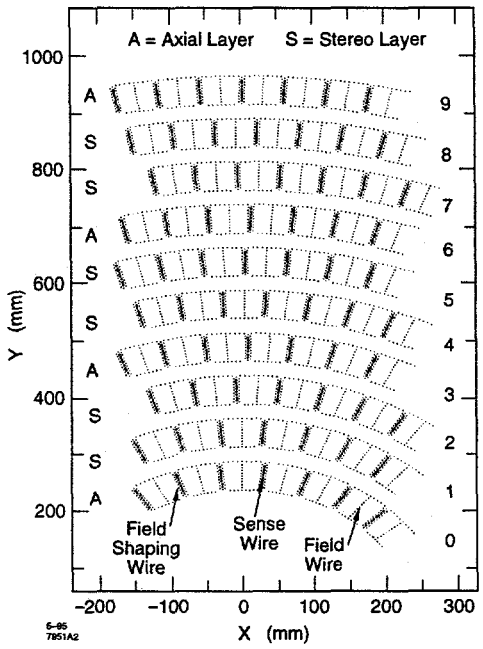

Figure 3.13: SLD's Central Drift Chamber (CDC).

of the solid angle and operates in a uniform solenoidal magnetic field of 0.6 T. The outer diameter is 1 m, the inner diameter 20 cm and the length 2 m. There are 10 "superlayers" of drift cells, each approximately 6 cm $\times$ 5 cm in the CDC. The superlayers are staggered in orientation (figure 3.13), the sense wires in the superlayers having either an axial, or a 41-mrad stereo angle orientation with respect to the beam line.

Each cell contains field shaping wires, guard wires, and sense wires (figure 3.14). As the charged track traverses the cell, a trail of ions is produced in the CO_2 (75%), argon (21%), isobutane (4%), water (0.2%) drift gas. The drift field directs the ions onto the 8 sense wires. The position of the hit is known from the wire address, the

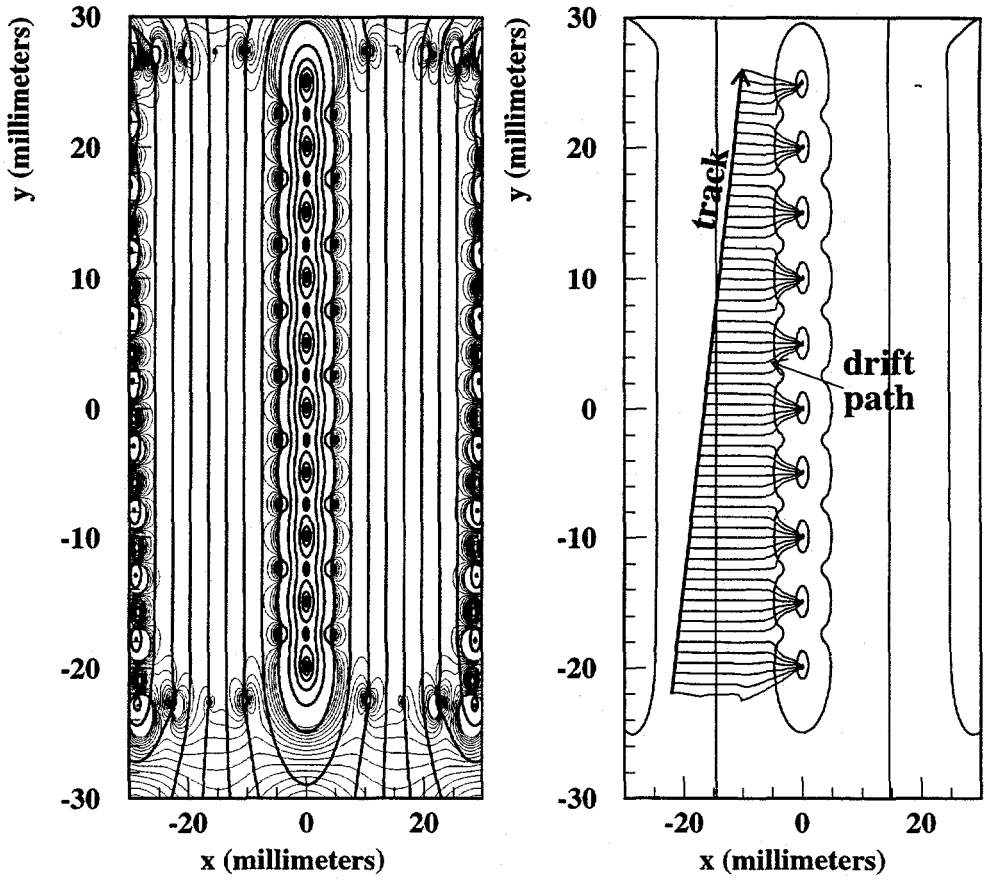

Figure 3.14: The field map for a drift cell of the CDC. The left figure shows the field configuration for a CDC cell. The right figure shows a drift path of charges caused by the passing of a charged track through the cell.

proximity to the wire hit (drift time) and the position on the wire (charge division). Information from other sense wires in the cell is used to form an approximate track vector (a vector hit). The sense wires in the cell are not staggered, so each vector hit has a mirror image on the opposite side. A pattern recognition program is then used to combine vector hits starting from the outer layers and form track candidates. Each candidate is validated, modified or rejected by a program that takes into account all known information: electric and magnetic field variations, energy loss, scattering. The momentum resolution function for the CDC has been measured to be $(dp_t/p_t)^2 = 0.0050^2 + (0.010/p_t)^2$, where p_t [GeV/c] is the momentum of the charged track in the plane perpendicular to the beam axis. The first term in the resolution function is the multiple scattering error, while the second, the measurement error [45].

3.3.4. The Čerenkov Ring-Imaging Detector (CRID)

The Čerenkov Ring-Imaging Detector (CRID) provides efficient charged particle identification over a wide momentum range. The CRID follows the general SLD partition into an End Cap and a Barrel system. The operating principle of the CRID is that particles traveling faster than the speed of light in a given medium emit a shock wave of Čerenkov photons at an angle to the track of $\cos\theta_c = 1/\beta n$ where $\beta = v/c$ and n is the medium's index of refraction. This implies that the particle needs to have a minimum velocity $\beta_{threshold} = 1/n$. Čerenkov light is emitted uniformly along

the trajectory at the angle θ_c making possible the use of mirrors with focal plane the detector, that collect the light into a ring.

The detector is a Time-Projection Chamber (TPC) filled with C_2H_6 drift gas and a gaseous photo-cathode additive, tetrakis(dimethylamino)ethylene (TMAE). TMAE is ionized by UV Čerenkov photons and it releases photo-electrons in the drift gas. The high voltage is set such that the drift of the photo-electrons to the anode plane of the detector achieves the best time to distance resolution. The other two coordinates are reconstructed from the wire address and the charge division on the wire. The full ring of reconstructed photo-electrons provides the necessary information for calculating the particle's velocity. Together with the momentum of the track it is possible to distinguish between electrons, muons, pions, kaons and protons, the five charged long lived particles ($c\tau > 1m$) tracked by the SLD drift chambers.

A detailed description of the CRID system is given in Chapter 4.

3.3.5. The Liquid Argon Calorimeter (LAC)

The Liquid Argon Calorimeter (LAC) is a lead-argon sampling calorimeter designed to measure the energy of charged and neutral particles [41]. The barrel LAC has an inner radius of 1.8 m and an outer radius of 2.9 m with a solid angle coverage of $\theta = 35° - 145°$. The two endcap sections have a coverage of $8° - 35°$. Overall, the LAC covers 98% of the solid angle around the IP.

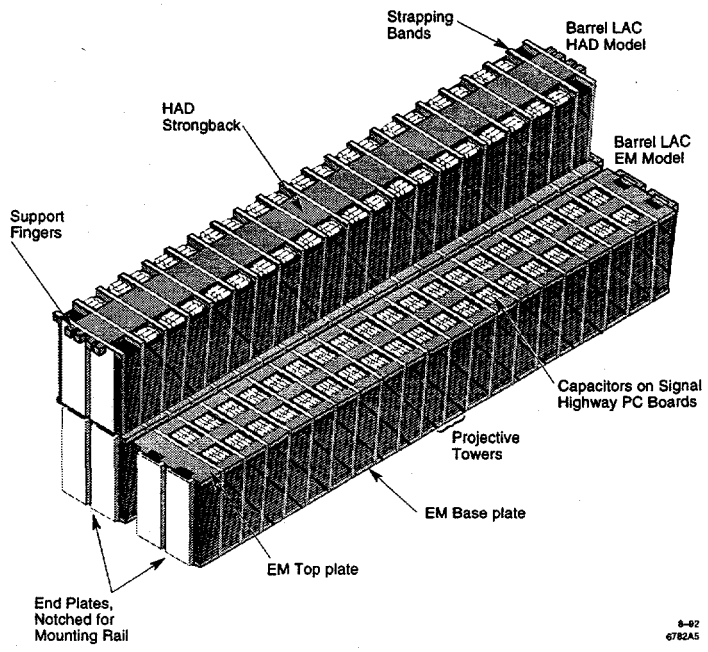

Figure 3.15: View of a LAC module, showing the inner EM and outer HAD sections.

The two innermost layers of the LAC are thin and designed to measure electromagnetic showers of electrons or photons. The two outer layers are denser and are designed to measure hadronic showers of neutral and charged hadrons.

There are 21 radiation lengths in the electromagnetic sections of the LAC and 2 interaction lengths[2] in the hadronic (HAD) sections. The overall hadronic stopping power is of $2.8\lambda_0$.

The LAC is divided into modules (figure 3.15), each consisting of radial layers of lead and argon. The layers are parallel plates of lead separated by non-conducting spacers immersed in liquid argon. Particles interacting with the lead produce sec-

[2]A hadron loses energy by a factor of $1/e$ over 1 interaction length (λ_0) of material via nuclear interactions [43]. The geometrical significance of $1\lambda_0$ varies with the material.

ondary showers of low energy particles which ionize the argon. High voltage is applied to every other layer of lead, producing a field that directs the charges onto the opposite layer. Several lead tiles from adjacent layers are connected electrically to form projective towers (units of constant cross-section viewed from the IP). Each tower is connected to an amplifier that measures the deposited charge. Argon provides no amplification of charge, hence the signal is proportional to the deposited energy.

The barrel and endcap portions of the LAC are segmented in polar and azimuthal angle, allowing for spatial determination of the energy shower. The segmentation and module thicknesses were chosen to maximize the amount of particle energy sampled and to differentiate between electromagnetic and hadronic particles. The energy resolution of the LAC is $\sim 15\sqrt{E}\%$ for electromagnetic (EM) showers and $\sim 60\sqrt{E}\%$ for hadronic (HAD) showers [46].

3.3.6. The Warm Iron Calorimeter (WIC)

The WIC (figure 3.16) serves four functions at SLD: flux return for the solenoid, calorimeter for residual hadronic energy leaked through the LAC, muon-identification system and structural support for the rest of detector components. The WIC consists of 18 layers of Iarroci streamer tubes sandwiched between 5 cm thick steel plates [6]. These tubes are instrumented with square readout pads for calorimetric purposes, and with long conducting strips for muon tracking. The strips are laid in two separate

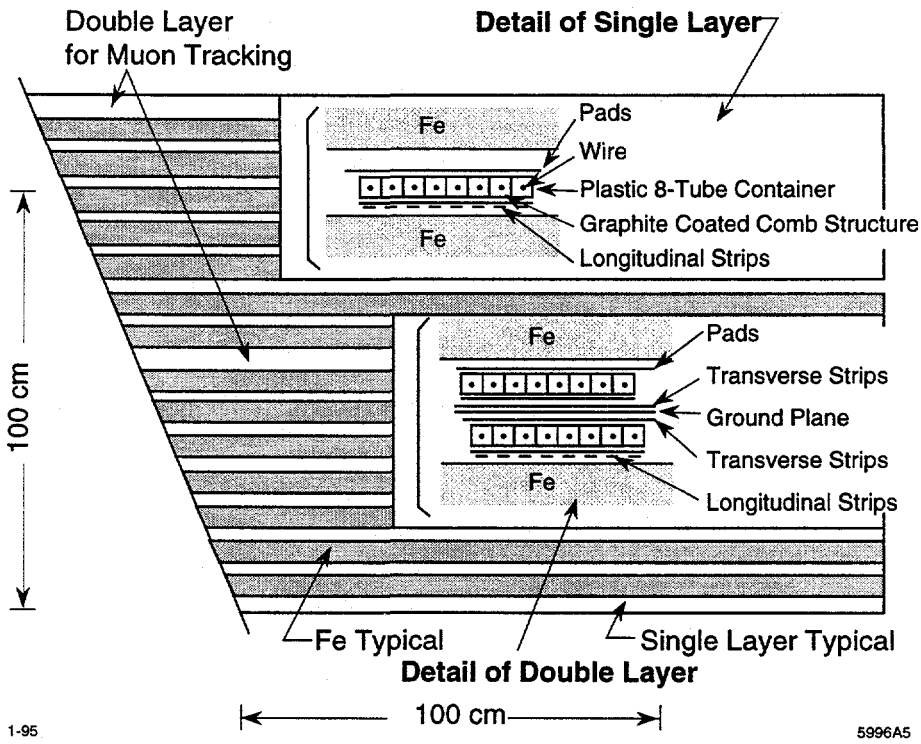

Figure 3.16: Cutaway view of the WIC.

arrays at 90° with respect to each other in order to measure the trajectory of the muon in two dimensions.

3.4. The SLD Readout Triggers

The seven SLD triggers used in the 1993-95 running periods are:

1. Energy Trigger: - Events with a sufficient amount of energy in the LAC will set this trigger to be flagged. The energy trigger requires minimum 8 GeV[3] of total deposited energy to be recorded by the electromagnetic (EM) and/or hadronic (HAD) calorimeter towers in the LAC. To eliminate noise, thresholds of 60 ADC counts for the EM towers (246 MeV) and 120 ADC counts for the HAD towers (1296 MeV) have been set. The full detector is read out for each energy trigger, however prior to the implementation of the trigger (October 1994), only the LAC, WIC and LUM systems were read out.

2. Tracking Trigger: - This trigger requires minimum two well separated (120°) charged tracks tracked by 9 (out of 10) CDC layers. CDC cells are marked as *hit* if 6 (out of 8) sense wires have pulses above threshold. The hit pattern of the cells is required to match one of the entries in a CDC pattern map. The map comprises of all possible trajectories originating at the IP with $p_T > 250\ MeV/c$.

[3]The standard LAC energy scale used is the *min-I* scale, referring to particles such as the muons that are minimum ionizing particles. In this scale ADC counts are converted to energy as 2.04 MeV for 1 ADC count in the electromagnetic (EM) towers and 5.41 MeV/ADC count in the hadronic (HAD) towers.

The trigger has a very high efficiency for hadrons and τ decays in the barrel region.

3. HAD Trigger: - This trigger is a combination of the first two triggers, requiring one charged track passing through 9 CDC layers and an energy deposition in the LAC slightly smaller than that for the Energy Trigger.

4. WAB Trigger: - This trigger is designed to flag two back-to-back charged tracks in the CDC. Unlike the tracking trigger, it allows for short track stubs, aimed at flagging wide angle Bhabha (WAB) events to the maximum of the detector acceptance.

5. Muon-pair Trigger: - This trigger requires one charged track in the event to pass through 9 CDC layers and calorimetric hits to be present in the opposite WIC octant.

6. Bhabha Trigger: - This trigger requires a total energy of minimum 12.5 GeV (EM scale) in both the North and South EM2 sections of the LUM (outer EM layers). The threshold is above background noise and the trigger requires only the LUM/MASiC to be read out.

7. Random Trigger: - This trigger records data every 20 seconds, regardless of detector status. It is used to provide information for background studies.

The SLD triggering efficiency for hadronic events is nearly 100% [47]. During good running conditions typical trigger rates are on the order of 0.1 Hz and during noisy beam conditions they can reach above 2 Hz.

3.4.1. Veto Triggers

There are several vetos in the triggering system that prevent excessive detector dead-time from noisy backgrounds. Beam sprays from the SLC due to various glitches in the SLC tunning can determine such running conditions especially in the summer when there are large temperature variations within 24 hours. The Tracking Trigger Veto prevents tracking information from being read out if more than 275 (out of 640 CDC) cells are *hit*. During normal beam conditions the veto has little effect on the number of recorded Z^0's. For a 40% span of the 1993 run this system was incorrectly set, resulting in a bias against high multiplicity events (5% of 1993 hadronic events). The 1993 run has been divided following this incident into a PRE-veto period, a VETO and a POST-veto period. Monte Carlo simulation had to be tuned to take into account this effect and it is currently in good agreement with the data.

Chapter 4

Particle Identification

This chapter gives a detailed description of the SLD Čerenkov Ring-Imaging Detector (CRID) used for the identification of the dominant five species of long-lived charged particles, electrons, muons, pions, kaons and protons.

The chapter is divided into three parts: the first gives an introduction to the functioning of the CRID, the second describes the calibration and alignment of the device in which the author was involved and the third gives a very brief overview of CRID performance in physics analyses.

4.1. Čerenkov Radiation

Radiation emitted by particles traveling at speeds faster than that of light in a translucent medium has first been observed by Čerenkov [48] and later explained by Frank and Tamm [49] in 1937.

The effect is similar to a vessel traveling on water at speeds greater than that of surface waves. The angle of the emitted photons with respect to the particle's track is $cos\theta_C = 1/\beta n$ where $\beta = v/c$ is the normalised particle velocity and n is the medium's index of refraction.

The photons are emitted in conical sheets continuously along the track. If collected by a lens or a mirror, these parallel sheets are focused into rings at the focal plane. This property is very useful for the creation of a device that can discern between rings of different radii and assert the particle's velocity in the respective medium. In conjunction with the momentum of the particle measured for instance by the tracking system, the mass can be inferred, and hence the species of the particle be known.

There are however a few elements of importance that need to be understood to make such a device functional. First, the fact that the Čerenkov photons are emitted predominantly in the UV spectral range. This places a number of constraints on the materials used. Second, the resolution of the device is a function of the radiating medium and particle momentum. For instance at SLD there are two radiators used, one liquid, optimised for low momenta, and one gaseous, for high momenta.

The number of photons emitted by a track of length L in the unit of spectral range is:

$$dN = \frac{e^2 L}{\hbar c^2}\left(1 - \frac{1}{\beta^2 n^2(\omega)}\right)d\omega \tag{4.1}$$

The total number of observed photons is the sum of the contributions from all spectral

domains weighted by the detector's efficiency:

$$N = \frac{\alpha L}{c} \int_0^{+\infty} \epsilon(\omega) \Big(1 - \frac{1}{\beta^2 n^2(\omega)} \Big) d\omega \tag{4.2}$$

Due to statistics associated with the discreteness of the medium, N is the mean value of the Poisson statistics followed by the number of observed photons. In a region away from any absorption band of the medium, where the index of refraction n is monotonic, the total number of photons can be written as $N = N_0 L sin^2\theta_C$, where $N_0 = \alpha/c \int \epsilon(\omega) d\omega$.

In such a region, the production as a function of wavelength is:

$$dN = \frac{2\pi L \alpha}{n(\lambda)} \Big(1 - \frac{1}{\beta^2 n^2(\lambda)} \Big) \frac{1}{\lambda^2} d\lambda \tag{4.3}$$

Since $n(\lambda)$ is approximately constant, it follows that there is a predominant production of Čerenkov photons at short wavelengths, in the UV range. The quartz windows used in the SLD CRID are a reflection of the need for UV transparent materials.

The second important aspect is the momentum dependence of the production:

$$dN = \frac{2\pi L \alpha}{n^3} \Big[(1 - n^2) - \frac{m^2}{p^2} \Big] \frac{1}{\lambda^2} d\lambda \tag{4.4}$$

In order to radiate Čerenkov light the particle's minimum momentum must be $p_{thr} =$

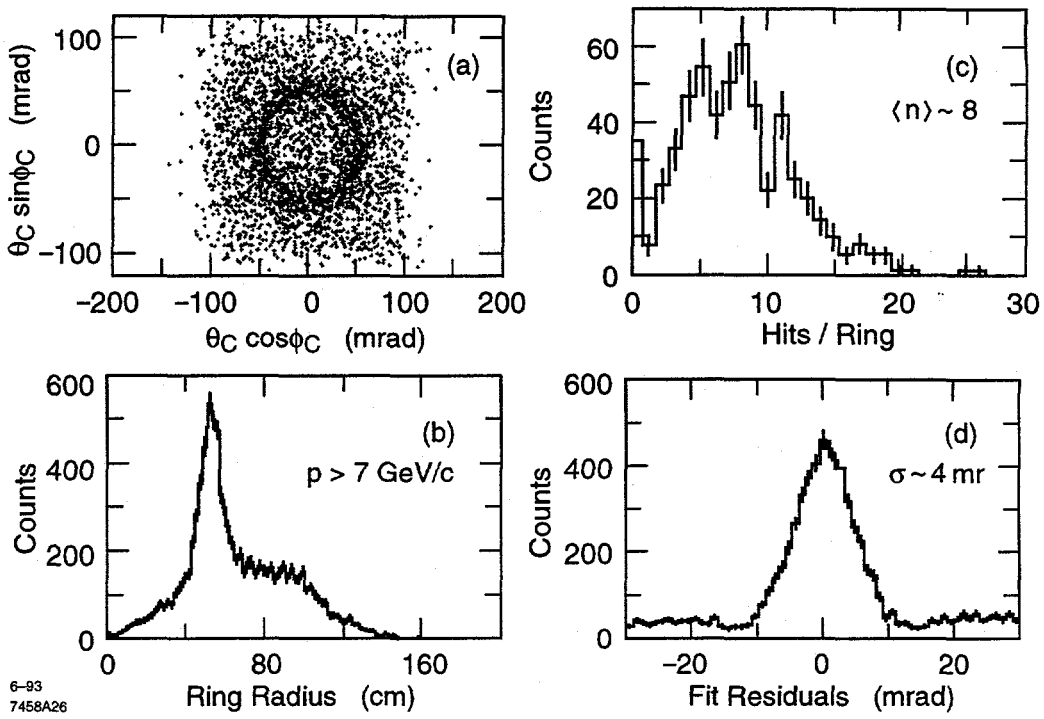

Figure 4.1: Gas CRID performance: rings in Čerenkov space (a), distribution of ring radii (b), number of photoelectrons per ring (c), ring radii residuals (d).

$mc/\sqrt{n^2(\lambda)-1}$, where m is the particle's mass.

4.2. The SLD CRID

The CRID mechanical structure observes the general SLD detector partition into a Barrel and an End-Cap system. The Barrel CRID (figure 4.2) radiator volumes are a 1 cm thin liquid C_6F_{14} radiator with $n = 1.27802\,|_{\lambda=1900\mathring{A}}$ and a 40 cm 85% $C_5F_{12}, 15\%N_2$ gas radiator with $n = 1.00163\,|_{\lambda=1900\mathring{A}}$. The conical sheet of Čerenkov light from the liquid radiator is thin and it is allowed to pass directly into the detector

through a quartz window. The Čerenkov photons from the gas are emitted along a 40 cm path and are focused by spherical mirrors onto the drift box as rings. They enter the drift box through the upper quartz window.

The rings are reconstructed in "Čerenkov Space" (figure 4.1), with the ordinate being $\theta_C sin\phi_C$ and the abscissa $\theta_C cos\phi_C$. The angle θ_C is the Čerenkov angle and ϕ_c the azimuthal angle in the plane perpendicular to the track. In this space the radius of the ring gives directly the Čerenkov angle. The actual computation in the multi-tracking environment of hadronic events is a hypothesis tester. Tracks start by being assigned pion hypothesis and based on the number of expected photons in the ring, the general background, and in the case of overlapping rings, the background from other tracks, a procedure establishes the identities of the tracks through an iterative process. The procedure converges typically in a maximum of 3 iterations and produces as output a log-likelihood vector of 5 entries (one for each hypothesis: e, μ, π, K, p) per track.

The End Cap CRID (figure 4.3) is similar to the Barrel CRID with the difference that it is a gas only system. This allows a simpler design with drift boxes separated in azimuth, that are equipped with quartz windows only on one side (figure 4.4). Unlike in the Barrel CRID, the electrons are drifting perpendicular to the magnetic field and this causes the drift to be at an angle with respect to the $\vec{E}$ field. The End Cap CRID extends particle identification capabilities of the Barrel CRID from $|\cos\theta| < 0.7$ into

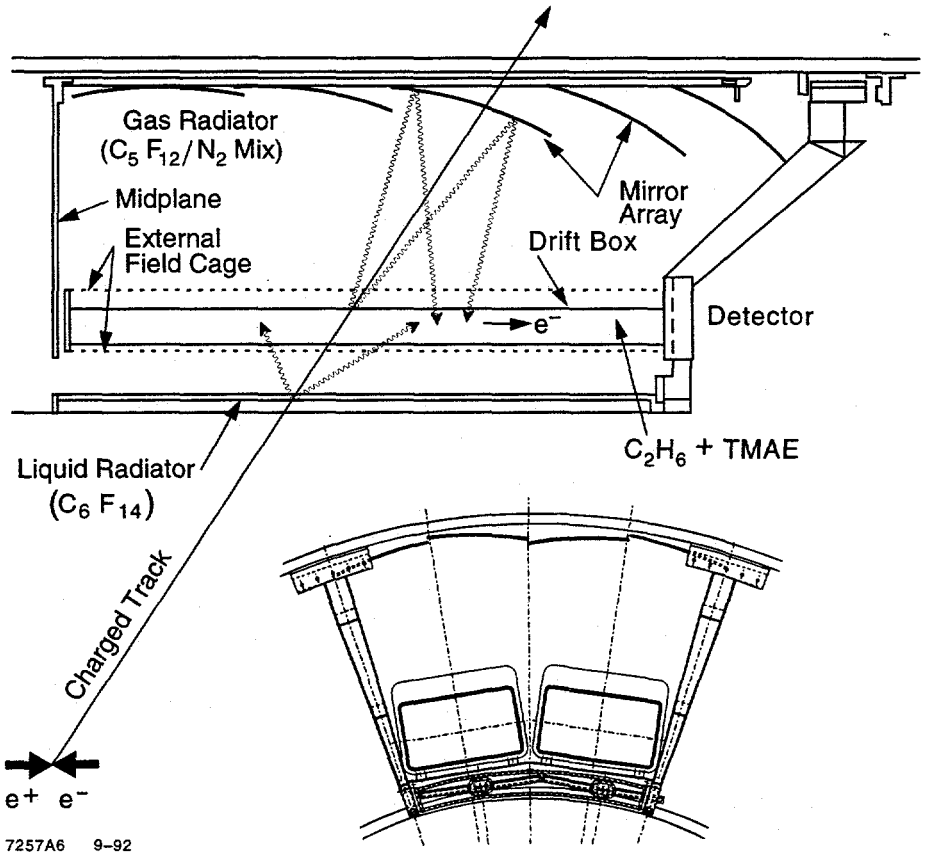

Figure 4.2: The Barrel CRID, longitudinal and transverse sections.

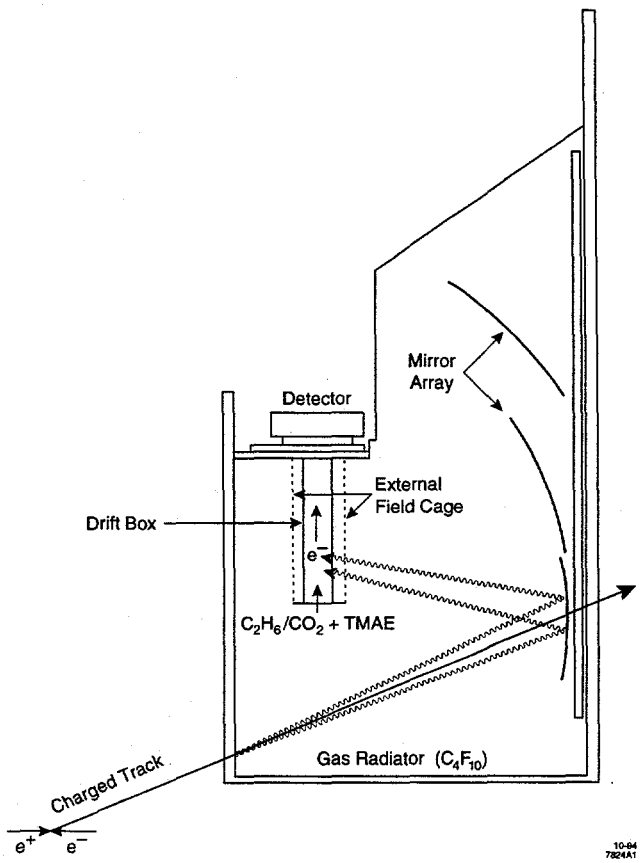

Figure 4.3: Side view of the End Cap CRID. Note the absence of the liquid radiator.

the low polar angle regions of $0.82 < |\cos\theta| < 0.98$.

The radiator gas used in the End Cap vessels is C_4F_{10} which at room temperature is gaseous and allows for a substantial simplification in the recirculation design. The drawback of C_4F_{10} is its slightly lower index of refraction of $n = 1.00153\ |_{\lambda=1770\mathring{A}}$, which results in a 6% higher momentum threshold [50], $p_\pi > 2.5 GeV/c$.

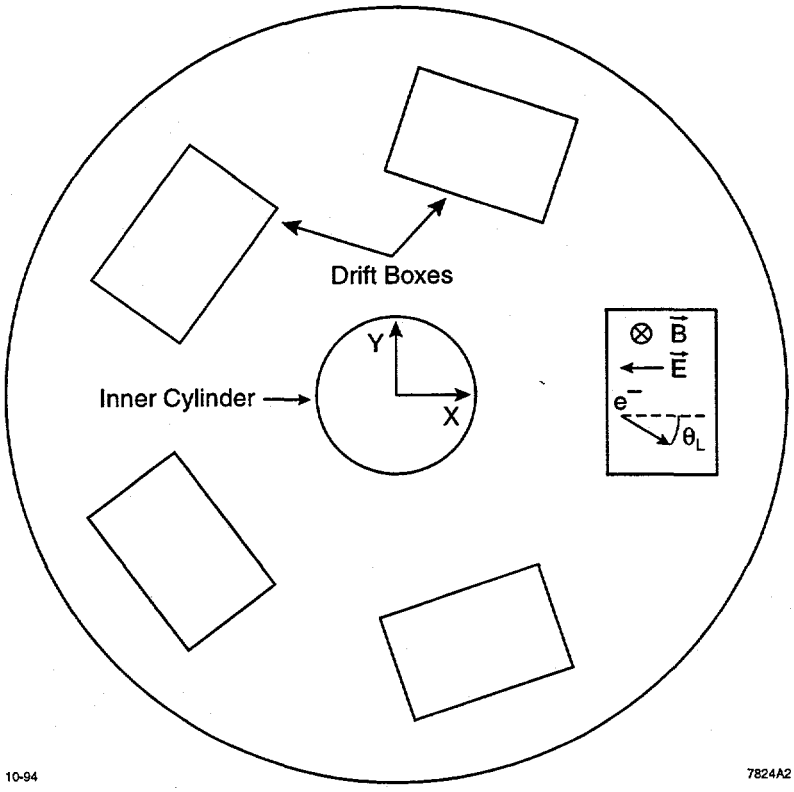

Figure 4.4: The End Cap CRID viewed perpendicular to the beamline. Note the drift of the photo-electrons at an angle with respect to $\vec{E}_{field}$.

4.2.1. Radiator Media

For discriminating between particle species in various momentum ranges different radiator media are needed. For instance for low momenta a dense medium is needed, such as a liquid radiator. At very high momenta however, dense media produce almost the same number of photons regardless the particle's mass:

$$\frac{dN}{N}(\lambda) = \frac{dm}{m} \cdot \frac{2}{p^2/p_{thr}^2 - 1} \tag{4.5}$$

In the above equation it can be seen that the discriminating power with respect to the particle's mass vanishes for very high momenta (figure 4.5). In this range a rarefied medium, with index of refraction close to unity, is needed. Physical intuition tells however, that such a medium has little substance to radiate photons. Indeed, from equation 4.2 it can be seen that for n approaching unity the production becomes zero. The optimisation of the two constraints led to the fabrication of a material called "aerogel" [51] which will be a major component of the particle ID system in the BELLE experiment at the KEK B-factory in Japan.

Table 4.1 shows the thresholds of the five particle species of interest in the radiators used at SLD.

The barrel CRID radiators are C_6F_{14} (liquid) for momenta in the range of 0.3 to 5.0 GeV/c and C_5F_{12} (gas) for momenta above 2.5 GeV/c [52]. This choice gives

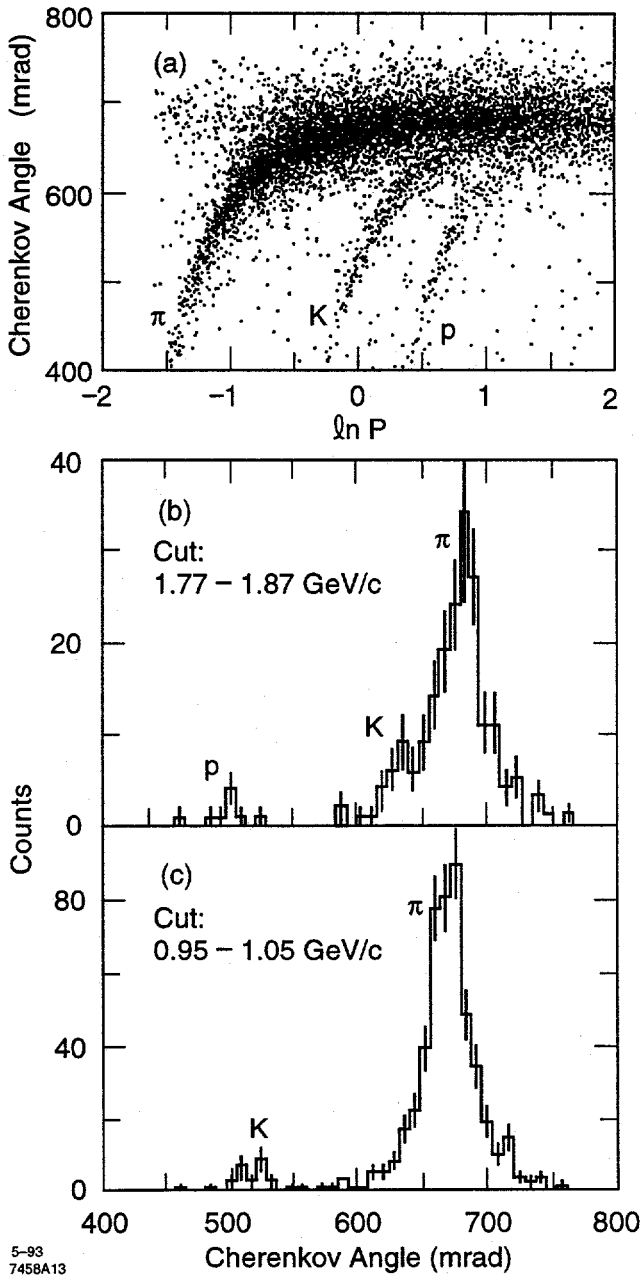

Figure 4.5: Separating power with respect to momentum and $\pi - K - p$ separation in the interval 1-2 GeV/c.

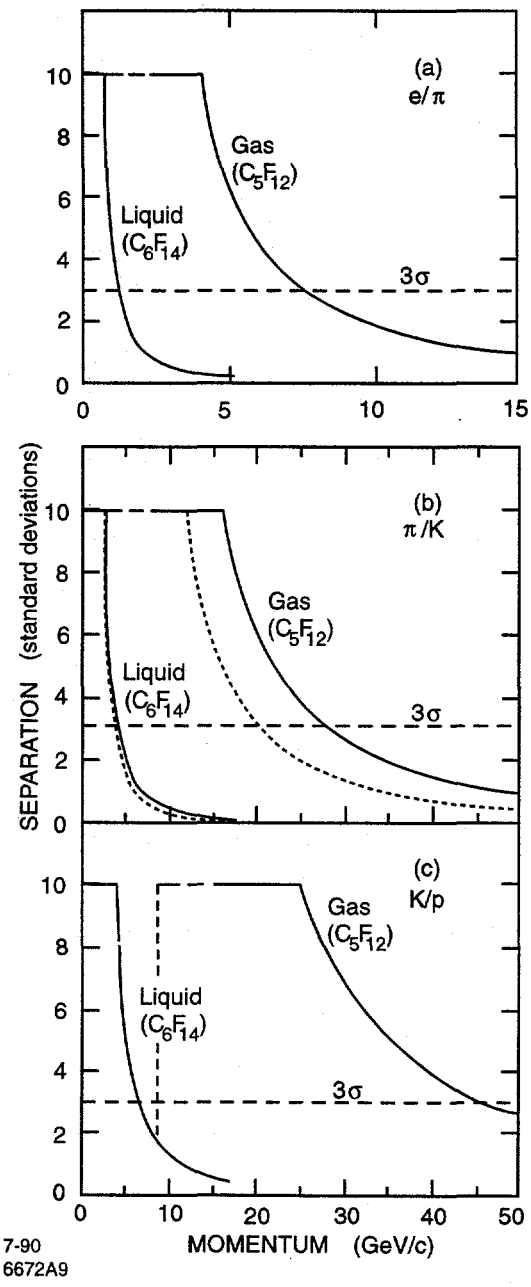

Figure 4.6: Separating power of different radiator media for pairs of particles close in mass.

Table 4.1: Momentum thresholds for producing Čerenkov rings in the CRIDs.

Radiators	$e^{\pm}$	$\mu^{\pm}$	$\pi^{\pm}$	$K^{\pm}$	$p/\bar{p}$
C_6F_{14}	0.001	0.133	0.176	0.621	1.179(GeV/c)
C_5F_{12}	0.009	1.856	2.451	8.649	16.422(GeV/c)
C_4F_{10}	0.009	1.915	2.530	8.927	16.950(GeV/c)

excellent momentum coverage with overlap in the intermediate range. Although at high momenta the liquid radiator has a small discriminative power, it is used as a consistency check that there actually existed a track that radiated the Čerenkov light.

The separation power for the two media used is shown in figure 4.6 for pairs of particles close in mass: e/π, π/K and K/p. It can be noted that pion-kaon separation, a very important issue in many experiments, is achievable at the 3σ level from 0.3 GeV/c to 27 GeV/c, a region spanning almost two orders of magnitude in momentum coverage.

4.2.2. Single Electron Sensitive Detector

The detector is a Time-Projection Chamber (TPC - figure 4.7) type, filled with C_2H_6 ($C_2H_6 + CO_2$ for ECRID) drift gas and a gaseous photo-cathode additive, abbreviated TMAE (tetrakis(dimethylamino)ethylene, or $C_2(N(CH_3)_2)_4$). The photo-cathode is ionized by UV Čerenkov photons and releases photo-electrons in the drift gas. The combination of TMAE quantum efficiency and transparencies of the drift

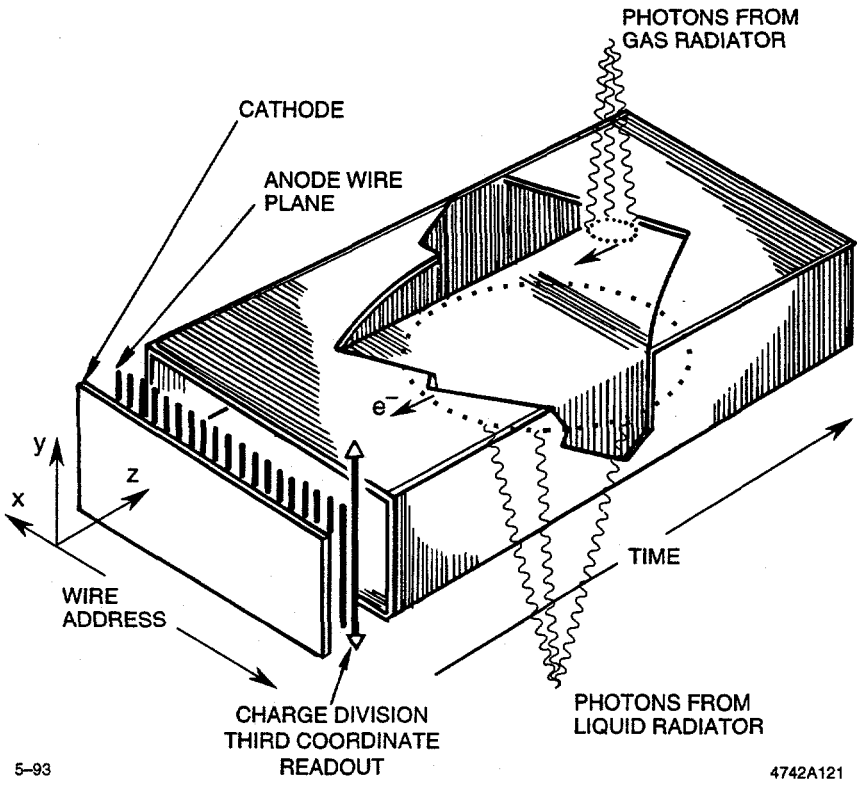

Figure 4.7: A CRID Drift Box, or TPC.

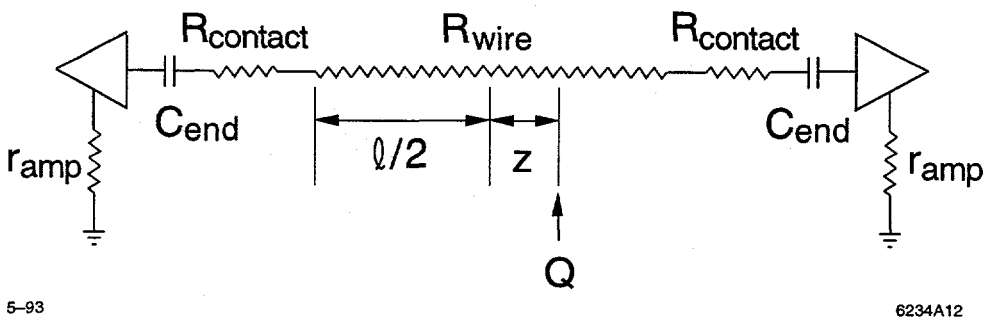

Figure 4.8: Schematic of the charge division measurement.

gas and quartz window peaks at approximately 6.5 eV ($\lambda = 1900\mathring{A}$), figure 4.9 . The high voltage applied sweeps the photo-electrons to the anode-plane, and is set for the best time to distance resolution in order to reconstruct the z coordinate. The other two coordinates are reconstructed, x from the wire address, and y from charge division on the wire (figure 4.8). Resolution on all 3 coordinates is within 1mm, giving approximately 4 mrad resolution in Čerenkov angle.

The structure of the barrel detector end is shown in figure 4.10. A set of field shaping wires and blinds is used to direct the electrons onto the wires, the latter being necessary in order to avoid photon feedback ionisation. The anodes collect the signal and pass it to the front end electronics.

Some technical differences exist in the End-Cap detectors due to the position with respect to the solenoidal magnetic field of the SLD, as shown in figure 4.4. The focusing structure for the wire plane had to be modified because the electrons do not drift parallel to the magnetic field lines and they impact the detector wires at a large Lorentz angle of approximately 15°.

The signals from the preamplifiers are stored in the Analog Memory Units (AMU's) in bins of 8 (119 MHz) clock units, that is "buckets" of 67.2 ns. When an event trigger occurs, the AMU data is multiplexed to Analog to Digital Converters (ADC's) and passed in digitised form to the Waveform Sampling Modules (WSM's). Each Barrel WSM processes 2/3 of the wires of a Barrel TPC and 1/2 of an End-Cap TPC. The

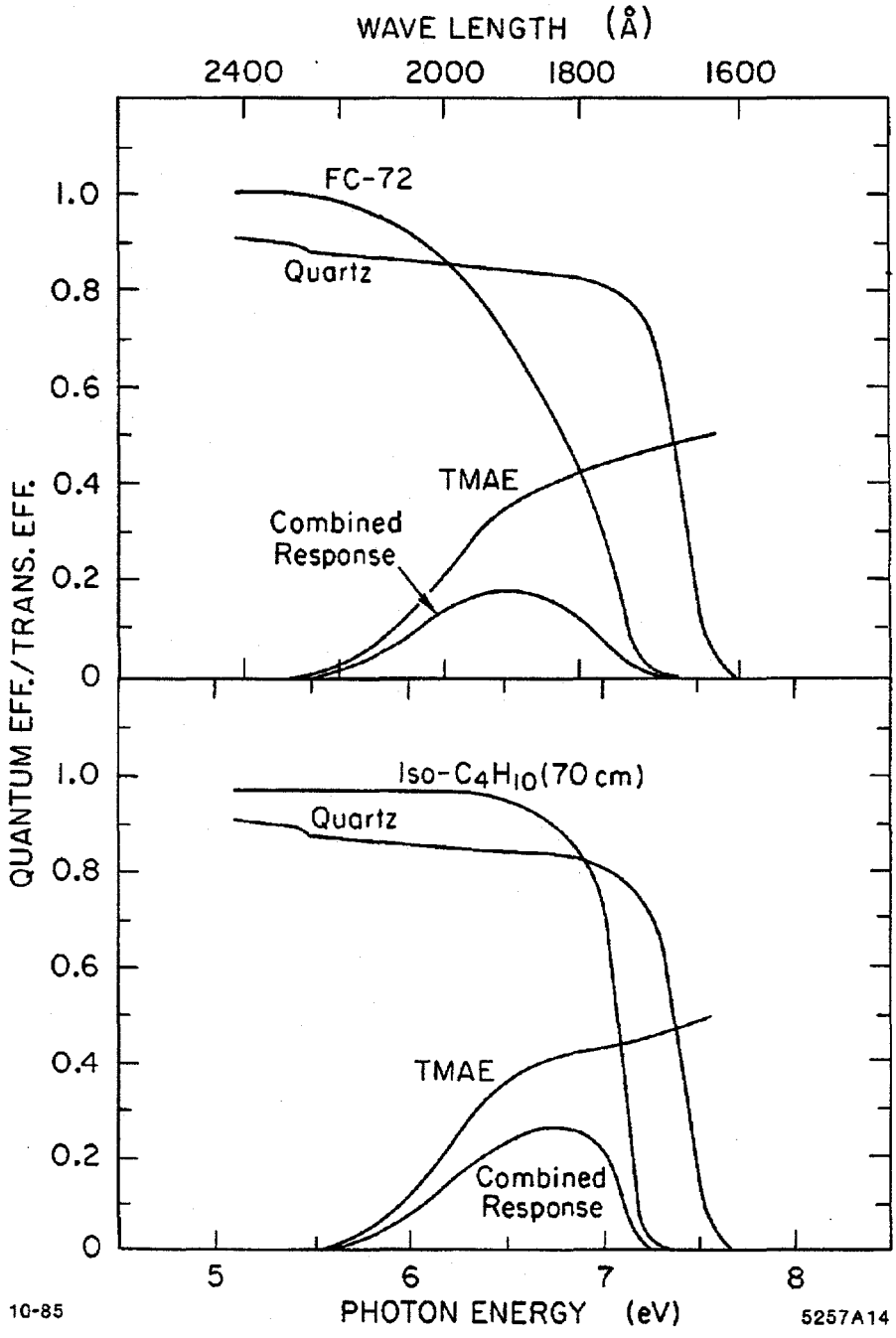

Figure 4.9: TMAE quantum efficiency and transparencies for the drift gas and quartz window.

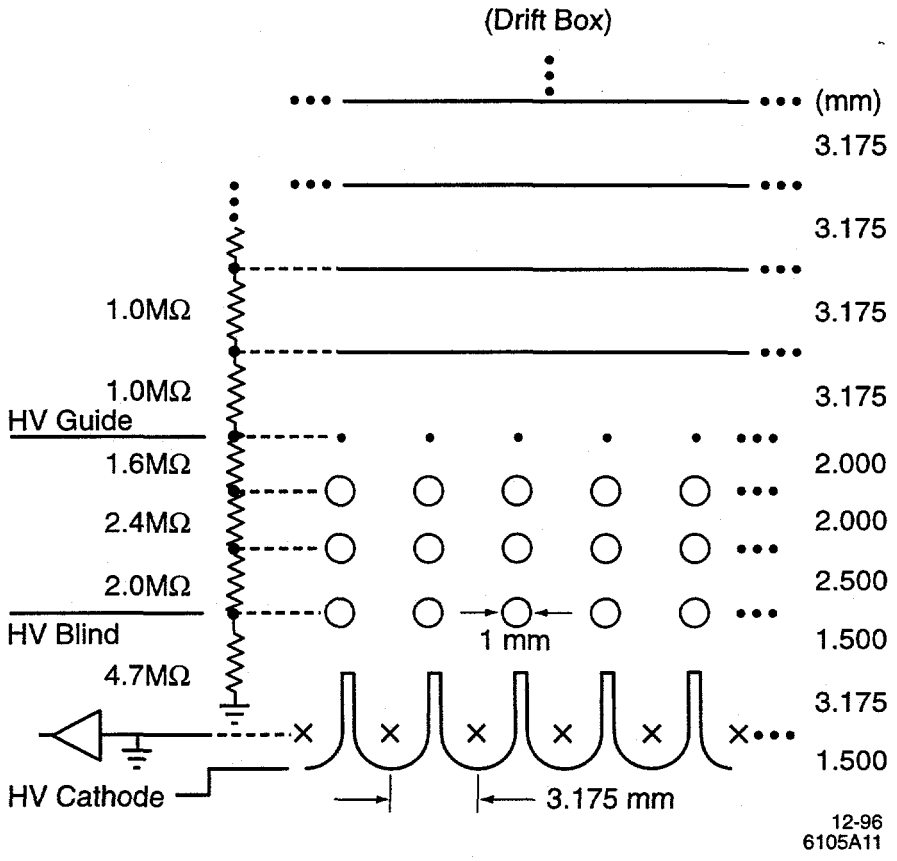

Figure 4.10: Detector end structure. Field shaping wires and blinds are used to direct the electrons onto the wires.

responsibility of the WSM is to correct the bucket by bucket AMU characteristics, zero-suppress the data, and apply a pulse-finding algorithm. The algorithm uses a discrete version of the Laplace transform, called a Z-transform. The advantage of this technique over derivative pulse finding algorithms is higher accuracy for closely following pulses. It is also 4-5 times less CPU intensive, and it is unaffected by pedestal levels. The data is processed in real time and passed to the CRID AEB (ALEPH Event Builder) electronics upon request. The latter formats the data for tape storage and transfers it to the main VAX online computer in the case the event is to be written to tape. The information stored from the CRID is the pulse leading edge time, the pulse height and width, and a 32 bit quality word describing the pulse as saturated, small, closely following another pulse, bad pedestal, *etc.*

This information is then processed off-line first to calibrate the detector (drift velocity, t_0 time offset, magnetic field distortions), adjust for geometrical mis-alignments with respect to the tracking system, and finally reconstruct Čerenkov rings.

Electron drift velocity is determined using a set of fixed optical fibers that inject UV photons into the drift boxes at regular time intervals to allow for detector calibration. Similarly, magnetic field distortions are also measured using these signals.

Offset time and geometrical mis-alignments with respect to the tracking system are described in the following sections of this chapter.

4.3. End Cap CRID Calibration

The t_0 time offset provides the calibration reference with respect to each detector's internal coordinate system, which in turn is related to the global coordinate system by a separate procedure.

During "physics" runs the SLC hardware trigger specifies beam-crossing times. Different SLD sub-systems are at different electrical lengths away from the trigger and have differents offsets. These time offsets relate to geometrical offsets in SLD systems that use time as one of the coordinates. To align the CRID to the tracking system these offsets have to be eliminated, together with the offsets of pure geometrical origin. The local CRID coordinate system for both Barrel and End-Cap transforms drift time into z-position, charge division into y-position and wire number into x-position. Drift time is sensitive to trigger jitter and temperature variations of the drift gas, both effects leading to z-coordinate distortions. To extract these distortions a gauged quantity is needed that can monitor the respective fluctuations.

4.3.1. End-Cap CRID t_0

The procedure for extracting t_0 relies on charged particles passing through the Drift Box. The particles leave a trail of charge as they pass through the drift gas, trail that widens due to diffusion as it drifts towards the Detector Plane. The sensitivity of the amplifiers is approximately 2 photo-electrons and they are saturated by the

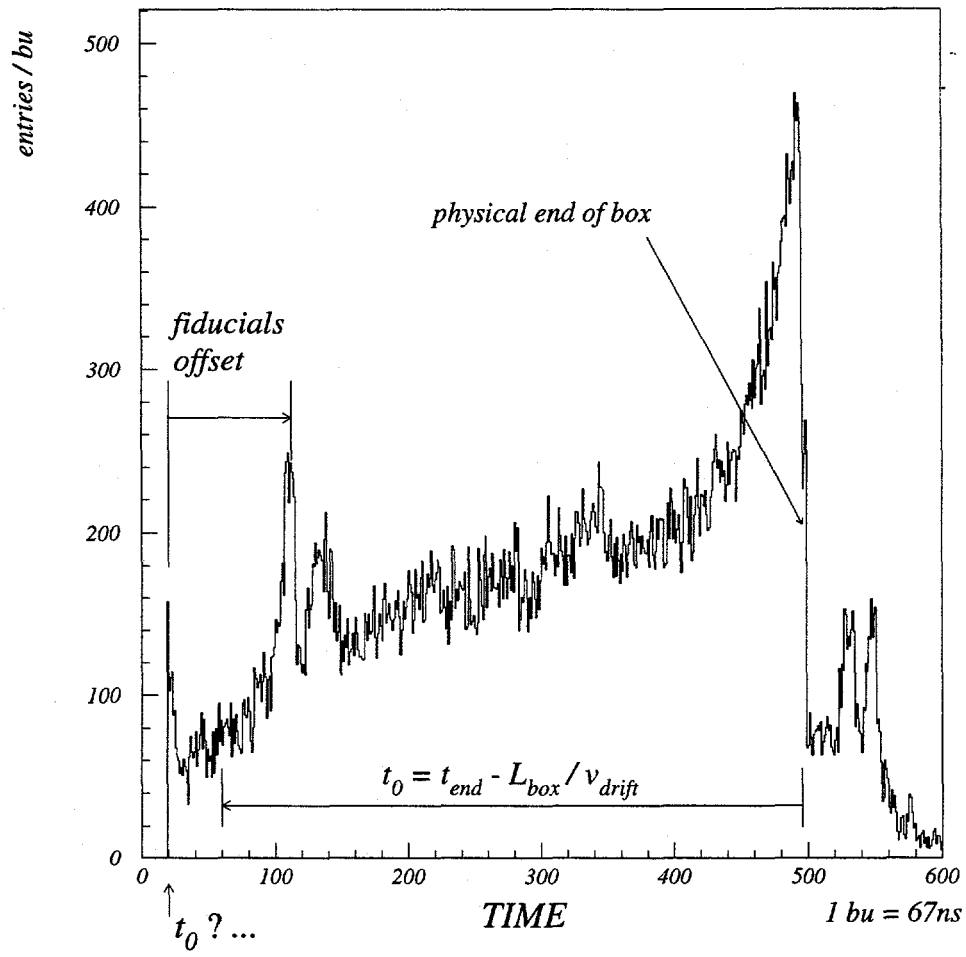

Figure 4.11: Time distribution of saturated hits from tracks passing through the TPC. Drift time of photo-electrons is used in the CRID to measure the z-coordinate.

ionisation signal of this trail which may contain several hundred electrons. Over the time period of a typical SLD run, tracks passing through a given TPC form a distribution of saturated hits over the length of the box (figure 4.11). Due to the close distance between the box end and the beam-pipe, there is a substantially higher concentration of saturated hits at the end of the box (figure 4.11). The sharp fall-off of the distribution indicates the physical end of the box. A time offset is evident from the front end of the box, where the distribution is not populated, however it is uncertain if the beginning of the distribution corresponds to the zero of the internal coordinate system.

The maximum drift time, is related to temperature and trigger jitter and as shown in figure 4.11, can be used to determine the real t_0. The falling edge of the distribution is identified with a program (RTZERO [53]) designed for specific pattern recognition. The code starts off by removing any spikes in the drift time distribution. Such spikes can occur (figure 4.12 RAW) in hot channels. The resulting histogram is then smoothed by taking into account 4 neighbouring bins with different weights (figure 4.12 SMOOTHED). To enhance visibility the distribution is contrasted using a power law and the average value of the histogram (figure 4.12 CONTRASTED). Finally a light smoothing procedure is applied to eliminate small fluctuations that may have been accentuated by the previous process (figure 4.12 FINAL). It was found that this procedure is very robust even in the case of low statistics and that accidental

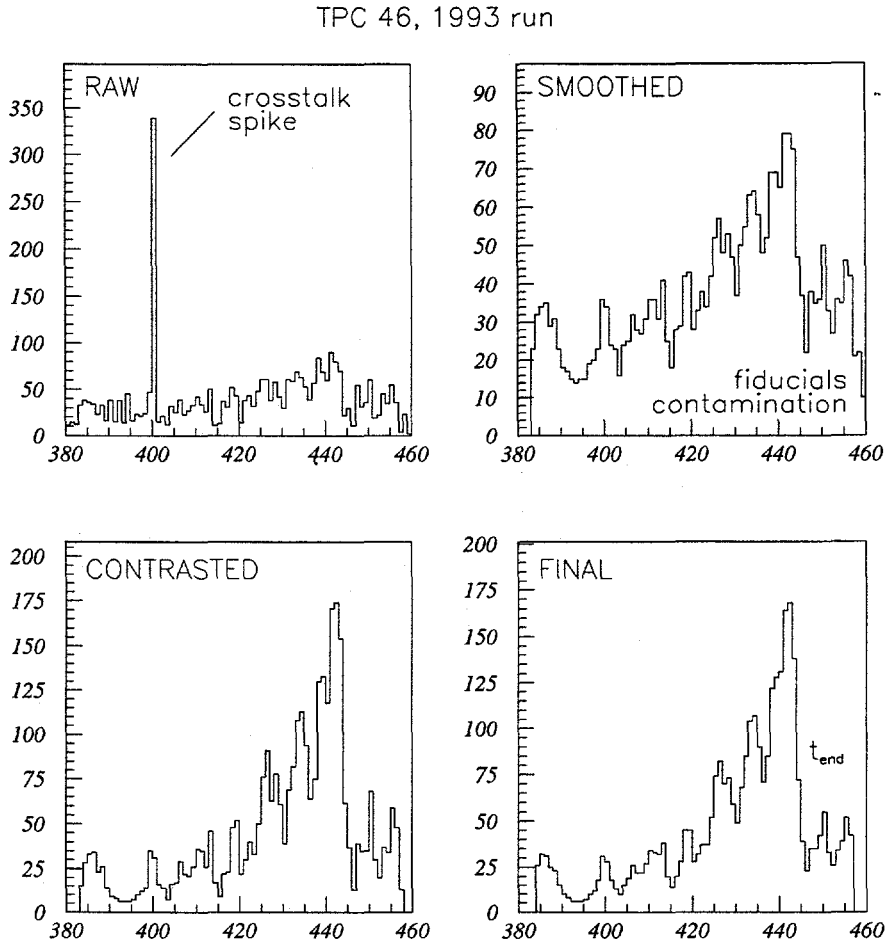

Figure 4.12: Saturated hits time distribution towards the box end during noisy beam conditions.

fluctuations are not mis-interpreted as the end of box slope. A comparison between RAW and FINAL in figure 4.12 demonstrates this point. The code then searches for the best slope that resembles a standard box end shape. The slopes are chosen by requiring a minimum gradient and absolute height, otherwise the procedure is reset. Bin to bin fluctuations are allowed, but they accumulate "sin" points. These points are "forgiven" if the slope continues with a good descent, otherwise they reset the investigation. If the slope has passed, it is parametrised by a set of quantities computed on the center two thirds. The quantities used are: maximum vertical drop, gradient, best local gradient and time interval. They are scaled to standard values from what was found to be a "good" run (TPC-46, in RAWS-23700, August 1993) and the relative values enter score functions. The score functions were adjusted on a sample of runs with low statistics as to give the best ratings. A final score is assembled and if there are two or more competing slopes, the one with the best "score" is chosen. This procedure fully automates data processing and it is robust with respect to low statistics data. Figure 4.13 shows a normal data taking situation, where it can be seen that the box end is well defined.

For the selected slope three time quantities are calculated: at mid-height, mid-length and fit point of inflection. The mid-height determination is protected against multiple solutions (as in figure 4.11) by the use of a simple algorithm. The mid-length is $\frac{1}{2}(t_{start} + t_{end})$ and the inflection time is determined using a third order spline fit.

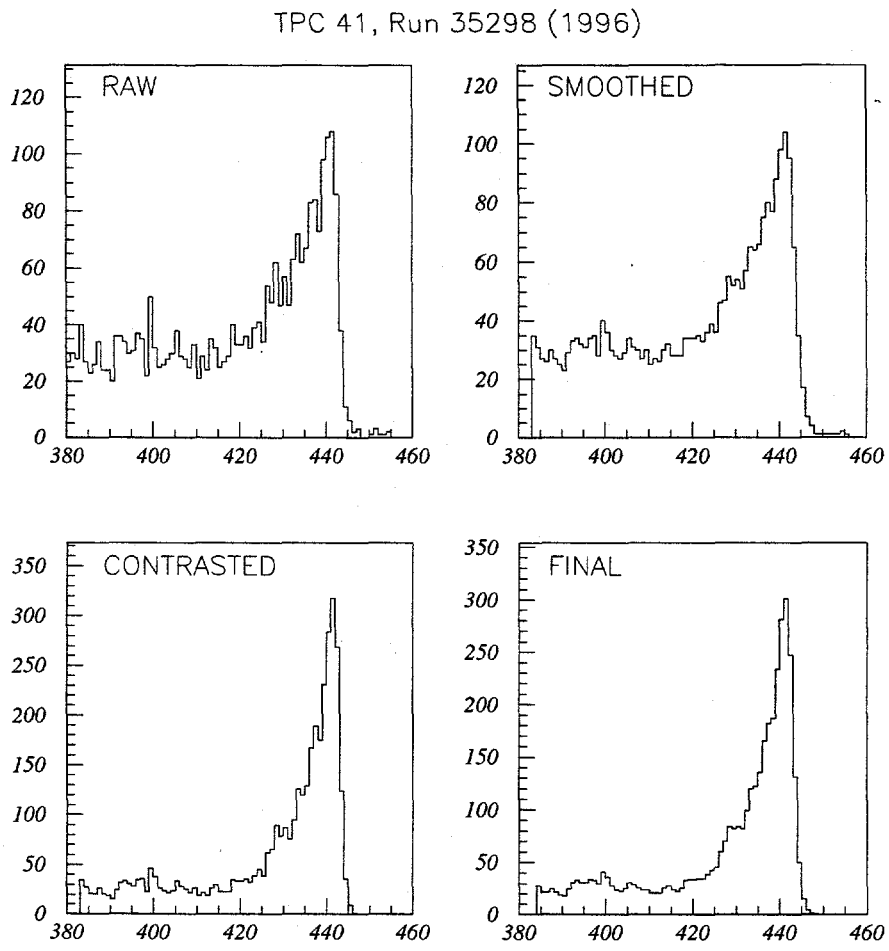

Figure 4.13: Saturated hits time distribution towards the box end during normal operation conditions.

To protect the fit from erroneous results, the shape of the function is fixed to a linear (slope) plus a third order term and the point of inflection is varied. The two best χ^2 points are retained. If the inflection points are within 20% of each other, the point with the best χ^2 is used. If not, the points are compared to the mid-height point. If they are on the same side, the one closest to the mid-height time is chosen. If they are on opposite sides, the one within 2.5 time buckets (167 ns) away is retained. Comparisons between the inflection time, mid-length and mid-height time are made, and in the case of agreement within 2 time buckets, the result is considered to be the inflection time. If the answers disagree in the range of 2 to 4 time buckets a weighted average is formed, and for more than 4 buckets disagreement the mid-height time is considered, as the most robust of the three.

The results of RTZERO on a sample of 150 runs from the 1996 data are shown in figures 4.14 (South) and 4.15 (North). There is a remarkable stability of t_0 which translates into an rms deviation equivalent to 0.3mm in the z-coordinate, making it the best calibration of the three coordinates [54]. The consistent values of the five TPC's in each End-Cap allows for an averaging of their values to a single t_0 value per End-Cap, with better precision. The consistency between average t_0 and the individual t_0's for each TPC is shown in the fit results of figures 4.14 and 4.15. A small difference of 70ns is observed between the t_0 of the two End-Caps. This is to be expected as the two systems have different electrical lengths to the trigger. The North

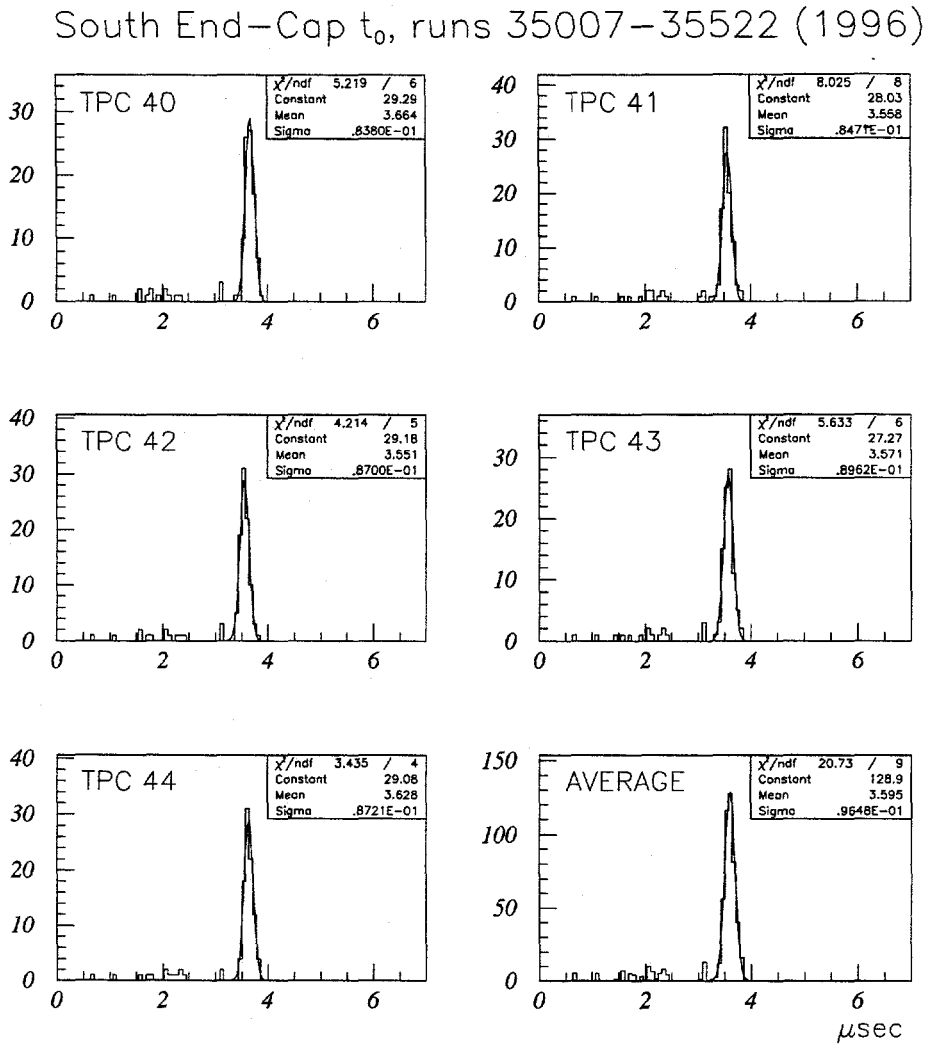

Figure 4.14: The t_0 distributions for South End-Cap TPC's, 1996 data

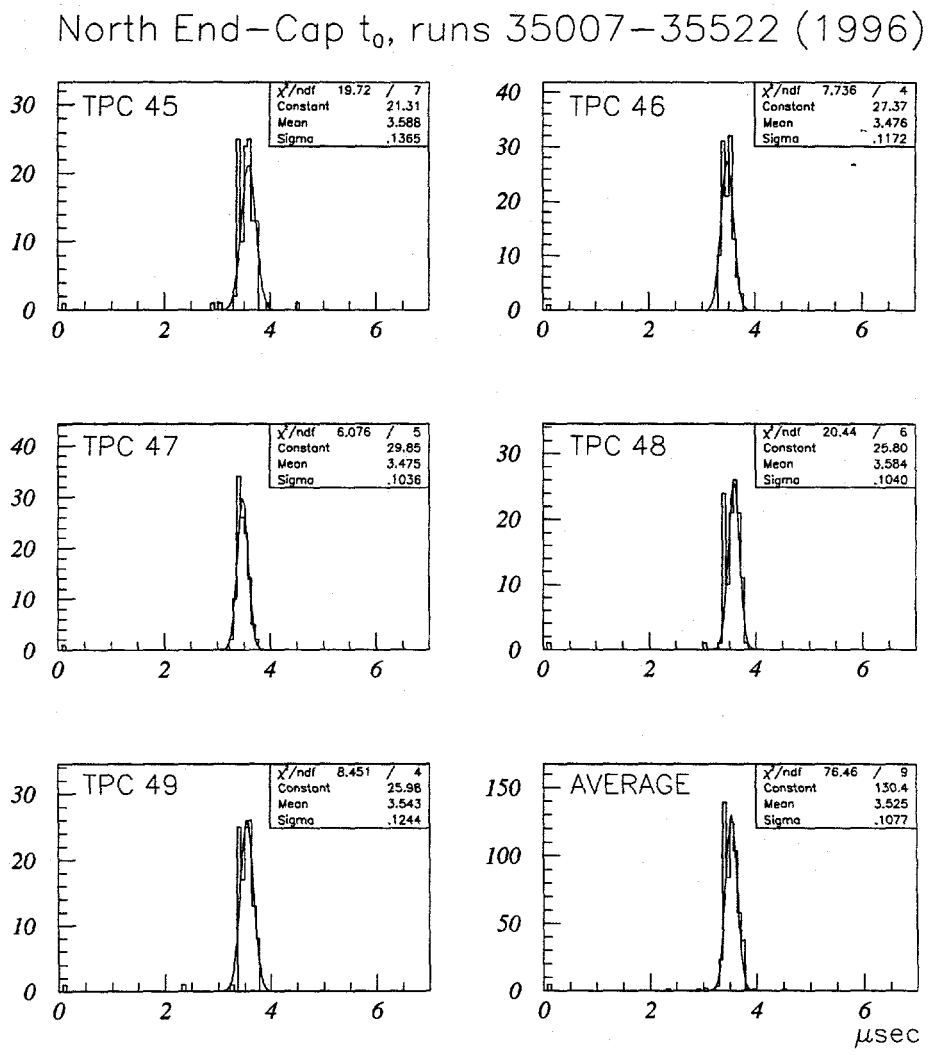

Figure 4.15: The t_0 distributions for North End-Cap TPC's, 1996 data

End-Cap shows a possible split in the distribution, probably due to two time periods with slightly different t_0. This is equivalent to approximately 1mm in z-distance and could require a fit on smaller blocks of runs.

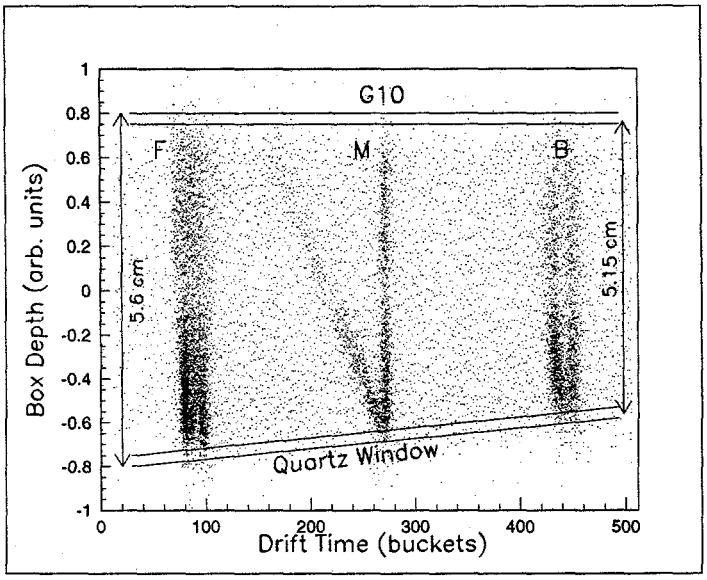

Figure 4.16: "Side-view" of the reconstructed hits produced by the UV fiber flashers. The horizontal axis is the drift time (z) coordinate, and the vertical axis is the charge division (y) coordinate.

4.3.2. The EC-CRID in Operation

Currently the EC-CRID is not actively used in physics analyses due to work in progress on the End Cap Drift Chambers tracking capability. However there are reliable indications that the EC-CRID hardware and online software is fully functional.

All Drift Boxes are equipped with UV fiber optic flashers placed outside the quartz windows, that are designed to produce survey points and to allow the monitoring of

drift velocities, electron lifetime, *etc.* The first data to be acquired from the EC-CRID drift boxes were of the reconstructed electrons produced by the UV flashers. Figures 4.16 and 4.17 show two views of the reconstructed photo-electron patterns.

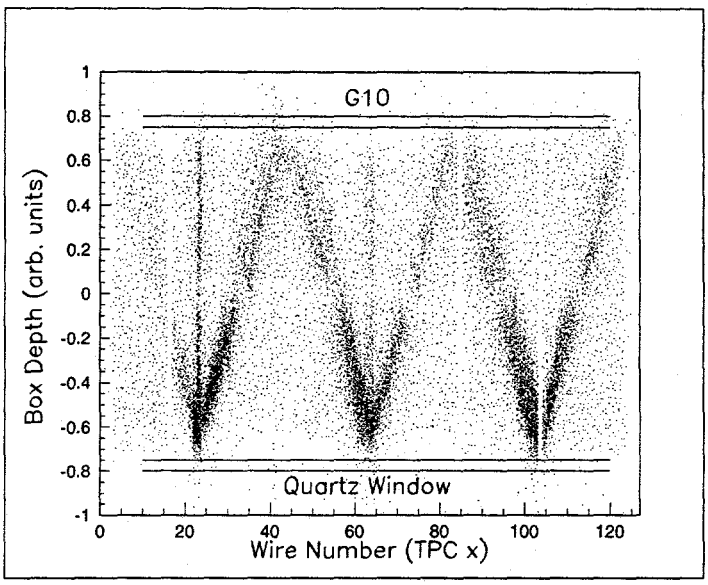

Figure 4.17: "Front-view" of the reconstructed hits produced by the UV fiber flashers. The horizontal axis is the wire address (x) coordinate, and the vertical direction is the charge division (y) coordinate.

For high momentum tracks it is possible to see ring candidates. An overlay of a number of such rings is shown in figure 4.18 and has the expected limiting radius in "Čerenkov space".

4.4. CRID Alignment

The geometrical alignment presented in this section refers to both Barrel and End-Cap CRID. Tracking information is used together with trails of saturated hits left by

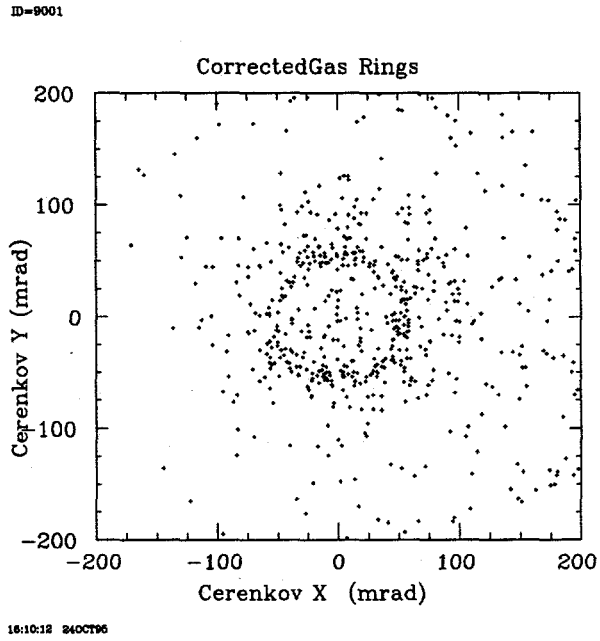

Figure 4.18: Overlay of reconstructed rings in the SLD End Cap CRID.

tracks in the CRID Time Projection Chambers (TPC's). The differences observed between tracking expected positions of saturated hits and the CRID-measured positions are used to determine the offset constants that aligns the CRID to the tracking system.

4.4.1. Barrel-CRID Alignment

The Barrel CRID consists of 40 drift boxes of roughly 120 cm long arranged azimuthally on top of the Drift Chamber. Boxes 0 through 19 are on the South side and 20 through 39 on the North. The transverse plane between the two sectors is

referred to as the "MIDPLANE", while the TPC ends are referred to as the "ENDS". After the magnetic field distortions and the t_0 offsets have been eliminated, only the geometrical offsets remain. There are six degrees of freedom for geometrical misalignments, three translational and three rotational. Using saturated hits from tracks passing through the detector it is possible to align four of these degrees of freedom: azimuthal shifts and tilts and radial shifts and tilts.

Although there existed an initial 1993 alignment, improvements in the reconstruction code, as well as a new set of magnetic field distortion constants rendered the old 1993 geometrical constants obsolete. The large 1994-95 data set used initially the 1993 constants and it too needed its own alignment constants.

The alignment uses tracks traversing the CRID Drift Boxes that leave trails of ionisation and compares their positions with those expected from the tracking system. Due to diffusion, the saturated hits do not have a well defined position at the level of accuracy required. To eliminate this problem the center of the charge segment left by the track in the CRID was considered: $x_{mid} = \frac{x_{entry}+x_{exit}}{2}$, where $x_{entry/exit}$ are the x-coordinates of the track's entry and exit points in the TPC. Equal diffusion of both ends of the segment ensures that the measured center, within statistical fluctuations, is the same as the initial one, before diffusing. For the z-coordinate it is not possible to do an average because of the unpredictable behavior of the saturation time of the amplifiers which does not reflect well the width of the saturated hits

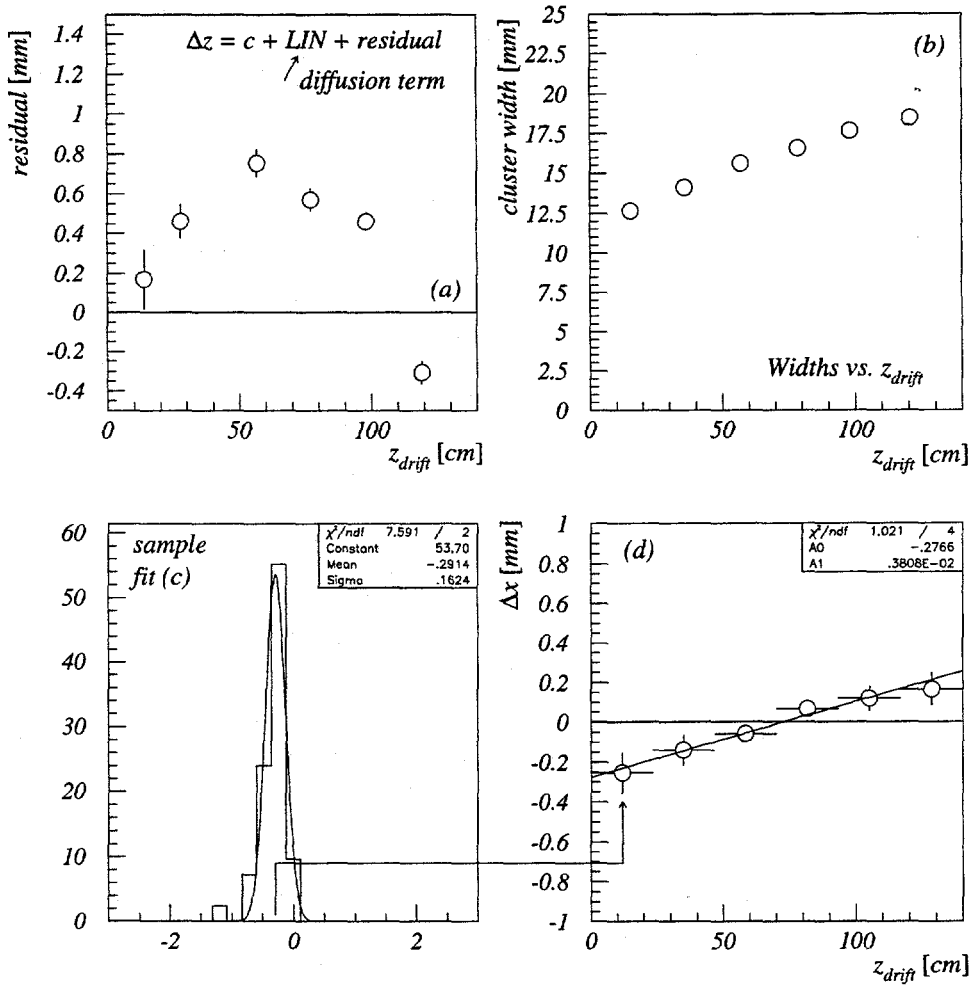

Figure 4.19: Schematic of alignment procedure: (a) calibration of the z-coordinate, (b) diffusion effect on cluster width, (c) sample fit for one z-slice of the TPC, (d) offset and tilt observed after surveying all six z-slices

trail. Likewise, the y-coordinate has charge division information from two saturated amplifiers and reconstructs all saturated hits at mid-length. The difference in x between the expected center, from tracking, and the found center, from the TPC, is used to monitor the mis-alignment. The z-coordinate is calibrated to within ±2mm precision. This is not precise enough to determine the z-offset, however it is adequate for finding the box tilts and for being used in other data filters. The z value used is the z-coordinate of the earliest drift time end of the segment. The difference between expected and found positions in z increases almost linearly with drift time. A calibration is thus made to adjust roughly for diffusions as a linear term plus a residual: $z_{found} = z_{expected}(1 - \alpha \cdot z_{expected}/L_{box}) + residual$. The residual term and the linear slope are determined together, figure 4.19 (a), the residual being on the order of 1mm over the entire 1200mm of the box. The fit performed on the accumulated data to find the z dependent local offset is shown in figure 4.19 (c). The z-coordinate is also used for sectioning the Drift Box in three to six pieces in length for the measurement of tilts, figure 4.19 (d).

Using saturated hits there are two possible alignments of the drift boxes with respect to the tracking system: azimuthal and radial. These alignments correct four degrees of freedom: the tangential translation and tilts on the outer drift chamber surface form the azimuthal alignment, and the radial translation and dip angle tilts, the radial alignment. The remaining two degrees of freedom, longitudinal translation

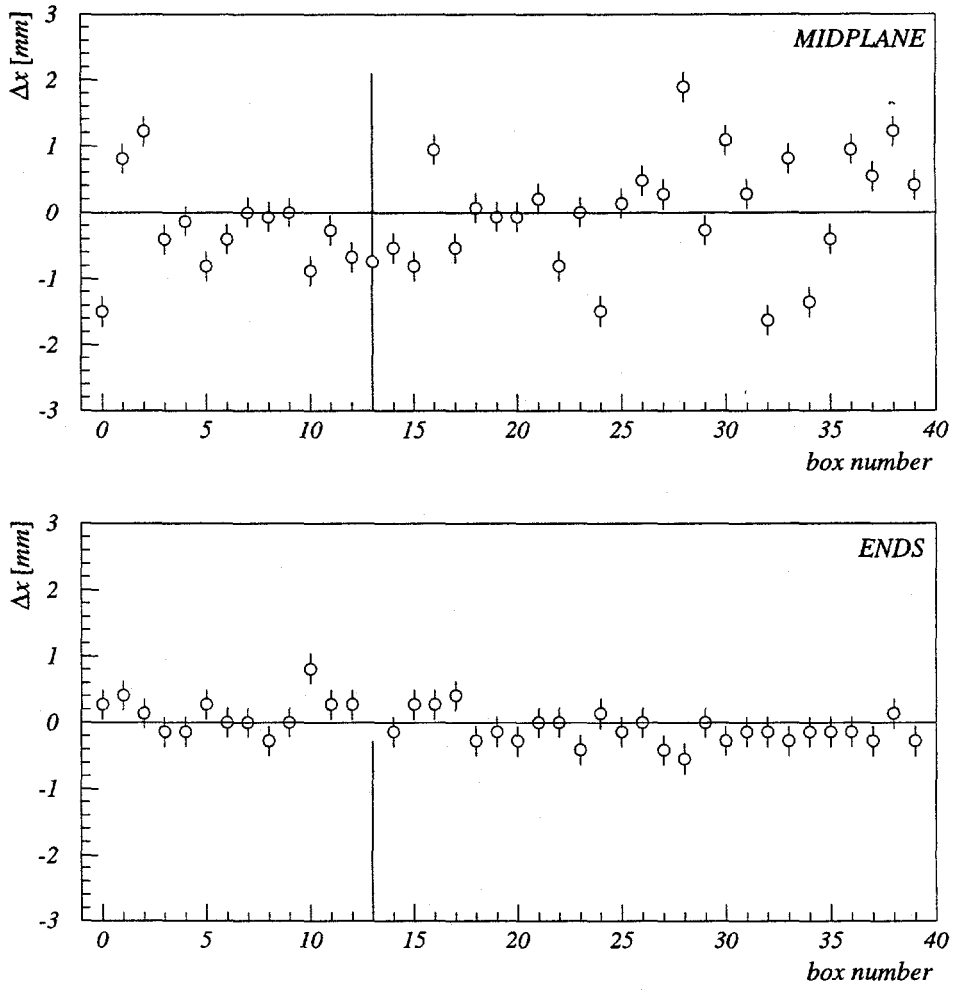

Figure 4.20: The 1993 alignment with the old geometrical constants and the new $\vec{B}_{field}$ distortion constants.

and roll angle are not determined using this procedure, the first due to uncertainty in the z-coordinate of saturated hits at a level below 1mm and the second due to the small width of the TPC which gives a short lever arm.

The azimuthal alignment uses stiff tracks, with momentum above 1.5 GeV/c, that do not bend significantly within the thickness of the Drift Box. These tracks originate at the IP and have various dip angles. Any azimuthal offset, such as a global shift or an increasing shift with the z-coordinate (a tilt) is directly observed as an x-coordinate shift. This is of importance since the x-coordinate is the only reliable monitoring parameter when using saturated hits for the alignment. The x-coordinate offsets at MIDPLANE and at the box ENDS are shown for each TPC in figure 4.20 for the old 1993 alignment constants with the new magnetic field corrections. It should be noted that the non-aligned CRID has mis-alignments on the order of 2-3 times larger than those shown here. The azimuthal shifts (ϕ rotations in the SLD system) and tilts were adjusted until the the observed x-offsets at midplane and at the box ends were eliminated at the level of 0.2mm. Figure 4.21 shows the x-offsets for all boxes with the new 1993 geometry constants.

The azimuthal tilts and z-offsets for the new 1993 alignment are shown in figure 4.22. The tilts are smaller than 0.3 mrad and the z-alignment is reliable at the level of 1-2mm.

The 1994-95 data with 1993 constants shows a possible tilt on the order of 1mm

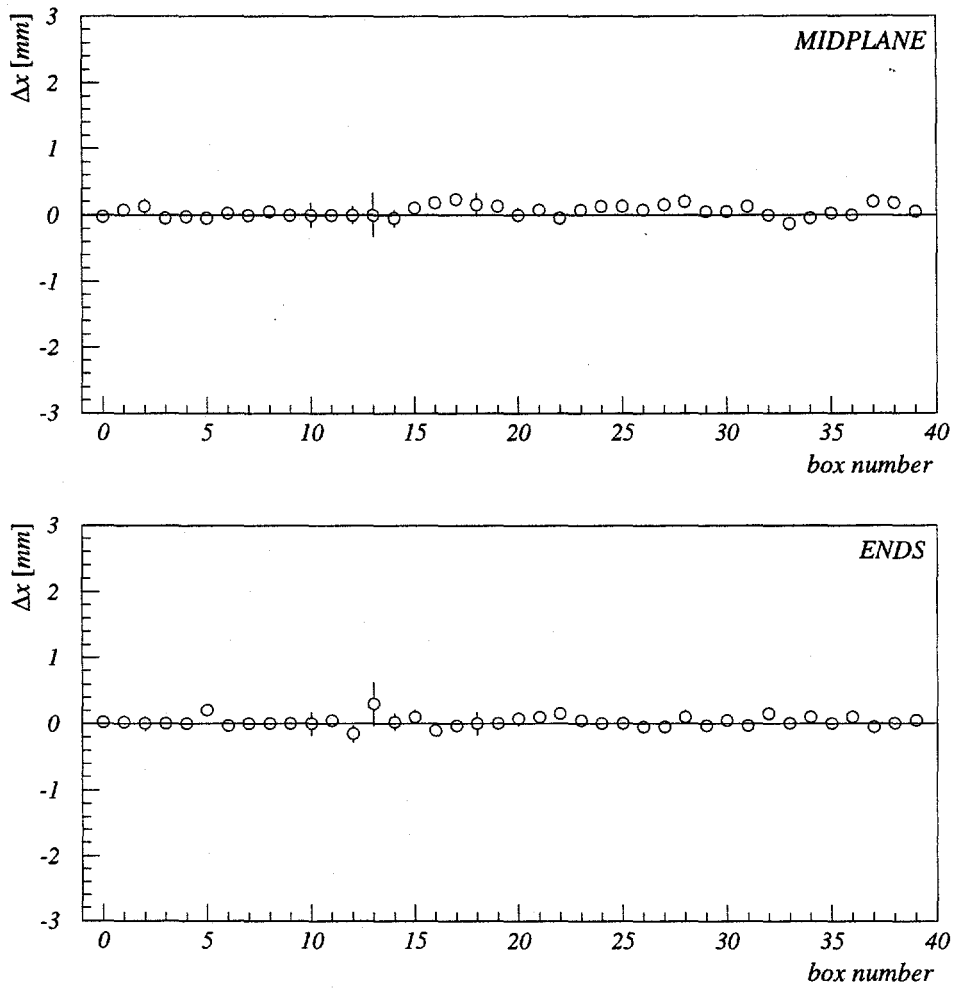

Figure 4.21: The 1993 alignment with the new geometrical constants.

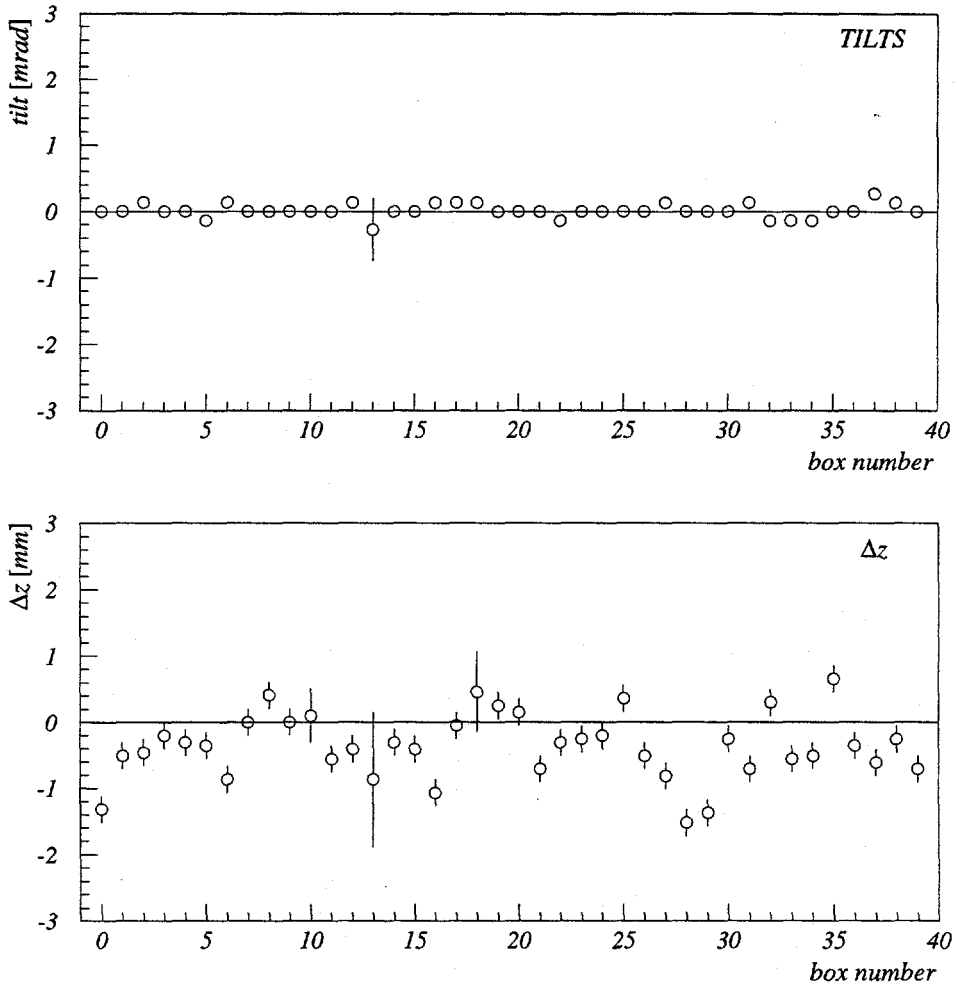

Figure 4.22: The 1993 alignment with the new geometrical constants. Top, box tilts and bottom, longitudinal approximate offsets.

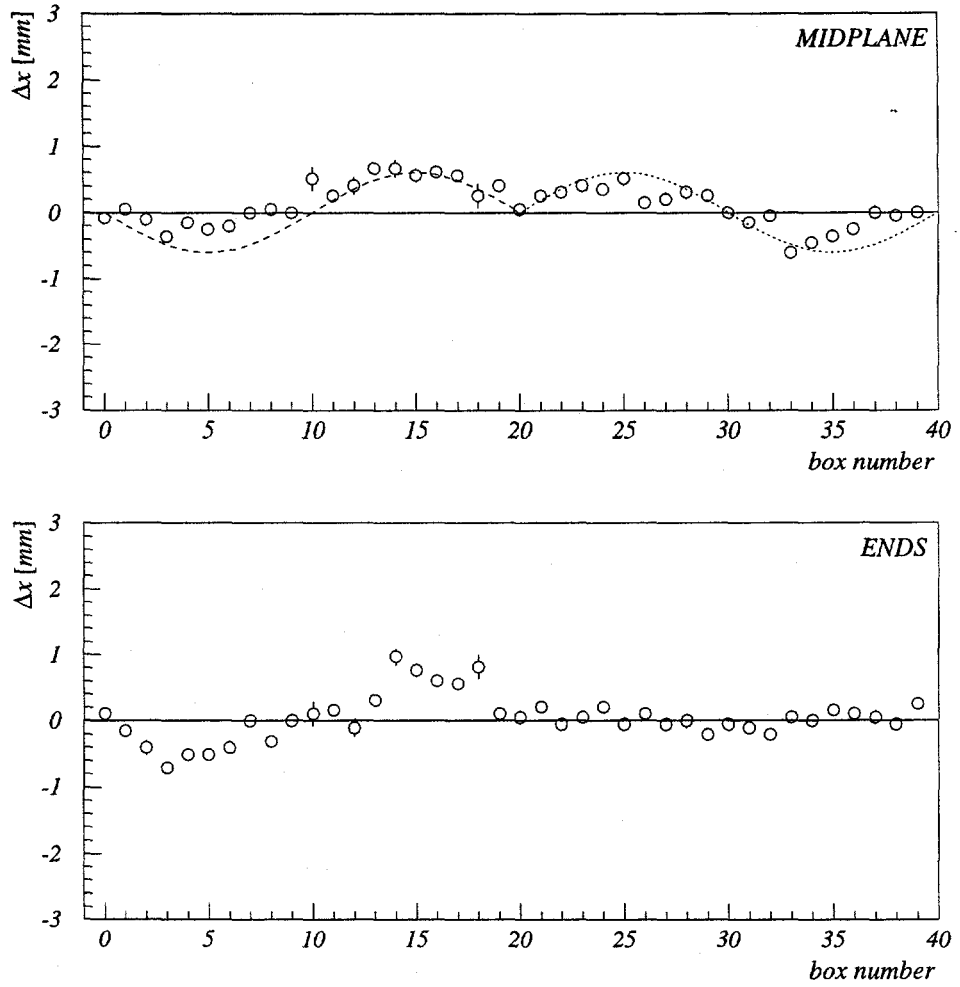

Figure 4.23: The 1994 alignment with 1993 constants. The top plot shows mis-alignments at the MIDPLANE and in dotted lines the effect of a global tilt of the CRID fixed at the ends. The bottom plot shows the mis-alignments at TPC ENDS.

of the whole Barrel CRID support system, figure 4.23. The azimuthal tilts, figure 4.24, are offset at the level of 0.5 mrad and the z-coordinate offset is on the order of 2-3mm.

After aligning the 1994-95 data, the results shown in figure 4.25 indicate x-offsets of less than 0.1mm, which is a very good alignment. All three 1994-95 datasets, PRESEP, FALL, WIN[1] are consistent with the global alignment. The smallest statistics dataset, PRESEP, is overlaid onto the global alignment for comparison and it shows a good agreement with the global sample. The tilts, figure 4.26 show also a very good alignment, with offsets of less than 0.1 mrad. The PRESEP data is generally within better than 1σ agreement with the global sample.

For the radial alignment, stiff tracks do not help because they enter the Drift Boxes almost perpendicular to the box. Consequently, any radial shift is un-noticeable at the mid-plane and at best on a 1:1 ratio at the ends. Consequently the radial alignment uses tracks with momenta in the range 0.25 ... 0.8 GeV/c. These tracks enter the TPC's at much shallower angles and curve within the TPC. Again x-coordinate differences are used to diagnose mis-alignment. Positive and negative tracks curve in opposite directions and are accumulated into separate histograms. The TPC's are divided into three sections: short, mid and long drift time and the offsets of these sections are shown as a function of TPC number in figure 4.27. Statistical fluctua-

[1]The 1994-95 run had three periods, delimited by the opening of the detector for component replacements. These periods were the summer of 1994 (PRESEP), the fall (FALL) and the 1995 winter (WIN).

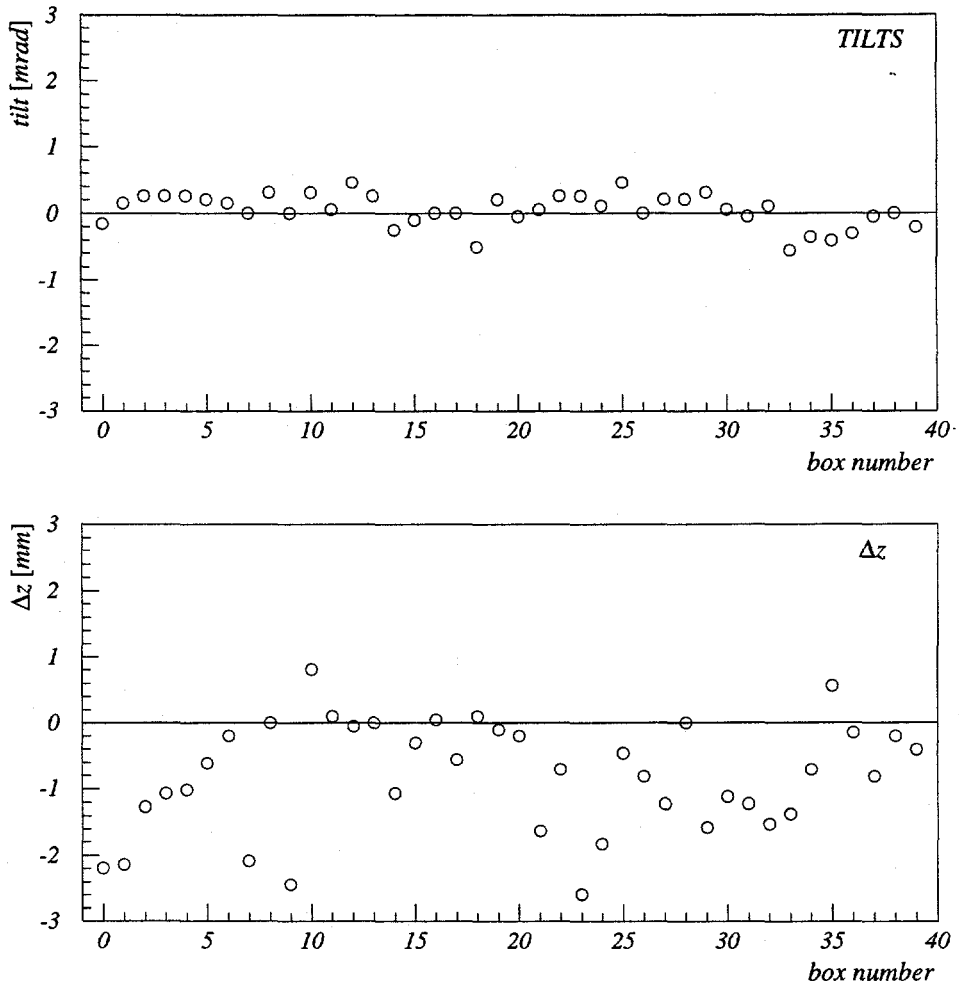

Figure 4.24: The 1994 alignment with 1993 constants. Top, box tilts and bottom, longitudinal approximate offset.

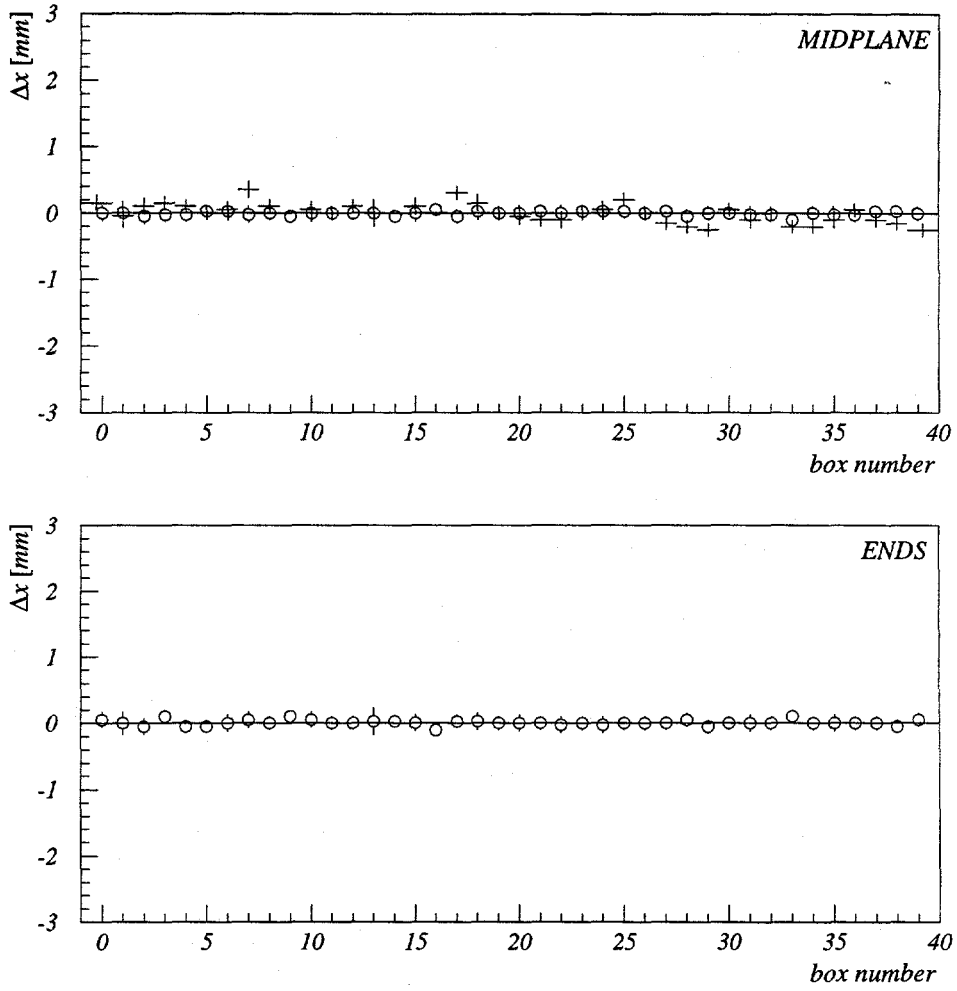

Figure 4.25: The 1994 alignment with new constants. Top, offsets at MIDPLANE and bottom, offsets at ENDS. Overlaid is the PRESEP data sub-set, in good agreement with the GLOBAL sample.

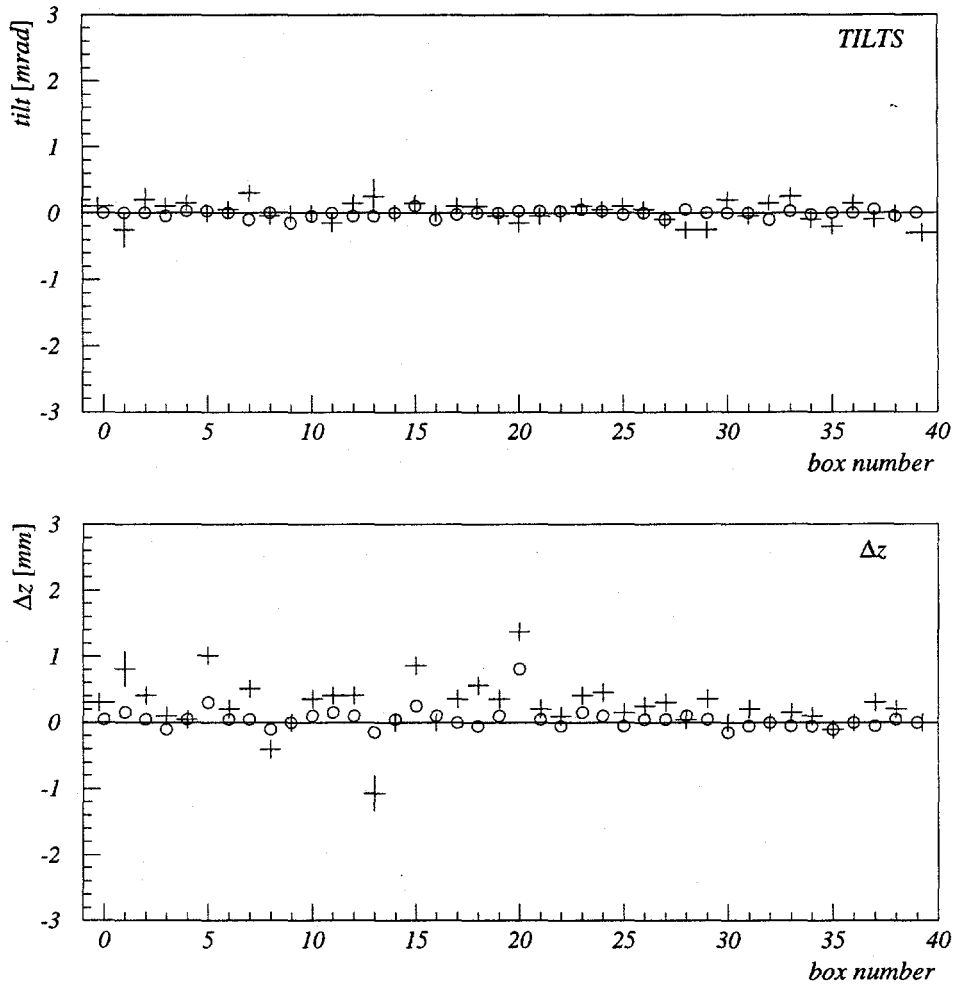

Figure 4.26: The 1994 alignment with new constants. Top, TILTS and bottom, approximate longitudinal offsets. Overlaid is the PRESEP data sub-set, in good agreement with the GLOBAL sample.

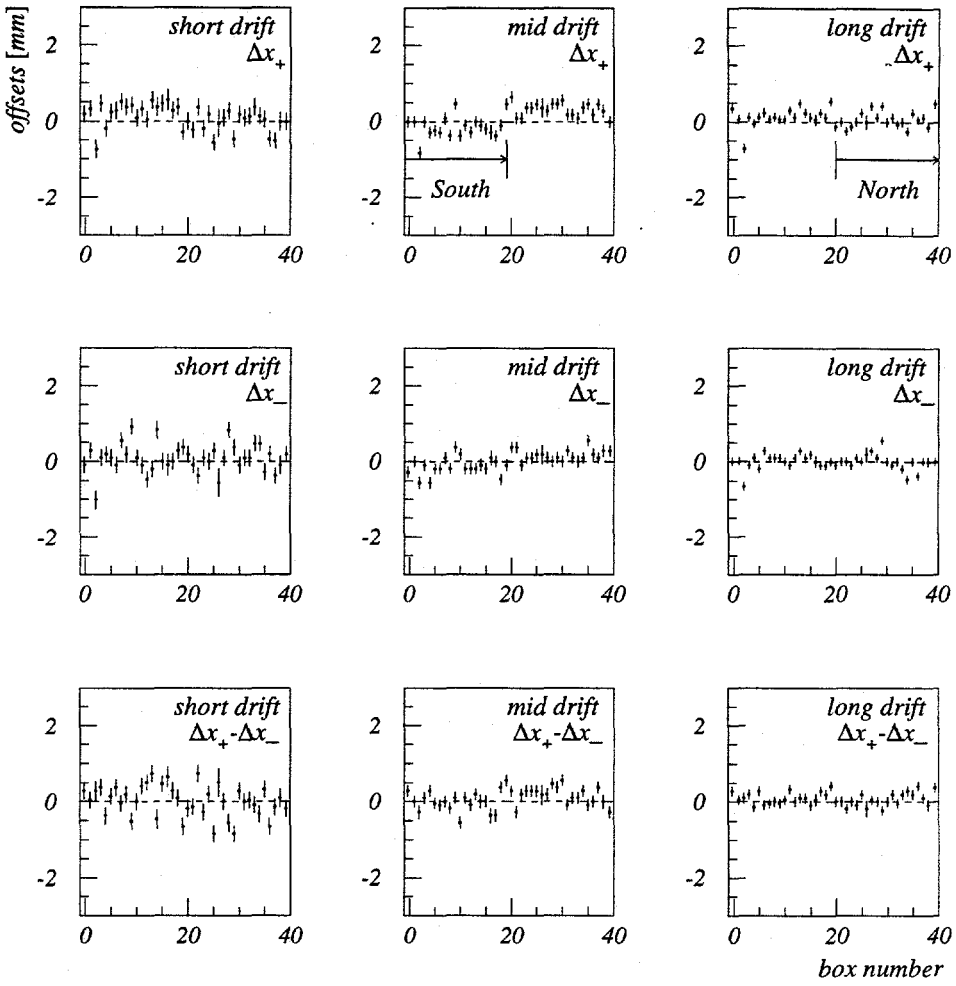

Figure 4.27: Offsets from positive (Δx_+) and negative (Δx_-) charged tracks with momenta in the range 0.25-0.80 GeV/c, in three sections of the drift boxes.

tions can be limited by plotting the x-offsets of positive tracks minus those of negative tracks. Figure 4.28 shows possible offsets in a South and North TPC pair for three z-slices in drift length. A straight line fit to the offsets determines the TPC's radial offset and tilt. Figure 4.29 shows the 1993 data with new radial alignment constants, where the North and South boxes are paired together. Offsets are less than 0.3mm and tilts less than 0.2mrad. The 1994-95 data shows mis-alignment at the level of 1mm if 1993 constants are used (figure 4.30), and 0.1mm for the new 1994-95 constants (figure 4.31). The 1994-95 constants were also investigated if they could be used for the 1993 data set. Figure 4.32 shows significant mis-alignment if these constants are used for 1993. As a result, two constants sets were created and retained, individually for the 1993 and 1994-95 data.

The small coupling between azimuthal and radial alignments was eliminated by a final adjustment on both sets of constants. All figures above describing the final 1993 and 1994-95 alignments are from this final tuning.

4.4.2. End Cap-CRID Alignment

The End-Cap CRID alignment benefited from the Barrel CRID experience, however, due to particularities in the End-Cap system it requires a somewhat different approach. Alignment cannot rely on low momentum tracks as their multiplicity and scatter in the material between the Inner and Outer Drift Chambers leads to un-

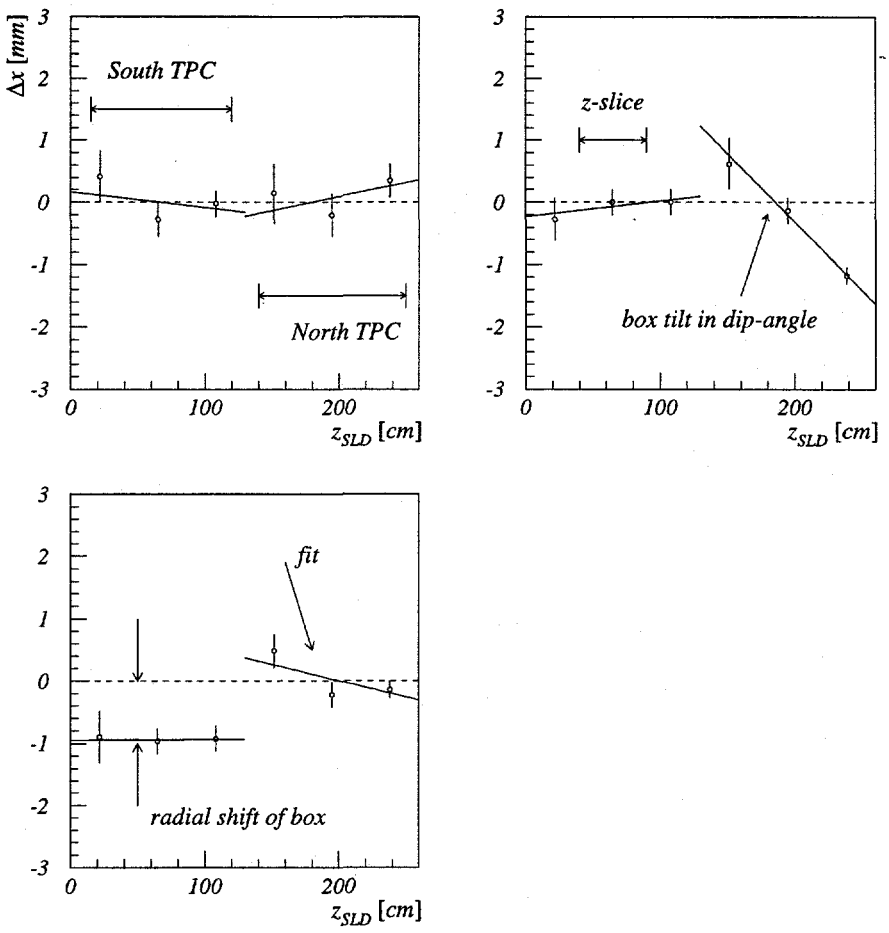

Figure 4.28: Radial x-offsets for 3 z-slices in drift length for a pair of North and South TPC's. The fits show how radial offsets and tilts are found.

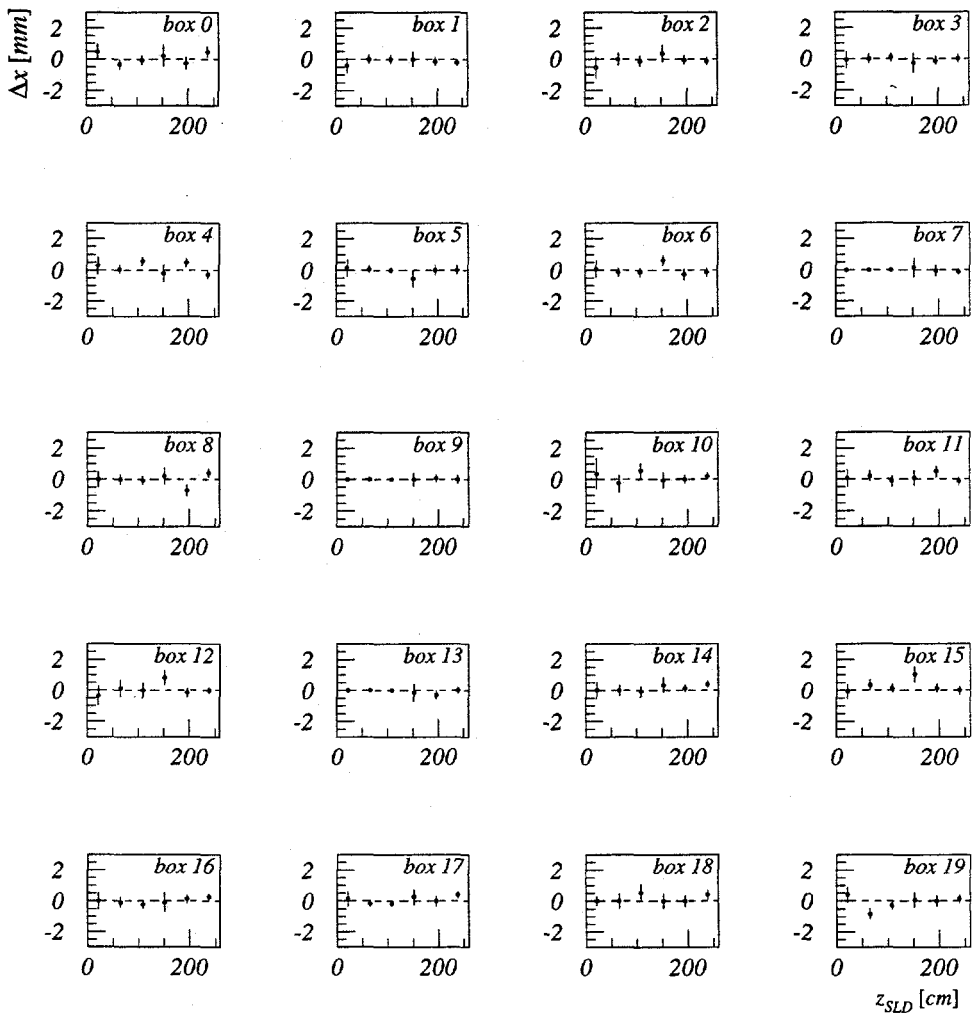

Figure 4.29: Radial mis-alignments for 1993 data with new constants.

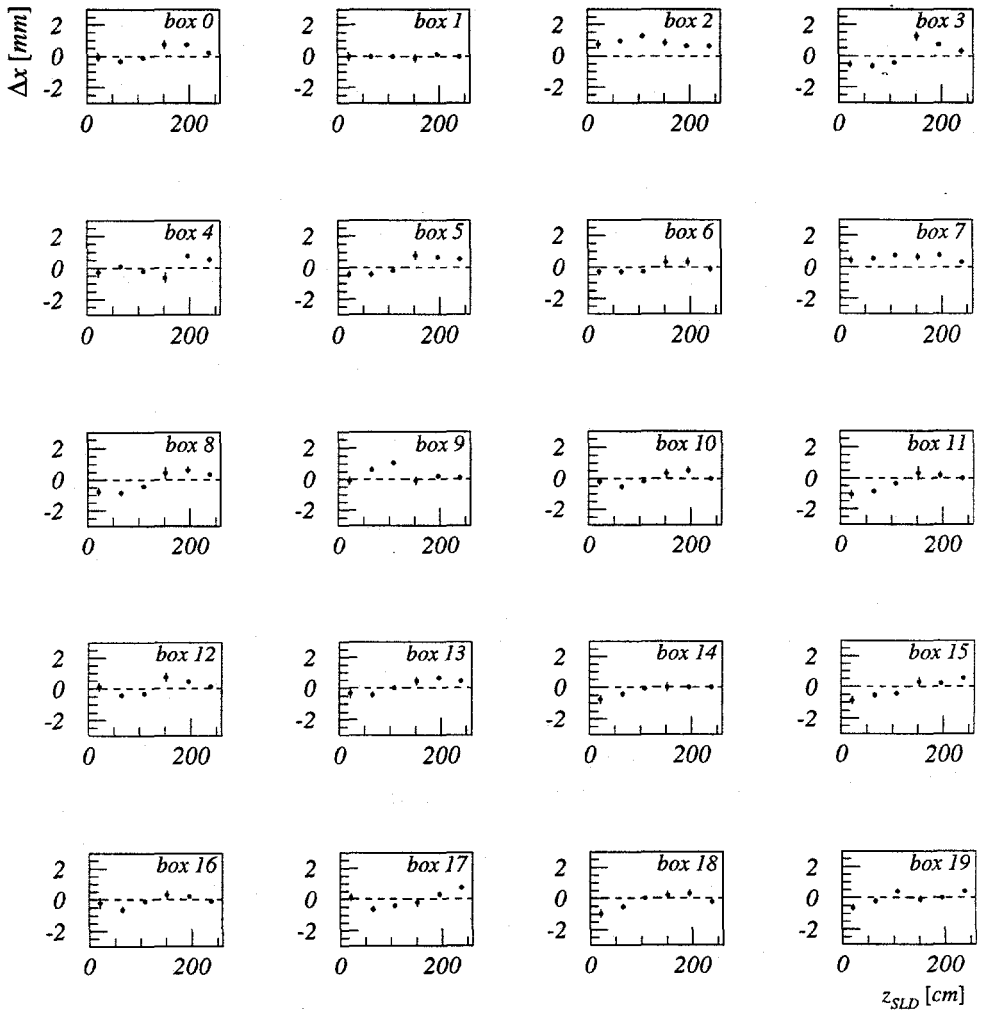

Figure 4.30: Radial mis-alignments for 1994 data with 1993 constants.

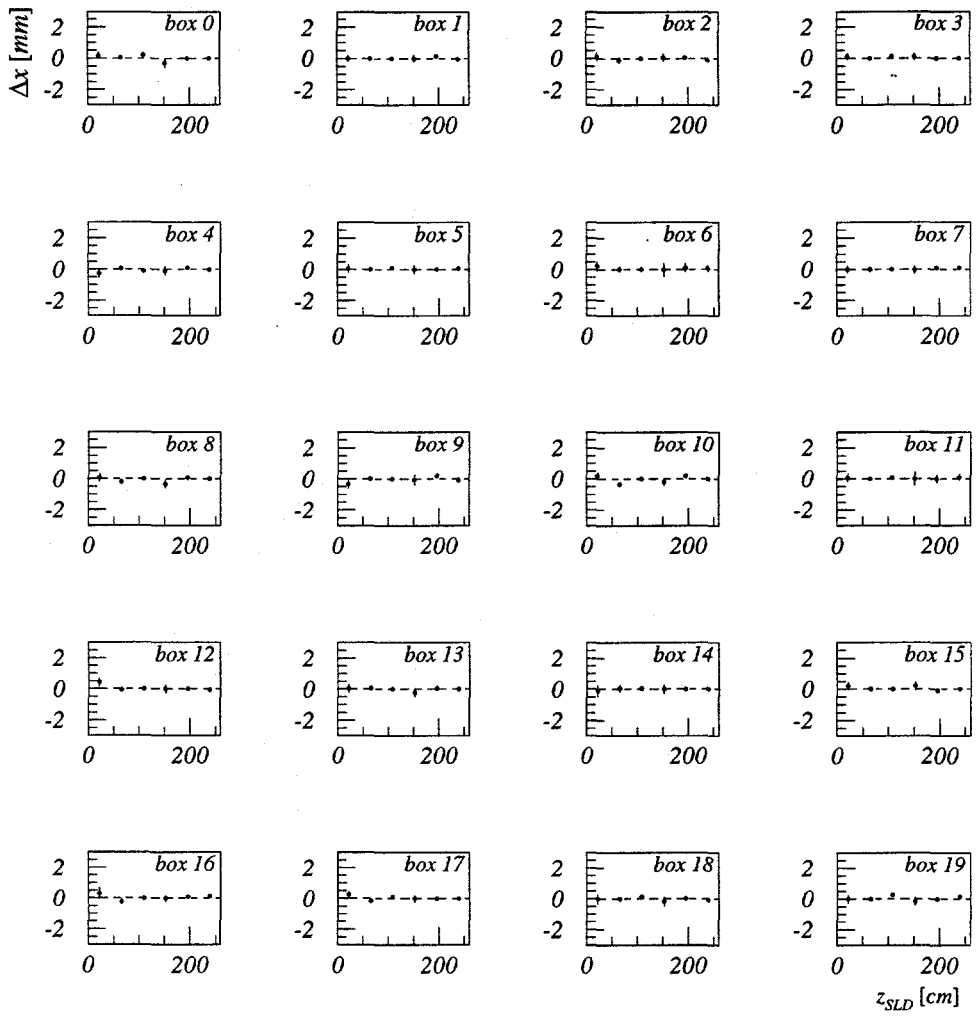

Figure 4.31: Radial mis-alignments for 1994 data with new constants.

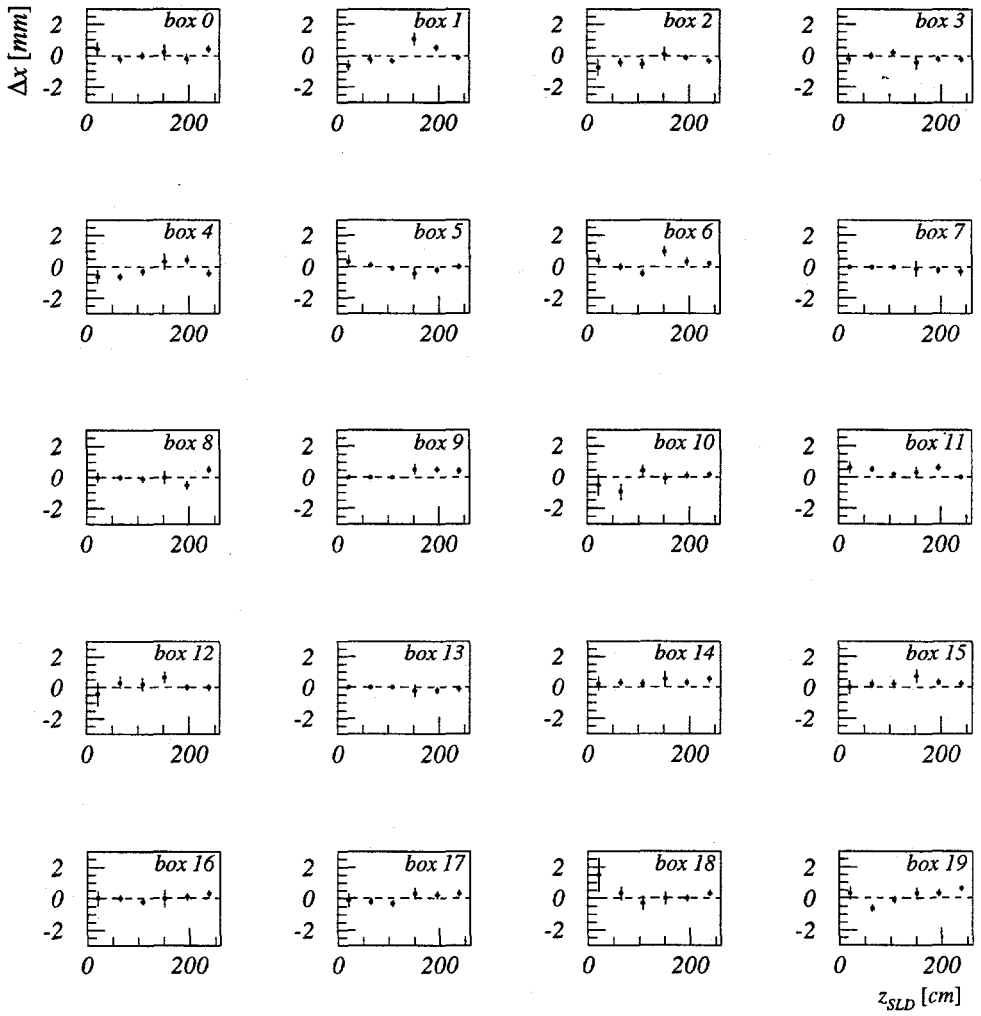

Figure 4.32: Radial mis-alignments for 1993 data with 1994 constants.

reliable reconstruction within the tracking system. An additional factor is that the box length is small and reduces the effective lever arm in all of the tilts alignments. Practically, the four degrees of freedom, out of six, that were tuned in the Barrel, are reduced to two for the End-Cap. The procedure for the EC-CRID is to use an exact solution method for all six degrees of freedom and discard the z-coordinate offset result.

The "exact" observable is again the x-coordinate of a trail's mid-point, however this point may be described with a y-coordinate as well. The two faces of the End-Cap CRID are almost parallel, so the y-coordinate is approximately in the middle. The z-coordinate gives a fine adjustment to this value, its error reflecting in a negligible 0.03mm y-error. The calibrated z-coordinate is also sufficiently precise to map the box tilts, so the points can be assigned 3D coordinates. Joining pairs of 3D points to form lines, a complete 3D alignment is possible. The imprecision in z leads to an unreliable z-offset, but the effect on the other alignment constants is to second order in z_{error}/L_{box} (equation 4.6), approximately 0.2%.

The lines are parametrised as: $\vec{r} = \vec{r}_0 + \lambda\vec{n}$, where $\vec{n}$ is the unit vector giving the direction of the line, and parameter $\vec{r}_0$ is an offset vector perpendicular to $\vec{n}$. In the following, let quantity A' denote A_{found} and A denote $A_{expected}$.

The mis-alignment consists of a rotation plus a translation: $\vec{r}' = \mathbf{R}\vec{r} + \vec{t}$, with $\vec{t}$ being the translation mis-alignment and $\mathbf{R}$ the rotation matrix: $\mathbf{R}\mathbf{R}^\dagger = \mathbf{1}, \mathbf{R} = e^{-\times\vec{\phi}}$,

where $(\times\vec{\phi})_{ij} \stackrel{\text{def}}{=} \epsilon_{ijk}\phi_k$ is the axis and angle of rotation combined.

The difference in line orientation is defined as: $\Delta\vec{n} \stackrel{\text{def}}{=} \vec{n}\,' - \vec{n}$. Using the information from the two lines the rotational mis-alignment is determined:

$$\begin{aligned} \vec{N} \stackrel{\text{def}}{=} \vec{\phi}/\phi &= \frac{\Delta\vec{n}_1 \times \Delta\vec{n}_2}{|\Delta\vec{n}_1 \times \Delta\vec{n}_2|} \\ sin\phi &= \frac{\vec{n}_1 \cdot (\vec{n}\,'_1 \times \vec{N})}{1 - (\vec{n}_1 \cdot \vec{N})^2} \\ cos\phi &= \frac{\vec{n}\,'_1 \cdot \vec{n}_1 - (\vec{n}_1 \cdot \vec{N})^2}{1 - (\vec{n}_1 \cdot \vec{N})^2} \end{aligned} \tag{4.6}$$

The translational mis-alignment follows as $\vec{t} = \vec{r}\,'_0 - e^{-\times\vec{\phi}}\vec{r}_0$, equation that again can be written for any of the lines, similarly to $sin\phi$ and $cos\phi$ in the equation 4.6 above.

To reduce the combinatorial background, not all the points within a search distance from the "expected" ends are considered, but only those that are the end-points of a cluster. The clustering algorithm used delimits a window around the "expected" segment and the hits are clustered by checking pulse width overlaps between hits on adjacent wires. Missing hits, of at most one wire, are allowed and clusters are given points for how many hits form the cluster. A trim is performed at the end, letting only hits that are in the upper third range of scores to be considered. To those a straight line fit is performed. The matrix M, below (4.7), describes the spatial arrangement

of points:

$$M_{ij} \stackrel{\text{def}}{=} \overline{R_i R_j} - \overline{R_i} \cdot \overline{R_j} \tag{4.7}$$

where $\vec{R}$ are the point positions, and the overbar signifies average over the entire sample of points. The fit solution has orientation $\vec{n}$ satisfying $M\vec{n} = \mu_0\vec{n}$, where μ_0 is the largest eigenvalue of the matrix. The intuitive image is simple: if the cluster of points forms a 3D "ellipsoid" nebula, then the three eigenvalues of M are the axes of the ellipsoid. If the nebula resembles to any degree a line, then the largest of the axes corresponds to the solution of the fit. The remaining two eigenvalues are the errors on the two directions orthogonal to the line. The offset of the line follows then as: $\vec{r}_0 = (\mathbf{1} - \vec{\mathbf{n}}\vec{\mathbf{n}}) < \vec{R} >$.

After the line is known a selection procedure ensures finding the proper ends of the cluster. The in/out ambiguity of the cluster's ends is solved by referencing it to the "expected" segment and its known in/out identity of the two ends. Once the line is found, a center in x and y is computed, using the z information of the earliest of the its ends. The z assigned to the center is the z used above plus a correction of approximately half that of the "expected" segment given by tracking. The points obtained are stored in their "expected"/"found" versions and combinations of two points are formed to give lines with which the exact mis-alignments can be calculated. Histograms of the six mis-alignment constants are accumulated and the center values of the distributions used as alignment constants. The z-offset is used only as a first

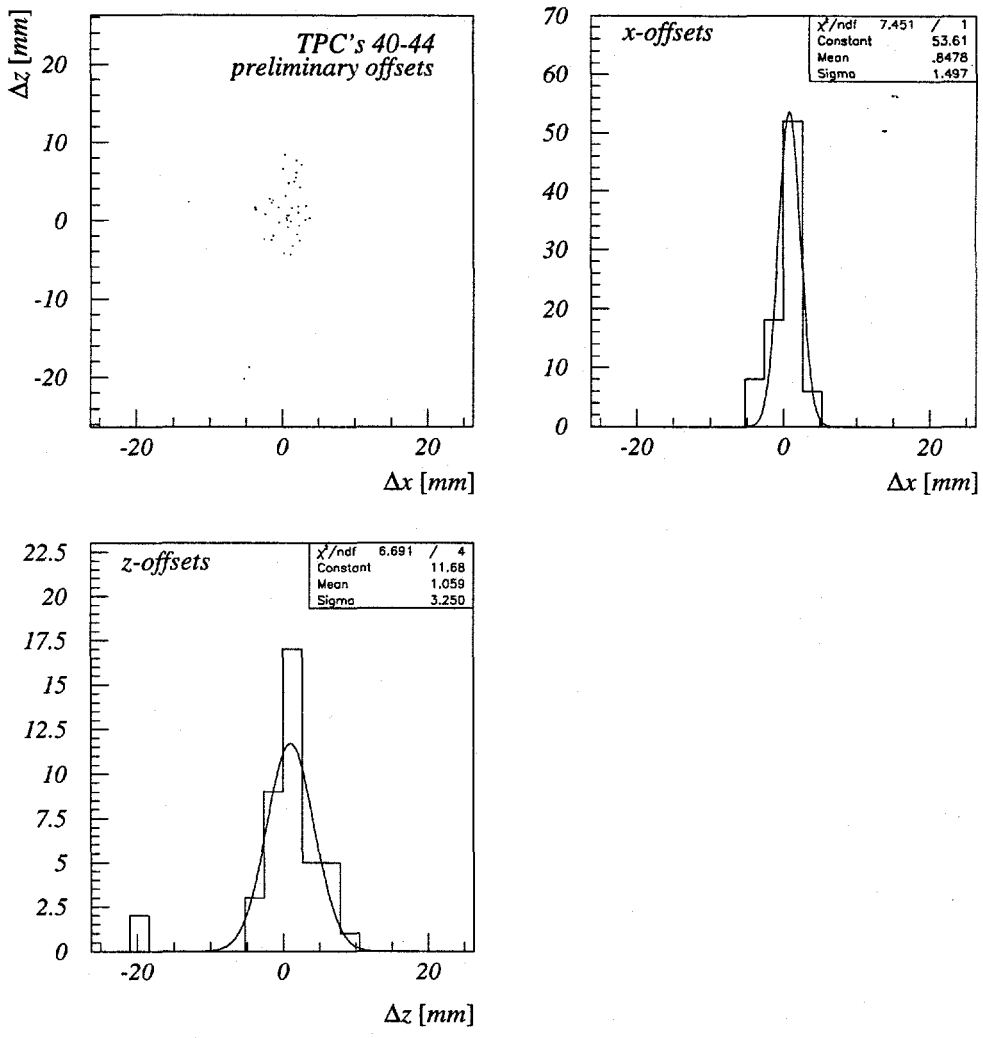

Figure 4.33: End-Cap CRID preliminary offsets for an overlay of all South End-Cap TPC's. The x-offsets are in the range of 1mm and the z-offsets, 3mm.

order correction, it being reliable only to about 1-2mm.

The End-Cap tracking system is currently progressing on the offline software and calibration/alignment code. The alignment code for the CRID has been tested to first order on data to check it's feasibility, however the final alignment constants must wait until the tracking system is fully aligned.

A test sample was extracted from the 1993 data to see if within an accuracy of a few mm the Drift-Chamber and CRID were in place. The data set is very small due to the fact that the North Outer drift chamber was off and the tracking reconstruction efficiency was low. Figure 4.33 shows an overlay of all South End-Cap TPC's. The z and x-coordinate offsets cluster around zero with a spread of about 5mm, confirming that the installment and the CRID t_0 calibration are correct.

4.5. CRID performance

For understanding the CRID, a benchmark analysis [52] was performed on a set of tracks that have stringent quality requirements. For this set of tracks the $\chi^2/d.o.f \leq 5$ for the drift fit, the track has to be recorded by CDC layer number 10 prior to the CRID, tracks identified in the liquid CRID have to have a saturating hit in one of the TPC's and those identified in the gas CRID must have the Čerenkov ring away from any saturated hits spray from other tracks. Second, pure sources of particles were selected from the data by using complementary techniques, such as vertexing

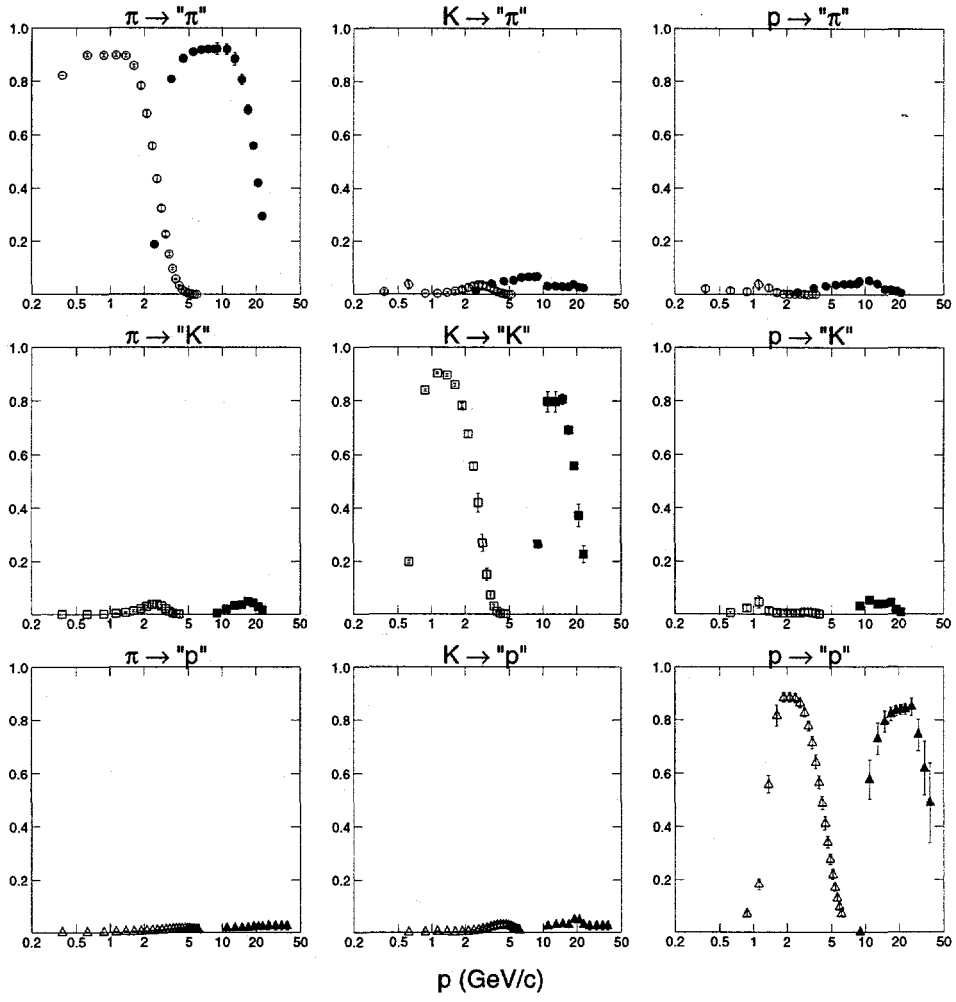

Figure 4.34: The particle identification efficiencies and mis-id rates for the SLD Barrel CRID versus momentum.

and tight invariant mass window cuts. The sources used were $K_s^0 \rightarrow \pi^+\pi^-$ and pions from τ decays. Protons from $\Lambda^0 \rightarrow p^+\pi^-$ decays have marginal statistical power, and are used only as a cross-check. Kaons from $\phi \rightarrow K^+K^-$ do not have enough statistical power. The two pion sources are complementary in geometry as well as in event sample, hadronic versus leptonic.

The general procedure is to use the identification efficiency measured in the data sample modified by the difference between the result of a similar (calibration-sample) analysis performed on Monte Carlo and the expected Monte Carlo efficiency for the full hadronic sample. This difference corrects for effects such as the impurity of the calibration sample and any systematic differences in track quality between the calibration sample and the inclusive track sample.

The resulting charged hadron identification matrix is shown in figure 4.34. The diagonal elements are the identification efficiencies versus track momentum, typically above 80%, and the off-diagonal elements, mis-identification rates, typically much lower than 5%.

The CRID output data is in the form of a 5-vector that gives the log-likelihood (LLIK) probability for the respective track to be an electron, muon, pion, kaon, or proton. To discriminate between a pion and a kaon for instance, the most common case, it is required that $LLIK(K) - LLIK(\pi) \geq +3 \ldots +5$. A cut at 3 is considered an optimal cut in view of efficiency and purity, while a cut at 5 is considered a hard cut.

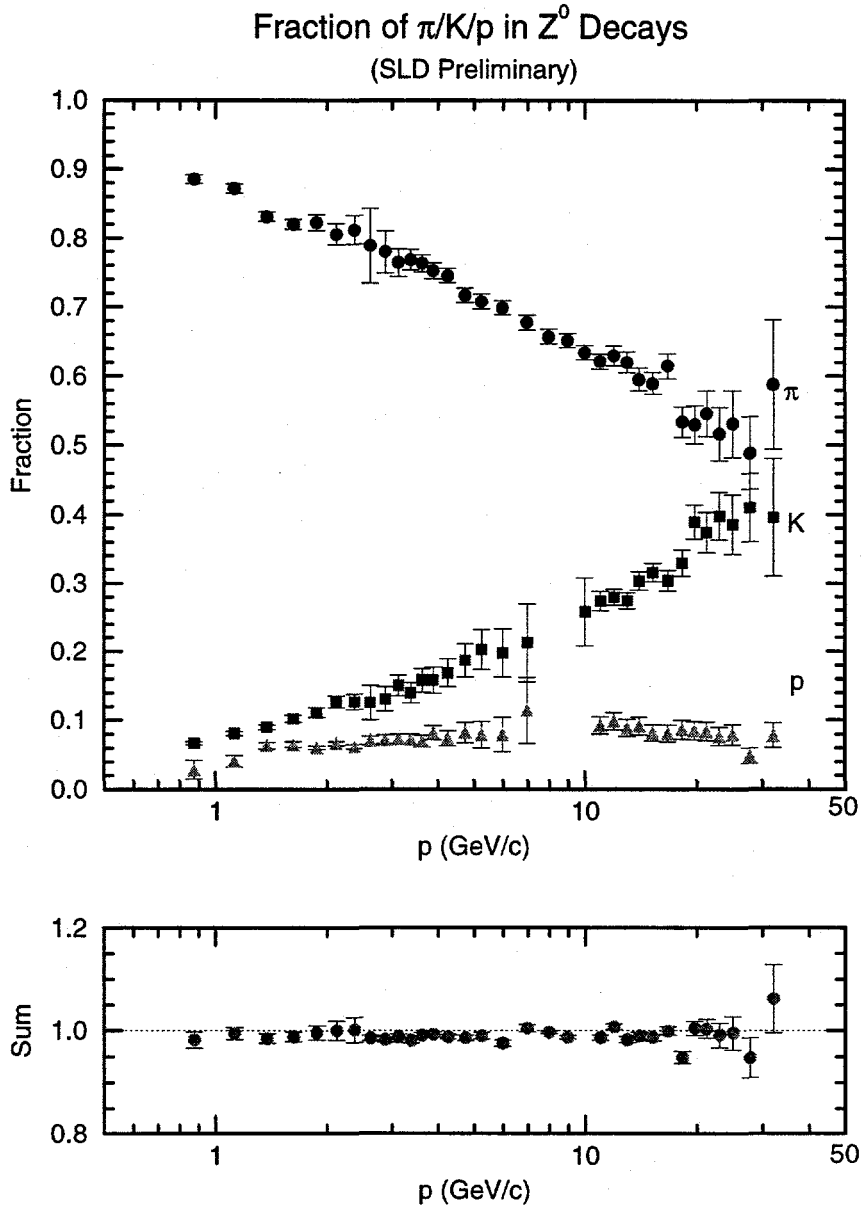

Figure 4.35: The charged hadron fractions versus momentum. The bottom plot shows the sum of the three fractions and a good agreement with unity is observed.

Using the latter identification level, the fractions of charged hadrons was measured as the first CRID analysis [52]. The results are shown in figure 4.35 for the fractions versus momentum. In this analysis all fractions are measured and the constraint to add up to unity is left as a consistency check that, as shown in figure 4.35 is well satisfied.

As a function of momentum the CRID information used is from the liquid system in the range of 0.2 - 2.5 GeV/c, system combined for 2.5 - 3.5 GeV/c and gas information above 3.5 GeV/c. The impact of K/π separation on physics analyses reconstructing heavier strange particles can be dramatic. For instance in the charged decay mode of the $\phi \rightarrow K^+K^-$, figure 4.36 shows the emergence of the ϕ peak for increasing levels of kaon identification. The "level 1" identification in the figure refers to a kaon-pion log-likelihood difference of 0, while "level 2" to a difference of +5.

Compared to traditional dE/dx loss measurements this is an impressive achievement, however, to achieve this high performance an elaborate design of the system and careful maintenance and a precise alignment were needed.

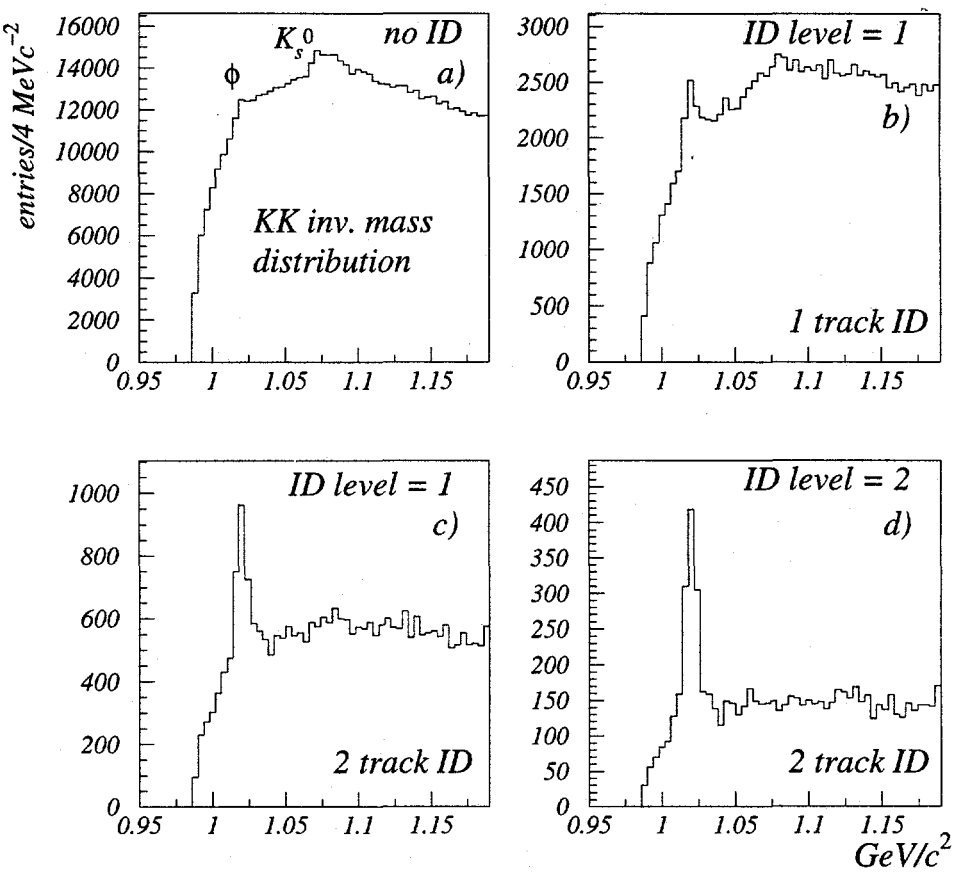

Figure 4.36: Effect of clean K/π separation on the $\phi \rightarrow K^+K^-$ signal.

Chapter 5

Hadronic Event Selection

This chapter describes the hadronic event selection, flavor and quark-jet tagging techniques used in the ϕ and K^{*0} analyses.

5.1. The Hadronic Event Filter

Data passing the trigger system is written to tape and then processed off-line to select Z^0 candidates and reject a large fraction of the background. The filtering is performed using information from the CDC (pattern recognition level), LAC and WIC systems. The first filter, the Energy Imbalance Trigger (EIT), uses information from the LAC to select events with a good forward-backward energetic balance and a minimum total energy. The second trigger, the Track Trigger, requires at least one track (pattern recognition level) to be above 1 GeV/c in momentum. Hadronic events are selected by requiring either one of the filters to be passed.

The EIT (Pass 1) filter requires:

1. $NEMHI \geq 10$
2. $EHI > 15$ GeV$|_{min-Iscale}$
3. $ELO < 140$ GeV$|_{min-Iscale}$
4. $2 \cdot EHI > 3 \cdot (ELO - 70GeV)$
5. $NEMHI > 0$ for both North and South hemispheres

where:

- NEMHI is the number of LAC EM towers with signal above the Hi-threshold of 60 ADC counts,
- EHI is the sum of energy deposited in all LAC EM (HAD) towers above the Hi-threshold of 60 (120) ADC counts, and
- ELO is the sum of energy deposited in all LAC EM (HAD) towers above the Low-threshold of 8 (12) ADC counts.

Requirements 3 and 5 remove muons produced in the beam pipe prior to the detector and other accelerator-based background events. Item 4 removes events with large numbers of SLC muons passing through the LAC. Approximately 97% of the background events, that were flagged by the trigger system and written to tape, are

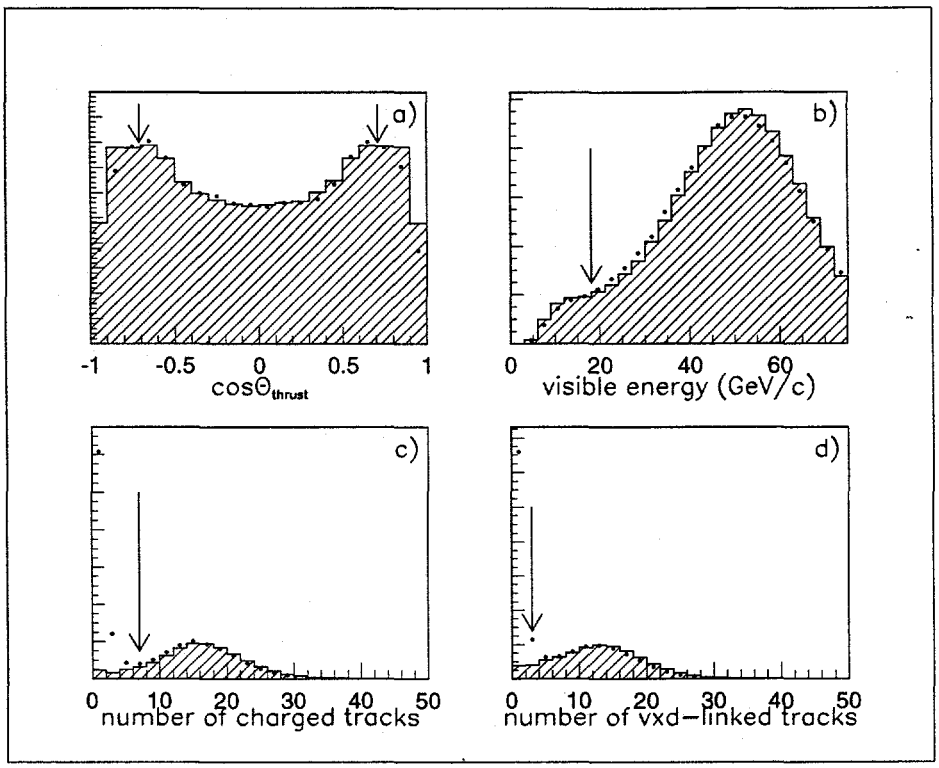

Figure 5.1: Data (points) and Monte Carlo (hatched) comparisons for events that pass the EIT hadronic filter. The arrows indicate the cut values used in the final event selection. The excess of events with low charged track multiplicities is due to the $Z^0 \rightarrow \tau^+\tau^-$ contamination in the EIT-filtered event sample.

rejected by the Pass 1 filter. The combined efficiency, trigger system plus Pass 1 filter, for the hadronic Z^0 decays is approximately 92% [47]. Events that pass the Pass 1 filter are run through the Pass 2 filter, which classifies the event into a potential Wide Angle Bhabha (WAB), a μ-pair, or a hadronic event. Figure 5.1 shows several event-variable comparisons between the data and the full Hadronic Monte Carlo simulation.

The filtered events are then passed through a full detector reconstruction program to produce a summary data tape (DST) ready for physics analyses. SLD analyses

however, use often a subset of this information compacted into a mini-DST, or a micro-DST format.

5.2. Hadronic Event Selection

The selection cuts are grouped into three sets, a general hadronic set:

1. minimum 18 GeV of visible energy,
2. minimum 7 charged tracks with $p_T \geq 0.2\ GeV/c$,
3. $|\cos\theta_{thrust}| \leq 0.71$, with θ_{thrust} the thrust axis angle to the positron-beam, and
4. pass EIT filter,

a particle ID (CRID) and flavor tagging set of cuts:

1. CRID High-Voltage ON,
2. CRID velocity calibration done,
3. CRID data not truncated,
4. no suspect low CRID vs. CDC data size.
5. the Silicon Vertex Detector (VXD) ON,
6. no VXD related problems for the particular run,
7. well measured interaction point (IP), and

8. minimum 3 charged tracks with 2 or more VXD hits,

and a quark/antiquark tagging set:

1. $|\cos\theta_{thrust}| \geq 0.20$,

2. no polarisation related problems for the respective run, and

3. time lag to the nearest polarisation measurement, PDTIME $\leq$ 10 minutes.

The thrust axis of the event is defined as the axis $\hat{t}$ that maximizes the quantity

$$T = \frac{\sum_{clusters} |\vec{p} \cdot \hat{t}|}{\sum_{clusters} |\vec{p}|}, \tag{5.1}$$

where $\vec{p}$ is the 3-momentum of the energy cluster, assuming the IP as the origin of the vector and the particles having pion mass. The requirement that the thrust axis satisfy $|\cos\theta_{thrust}| \leq 0.71$ guarantees that the event is well contained in the barrel portion of the detector.

Figure 5.2 shows a comparison between data and Monte Carlo for several event variables, all of which show good Monte Carlo to data agreement. This gives confidence that the Monte Carlo simulation reproduces the data faithfully. Table 5.1 shows the number of events used in the three sub-analyses for ϕ and K^{*0} for all six run periods of the 1993-95 SLD data set. The first column shows number of hadronic events. The second column is a sub-set of the first where events are required to be flavor tagged and similarly, the third, quark jets to be tagged.

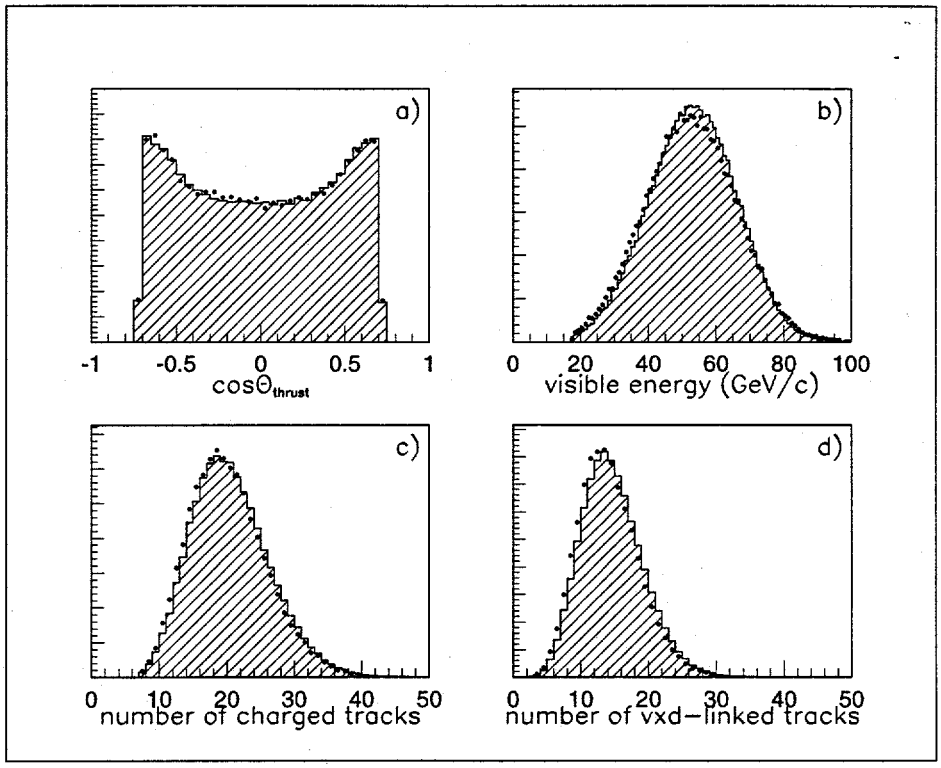

Figure 5.2: Data (points) and Monte Carlo (hatched) comparisons for selected events. It is estimated that there is less than 0.2% τ contamination in the final hadronic event sample.

Table 5.1: Selected Hadronic Z^0 statistics for the 1993-1995 data run.

Run Period	Hadronic	Flavor tagged	Quark tagged
1993 Pre-Veto	8536	5149	3894
1993 Veto	11558	10211	7699
1993 Post-Veto	7962	6283	4724
1994 Summer	12069	9086	6820
1994 Fall	29410	28300	21351
1995	20105	19220	14568
TOTAL:	89640	78249	59056

5.2.1. Precision Determination of the Interaction Point

The determination of the IP position at SLD has two parts: (i) determination of the IP transverse position with respect to the beam axis and (ii) IP longitudinal position.

For the transverse measurement, sets of 30 sequential Z^0 decays are accumulated and used to determine an average IP position. This procedure relies on the fact that the SLC IP is very stable and highly focused in the transverse plane (1-3 μm). The event by event IP is determined by extrapolating all charged tracks towards the SLD beam pipe, and fitting for a common vertex. The error ellipse is approximately 100 μm major axis by 15 μm minor axis (figure 5.3). Averaging reduces thrust axis dependencies as well as biases from isolated tracks and displaced secondary vertices, such that error becomes isotropic and it is substantially reduced (~ 7 μm). In practice,

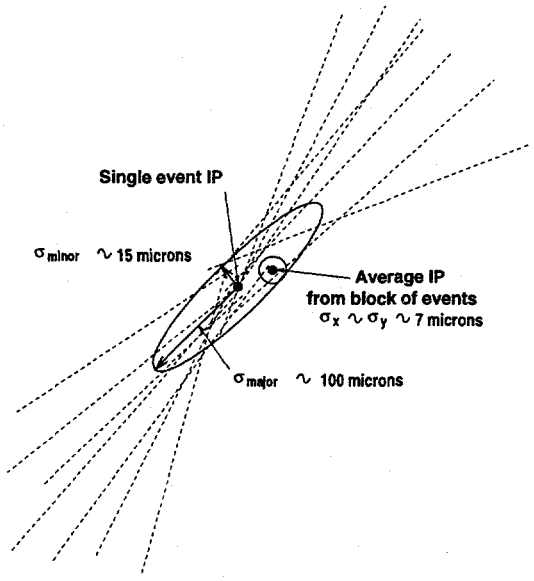

Figure 5.3: The differences in the transverse IP position and errors determined from a single event and from the average over a block of events. Note how the jet bias in the error ellipse is essentially removed by averaging over many events.

the averaging procedure uses a fit that typically converges in roughly 5 iterations and has an overall $\chi^2/d.o.f. < 1.3$.

This technique has been cross-checked with a complementary data sample to the hadronic data, $Z^0 \rightarrow \mu^+\mu^-$ events (figure 5.4). By extrapolating both muon tracks to the IP and subtracting the extrapolation errors, the resulting distribution width is $7 \pm 2\mu$m, consistent with the above resolution.

The longitudinal position is determined on an event by event basis since the SLC longitudinal spread is substantially larger (0.7 mm) than the transverse spread. Tracks with associated VXD hits are extrapolated in the transverse plane to the point of closest approach to the average $xy_{|IP}$ previously determined. The z position of this

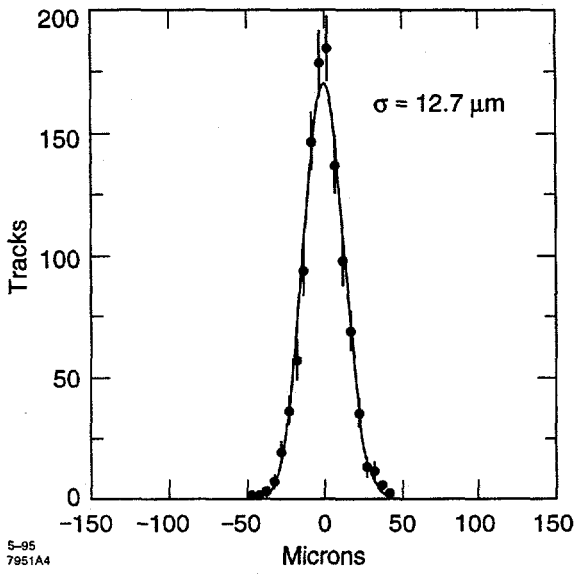

Figure 5.4: The xy impact parameters of tracks in $\mu^+\mu^-$ events. After correcting for extrapolation errors, a resolution of ~ 7 μm on the transverse position of the IP is obtained.

point is computed and if it is less than 3σ and 500 μm away from $\mathrm{xy}_{|IP}$, it is validated as $\mathrm{z}_{|IP}$. The resolution of the z position is flavor dependent [5] due to the different charged track multiplicities of the events. A Monte Carlo study shows resolutions of 32 μm in *uds* events, 36μm in charm and 52 μm in beauty events.

5.3. Hadronic Event and Detector Simulation

The Monte Carlo production at SLD is organized as follows. A generator level Monte Carlo produces particles using JETSET 7.4 [29] for the 1994-95 run and JETSET 6.3 for 1993 run. The particles are passed onto the detector simulation package, GEANT 3.21 [55], to produce tracks, showers, calorimetry clusters, *etc.* Data from

random triggers is overlaid to simulate real backgrounds. The simulated Monte Carlo data is then reconstructed using the same programs as the real data.

JETSET 7.4 is used with LUND fragmentation parameters extracted from the TASSO [56] and OPAL [57] experiments and tuned for particle production rates from other Z^0 experiments [58]. The fragmentation function for b and c quarks follows the Peterson representation [59] combined with an SLD B-hadron decay model [60].

5.4. Flavor Tagging, and Quark-Jet Tagging

For the first section of the analysis, the determination of inclusive and differential production rates of ϕ and K^{*0} in hadronic decays, it is sufficient to use the "standard" hadronic sample. We are able to capitalize, however, on the SLC/SLD outstanding features: polarised electron beam, highly stable IP and the SLD precision vertex detector to study hadronization in *light quark* events and K^{*0} production in *quark* and *anti-quark* jets.

5.4.1. Flavor Tagging and Normalised Impact Parameter

To tag light (u, d, s) and heavy (b, c) quark events the number of *significantly displaced* tracks from the IP is used. This technique, originally proposed by Hayes [61], exploits the fact that heavy quarks produce hadrons with lifetimes on the order of the weak interaction scale. The hadrons, with energies of 7-9 GeV, travel a typical

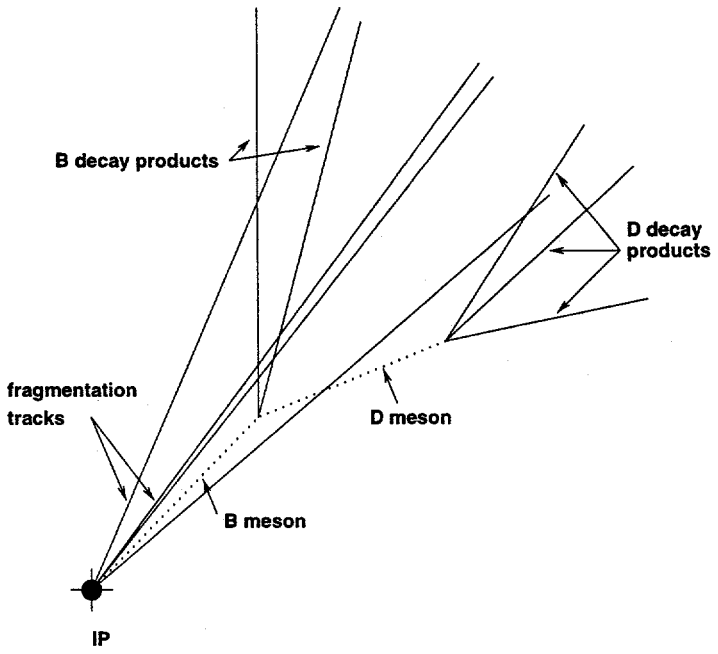

Figure 5.5: An example of a B meson decay. The fragmentation tracks tend to point back toward the IP, while the tracks from the neutral heavy meson decays may or may not.

distance of 500μ (figure 5.5). The flight distance is proportional to the hadron's boosted lifetime. With the precision SLD vertexing it is possible to discern the secondary vertices and establish the number of tracks displaced from the IP by more than 3 σ. The multiplicity of these tracks categorises the event into: u, d, s, c or b (figure 5.9).

An improvement [62; 63] to this technique is to associate algebraic sign to the impact parameter of the track based upon where it crossed the jet axis. Tracks crossing the jet axis in front of the IP are assigned a positive sign, while those crossing behind the IP a negative sign (figure 5.6). This creates a positive-asymmetric distribution of

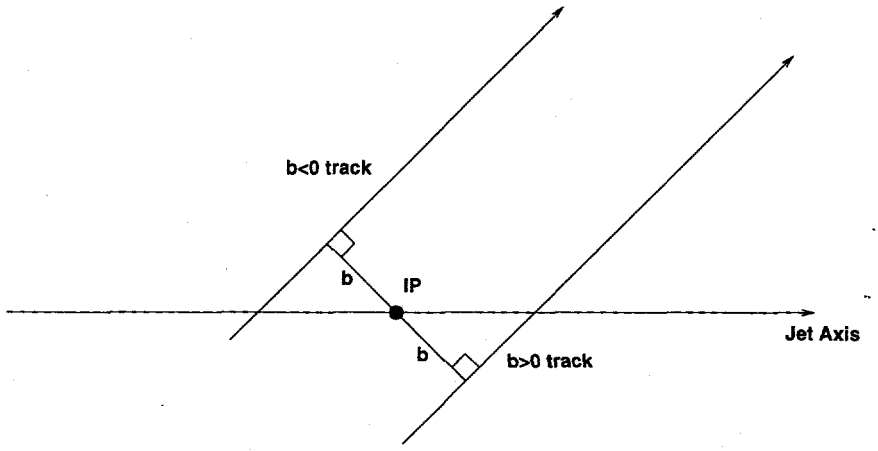

Figure 5.6: The sign convention for the signed impact parameter technique. The jet axis is used as an approximation of the heavy-quark hadron flight direction.

impact parameters in the case of the heavy quark decays (figure 5.7).

Since the SLD vertex detector has the best performance in the transverse plane to the beam axis, a version of the technique is used, adapted for two dimensions. In addition, to reduce sensitivity to track reconstruction errors and material interactions, the tagging uses only well reconstructed, *quality* tracks, defined by:

- first CDC hit of the track is no further than 39 cm radially from the IP. This requirement limits the extrapolation distance back to the VXD,
- minimum 40 CDC hits per track,
- track extrapolation to IP within 1 cm radially and 1.5 cm longitudinally of the IP. This is required in order to reject tracks that are potentially from nuclear interactions in the beam pipe,

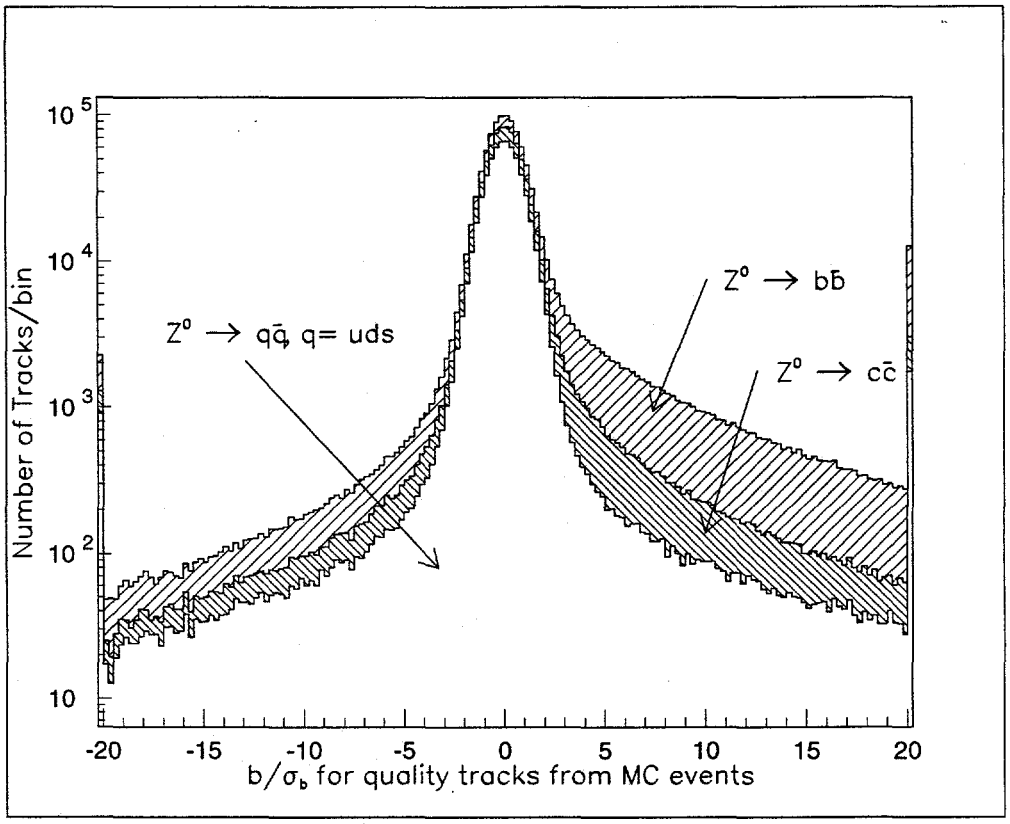

Figure 5.7: The normalized impact parameter (b/σ_b) distribution for light and heavy quark decay modes. The first and last bins show the amount of under- and over-flows.

- $\chi^2/d.o.f. < 5$ for the CDC drift fit,
- tracks of opposite charge forming a good V^0 vertex that are consistent with the K_s^0, Λ^0, or γ-conversion mass are rejected,
- minimum of one associated VXD hit.

Tracks passing the above requirements are restricted to additional physics related constraints:

- 2D (xy) impact parameter of the track to the IP less than 3 mm,
- uncertainty on the impact parameter less than 250 μm,
- $\chi^2/d.o.f. < 5$ for the CDC+VXD fit.

After applying these selection criteria a number of 12.81 quality tracks/event were observed in the Monte Carlo and 12.24/event in the data. Corrections [64] depending on momentum and dip-angle were applied to the Monte Carlo in order to provide a good agreement with the data. Figure 5.8 shows a comparison between data and Monte Carlo of the normalized impact-parameter distributions after these corrections were applied.

Significant tracks are quality tracks with normalized impact parameter to the IP greater than 3.0. Figure 5.9 shows the number of significant tracks per event, n_{sig}, in data and Monte Carlo. The two are found to be in very good agreement.

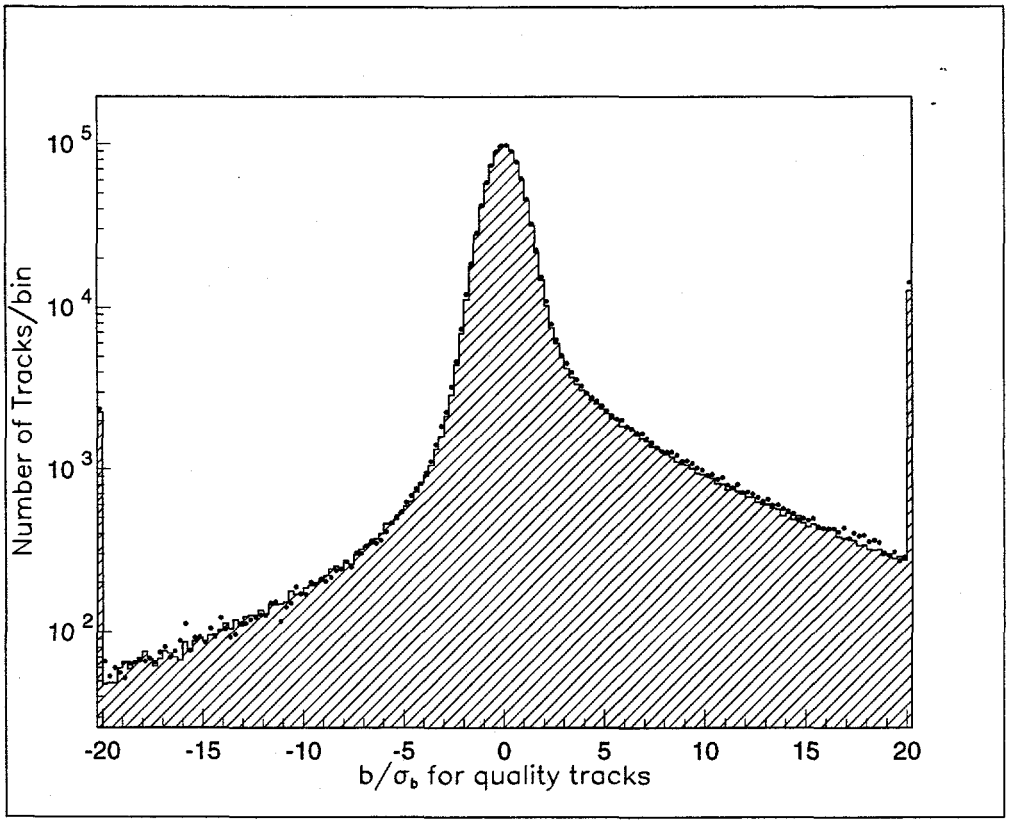

Figure 5.8: A comparison of the normalized impact parameter distributions for data (points) and Monte Carlo (hatched). The first and last bins show the under- and over-flow number of tracks. A *significant* track is defined as a track displaced by more that 3σ in impact parameter from the IP.

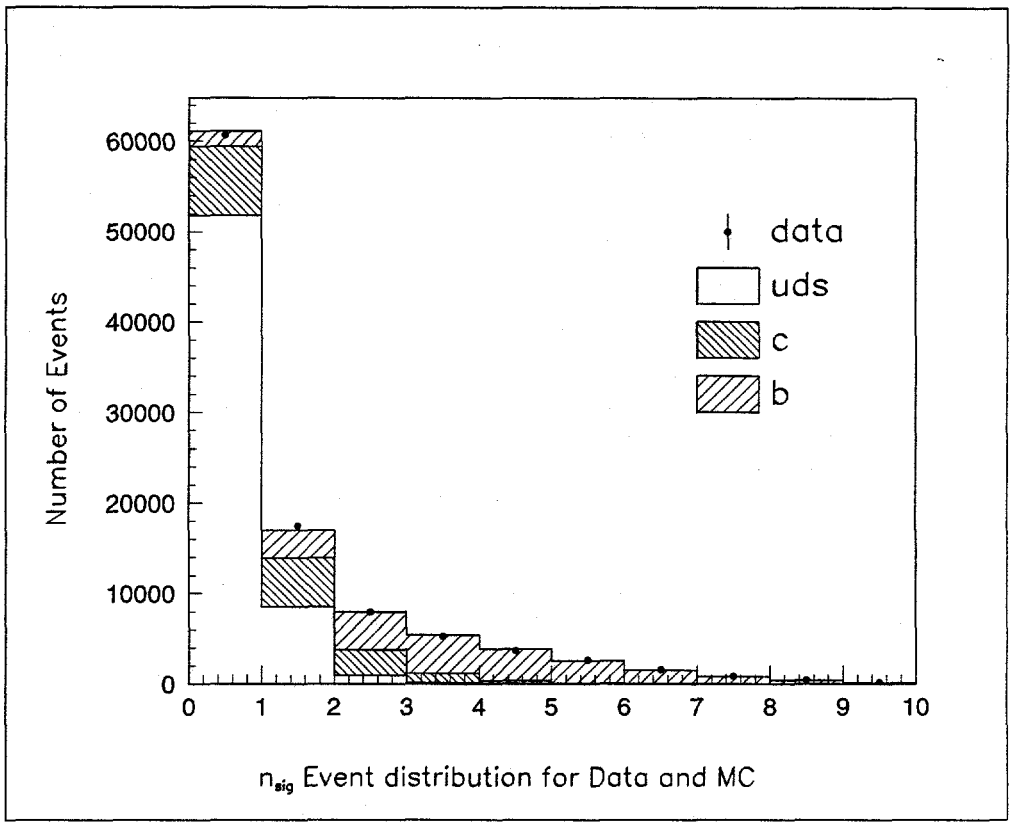

Figure 5.9: A comparison of the n_{sig} distributions for the data (points) and the Monte Carlo (histogram). Events with 3 or more significant tracks are tagged as b-quark events; events with 0 significant tracks are tagged as *uds* quark events, and the remaining events are tagged as c-quark events.

Table 5.2: Estimated event purities for the event flavor tags. The sum of each row equals 1.

	$\mathcal{P}_{uds}$	$\mathcal{P}_c$	$\mathcal{P}_b$
$n_{sig} = 0$	0.843	0.126	0.031
$n_{sig} = 1, 2$	0.382	0.328	0.289
$n_{sig} \geq 3$	0.009	0.105	0.886

Table 5.3: Estimated tagging efficiencies for selecting *uds*−,*c*−, and *b*−quark events using the n_{sig} tag. The sum of each column equals 1.

n_{sig} tag	uds tag eff.	c tag eff.	b tag eff.
0	0.846	0.439	0.076
1 or 2	0.151	0.477	0.330
≥ 3	0.002	0.083	0.594

A Monte Carlo study shows that events with large numbers of significant tracks are predominantly *b*-quark events, while those with few significant tracks are *uds* events. This result is in agreement with physical intuition since B hadrons obviously decay at some positive distance along the jet axis. Hence it is possible to divide the hadronic event sample into three sub-samples as follows:

- a *uds-enriched* sample of events with no significant quality tracks, $n_{sig} = 0$,
- a *c-enriched* sample of events with n_{sig} =1 or 2,
- a *b-enriched* sample of events with $n_{sig} \geq 3$.

The nominal efficiency and purities for the event tags are shown in tables 5.2 and table 5.3.

5.4.2. Quark Jet Tagging

The SLC electron beam polarisation induces a large asymmetry in the quark production polar angle distribution. Spin conservation in the decay of the Z^0 boson creates a forward-backward asymmetry in the directions followed by quarks and anti-quarks. Quarks will thus tend to follow the electron direction for left-handed beams and anti-quarks do so for right-handed beams. Figure 5.10 shows the calculated quark production asymmetry for the $72.3 \pm 0.4\%$[1] average polarisation obtained during the 1993 and 1994-95 physics run.

The thrust axis approximates within a few degrees the initial quark-antiquark direction. To point this axis into the quark direction the quark asymmetry is used (figure 5.10), such that for left-handed polarised electron beams the axis points into the same hemisphere as the incident electron.

The purities for this tag as a function of $|\cos\theta_{thrust}|$ are shown in figure 5.11. The degradation in tag purity at the detector level is due to acceptance cuts and the approximation of the quark direction with the thrust axis. To determine the optimal $\cos\theta_{thrust}$ cut value, the *quality* of the tag was considered. This figure of

[1]The events used in this analysis have an average electron-beam polarisation of $61.8 \pm 0.40\%$ for 1993, and $77.2 \pm 0.24\%$ for the 1994-95 physics run

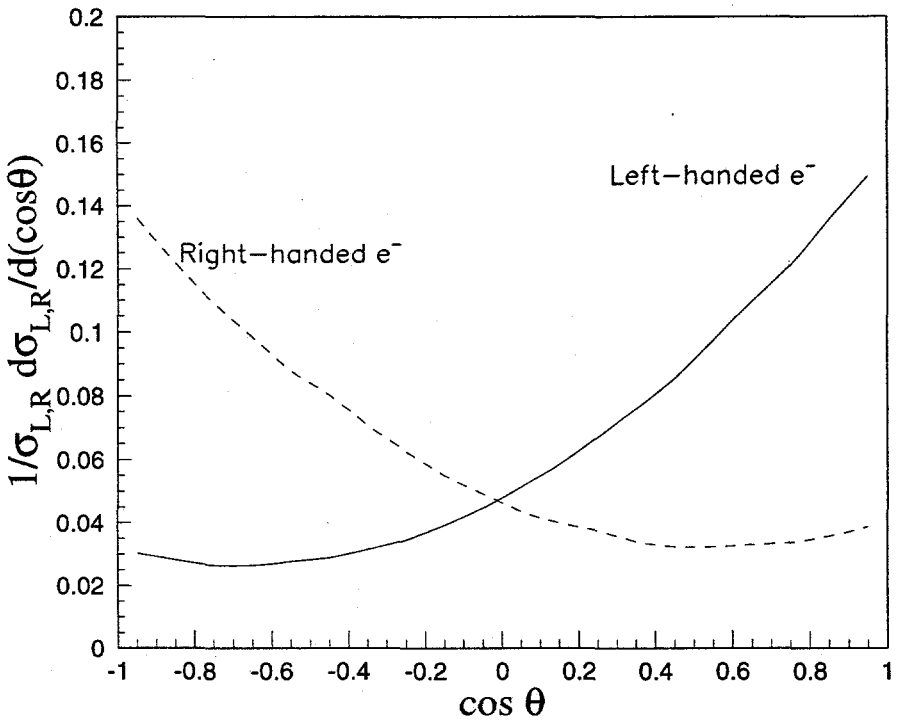

Figure 5.10: Quark production asymmetry in left and right-handed electron beams.

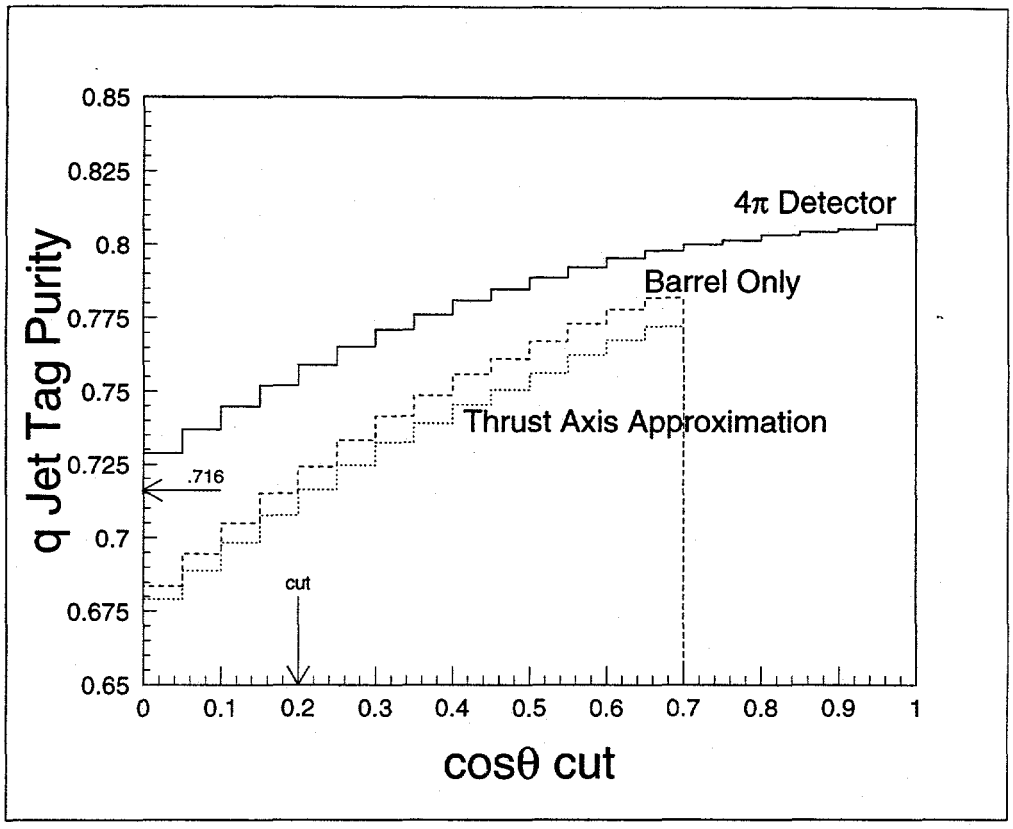

Figure 5.11: The calculated quark-jet tag purities as a function of the polar angle cut, assuming an average electron beam polarisation of 72.3%. Shown are the tag purities for a perfect 4π steradian solid angle coverage detector, after acceptance cuts, and after using the thrust axis for the tag. For the $|cos\theta_{thrust}|$ chosen, an estimated quark jet purity of 71.6% is obtained.

merit, equal to $(N_{correct-tag} - N_{incorrect-tag})/\sqrt{(N_{total})}$, was used to maximize the purity while minimizing the statistical error. The tag quality as a function of the cut's polar angle is shown in figure 5.12. In order to improve the *purity* of the tag, events with $|\cos\theta_{thrust}| < 0.2$ were rejected.

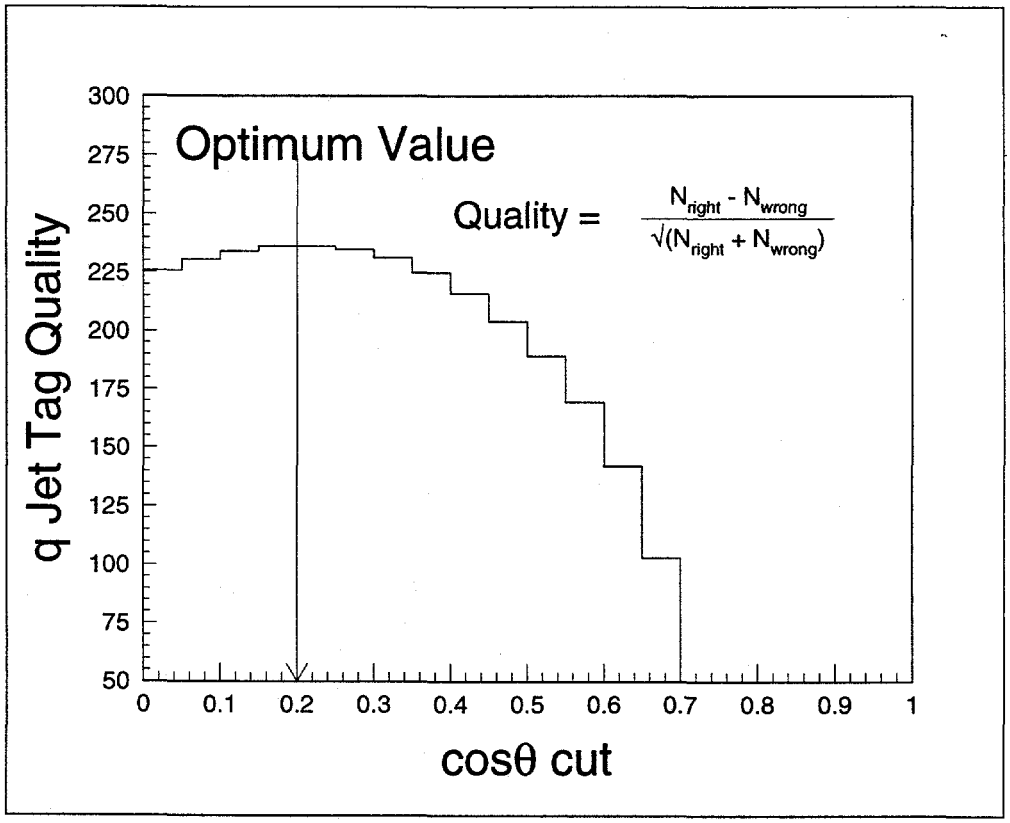

Figure 5.12: The *quality* of the quark-jet tag as a function of the thrust axis polar angle cut.

Chapter 6

Charged Hadron ID and the ϕ and K^{*0} Analysis

6.1. Introduction

This chapter presents the analysis of the production rates of ϕ and K^{*0} at the Z^0 mass in the charged decay modes $\phi \rightarrow K^+K^-$ and $K^{*0} \rightarrow K^+\pi^-$. The ϕ is a 4 MeV/c^2 wide state, at 1019.4 MeV/c^2 and the K^{*0} a 50.5 MeV/c^2 wide state, at 896.1 MeV/c^2 [43].

The ϕ is produced close to the invariant mass distribution's kinematic threshold and it is situated on the steep slope of the large combinatorial background near the threshold (figure 6.1-a).

The K^{*0} is produced at the peak of the combinatorial distribution (figure 6.2-a). The traditional measurement [65] for the K^{*0} is a simultaneous fit in the $K\pi$ and $\pi\pi$ invariant mass distributions for K^{*0} and ρ^0 deducting iteratively the contribution of the wrong particle in the wrong mass distribution. Although this accounts for ρ^0, an

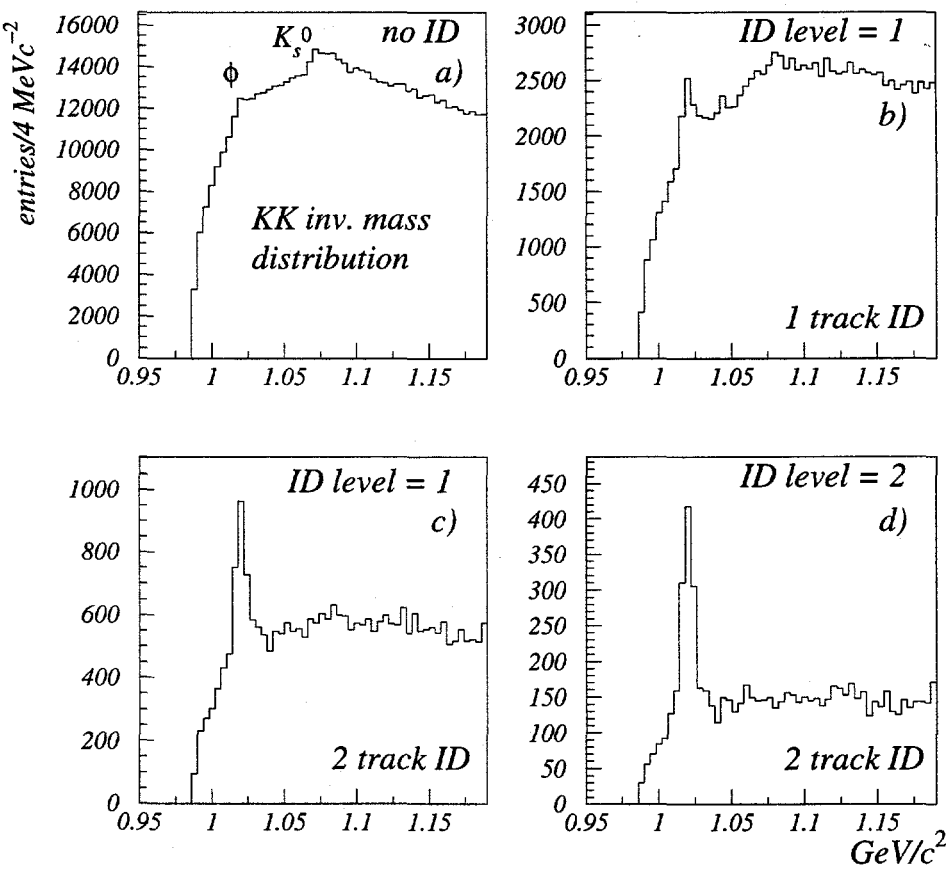

Figure 6.1: Effect of particle ID on the K^+K^- invariant mass distributions. Level one ID is a +0 difference between kaon and pion log-likelihood hypotheses and level two, a +5 difference.

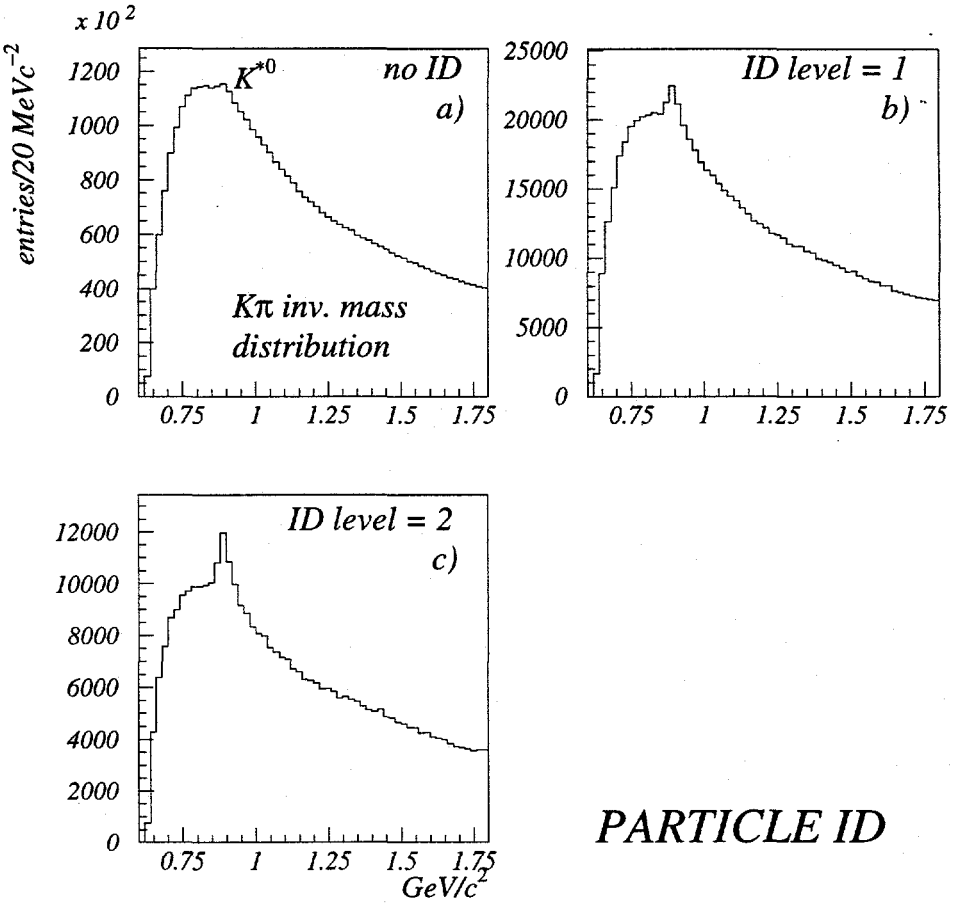

Figure 6.2: Effect of particle ID in the $K\pi$ invariant mass distributions. Level one ID is a +0 difference between kaon and pion log-likelihood hypotheses and level two, a +5 difference.

equally important signal, the ω^0, is not considered. The ρ^0 and ω^0 form a "saddle"-like background (figure 6.6 - insert) almost at the center of the K^{*0} signal and if not sufficiently suppressed, uncertainties in their rates lead to systematic errors on the order of 30% in the K^{*0} rate. With no particle ID the measurement is systematics limited, as both the shape of the ρ^0 [66] and of the large combinatorial background cannot be controlled at a level better than that of the K^{*0} signal.

In both cases, ϕ and K^{*0}, the use of a signal to noise enhancing device is crucial to the analysis. Figures 6.1 and 6.2 exemplify the signal to noise enhancement using particle ID for the ϕ and K^{*0} analyses.

6.2. Candidate Selection

The invariant mass distributions are formed by combining pairs of opposite charged tracks with a minimum of 40 hits in the tracking system (CDC) and a track fit of $\chi^2/d.o.f. < 7$. In the case of the ϕ the tracks are assigned kaon mass and in that of the K^{*0}, kaon and pion.

The main selection on which the analysis depends is the particle ID. The reconstruction code provides a bank of information on each track successfully identified. The bank contains information on the background environment, the liquid, gas and combined identification log-likelihoods and the number of photo-electrons in the Čerenkov ring. In this analysis liquid radiator information was used for tracks

with momentum below 2.5 GeV/c, combined identification information for the range 2.5-3.5 GeV/c and gas information above 3.5 GeV/c. The tracks with an associated particle ID bank are required the BADID flag not set and a log-likelihood difference between kaon and pion hypotheses of at least +3.

For the ϕ both tracks are required to be identified as kaons, while for K^{*0} only one track is required, the other being assumed "pion" ID. For K^{*0} both track combinations are attempted, kaon-pion and pion-kaon.

6.3. Production Rates versus Momentum

This section presents the specific backgrounds of the ϕ and K^{*0}, the fitting [67] procedure, the reconstruction efficiencies, ϕ and K^{*0} rates and the statistic and systematic errors.

6.3.1. Backgrounds

The background for the ϕ after the use of particle ID is purely combinatorial, the main reflection[1], K_s^0 at 1070 MeV/c^2 (figure 6.1-a), being completely eliminated by the use of particle ID.

[1] "Reflections" are backgrounds in the invariant mass distribution arising from track pair combinations with a distinct source, such as the K_s^0, ρ^0, *etc.* They are sometimes referred to as "resonant backgrounds" due to the resonant nature of the primary source. Their shape is asymmetric and widened compared to the original resonance since one, or both tracks have the mass mis-assigned. Sources that decay to more than two particles are further widened and distorted. *Ad hoc* the latter are termed "semi-resonant backgrounds".

The case of the K^{*0} is considerably more complicated than the ϕ due to the reflections that appear in the invariant mass distributions. A number of reflections were studied from a variety of sources. High multiplicity sources such as charm and beauty mesons[2] were found to have a monotonic shape resembling the combinatorial background which allows them to be combined with the latter. The two η sources were found very similar in shape and are considered together. The main sources treated separately in this analysis are shown in figure 6.3 and can be grouped into four categories:

- $\pi\pi$ - these reflections appear from sources that decay to at least two charged pions, such as: $\rho^0 \to \pi^+\pi^-$, $K_s^0 \to \pi^+\pi^-$, $\omega^0 \to 3\pi$ and $\eta, \eta' \to 3\pi, 5\pi$.

- $p\pi$ - proton mis-identified as a kaon: $\Lambda^0 \to p^+\pi^-$.

- ee - this case is well suppressed, but the $\gamma \to e^+e^-$ source is strong.

- KK - this signal is $\phi \to K^+K^-$ and it passes naturally the K^{*0} cuts.

Additional cuts against some of these reflections are:

- *kinematic* - for γ a cut on the e^+e^- invariant mass is imposed on all candidates: if $m_{e^+e^-} < 70$ MeV/c^2 the pair is rejected.

[2]Tracks from distinct sources such as ρ^0, K_s^0 originating in charm and beauty decays are included in the appropriate categories of ρ^0, K_s^0, *etc.* reflections and not in the heavy flavor group.

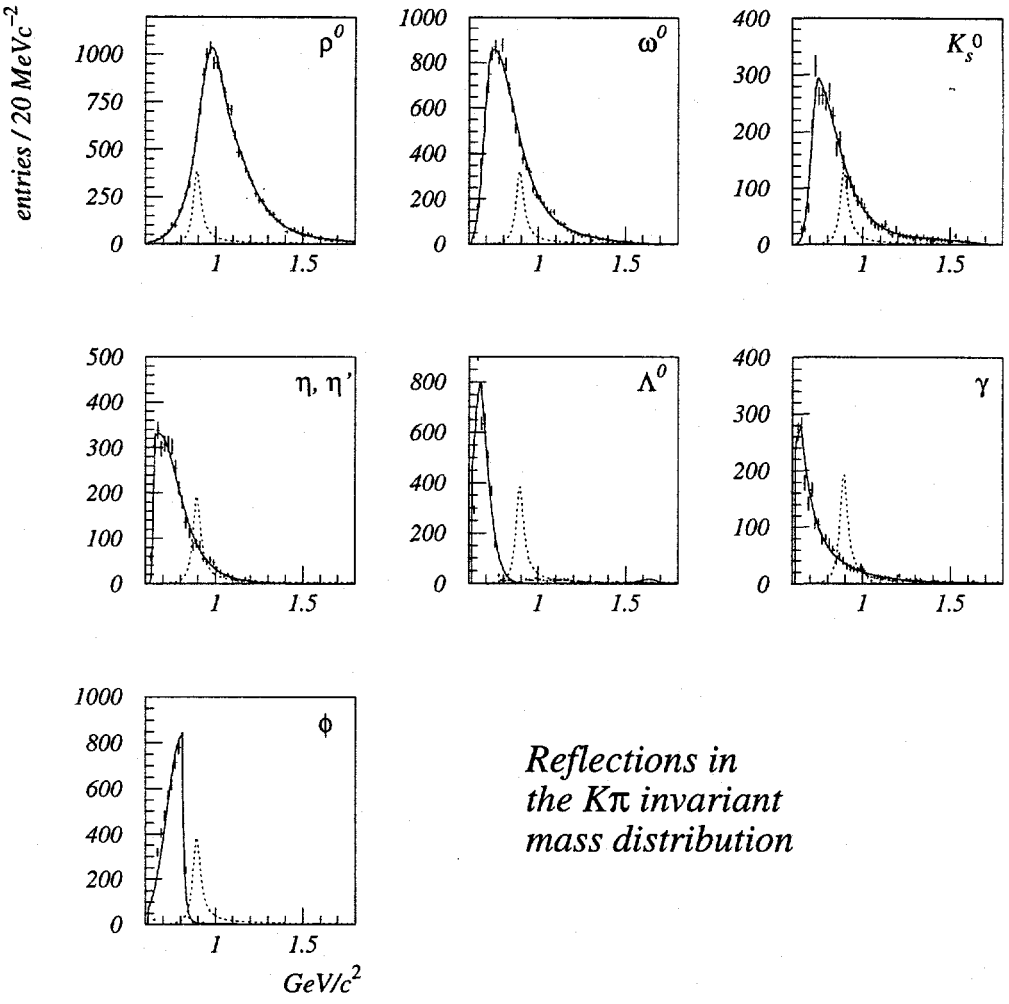

Figure 6.3: The main reflections in the $K\pi$ invariant mass distribution. The K^{*0} signal is plotted in a dotted line to reference the reflection's position.

- *particle ID* - the ϕ passes unhindered the K^{*0} cuts, thus if the "pion" track has been successfully identified and it is recognised as a "kaon" at the level of +5 or more in log-likelihood (definite "kaon"), then the combination is rejected. The removal of the ϕ is important because this reflection appears as a very inconvenient shoulder on the low side of the K^{*0} peak and perturbs the quality of the fit. The cut used against the ϕ also rejects the K^{*0} self-reflection down to a level of approximately one seventh that of background fluctuations.

- *vertexing* - to eliminate long lived species such as γ, Λ^0 and K^0_s, a flight distance cut is used. Similar to the ϕ these reflections all peak on the lower side of the signal (figure 6.3) and distort the monotonic shape of the combinatorial background. The vertex fit is performed in two stages: the first stage assumes that the vertex is close to the IP and uses VXD information, and secondly, if the fit fails, the vertex is reconstructed with CDC information only. If the vertex reconstruction was successful, a cut on the flight distance is considered: if the momentum of the two track combination points back to the IP within 10° in 3D (5° in 2D) and the vertex is displaced from the IP by more than 4 cm (10 cm) with a normalised impact parameter greater than 6 (9), then the combination is assumed to originate from the decay of a long lived particle and it is rejected. The cut is most efficient in the momentum range of 3-7 GeV/c.

6.3.2. Fitting Procedure

In the case of the ϕ, the signal shape is completely dominated by the detector resolution. To describe the signal shape, with respect to the momentum dependence of the detector resolution, a sum of five gaussians was considered. This choice is redundant for the low momentum bins, however it is essential at high momentum and for the inclusive bin where the signal spans a large range in momentum. The sum has an overall normalisation factor and the gaussians enter with individual widths and contribution fractions. The shape is determined from a fit to the Monte Carlo signal which fixes the individual contribution fractions of the gaussians and gives an estimate of the widths. Fitting to the data, the signal is allowed to broaden using a single "resolution" parameter: $width_{DATA} = \sqrt{width_{MC}^2 + resolution^2}$ for all component gaussians. To check that the fit produces physically meaningful results, an equivalent width of the signal was calculated for both data and Monte Carlo:

$$\Gamma_{equiv.} = \sum^{-1/2} \frac{\lambda_i}{\Gamma_i^2} \qquad \sum \lambda_i = 1 \tag{6.1}$$

where Γ_i are the widths of the gaussians that enter the signal function and λ_i the corresponding fractions in the signal function. The width in the data is consistent with the expected 7-9% broadening with respect to Monte Carlo and gives confidence that the procedure is adequate. An overall check was performed by adding the observed

numbers of ϕ in all momentum bins and comparing it to the number observed in the inclusive bin. Since there are six momentum bins, all with different resolutions and backgrounds, the observed agreement at a level of less than 0.2 σ is a good indication that the fit computes physically meaningful results.

The K^{*0} signal is parametrised using a relativistic Breit-Wigner resonance. The center and width are allowed to float in a small range following a recent study [68] that observed deviations on the order of 2 MeV/c^2 from world average values [43].

The backgrounds are composed of two pieces: combinatorial and "resonant" backgrounds. In the case of the ϕ, the background after particle ID cuts is purely combinatorial and can be parametrised as a threshold term multiplied by a slowly decreasing exponential:

$$BG(m) = Nx^{\gamma}e^{c_1x+c_2x^2+c_3x^3+c_4x^4+c_5x^5} \tag{6.2}$$

where $x = m - m_{threshold}$, N is an overall normalisation factor, and $\gamma, c_{1...5}$ are parameters. The background can be studied in two samples : Monte Carlo true combinatorial background and data likesign combinatorial track pairs. The good agreement between the two samples led to their concaternation for better statistics. The background fit is first tuned on the concaternated sample and it is then used together with the signal function described above to the data. The parameters describing the background were allowed to float within 20% of their initial values. Figures 6.4 and 6.5 show the fits to the inclusive data and the six momentum bins for the ϕ.

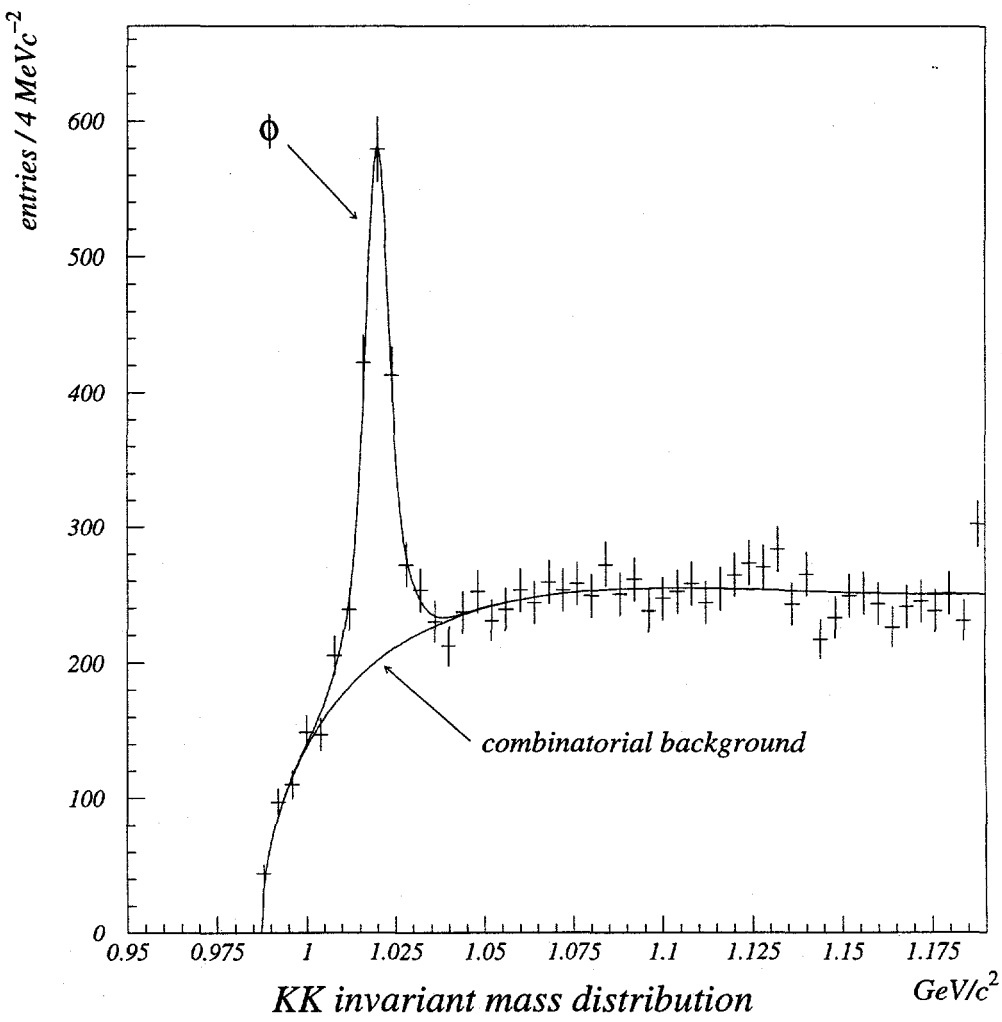

Figure 6.4: Fit for ϕ in the inclusive bin.

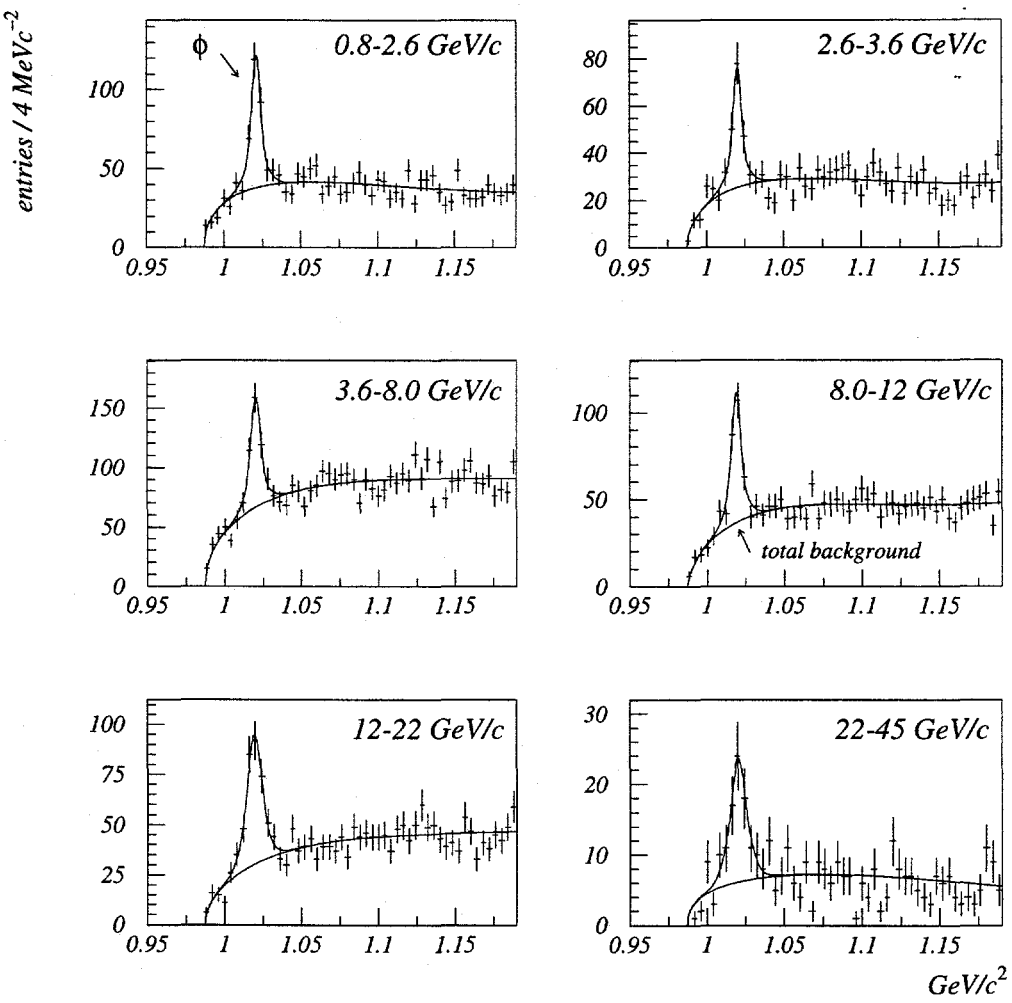

Figure 6.5: Fits for ϕ in the six momentum bins.

The case of the K^{*0} background is complicated by the presence of the numerous "resonant" backgrounds. Knowledge of these components is essential to the fit since the K^{*0} is a wide state and non-monotonic background variation within its width can lead to systematic errors in the measured rate. The shapes of these reflections are determined from Monte Carlo and their rates are set to the world average [43]. The combinatorial background is described by a parametrisation similar to that of the ϕ, with the difference of having seven ($c_1 ... c_7$) polynomial parameters. The initial shape of the background is determined from likesign combinations in the data. However, neither Monte Carlo true combinatorial background, nor data likesign combinations approximate well the actual data background, and are used only as initial input parameters. The free parameters of the fit are the signal shape and rate, the combinatorial background normalisation and shape, and four mis-ID adjustments corresponding to the four classes of reflections. The large number of parameters used in the fit makes it sensitive to the initial input values and careful tuning is required in order to obtain a good χ^2 fit. This procedure is determined by the fact that fragmentation is not sufficiently well known in Monte Carlo to describe the real combinatorial background. As a cross check on the results of the fit, the mis-ID adjustment of the largest "resonant" background contribution, the $\pi - \pi$ class, is found to be consistent with the expected correction from other studies [69].

The additional check of adding the six momentum bins and comparing the sum

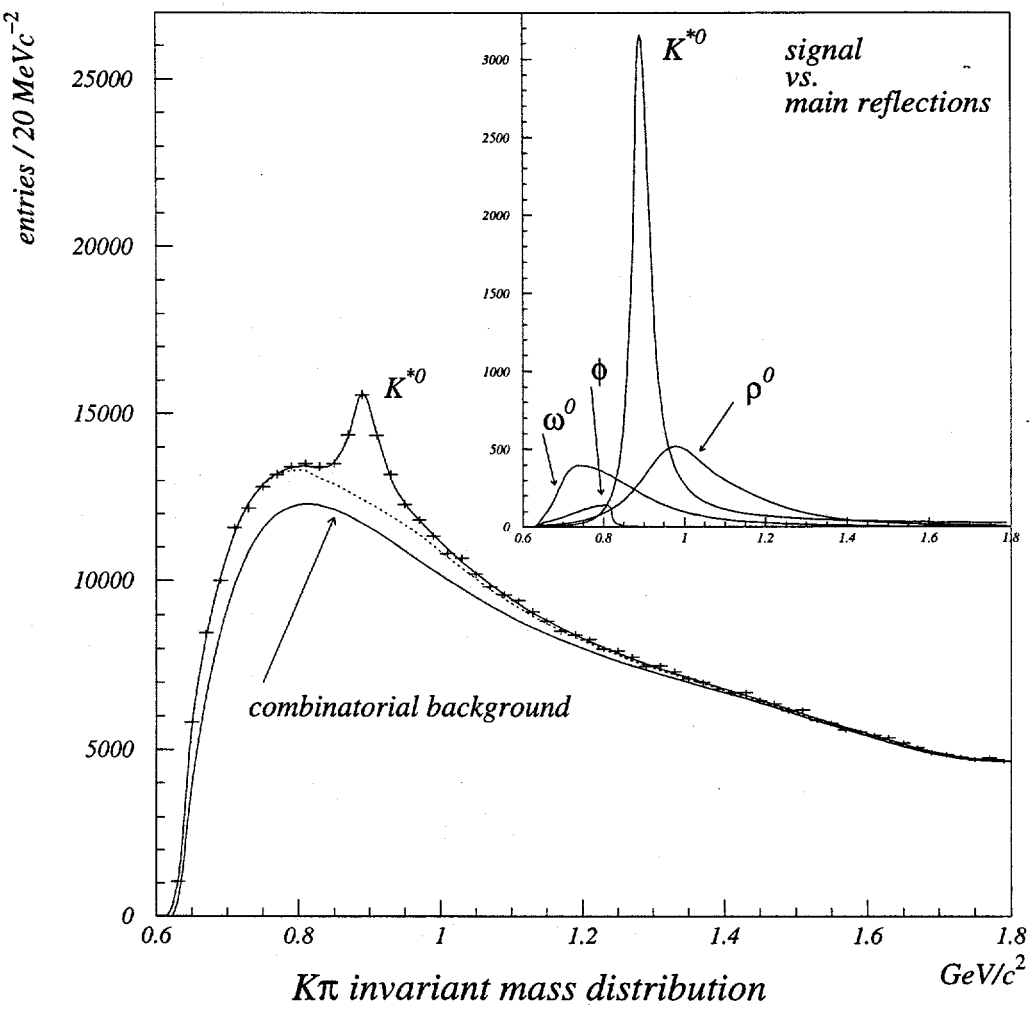

Figure 6.6: Fit for K^{*0} in the inclusive bin.

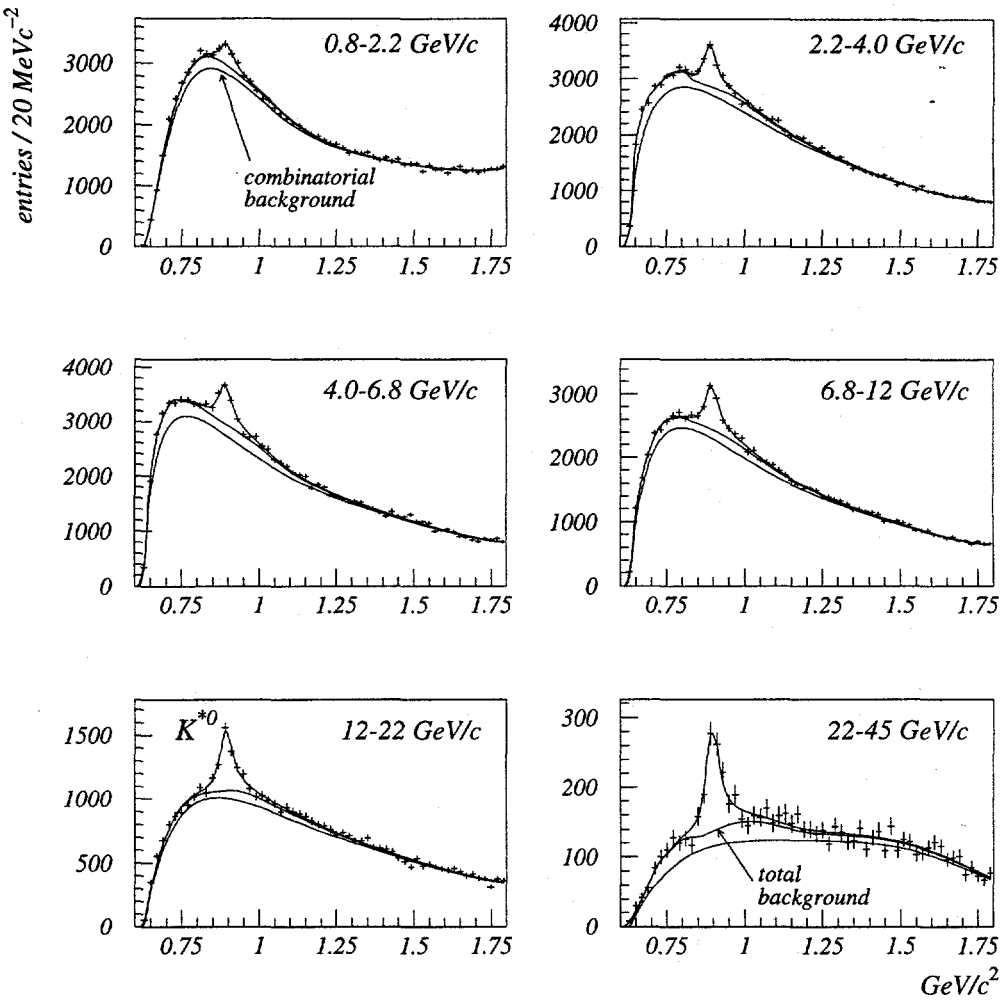

Figure 6.7: Fits for K^{*0} in the six momentum bins.

to the the number of particles in the inclusive bin is even more impressive than in the case of the ϕ since the backgrounds are considerably different in the six momentum bins (figure 6.7) and the inclusive bin (figure 6.6). The agreement observed is again at the level of less than 0.2 σ.

Finally, the number of particles is obtained by integrating the signal function in the range of the kinematic threshold to 1.5 GeV/c^2 for the ϕ, and kinematic threshold to $m_0 + 2.5\Gamma_0 = 1.022$ GeV/c^2 for the K^{*0}.

6.3.3. Reconstruction Efficiencies

The reconstruction efficiency was determined for a chain of steps determined from Monte Carlo, data, or corrected Monte Carlo. To check Monte Carlo efficiencies against data, a "mass window" was defined from 1.000 to 1.040 GeV/c^2 for the ϕ and from 0.796 to 0.996 GeV/c^2 for K^{*0}. This window includes almost all the signal and at the same time it is sufficiently narrow to define a region in which the combinatorial background candidates have the same kinematics as the signal itself. Monte Carlo was tuned to observe the world average rates for the reflections and the signal, and the efficiencies derived in the "mass window" were compared between data and Monte Carlo. The largest discrepancies observed were on the order of 1% in the inclusive bin and are due to the different proportions of $\pi\pi$, $K\pi$, *etc.* combinations from fragmentation existent in Monte Carlo with respect to the data. The steps used for

determining the efficiency are:

- *event selection*: the effect of event selection was studied by comparing Monte Carlo rates at the generator and selected hadronic events level. Within statistics the two rates agree.

- *branching ratio*: 0.667 for $K^{*0} \rightarrow K^{+}\pi^{-}$ and 0.491 for $\phi \rightarrow K^{+}K^{-}$.

- *integration range*: the "mass window" described above has approximately 5% less signal than the previously mentioned range used for integration in the case of the K^{*0} signal.

- *tracking and vertexing*: efficiency referring to the two tracks being reconstructed and passing quality and vertexing cuts that is determined from Monte Carlo. A correction of 0.947 was applied based on independent tracking studies [70], which has an uncertainty of 3.4%.

- *CRID visible*: efficiency referring to candidates with tracks passing the preliminary CRID cuts and RC $\neq$ BADID, that is determined from data candidates in the "mass window". For the ϕ and K^{*0} analysis the Monte Carlo efficiency is consistent with the data efficiency within statistics. The error for this efficiency is a fraction of a percent for K^{*0} and typically 1-2% for ϕ.

- *kaon-ID* efficiency: efficiency for true kaons with good CRID identification to be identified as "kaons" at the +3 log-likelihood level.

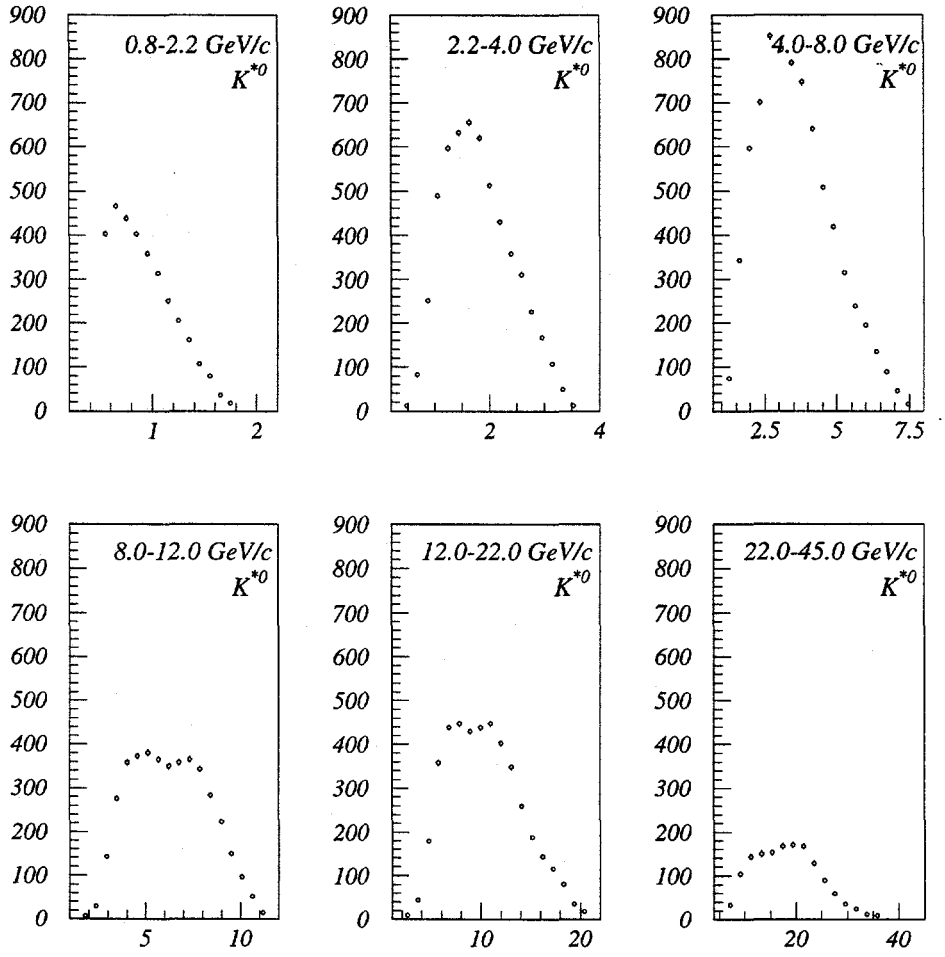

Figure 6.8: Momentum distributions of kaons from K^*0 decays.

The efficiency was determined from Monte Carlo and correceted by 0.94-1.00 per identified kaon from independent studies [69] of K^0_s and τ samples. Since both the ϕ and the K^{*0} have a distribution of the daughter momenta, the corrections were weighted over the appropriate momentum distributions (example in figure 6.8 for K^{*0}). The error is the quadratic sum of the correction error and the statistics of the weighting distributions. For the ϕ both tracks are identified and the correction was performed weighting over the correlated distribution of the two tracks. The error for this efficiency is at the level of 5-8% for ϕ and 2-3% for K^{*0}, again momentum dependent.

- *pion-cut*: for K^{*0} the combination is rejected if the candidate "pion" is identified as a "kaon". This correction to the efficiency for the cut is at the level of 1% with errors of a fraction of a percent for most bins.

6.3.4. K^{*0} and ϕ Rates versus Momentum

The inclusive cross section $1/\sigma_{had}\, d\sigma/dp$ is calculated from the number of particles observed in each momentum bin as:

$$\frac{1}{\sigma}\frac{d\sigma}{dp} = \frac{1}{\mathcal{R}(p)}\frac{1}{\Delta p}\frac{N_{obs}(p)}{N^{events}_{recon}} \tag{6.3}$$

where $\mathcal{R}(p)$ is the momentum dependent reconstruction efficiency, $N_{obs}(p)$ the number of particles in the fit for the respective momentum bin and N_{recon}^{events} the number of hadronic events in the sample. The production rate in the very low momentum region (p $<$ 0.8 GeV/c) is invisible experimentally and was determined from Monte Carlo. The difference in predictions between JETSET 7.4 and HERWIG 5.8 for this region was taken as a systematic error. The resulting rates for the momentum binned measurements are listed in tables 6.1 for ϕ and 6.2 for K^{*0}.

Table 6.1: ϕ rates.

	bin 1	bin2	bin3	bin4	bin5	bin6
limits $[GeV/c]$	0.8-2.6	2.6-3.6	3.6-8.0	8.0-12.0	12.0-22.0	22.0-45.6
ϕ/event	0.0294	0.0090	0.0246	0.0146	0.0162	0.0046
x_p size	0.0394	0.0219	0.0964	0.0877	0.2191	0.5179
$1/\sigma_h \cdot d\sigma/dx_p$	0.7445	0.4112	0.2551	0.1670	0.0739	0.0089
ξ size	1.1787	0.3254	0.7985	0.4055	0.6061	0.7296
$1/\sigma_h \cdot d\sigma/d\xi$	0.0249	0.0277	0.0308	0.0361	0.0267	0.0063

6.3.5. Statistical and Systematic Errors

The statistical error [43] is calculated from the fits and it includes statistics from all backgrounds plus the signal:

$$\delta rate = rate \cdot \left(\int \frac{sgn(x)^2}{glb(x)} dx / bin_{size} \right)^{-1/2} \tag{6.4}$$

Table 6.2: K^{*0} rates.

	bin 1	bin2	bin3	bin4	bin5	bin6
limits $[GeV/c]$	0.8-2.2	2.2-4.0	4.0-6.8	6.8-12.0	12.0-22.0	22.0-45.6
K^{*0}/event	0.1439	0.1495	0.1366	0.1153	0.0750	0.0266
x_p size	0.0307	0.0394	0.0614	0.1139	0.2191	0.5179
$1/\sigma_h \cdot d\sigma/dx_p$	4.6906	3.7902	2.2263	1.0119	0.3423	0.0514
ξ size	1.0116	0.5978	0.5306	0.5680	0.6061	0.7296
$1/\sigma_h \cdot d\sigma/d\xi$	0.1422	0.2501	0.2575	0.2031	0.1238	0.0365

where $sgn(x)$ is the signal, and $glb(x)$ the total fit function.

The systematic errors for this analysis are grouped into efficiency and fit related errors. The errors from efficiency determinations are:

- *statistics*: while not systematic errors in the classical sense, the statistical fluctuations of the data sets used for the calculation of efficiencies are treated as systematic errors. Monte Carlo was used for the *kaon-ID* and for the *tracking and vertexing* efficiency, while data was used for the *CRID visible* efficiency. The statistics contribute to approximately one fourth of the global efficiency error for K^{*0}, and two thirds for ϕ.

- *tracking and vertexing* correction: this error was estimated in tracking studies [71] on the CDC and it is mostly due to the calibration to the world average number of charged tracks per hadronic event.

- *kaon-ID* correction: this error was estimated in CRID studies [69] and added in quadrature with the momentum distribution statistics of the kaon tracks.

- *pion-cut* correction: this error is approximately 20% of the K^{*0} loss from the cut and translates into a fraction of a percent error to the efficiency.

The fitting systematic errors are determined by changing, fixing the parameter of study and performing a re-fit. Two options are available: a re-fit with the full set of parameters floating, or with a reduced set, consisting of signal and combinatorial background normalisations only. In the first case there is the possibility that the fit, while trying to accommodate a certain change in shape away from the signal region, could yield unreasonably large errors in the signal region. Conversely, certain favorable shape changes could be completely absorbed by the large number of fit parameters and give underestimates of the systematic errors. To avoid these problems a window region around the signal was defined using a weight function (figure 6.9 - for K^{*0}) in which the re-fit is performed, and the latter option for the parameter set considered. It is possible that this procedure slightly overestimates the systematic errors, however it was preferred in view of its robust behaviour with respect to statistics. The following fit systematic errors were studied:

- *signal shape*: for the ϕ, the fractions of the gaussians that form the signal function were varied within $\pm$ 10%, while for the K^{*0} the shape distortion is studied by the variation of the signal width. K^{*0} shape distortions were studied

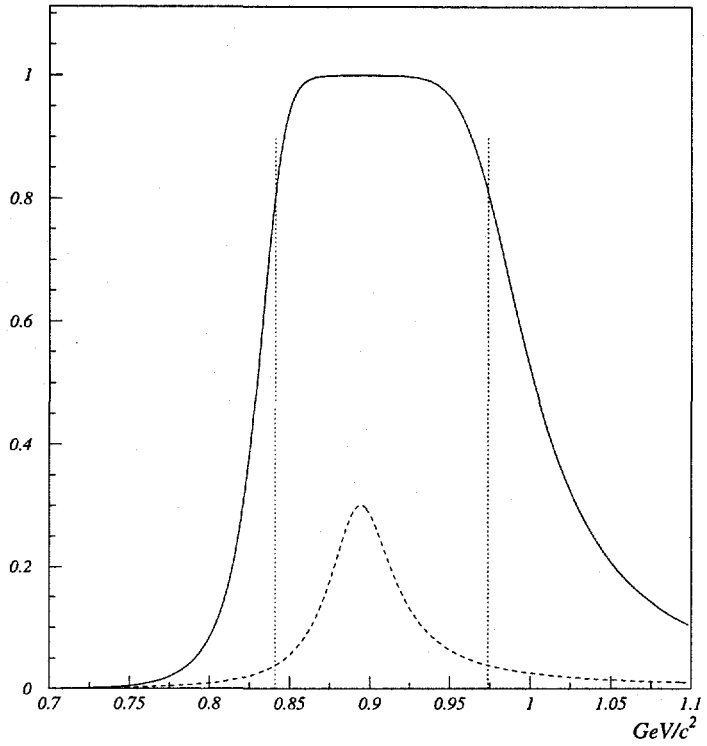

Figure 6.9: Function used to define the re-fit window for systematic studies in the case of the K^{*0}.

due to a recent report [68] on shape uncertainty at the level of 2 MeV/c^2.

- *signal center and width*: a 2.0 MeV/c^2 variation was studied as systematic for the ϕ center, and a 2.4 MeV/c^2 variation for the K^{*0} center and width.

- *background fluctuations*: taking an arbitrary background fluctuation $\Delta_{i=\overline{1,N}}$, the

induced fluctuation for one of the combinatorial background parameters is:

$$\delta c_n = \frac{\sqrt{\sum \Delta_i^2 h_i^2 f_n(x_i)^2}}{\sum h_i^2 f_n(x_i)^2} \tag{6.5}$$

where h_i is the histogram content in bin i, Δ_i the background fluctuation in this bin, and $f_n(x)$ the function controlled by parameter c_n in the exponent. For a 1σ fluctuation in all bins ($\Delta_i^2 = h_i$) a nominal δc_n is computed for all parameters. A worst case scenario is then calculated out of the 2^n possible refits that correspond to the plus or minus variations of the n parameters. The variation due to parameter γ is superimposed and a final systematic error is reported.

In the case of the K^{*0} a much more comprehensive program of systematic errors is pursued due to the large number of additional background parameters:

- *mis-ID adjustments*: the $\pi\pi$, ee and $p\pi$ mis-ID's were varied by -50 ... +100% and the KK identification rate used for ϕ rejection was varied by $\pm$ 15%. Of the possible combinations a worst case scenario is calculated and reported as systematic uncertainty.

- *reflection rates*: the PDG[3] uncertainties on the rates of the contributing

[3]The Particle Data Group published a compilation [43] of all measurements of particle properties and the results from different experiments are combined to form a weighted average. This compilation is considered to be the authoritative presentation of these data.

particles are studied as variations and systematics reported in each case.

- ρ^0-ω^0 *"saddle"* (figure 6.6-insert): the ρ^0 and ω^0 are varied by $\pm$ 30% and $\pm$ 10% respectively, then a worst scenario combination reported.
- ρ^0 *shape*: the uncertainty in the ρ^0 shape was accounted for as a 40 MeV/c^2 downshift [72] of the ρ^0 reflection. Modulating the ρ^0 shape at a 30% level was also studied, the effect being much smaller than that due to the shift.

Tables 6.3 and 6.4 show the breakdown of the errors into the above discussed categories for the ϕ and K^{*0} respectively.

6.4. Discussion of Results

This section describes the ϕ and K^{*0} results in the larger context of SLD measurements and compares these results with Monte Carlo fragmentation models, QCD theoretical predictions of the MLLA/LPHD model and other experiments. Useful information about the strangeness suppression parameter γ_s, which is the probability ratio of pulling out of the QCD vacuum an $s\bar{s}$ pair versus another light quark pair, is extracted from ϕ to K^{*0} production rate ratios.

6.4.1. Hadronisation Physics

Figure 6.10 shows the ϕ and K^{*0} production rates as a function of momentum in the context of the full SLD measurement of hadrons. All production rates de-

crease with momentum due to phase space constraints. The noticeable features of the data are the equal production rates of charged and neutral kaons that indicates equal strangeness suppression in u- and d-quark systems, and the convergence of light and heavy kaon production rates at high momenta. The latter is an indication of "leading particle" effect, which asserts that high momentum particles contain one of the primary quarks from the Z^0 decay as a valence quark. Indeed, at high momentum the structure of the kaons becomes negligible and the production rate is determined only by the valence constituents. Since light quarks all have similar, or equal, partial widths from the Z^0 decay, the light to heavy kaon production rate ratio is determined at high momentum only by the s-quark suppression with respect to the u- and d-quarks. These two factors are very close to each other and hence the small difference observed at high momenta between light and heavy kaon production rates indicates that indeed the production process is dominated by a "leading particle" mechanism, as opposed to the lower momenta string-breaking mechanism, where a significant difference is observed.

Another important feature of figure 6.10 is the production rate ratios of particles with none, one, or two strange quarks. For instance the ϕ production rate is lower than that of the K^{*0}, the Λ^0 is lower than that of the proton, the are kaons lower than the pions, *etc.* This aspect can provide information about γ_s, the strangeness suppression parameter. Assuming a naive string-breaking model for low momenta

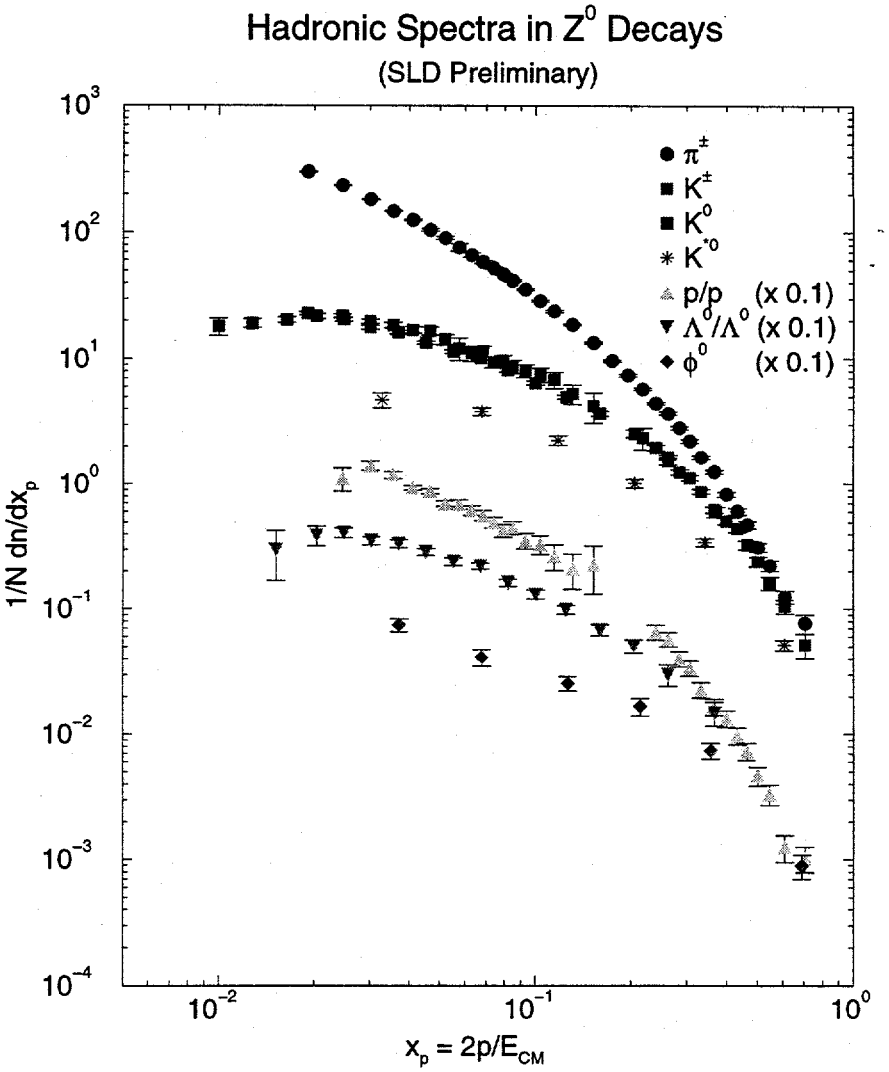

Figure 6.10: Particle production rates measured at SLD as a function of $x_p = p/p_{beam}$. The diamonds show the ϕ and the stars, the K^{*0}. Notice the convergence of rates for light and heavy kaons, and for the baryons with the ϕ at high momentum. This is an indication of "leading particle" effect and of equal strangeness suppression in the u- and d-quark systems. Note the difference in scale for the baryons and the ϕ.

particle production, this quantity is given by rate ratios such as $\gamma_s = 2\phi_{rate}/K^{*0}_{rate}$. This is based on the probability combinations for breaking the color field string to form a ϕ versus a K^{*0}. At high momentum however it is unlikely that the hadron originated from the string and more likely that it is a "leading particle". Under this assumption, γ_s is expected to be expressed as: $\gamma_s = \phi_{rate}/(K^{*0}_{rate} - \phi_{rate})$. This is based on the probability for a primary d or s quark to pull out of the QCD vacuum the right combination to form a ϕ, or a K^{*0} meson.

Using the rates for ϕ and K^{*0} observed in this measurement, the low momentum $\gamma_s = 0.350 \pm 0.037(stat.) \pm 0.054(syst.)$ and the high momentum $\gamma_s = 0.209 \pm 0.042(stat.) \pm 0.045(syst.)$. These values have only measurement errors, and are naive model expectations, however, they are consistent with the world average of 0.290 ± 0.015. The discrepancy in these results indicates the extent to which there is a substantial model dependence in the final result. For instance in a recent paper [73] from the UA1 experiment, γ_s relates to the observed particle production rates as:

$$\frac{2K^0_{s\,rate}}{\pi^{\pm}_{rate}} = \frac{12\gamma_s + 3\gamma_s^2}{31 + 12\gamma_s + 3\gamma_s^2 + \lambda(\frac{16}{3} + 4\gamma_s + \frac{8}{3}\gamma_s^2)} \tag{6.6}$$

where $\lambda = \frac{4+4\gamma_s+\gamma_s^2}{5+5\gamma_s+3\gamma_s^2+\gamma_s^3}$. Intricate details of particle production models such as those in equation 6.6 can lead to substantial systematic errors and it would be preferable to measure γ_s in a simpler, direct way. In a certain sense, the high momentum measurement depends less on the fragmentation function, hadron structures, *etc.* and

it is more direct than the low momentum measurement, which in turn is less model dependent than the inclusive measurement described above. A direct measurement of this quantity will be described in Chapter 7.

6.4.2. Comparison to Fragmentation Models

Figures 6.11 and 6.12 show the SLD results for ϕ and K^{*0} plotted against JETSET 7.4 and HERWIG 5.8 predictions. The horizontal bars denote the bin size, and the Monte Carlo function integrated over this interval has to be compared with the data point. However, for all bins other than the high momentum bin, the integrated value practically coincides with the function point at the bin center and can be directly compared to the data.

The ϕ production is modeled well in JETSET other than at low momentum ($x_p < 0.05$). The HERWIG model is consistent with the data at low momentum and in the intermediate region, however disagrees strongly at high momentum. It is to be noted that this "strong" disagreement is in fact a much better agreement than that of the earlier versions of these models. The K^{*0} production is modeled well by HERWIG in the intermediate momentum region, however, in this case both models are in disagreement with the data at high momentum.

It is clear that the models have tuned well the fragmentation function in the intermediate momentum range, however it is possible that additional parameters

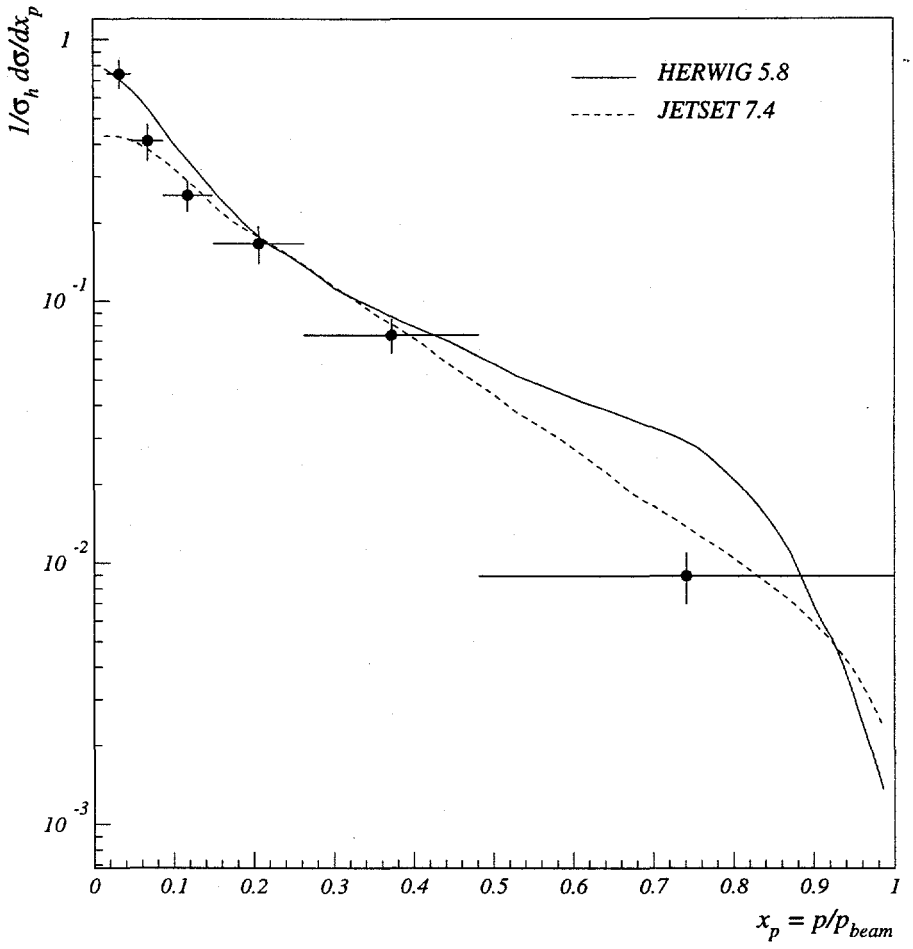

Figure 6.11: ϕ rates as a function of $x_p = p/p_{beam}$ compared to JETSET and HERWIG fragmentation models.

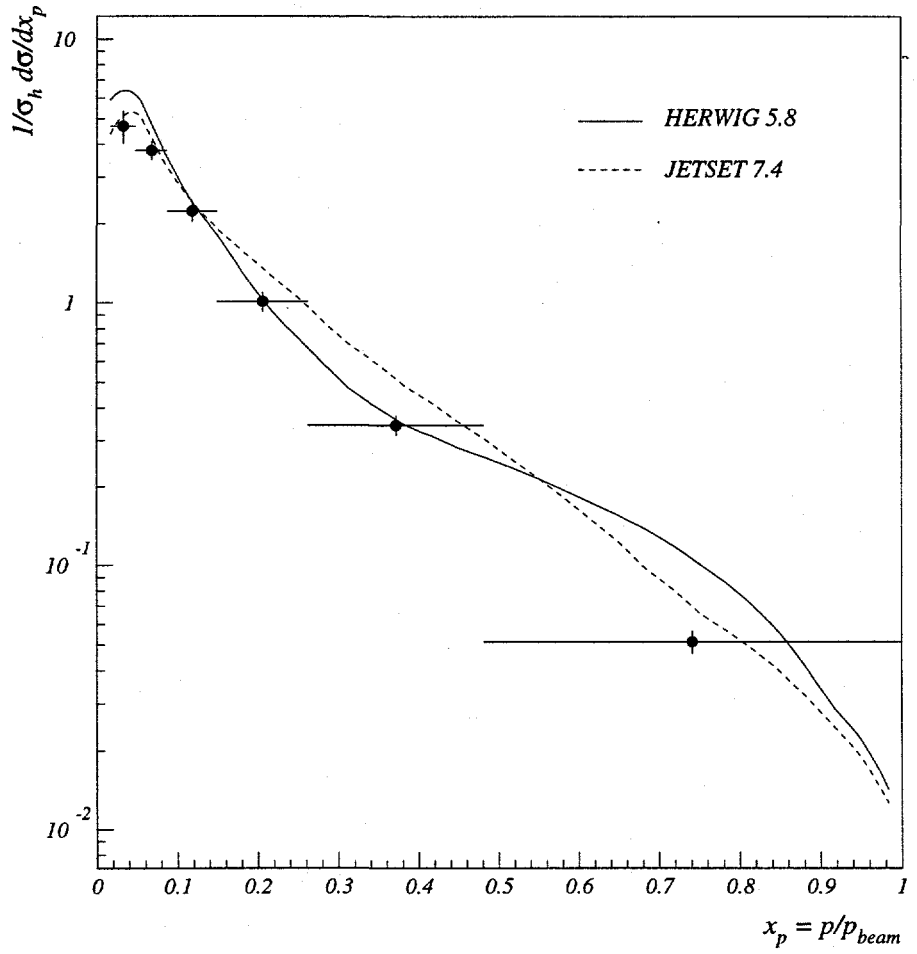

Figure 6.12: K^{*0} rates as a function of $x_p = p/p_{beam}$ compared to JETSET and HERWIG fragmentation models.

such as R_b, and R_c that dictate contamination from heavy hadron decays do not inter-relate well with the rest of the model at low momentum. At high momentum the data is scarce and does not allow for a finer binning that could constrain the models. In this momentum region the dominant effect on the production rate is from the fragmentation function.

6.4.3. Comparison to QCD Predictions

QCD calculations based upon the Modified Leading Log Approximation (MLLA) predict the shape of the ξ-distribution for soft partons. Under the assumption of Local Parton-Hadron Duality (LPHD), this distribution is directly comparable to that of the observed hadrons. The distribution is expected to be approximately gaussian, with the peak position ξ^* being inversely dependent on the hadron mass.

Figures 6.13 and 6.14 show the SLD results plotted in the $\xi = -ln(p/p_{beam})$ variable and fitted to a gaussian function in order to test the MLLA/LPHD theoretical predictions. Since the kaon identification errors are correlated in the liquid and the gas radiators, the points corresponding to identification using the two systems were collectively varied within 1 σ (2×2 combinations) and the best fit consistent with the gaussian hypothesis plotted.

The ϕ fit has a $\chi^2/d.o.f.$ of 3.73 for 3 degrees of freedom with an integrated probability of obtaining a $\chi^2/d.o.f. \geq 3.73$ of 1.07%, a rather poor agreement with

the gaussian hypothesis. The K^{*0} fit on the other hand has a $\chi^2/d.o.f.$ of 0.62 for 3 degrees of freedom with an integrated probability of obtaining a $\chi^2/d.o.f. \geq 0.62$ of 60.20%, which represents an excellent agreement with the gaussian hypothesis.

The reason for the ϕ fit being distorted is that the direct ϕ production from fragmentation is strongly suppressed, while contaminating sources such as heavy hadron decays are relatively abundant and perturb this inclusive sample measurement. The K^{*0} on the other hand is produced abundantly directly from fragmentation and somewhat suppressed in charm events (Chapter 7). As a result the percent contamination from non-fragmentation sources for this particle is much smaller. The LPHD assumption ties the parton spectrum to the *primary* hadron spectrum, hence this inclusive measurement is not expected to be in total agreement with the predicted gaussian shape. Most of the lighter particles also have this contamination from non-fragmentation sources, however, for them the decay sources are from both heavy and light quark events. The ϕ and the K^{*0} on the other hand are particles with masses on the order of 1 GeV/c^2 and the hadrons that can decay to them are mostly charm and beauty hadrons which can be removed with an event tag. By selecting light quark events it is thus possible to reach closer to the working hypotheses of the MLLA/LPHD model, that is particle production directly from fragmentation. Chapter 7 will describe the ϕ and K^{*0} measurements in the *uds*, charm and beauty events.

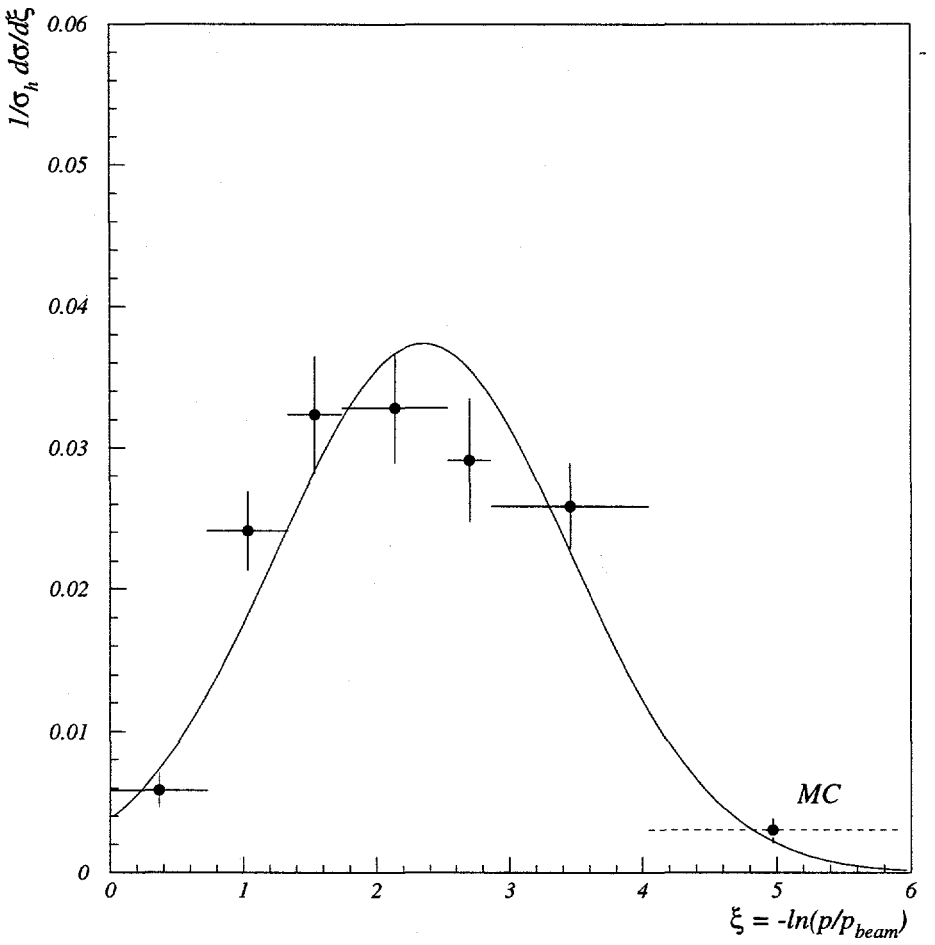

Figure 6.13: ϕ MLLA/LPHD fit. The fit has a $\chi^2/d.o.f.$ of 3.73 for 3 degrees of freedom, corresponding to an acceptable agreement with the gaussian hypothesis.

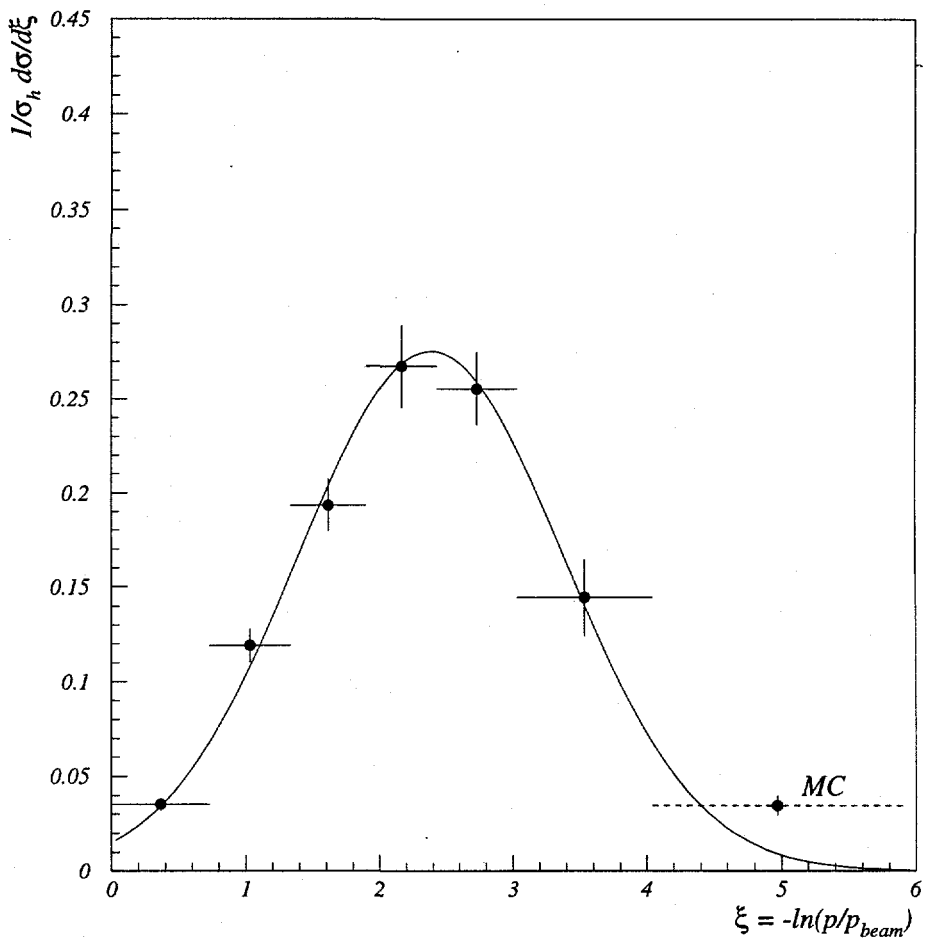

Figure 6.14: K^{*0} MLLA/LPHD fit. The fit has a $\chi^2/d.o.f.$ of 0.62 for 3 degrees of freedom, corresponding to an excellent agreement with the gaussian hypothesis.

The peak value of the ϕ distribution is at $\xi^* = 2.298 \pm 0.084$, and the contributions to the error are: 0.059 from statistics, 0.026 from rate fits systematics, 0.038 from uncorrelated reconstruction efficiencies and 0.038 from the kaon ID correlated systematics. The world average value is at $\xi^* = 2.210 \pm 0.040$ and it is completely dominated by the dE/dx experiments (DELPHI has not published a ξ^* value). For K^{*0}, $\xi^* = 2.353 \pm 0.042$, and the contributions to the error are: 0.027 from statistics, 0.013 from rate fits systematics, 0.017 from uncorrelated reconstruction efficiencies and 0.023 from kaon ID correlated systematics. The world average value is at $\xi^* = 2.350 \pm 0.070$, again totally dominated by dE/dx experiments. For this measurement the SLD value has a smaller error than the world average.

The MLLA/LPHD model predicts a $log(1/M) + C$ dependence of the peak position ξ^* on hadron mass, by the scale set at which the parton shower must terminate. Figure 6.15 shows the peak position dependence on particle mass from experiments at the Z^0 energy. Considering both baryons and mesons together, there is no obvious ξ^* dependence on the mass that can be seen. However, considering baryons or mesons separately, a dependence consistent with the MLLA/LPHD prediction can be observed.

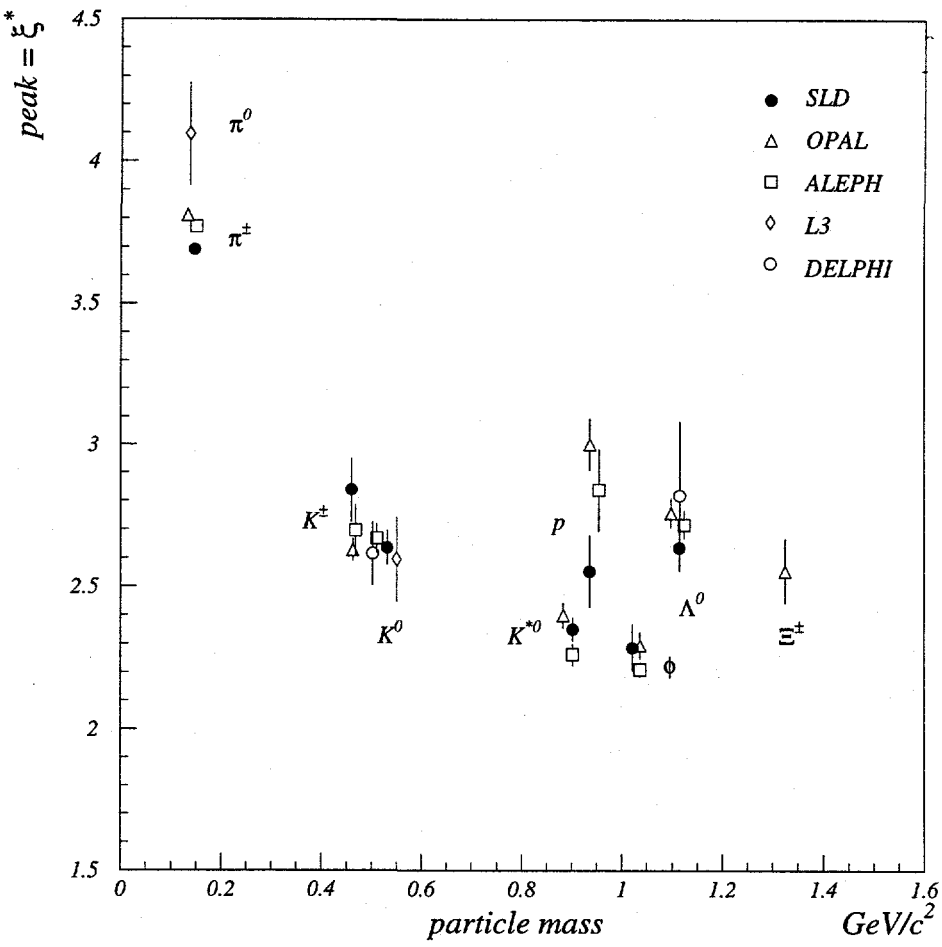

Figure 6.15: ξ^* dependence on particle mass at the Z^0 energy.

6.4.4. Inclusive Rate Checks

The inclusive rates for ϕ and K^{*0} were measured in the inclusive bins (table 6.5), but also cross checks were performed that used all six momentum bins.

The sums of the six momentum bins give inclusive rates of $0.1040 \pm 0.0051(stat.) \pm 0.0041(syst.) \pm 0.0022(extr.)$ ϕ per event and $0.7070 \pm 0.0220(stat.) \pm 0.0250(syst.) \pm 0.0140(extr.)$ K^{*0} per event, which are in very good agreement with the rates from the inclusive fits given in table 6.5. The systematic errors are 0.0025 (0.0110) from uncorrelated reconstruction efficiencies, 0.0015 (0.0190) from fit systematics and 0.0030 (0.0120) from the correlated kaon ID systematics.

The MLLA fit can also be used to obtain an inclusive rate by integrating the fit function. The first approach was to integrate the function in the interval $\xi = 0 \ldots 20$. The result is $0.1000 \pm 0.0086(stat.) \pm 0.0106(syst.)$ for the ϕ and $0.673 \pm 0.028(stat.) \pm 0.026(syst.)$ for K^{*0}, where 0.0037 (0.0150) error is from the individual fit errors, 0.0053 (0.0170) from reconstruction efficiencies and 0.0084 (0.0120) from kaon ID efficiencies. An additional fit was performed including the Monte Carlo point at very low momenta (figure 6.14), the results being $0.0994 \pm 0.0072(stat.) \pm 0.0101(syst.)$ for ϕ and $0.6970 \pm 0.0280(stat.) \pm 0.0230(syst.)$ for K^{*0}.

Another version of using the MLLA fit was to integrate only in the experimentally visible momentum range and to add the Monte Carlo extrapolation for very low momenta. The results are $0.1032 \pm 0.0063(stat.) \pm 0.0083(syst.) \pm 0.0025(extr.)$ ϕ

and $0.7030 \pm 0.0260(stat.) \pm 0.0240(syst.) \pm 0.0140(extr.)$ K^{*0} for the fit without the Monte Carlo point and $0.1002 \pm 0.0053(stat.) \pm 0.0087(syst.) \pm 0.0140(extr.)$ ϕ and $0.7160 \pm 0.0260(stat.) \pm 0.0220(syst.) \pm 0.0140(extr.)$ K^{*0} for the fit with the Monte Carlo point.

6.4.5. Comparisons to Other Experiments

Figures 6.16 and 6.17 show the SLD results together with measurements made by the LEP collaborations [74] and Monte Carlo predictions. The rates are plotted versus the $\xi = -ln(p/p_{beam})$ variable. The experiments agree at the 1σ level, however in the range of $\xi = 2 \ldots 3$ the dE/dx particle ID experiments (ALEPH and OPAL) seem to have larger errors and are slightly higher in rate than the Čerenkov Imaging particle ID experiments (DELPHI and SLD). In the same range, the SLD K^{*0} points have a substantially smaller error than the dE/dx particle ID measurements, giving an inclusive K^{*0} measurement very close in error to the world average.

The JETSET predictions at intermediate-high and high momenta are consistent with all the ϕ measurements. At intermediate-low momenta the dE/dx measurements tend to validate HERWIG, while CRID experiments continue to agree with JETSET. At low momentum all experiments validate HERWIG.

For K^{*0}, JETSET and HERWIG are very close to each other in the low momentum region, however the data points seem to favor the JETSET prediction. In the very

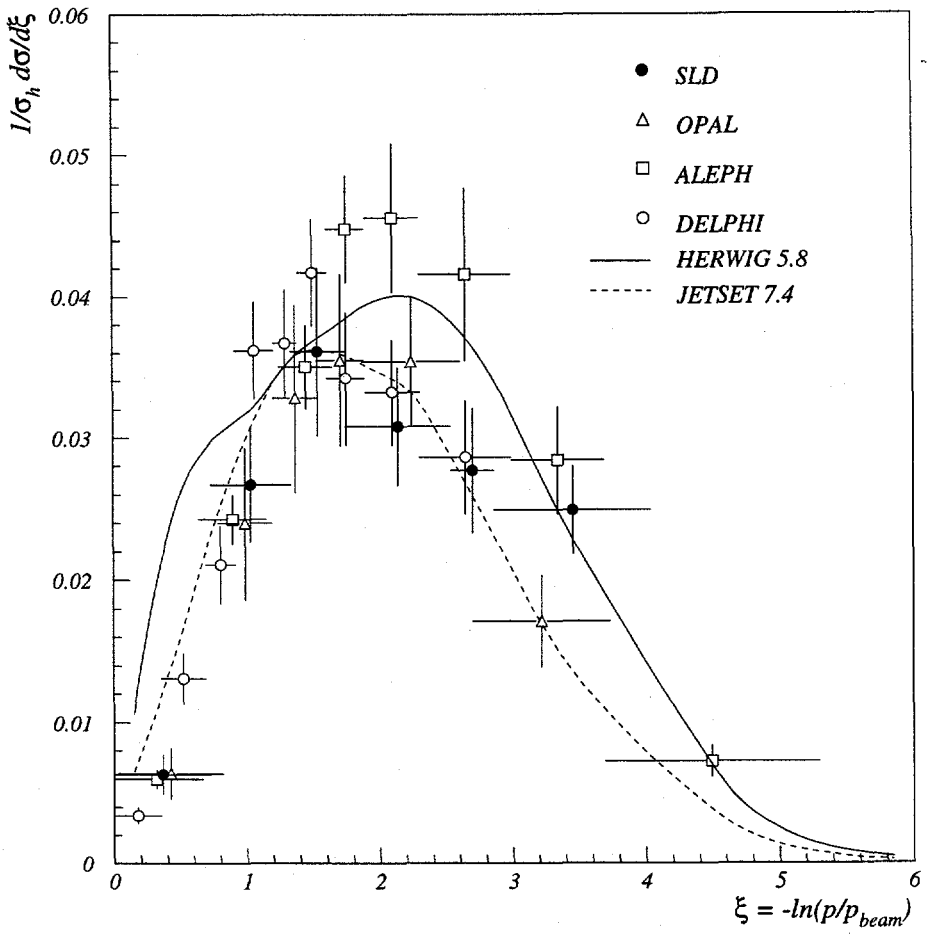

Figure 6.16: ϕ rates as a function of $\xi = -ln(p/p_{beam})$ showing SLD and LEP results together with Monte Carlo predictions.

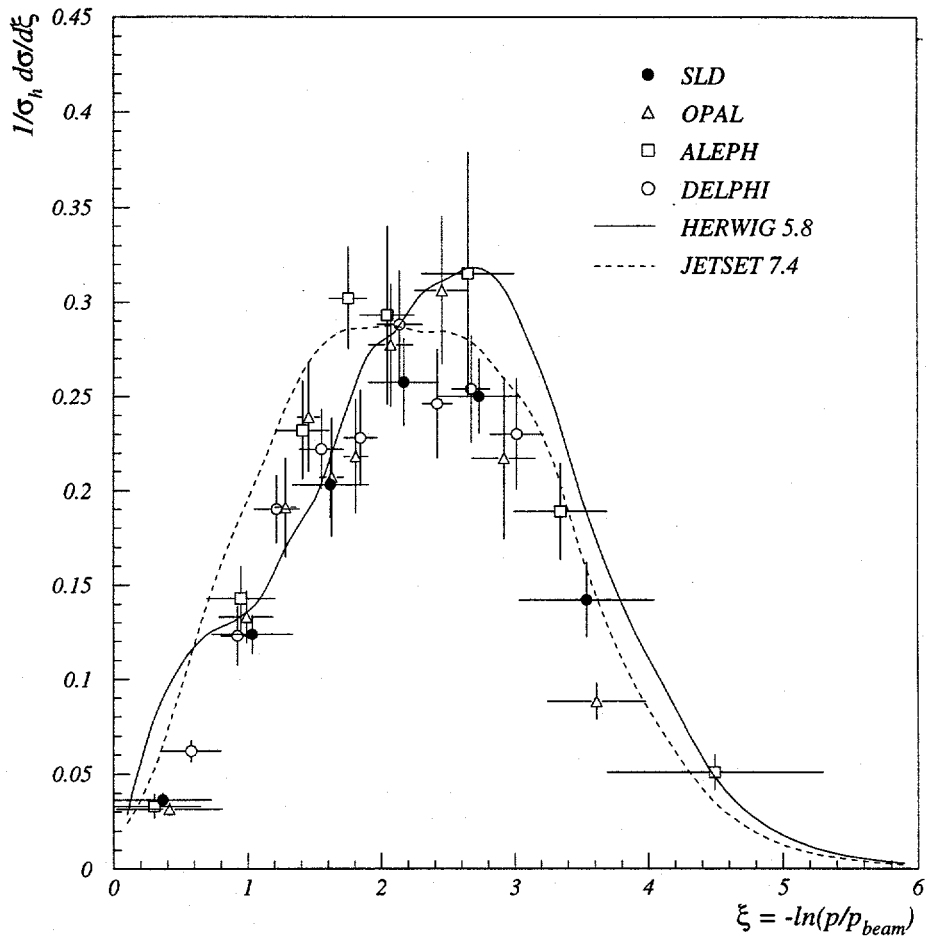

Figure 6.17: K^{*0} rates as a function of $\xi = -ln(p/p_{beam})$ showing SLD and LEP results together with Monte Carlo predictions.

high momentum region JETSET is again preferred, however in the intermediate-high momentum region it is unclear, the dE/dx measurements favoring JETSET and the CRID measurements HERWIG.

Table 6.3: ϕ errors in % in the six momentum bins. The first group are fit systematic errors and the second, efficiency related errors. Each group has the quadrature sum at the bottom. The bottom part of the table has the quadrature sum of the systematic errors, the statistical error and the grand total error.

	bin 1	bin2	bin3	bin4	bin5	bin6
limits $[GeV/c]$	0.8-2.6	2.6-3.6	3.6-8.0	8.0-12.0	12.0-22.0	22.0-45.6
ϕ center	2.1060	1.0375	2.7847	0.5563	0.7004	1.4644
ϕ width	1.9031	2.1258	1.7967	1.7769	1.1251	0.5380
RCBG	0.8705	1.6632	1.5421	3.3938	3.5391	7.5576
fit total	2.9690	2.8917	3.6552	3.8710	3.7791	7.7170
trk/vtx	3.4000	3.4000	3.4000	3.4000	3.4000	3.4000
CRID vis.	0.6590	1.0554	0.8741	1.9584	2.5285	6.6158
kaon-ID	3.8229	5.1199	6.5260	10.4399	9.7489	7.6250
MC stat.	4.2044	5.2470	3.5023	4.5692	4.1457	7.1006
eff. total	6.6548	8.1498	8.1963	12.0526	11.4098	12.8019
SYST.	7.2871	8.6476	8.9744	12.6590	12.0194	14.9479
STAT.	9.9651	13.3641	10.1598	10.6337	9.2073	16.4208
TOTAL $\diamondsuit$	12.3452	15.9180	13.5559	15.1407	15.1407	22.2055

Table 6.4: K^{*0} errors in % in the six momentum bins. The first group are fit systematic errors and the second, efficiency related errors. The bottom part shows the total systematic error, the statistical error and the grand total error.

	bin 1	bin2	bin3	bin4	bin5	bin6
limits $[GeV/c]$	0.8-2.2	2.2-4.0	4.0-8.0	8.0-12.0	12.0-22.0	22.0-45.6
K^0_s rate	0.0580	0.0024	0.0140	0.0195	0.0126	0.0072
ρ^0 rate	1.1041	0.2615	0.1472	0.1474	0.0633	0.1370
ω^0 rate	1.0925	0.0506	0.3719	0.1678	0.0753	0.2478
η, η' rates	0.2090	0.0205	0.0926	0.0468	0.0536	0.1447
Λ^0 rate	0.0243	0.0033	0.0093	0.0087	0.0030	0.0042
γ rate	0.0537	0.1431	0.0140	0.1142	0.0067	0.0118
ϕ rate	0.0250	0.1869	0.0640	0.0528	0.0306	0.0812
$\rho\omega$ saddle	3.3021	0.7834	0.4366	0.4401	0.1894	0.4092
ρ^0 shape	0.2636	0.5842	2.7873	1.1953	1.1102	0.0567
K^{*0} center	1.1614	0.6901	0.5391	1.0710	1.0581	1.2776
K^{*0} width	1.2586	1.2406	1.1963	1.1202	1.1103	0.7812
mis-ID	3.4438	2.3468	2.9960	0.8130	0.7059	2.3186
RCBG	3.4998	1.4409	1.7020	1.5372	1.5506	2.7771
fit total	6.3622	3.2681	4.6613	2.6677	2.5567	3.9508
trk/vtx	3.4000	3.4000	3.4000	3.4000	3.4000	3.4000
CRID vis.	0.2538	0.2572	0.3139	0.3967	0.6248	1.5799
kaon-ID	1.4270	2.1139	3.7699	4.8030	3.8449	3.4499
pion-cut	0.5411	0.6001	0.6811	0.9478	1.0918	0.8520
MC stat.	1.4558	1.2207	1.2532	1.2677	1.4858	2.6946
eff. total	4.0091	4.2362	5.2826	6.1067	5.4894	5.8263
SYST.	7.5200	5.3503	7.0451	6.6640	6.0556	7.0395
STAT.	11.8455	5.6239	5.6510	5.5061	5.6563	7.3171
TOTAL $\diamondsuit$	14.0309	7.7624	9.0315	8.6444	8.2863	10.0154

Table 6.5: ϕ and K^{*0} inclusive rates and errors.

quantity	ϕ	K^{*0}
inclusive rate	0.101/ev.	0.710/ev.
width error	1.681 %	1.233 %
center error	1.047 %	0.965 %
mis-ID	-	1.207 %
RCBG	1.593 %	1.207 %
ϕ rate	-	0.047 %
γ rate	-	0.126 %
Λ^0 rate	-	0.019 %
η, η' rates	-	0.071 %
K_s^0 rate	-	0.276 %
K_s^0 rate	-	0.276 %
ω^0 rate	-	0.296 %
ρ^0 rate	-	0.276 %
$\rho\omega$ saddle	-	0.826 %
ρ^0 shape	-	1.562 %
TOTAL fit	2.542 %	2.804 %
tracking error	3.400 %	3.400 %
CRID visible	0.449 %	0.141 %
kaon ID	6.202 %	2.827 %
pion rej.	-	0.777 %
MC stat.	1.802 %	0.566 %
TOTAL eff.	7.313 %	4.527 %
TOTAL syst.	7.742 %	5.325 %
STAT.	4.532 %	2.719 %
EXTR.	2.435 %	2.037 %
TOTAL $\diamondsuit$	9.296 %	6.316 %

Chapter 7

The Flavor and Quark-Jets Analysis

7.1. Introduction

Production rates in flavor tagged samples as well as in quark and anti-quark jets can be used to further explore the hadronisation process.

The study of particle production in light flavor events eliminates events with heavy hadrons that contaminate the production rates of particles from fragmentation. The ϕ and K^{*0} are mesons with masses on the order of 1 GeV/c^2, hence in light flavor events there are only few particles heavy enough to decay to them. Thus their distributions in light flavor events are very close to those originating directly from fragmentation and allow for a clean comparison to the MLLA/LPHD predictions.

Particle production in quark and antiquark jets has not been previously studied at the Z^0 mass. This analysis reveals very interesting features of the hadronisation process such as the "leading particle" effect [75] and strangeness suppression. The

K^{*0} production rates in quark and antiquark jets are used to perform a first direct measurement of the strangeness suppression parameter γ_s without model dependencies.

7.2. The Flavor Analysis

Significant[1] tracks are used to divide the data into three samples: hadronic events with $n_{sig} = 0$, defined as the *uds* sample, $N_{uds} = 46875$, $n_{sig} = 1$ or 2, the *charm* sample with $N_c = 19258$ events and $n_{sig} \geq 3$, the *beauty* sample with $N_b = 12116$ events. Particle production rates were measured in the tagged samples and were unfolded to give the true rates in light, charm and beauty flavor events.

7.2.1. Unfolding Procedure

A sample of N hadronic events is composed of N_{uds}, N_c and N_b flavor events. Conversely, the same sample can be viewed as the sum of N^{uds}, N^c and N^b tagged events, in the total sample being nine N^{tag}_{flv} samples of events. The purity of the tag is defined as $\mathcal{P}^{tag}_{flv} = N^{tag}_{flv}/N^{tag}$ and the efficiency of a certain flavor passing into a tagged sample as $\epsilon^{tag}_{flv} = N^{tag}_{flv}/N_{flv}$. Table 7.1 lists the Monte Carlo purities and efficiencies of the tags in the hadronic sample used.

Similarly to the event partition, there are nine samples in which particle produc-

[1]Tracks displaced from the IP by more than 3σ in impact parameter. Events with many such tracks contain decays of long lived particles, usually heavy flavor particles (e.g. B or D mesons).

Table 7.1: Estimated tagging efficiencies and purities for selecting *uds*, *c*, and *b* quark events. The column sums of the efficiencies and the row sums of the purities are equal to unity.

	ϵ_{uds}	ϵ_c	ϵ_b	$\mathcal{P}_{uds}$	$\mathcal{P}_c$	$\mathcal{P}_b$
uds_{tag}	0.846	0.439	0.076	0.843	0.126	0.031
c_{tag}	0.151	0.477	0.330	0.382	0.328	0.289
b_{tag}	0.002	0.083	0.594	0.009	0.105	0.886

tion rates can be measured and a bias term can be defined as:

$$bias^{tag}_{flv} = \frac{X^{tag}_{flv}/N^{tag}_{flv}}{X_{flv}/N_{flv}} \tag{7.1}$$

where X^{tag}_{flv} is the number of particles of species X produced in the N^{tag}_{flv} sample. The $bias^{tag}_{flv}$ matrices were obtained for both ϕ and K^{*0} in the six momentum bins from Monte Carlo (figures 7.2 and 7.1). The deviation from unity of the bias matrix elements is caused by tracking and vertexing effects. Low momentum particles are more likely to give erroneous significant impact parameters and contribute to the number of significant tracks, which can cause *uds* events to be tagged as heavy. Also, in the case of the K^{*0} one third of the decays are to $K^0\pi^0$ that contribute on the average very few tracks. Similarly, one third of the ϕ decays are to $K^0_L K^0_S$. This lowers the number of tracks available for tagging and mis-assigns the event to a different sample.

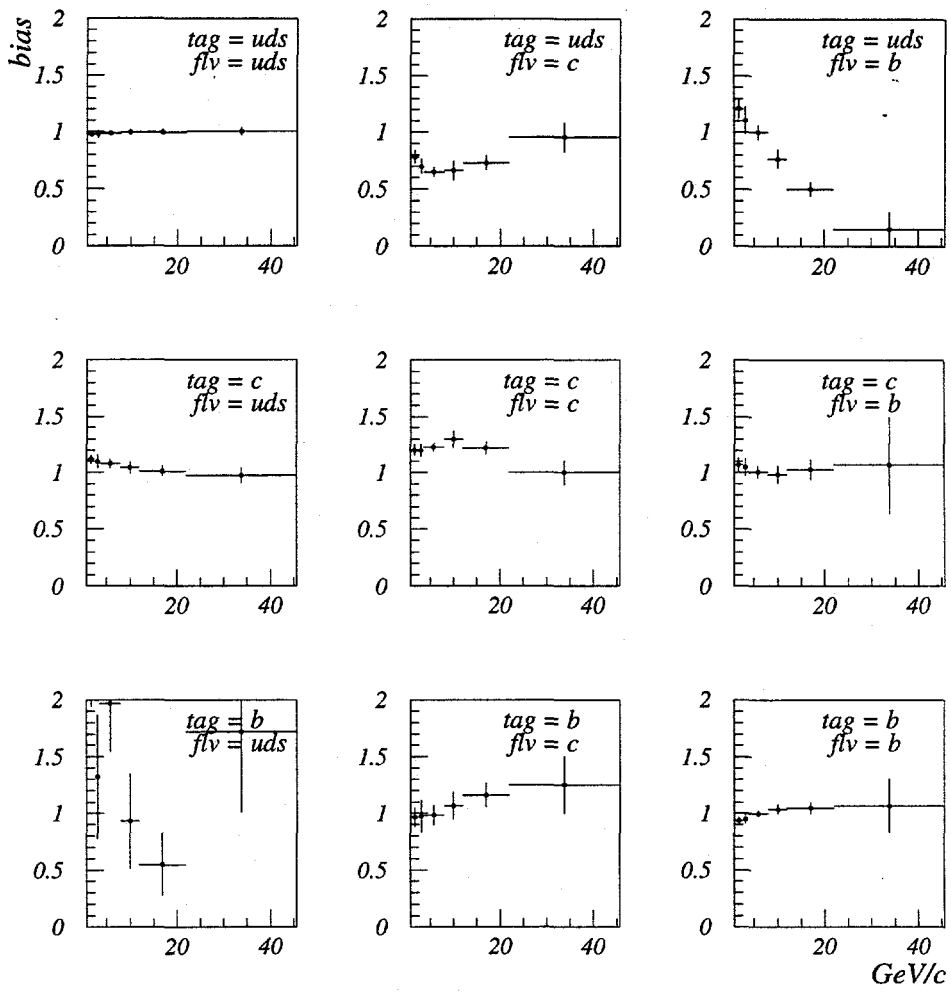

Figure 7.1: The 3×3 matrix $bias_{flv}^{tag}$ for ϕ as a function of momentum.

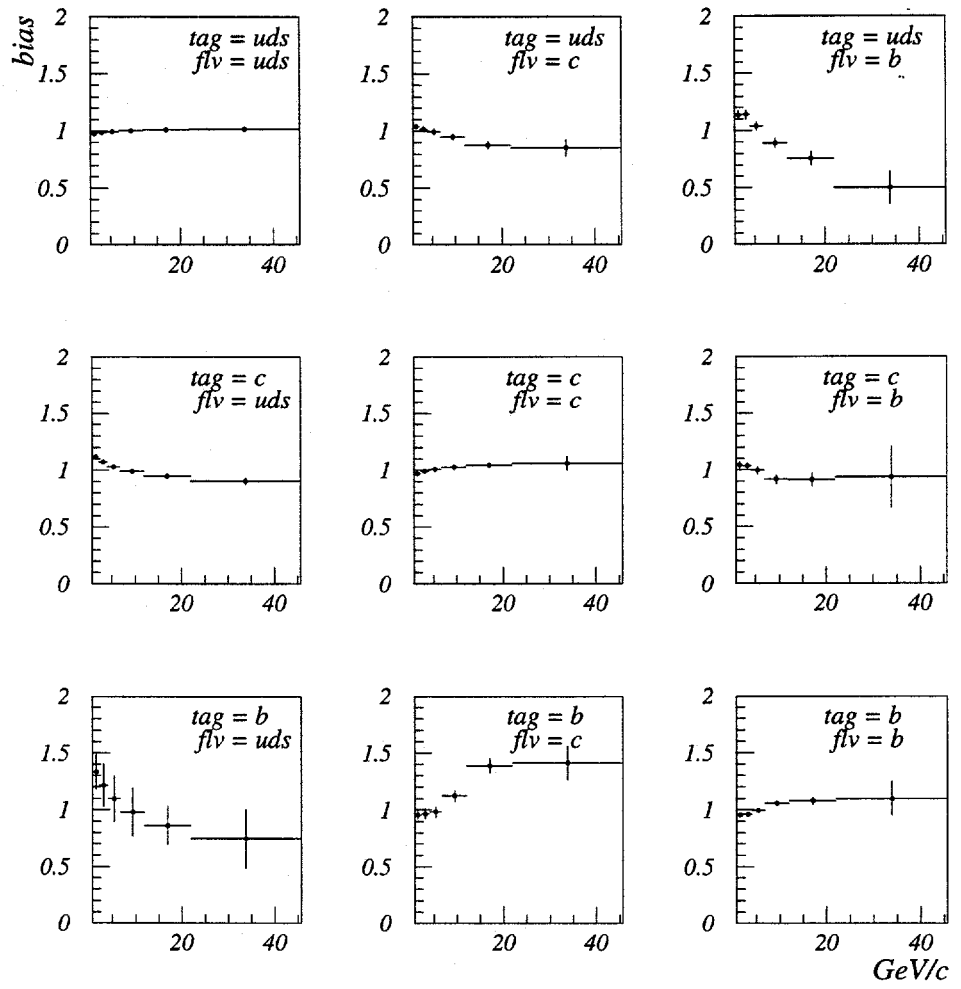

Figure 7.2: The 3×3 matrix $bias_{flv}^{tag}$ for K^{*0} as a function of momentum.

The numbers of particles produced in each momentum bin was determined with fits following exactly the same procedure as the inclusive measurement. The production rates versus $x_p = p/p_{beam}$ are shown in figures 7.3 and 7.4 where lower rates can be observed for the charm and beauty samples at high momenta.

A cross check was performed on the fits by adding the flavor samples and comparing the sums to the inclusive sample, figures 7.5 and 7.6. Considering the different backgrounds from flavor to flavor, the good agreement that is observed indicates that the fits produced physically meaningful results.

The number of particles produced in a *tag* sample can be written as:

$$X^{tag}(p) = \sum_{flv} \underbrace{\underbrace{\underbrace{Nf_{flv}}_{nr.\,q\bar{q}_{flv}}\, p_{flv}(p)}_{X\,in\,q\bar{q}_{flv}} \cdot \epsilon^{tag}_{flv}(p)}_{X_{q\bar{q}_{flv}}\,in\,\text{“}tag\text{”}\,type\,events} \cdot \underbrace{bias^{tag}_{flv}(p)\mathcal{R}_{flv}(p)}_{bias\,correction} \tag{7.2}$$

where p_{flv} is the production rate of particle X in *flv* flavor events, f_{flv} the Standard Model $Z^0 \rightarrow q\bar{q}_{flv}$ fractions: $f_{uds} = 0.621$, $f_c = 0.157$ and $f_b = 0.222$, and $\mathcal{R}_{flv}$ the reconstruction efficiencies. Monte Carlo studies, as well as data to Monte Carlo comparisons of two track candidates in the mass windows of the two particles, confirmed that the reconstruction efficiency is flavor independent, as expected. In this case $\mathcal{R}_{flv}$

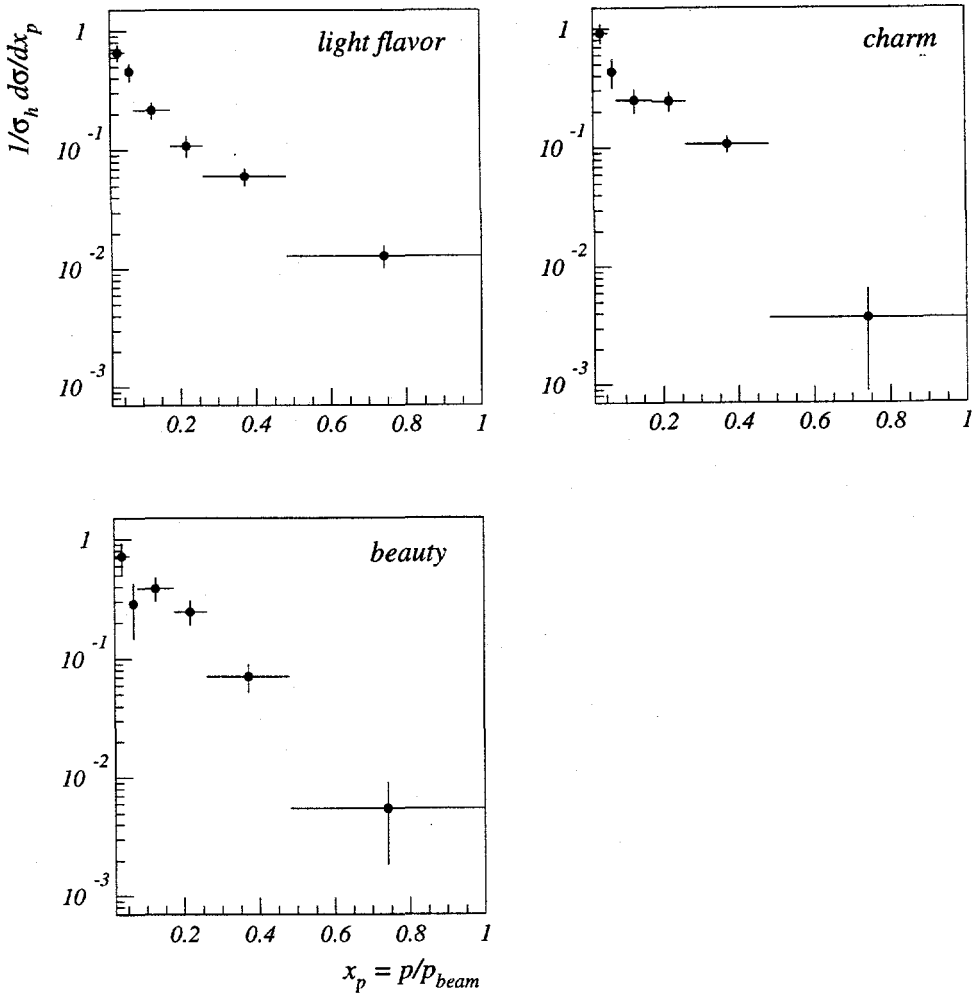

Figure 7.3: ϕ production rates in the flavor enhanced samples versus $x_p = p/p_{beam}$.

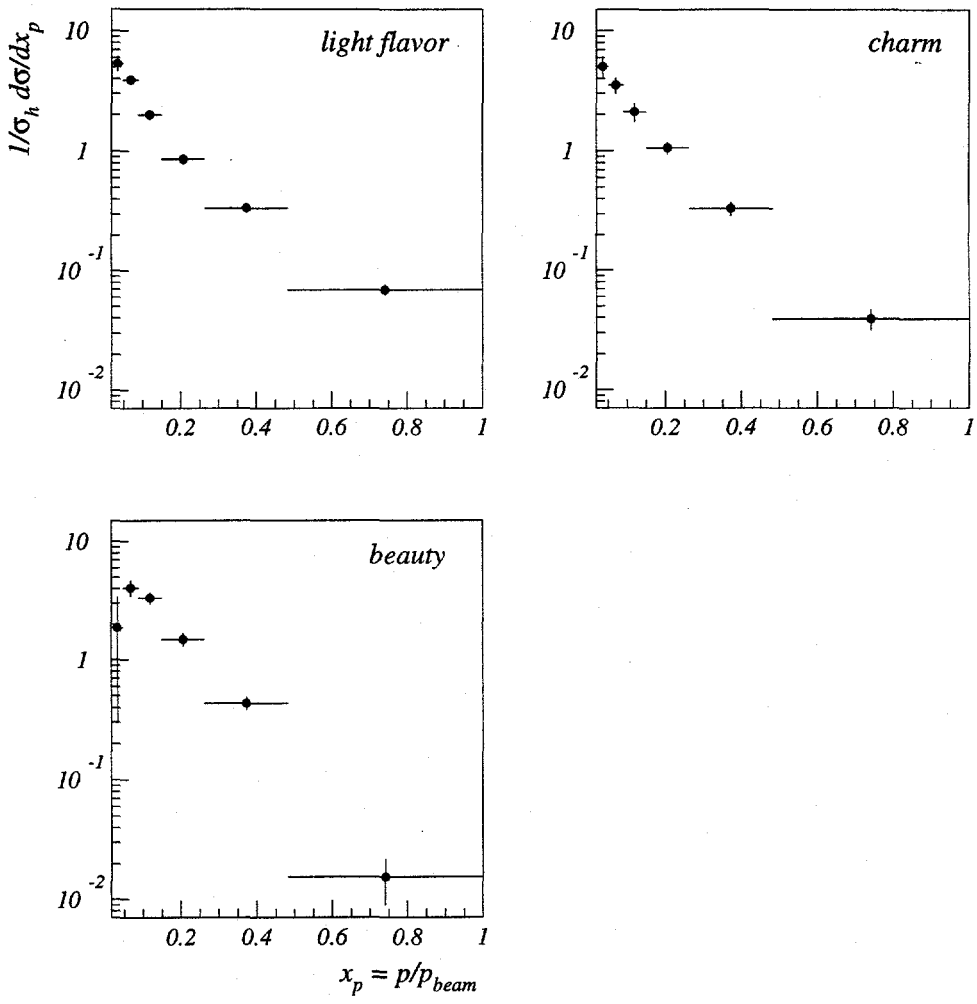

Figure 7.4: K^{*0} production rates in the flavor enhanced samples versus $x_p = p/p_{beam}$.

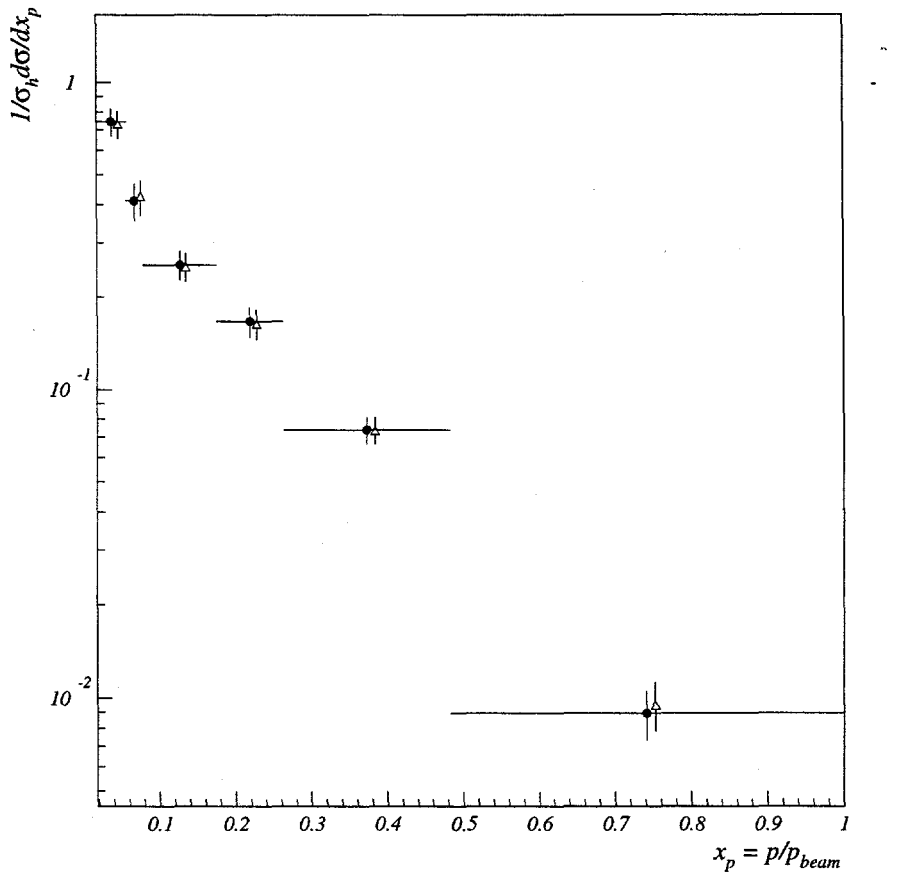

Figure 7.5: Cross check that the flavor samples sum (triangles) to the inclusive measurement for ϕ (filled circles). The triangles have been shifted horizontally for comparison purposes.

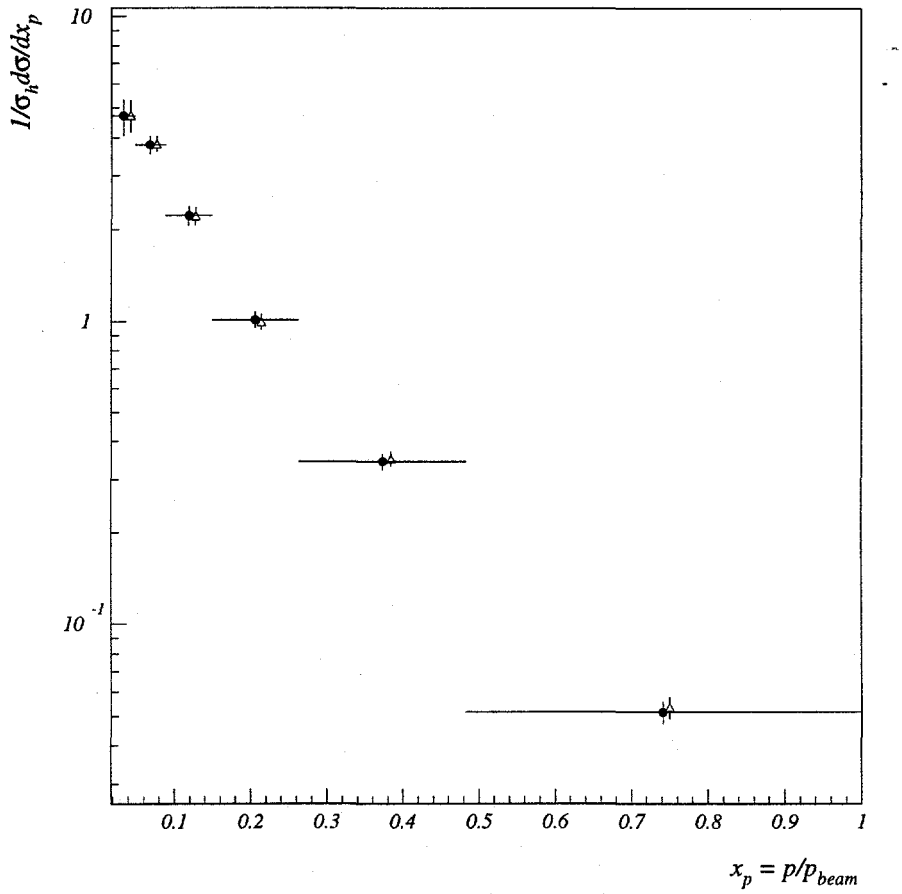

Figure 7.6: Cross check that the flavor samples sum (triangles) to the inclusive measurement for K^{*0} (filled circles). The triangles have been shifted horizontally for comparison purposes.

is common factor for the whole sum and equation 7.2 can be written as:

$$p^{tag} \pm \sigma_{tag} = \sum_{flv} bias^{tag}_{flv} \left(\frac{\epsilon^{tag}_{flv} f_{flv}}{\sum_{flv} \epsilon^{tag}_{flv} f_{flv}} \right) \cdot p_{flv} \tag{7.3}$$

where p^{tag} is the production rate in events tagged as tag.

A χ^2 procedure is used to obtain the pure rates by maximising the agreement between the left and the right hand side of equation 7.3 taking into account the measurement errors on $p^{tag}(p)$. If equation 7.3 can be written as:

$$p^{tag} \pm \sigma_{tag} = \sum_{flv} m^{tag}_{flv} p_{flv} \tag{7.4}$$

then the χ^2 method equation is:

$$\sum_{flv} \left(\sum_{tag} \frac{m^{tag}_i m^{tag}_{flv}}{\sigma^2_{tag}} \right) p_{flv} = \sum_{tag} \frac{p^{tag} m^{tag}_i}{\sigma^2_{tag}} \tag{7.5}$$

The advantage of this method, besides taking into account the actual measurement errors, is that the matrix $M_{i,flv} = \sum_{tag} (m^{tag}_i m^{tag}_{flv} / \sigma^2_{tag})$ can include a number of measurements bigger than three. This feature was used as a cross check on the unfolded rates by including the global sample rates also. In this configuration there are four measurements, each with a σ_i error, that can be switched off at will by turning a given $\sigma_i \rightarrow \infty$ and excluding the information from the respective equation.

The cross check performed was to include the global sample measurement, turn off the b-tagged sample, and then to restore the b- and turn off the c-tagged sample. In all cases the unfolded rates varied less than 2% of the nominal value. The statistical and systematic errors of the measured rates were transported through the unfolding procedure and the uncertainties in the input parameters of the unfolding procedure were divided into three classes: uncertainties of the Standard Model parameters R_b and R_c, uncertainties of the bias terms, and uncertainties of the tagging efficiencies. The uncertainties on R_b and R_c are on the order of 1.4% and 11.7% respectively, and were varied accordingly in the unfolding procedure for an estimate of the systematic errors. The bias matrix diagonal elements are known at a level of better than 20% of the offset from unity. To study the systematics induced by this uncertainty, the diagonal and off-diagonal elements in a row were varied by the same fraction of the deviation from unity, variation that keeps the bias normalisation $\sum_{tag} \epsilon^{tag}_{flv} bias^{tag}_{flv} = 1$ constant in virtue of $\sum_{tag} \epsilon^{tag}_{flv} = 1$. A vertexing study [5] cites the errors on the impact parameter tagging efficiency at a level of less than 0.01. This variation is the maximal error on the beauty sector diagonal element, the rest being smaller than this. A conservative variation of ± 0.01 was thus applied to each diagonal element and the same variation, with opposite sign, was divided into two and assigned to the other two elements in a row to keep the normalisation $\sum_{tag} \epsilon^{tag}_{flv} = 1$ intact.

The unfolding errors are shown for the inclusive samples in table 7.2. It can be

seen that the largest contributions to the unfolding are from the bias terms and the tagging efficiency.

Table 7.2: Inclusive production rates and errors.

	ϕ uds	ϕ charm	ϕ beauty	K^{*0} uds	K^{*0} charm	K^{*0} beauty
rate/event	0.0773	0.1946	0.1036	0.7744	0.2628	0.9922
Errors						
stat.	0.0046	0.0129	0.0130	0.0179	0.0429	0.0577
fit syst.	0.0022	0.0055	0.0055	0.0253	0.0114	0.0307
eff. syst.	0.0030	0.0075	0.0040	0.0274	0.0929	0.0337
kaon ID	0.0048	0.0121	0.0064	0.0219	0.0074	0.0269
tag eff.	0.0020	0.0101	0.0020	0.0163	0.0827	0.0164
bias	0.0036	0.0164	0.0022	0.0231	0.0101	0.0095
R_b	-	0.0002	0.0001	0.0004	0.0036	0.0004
R_c	0.0004	0.0067	0.0004	0.0008	0.0482	0.0022
TOTAL $\diamondsuit$	0.0087	0.0286	0.0163	0.0547	0.1468	0.0806

7.2.2. Production Rates in *usd*, *c* and *b* Flavor Events

The unfolded rates in the *uds*, *c* and *b* samples are shown in figures 7.7 and 7.8 together with JETSET 7.4 predictions. For both particles JETSET describes well the production rates in light flavor events over a wide momentum range, with a few sigma disagreement in the high momentum region. For the charm sector the statistical and the unfolding errors give errors that do not permit a good comparison, however the K^{*0} seems to be in agreement with JETSET. The beauty sector is very interesting in

both cases. As expected there is a lower production rate at high momenta, however JETSET seems overly pessimistic about this cut-off. This is an indication that there are more next-to-leading ϕ's and K^{*0}'s[2] in beauty events than expected. This is a very interesting aspect for heavy flavor physics, where it is expected that the hard spectra are dominated by the heavy mesons.

Another interesting feature is observed from the rate ratios in heavy flavor events versus light flavor events, figure 7.9. For the charm sample, again the errors prevent any affirmation, although for K^{*0} there seems to be an agreement with JETSET predictions. The interesting feature is observed however in the beauty sample where, at intermediate momenta, the expected effect of more abundant ϕ and K^{*0} production is much more pronounced than anticipated by JETSET. Especially for the ϕ, this implies more production directly from fragmentation since the decay probabilities of beauty, or charm to a double-strange plus two strange particles are very small. Also, for K^{*0} there is an unexpected low production at very low momentum. This indicates that most K^{*0} are produced either from heavy particle decays (with higher momenta), or via a next-to-leading fragmentation mechanism that gives them higher momentum.

The inclusive rates show the interesting feature of low production of ϕ in light flavor events, table (7.2). This is a reflection of the double strangeness suppression

[2]Particles with high momentum that are not "leading particles", i.e. - do not contain one of the primary quarks.

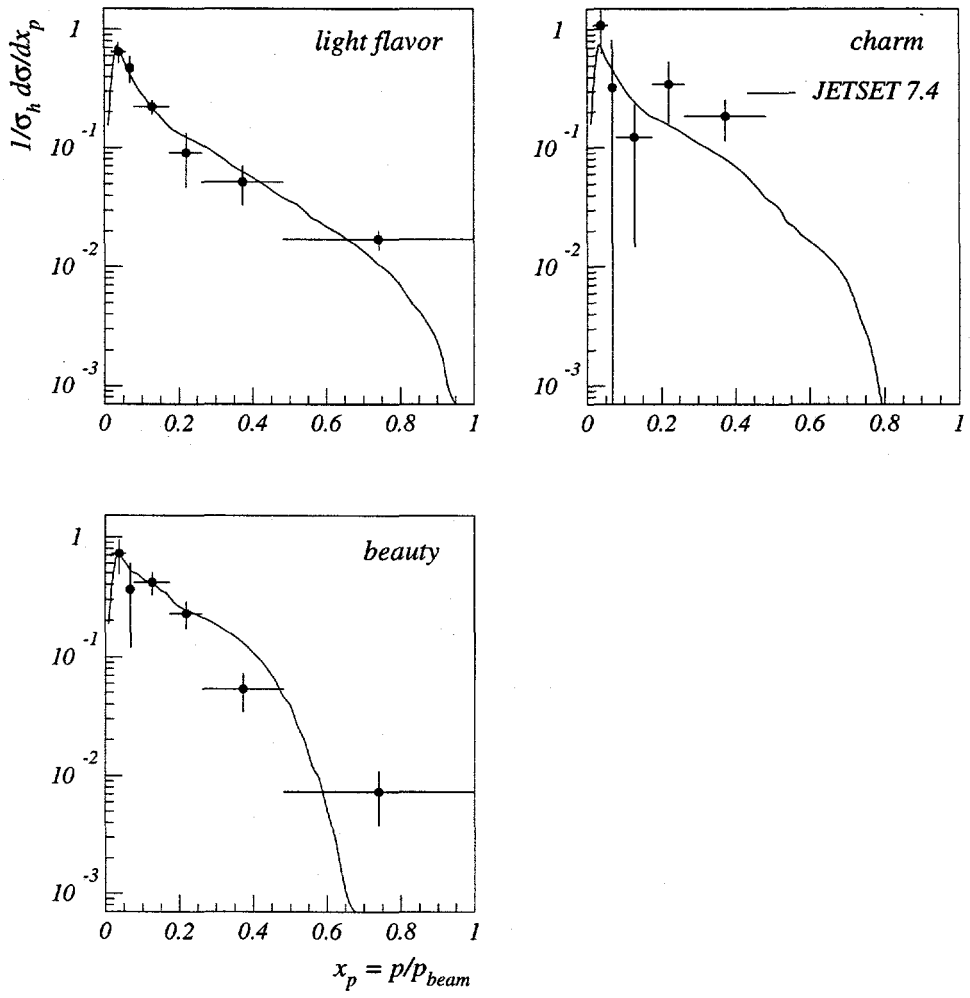

Figure 7.7: The unfolded production spectra for the ϕ versus $x_p = p/p_{beam}$ together with JETSET 7.4 predictions.

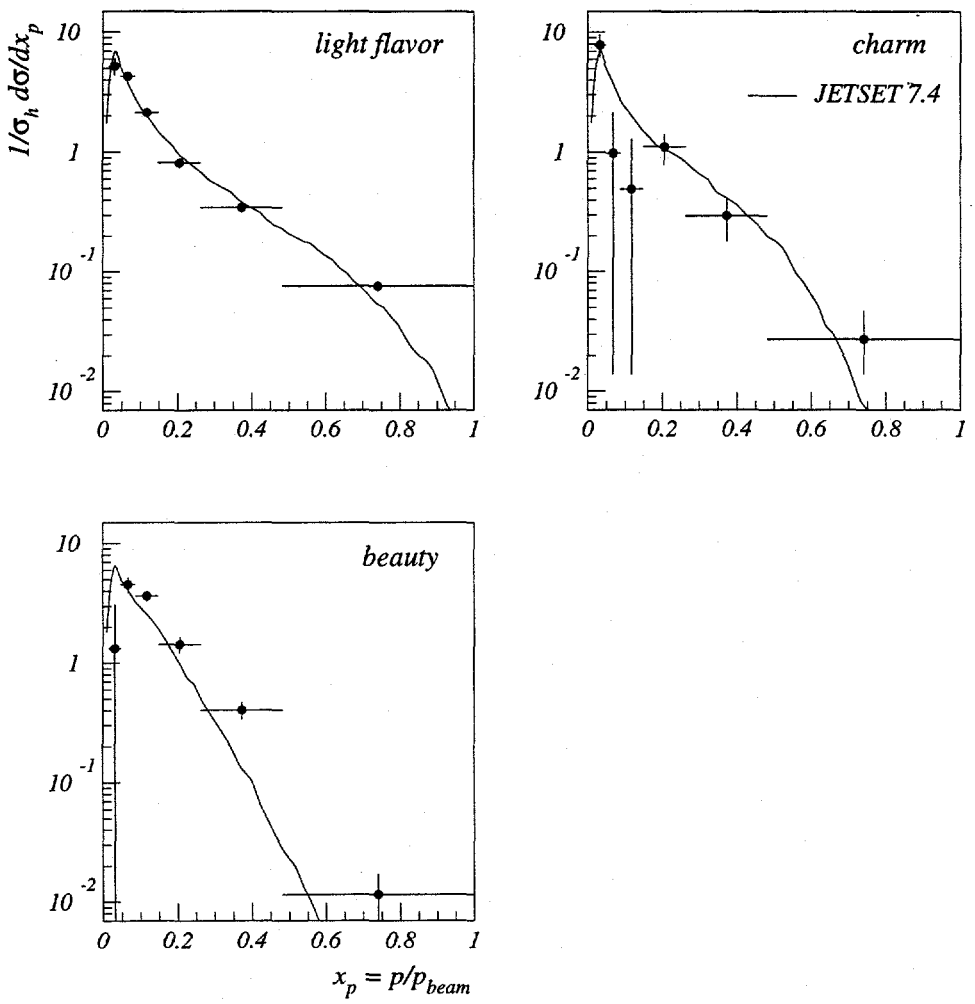

Figure 7.8: The unfolded production spectra for the K^{*0} versus $x_p = p/p_{beam}$ together with JETSET 7.4 predictions.

in fragmentation. In heavy flavor events the rates for ϕ are higher since additionally to the ϕ from fragmentation, there are ϕ from the charm to strange weak decay, as observed. For K^{*0} the interesting feature is a low production rate in charm events. This is most probably due to the large mass difference with respect to the light kaons that may be preferred in the charm to strange decays.

7.2.3. Comparisons to QCD Predictions in Light Flavor Events

For MLLA/LPHD comparisons, the ϕ and K^{*0} production rates versus $\xi = -ln(p/p_{beam})$ in the uds sample were fitted with gaussians (figures 7.10 and 7.11).

The production peaks are at $\xi^* = 2.43 \pm 0.14(stat.) \pm 0.08(syst.) \pm 0.11(unf.)$ for ϕ and $\xi^* = 2.56 \pm 0.03(stat.) \pm 0.02(syst.) \pm 0.03(unf.)$ for K^{*0}. The ϕ fit is dominated by the large statistical error bars and has a $\chi^2/d.o.f.$ of 0.18. The K^{*0} fit has a $\chi^2/d.o.f.$ of 2.25. Both particles are in agreement with the MLLA/LPHD predictions, however for an accurate comparison more data is needed and finer momentum binning.

7.2.4. Hadronisation Physics in Light Flavor Events

As pointed out in Chapter 6, the γ_s measurements in the inclusive samples are subject to contamination from heavy quark decays. Using the unfolded K^{*0} and ϕ rates for the light quark samples, the strangeness suppression factor from low momenta becomes: $\gamma_s = 0.249 \pm 0.047(stat.) \pm 0.022(syst.) \pm 0.038(unf.)$ where a naive string

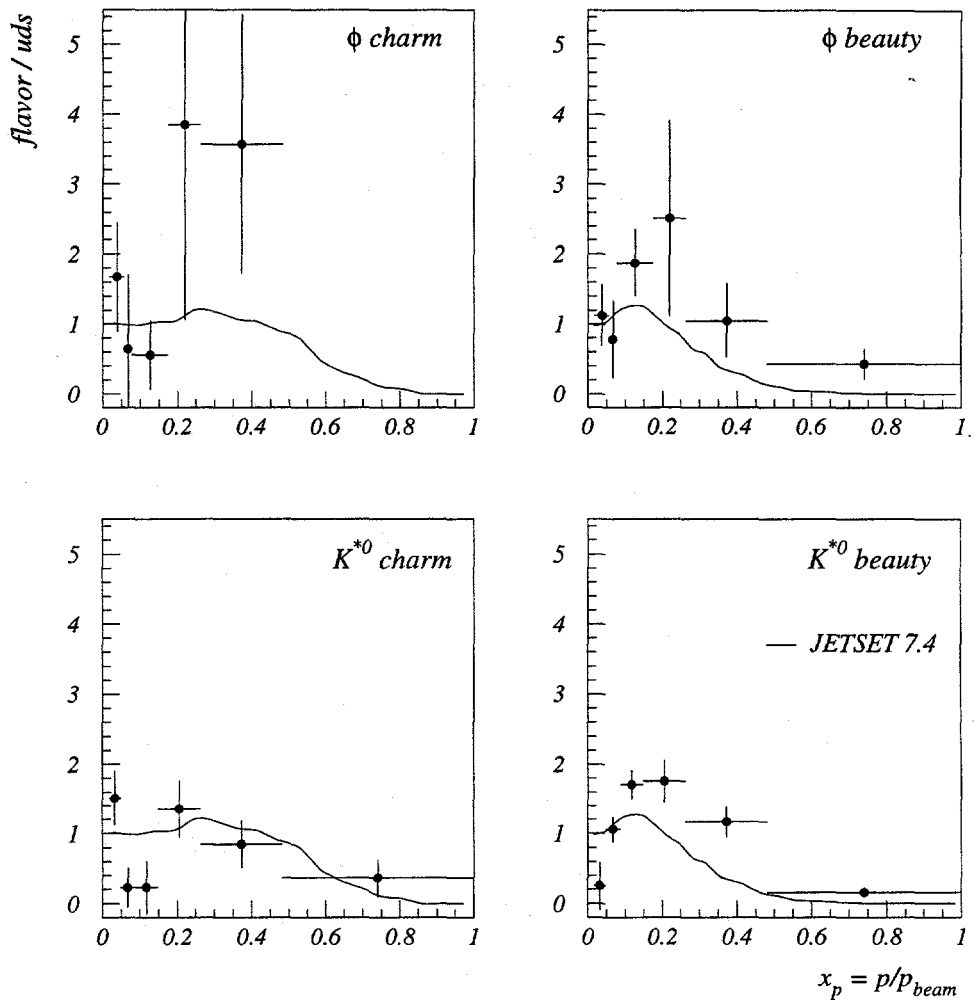

Figure 7.9: Rate ratios of ϕ and K^{*0} in heavy flavor events versus light flavor events as a function of $x_p = p/p_{beam}$ compared to JETSET 7.4 predictions.

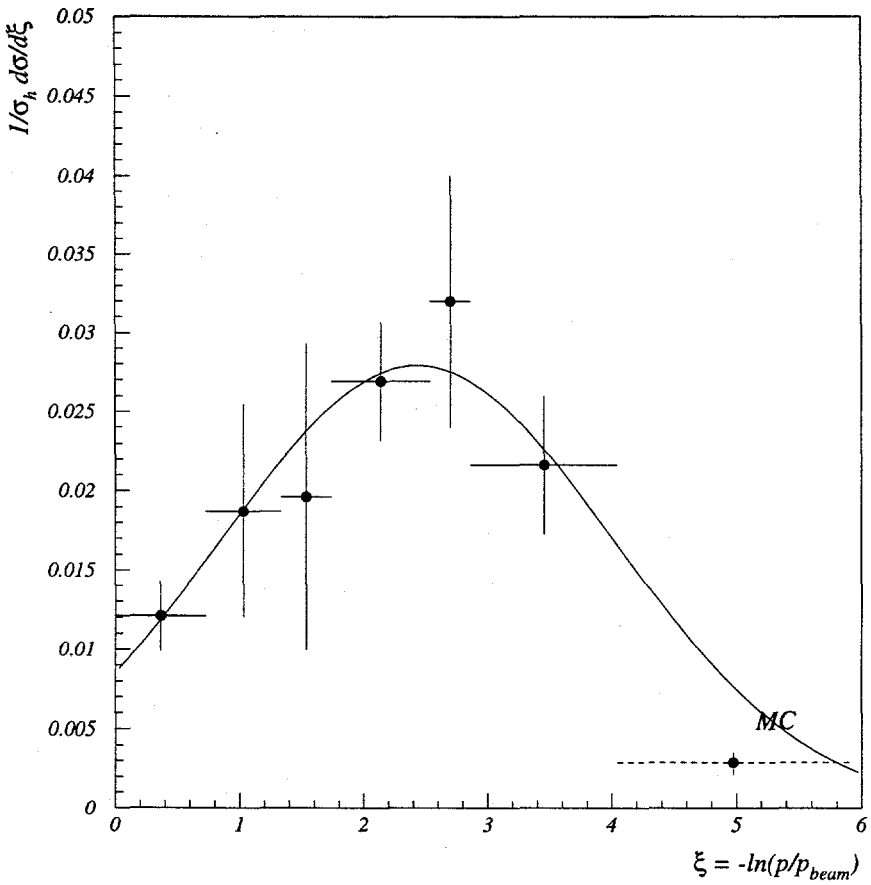

Figure 7.10: Gaussian fit to the ϕ production rate in uds events versus $\xi = -ln(p/p_{beam})$.

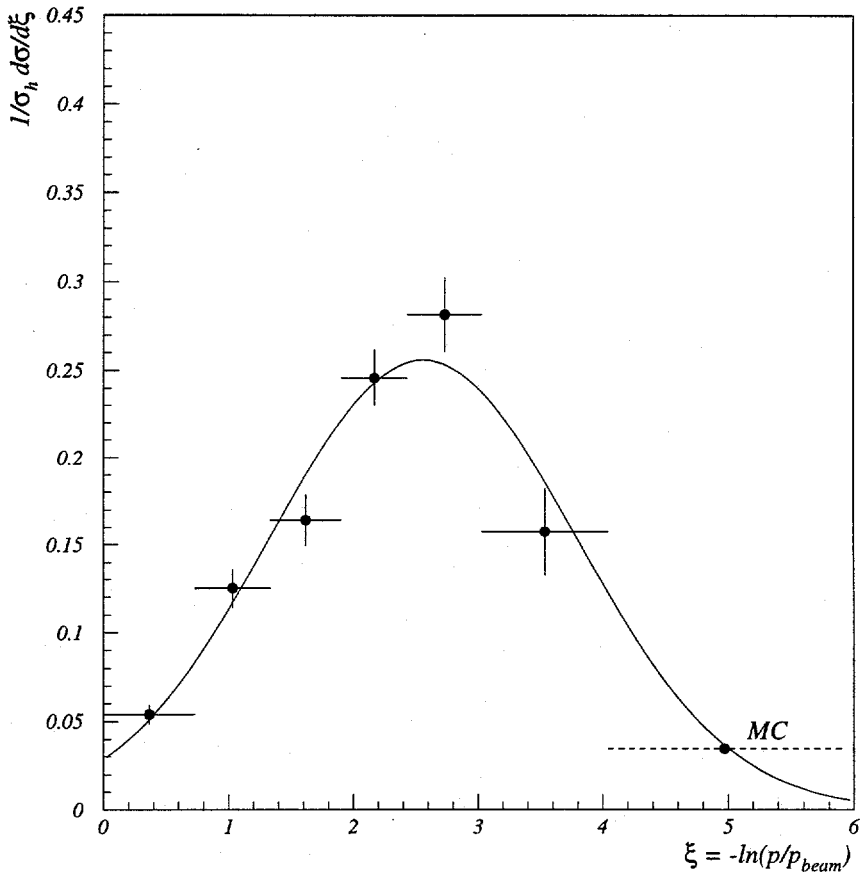

Figure 7.11: Gaussian fit to the K^{*0} production rate in uds events versus $\xi = -ln(p/p_{beam})$.

breaking mechanism is assumed, $\gamma_s = 2\phi_{rate}/K^{*0}_{rate}$. For the high momenta a leading particle mechanism is assumed, $\gamma_s = \phi_{rate}/(K^{*0}_{rate} - \phi_{rate})$ and the measurement becomes: $\gamma_s = 0.290 \pm 0.067(stat.) \pm 0.071(syst.) \pm 0.023(unf.)$. These measurements are less model dependent than the inclusive flavor, momentum inclusive measurements which depend both on the fragmentation function over a large momentum range and on the heavy quark fragmentation functions, particle production rates in heavy quark events and the R_b and R_c fractions.

Most of the previous measurements of this parameter use however ratios of flavor inclusive, momentum inclusive rates to determine γ_s and are subject to quite substantial model dependencies. As an example, a recent measurement [76] compares the rates of K^{*0} and ρ^0: $N(K^{*0})/2N(\rho^0) = 0.29 \pm 0.01 \pm 0.05$, K^{*0} and ω^0: $N(K^{*0})/2N(\omega^0) = 0.39 \pm 0.02 \pm 0.06$, and ϕ and K^{*0} (double strange to single strange): $2N(\phi)/N(K^{*0}) = 0.29 \pm 0.01 \pm 0.04$. These ratios have not been unfolded for model dependencies, but it can be observed the large difference made by the model and the different particles used.

The naive models described above do not account for particle structure and spin alignment of the K^{*0} and the ϕ, however a new method will be presented in the next part of this chapter that completely avoids these model dependencies.

7.3. K^{*0} Production in Quark and Antiquark Jets

This part of the analysis uses quark-tagging techniques to perform measurements of the K^{*0} quark and anti-quark fragmentation functions. The two functions are similar in the low momentum region, however they differ by a factor of more than 3 at high momentum in favor of the anti-quark jet fragmentation function. This indicates the existence of a "leading-particle" mechanism in the high momentum K^{*0} production which reveals the difference in mass between the d and $\bar{s}$ valence constituents of the K^{*0}. This discrimination allows for a *direct* measurement of the strangeness suppression parameter γ_s. The advantage of this method [77] over the traditional method of two particle inclusive rate ratios is that at high momentum the structure of the hadron is negligible, that this assumption is valid over the full momentum range of the measurement and that the valence/sea quark content of the particle is the same for both samples that are compared.

7.3.1. Depleted and Enhanced Samples

To experimentally eliminate heavy quark contamination, *uds* events are selected by using the significant track method, $n_{sig} = 0$. This reduces the Monte Carlo correction and the model dependencies associated with this unfolding.

Quark and anti-quark hemispheres are determined by using the thrust axis of the event. To point this axis into the quark hemisphere, the beam polarisation and

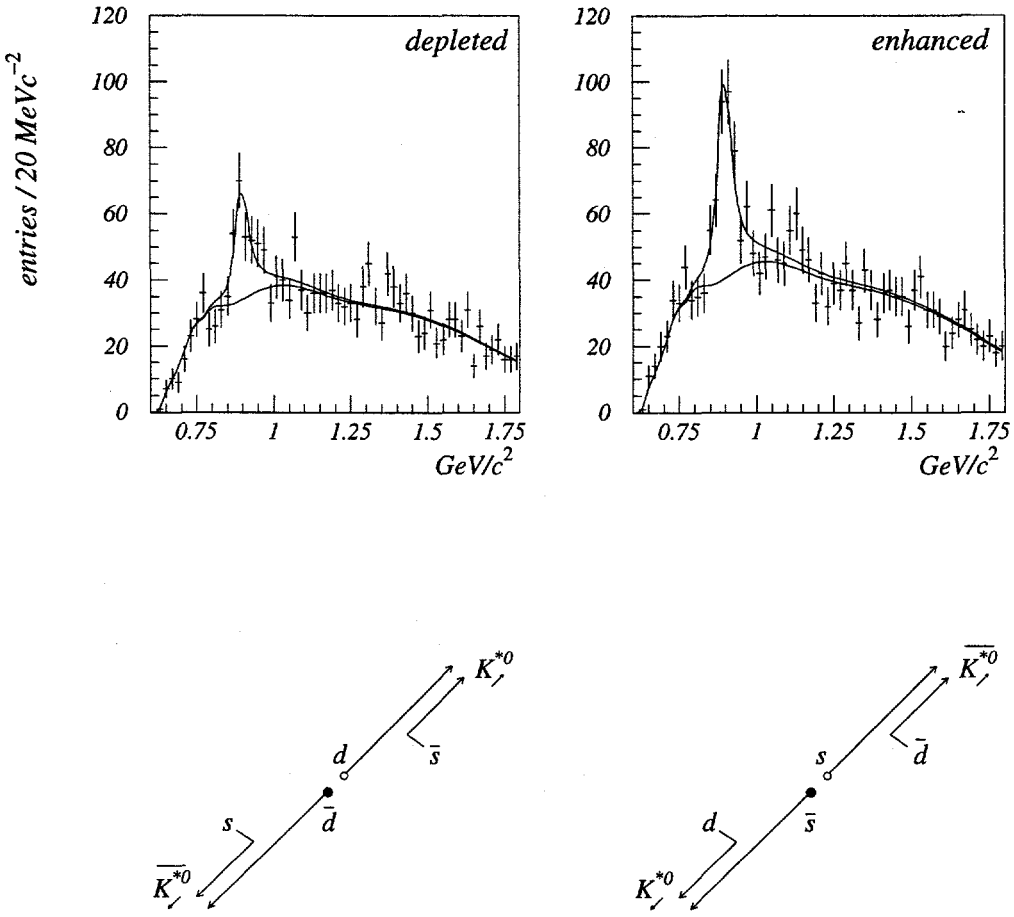

Figure 7.12: Depleted and enhanced samples in the 22-45 GeV/c momentum bin. The four possible cases are grouped into two: d, or $\bar{d}$ pulling an s, or $\bar{s}$ out of the QCD vacuum (depleted sample) and s, or $\bar{s}$ pulling a d, or $\bar{d}$ out of the QCD vacuum (enhanced sample).

quark asymmetries are used, such that for left handed electron bunches the thrust axis points into the same hemisphere as the incident electrons. To optimise the purity of this tag, a cut on $|cos\theta_{thrust}| > 0.2$ was used. The average purity for *uds* events is 73.3 % and for *d* and *s* events only, 75.5 %

Let particles with momenta pointing into the quark hemisphere be denoted by $K^{*0}_{\nearrow}$ and those pointing into the antiquark hemisphere by $K^{*0}_{\swarrow}$. Two samples can be defined: an *enhanced* sample, consisting of $K^{*0}_{\swarrow}$ and $\overline{K^{*0}_{\nearrow}}$, and a *depleted* sample consisting of $K^{*0}_{\nearrow}$ and $\overline{K^{*0}_{\swarrow}}$, the assignment of these sample names being evident from figure 7.12. The *depleted* sample is simply a statistically enriched version of the "K^{*0} in quark jets" ($K^{*0}_{\nearrow}$ sample) while the *enhanced* sample is a statistically enriched version of "K^{*0} in anti-quark jets" ($K^{*0}_{\swarrow}$ sample).

7.3.2. Leading Particle Effect

The light flavor event K^{*0} and $\overline{K^{*0}}$ rates in quark jets were measured and are shown in figure 7.13 along with other SLD measurements (the K^{*0} data plotted as stars). The tag purity used for unfolding the rates was the *uds* average purity. It can be seen that at low momenta the two rates are approximately equal, however at high momenta there is a marked increase in $\overline{K^{*0}}$ production over K^{*0}. This is equivalent to an increased production of K^{*0} in anti-quark jets with respect to quark jets. This phenomenon is a reflection of the difference in mass between the valence constituents

of the K^{*0}, the d and the heavier $\bar{s}$ quark. To reveal this structure of the meson a tagging of the quarks inside the meson had to be performed. The only way that this tagging was possible is through the onset of the "leading particle" effect, that is, high momentum particles in jets are assumed to contain one of the primary quarks from the Z^0 decay as a valence quark. The quark is distinguished from the anti-quark by the jet tag, thus in the case of the K^{*0} the d from the heavier $\bar{s}$.

The effect is yet even more pronounced in baryons which are quark only particles from the point of view of the valence quark model. As such, no anti-baryons are expected in quark jets at high momentum, which is in agreement with the experimental data in figure 7.13 for Λ^0 [78] and the proton.

7.3.3. Strangeness Suppression Parameter

The normalised difference of the rates in quark and anti-quark jets is proportional to $(1-\gamma_s)/(1+\gamma_s)$ where γ_s is the strangeness suppression parameter. This quantity:

$$D_h(p) \stackrel{\text{def}}{=} \frac{K^{*0}_{enh}(p) - K^{*0}_{dep}(p)}{K^{*0}_{enh}(p) + K^{*0}_{dep}(p)} \tag{7.6}$$

has the advantage that the rate systematic errors cancel out and the fit systematic errors are almost totally eliminated. The quantity is easily measured experimentally by a simultaneous fit to the "enhanced" and "depleted" samples, and benefits from increased statistics. The procedure adopted is to take the shapes of the signal and

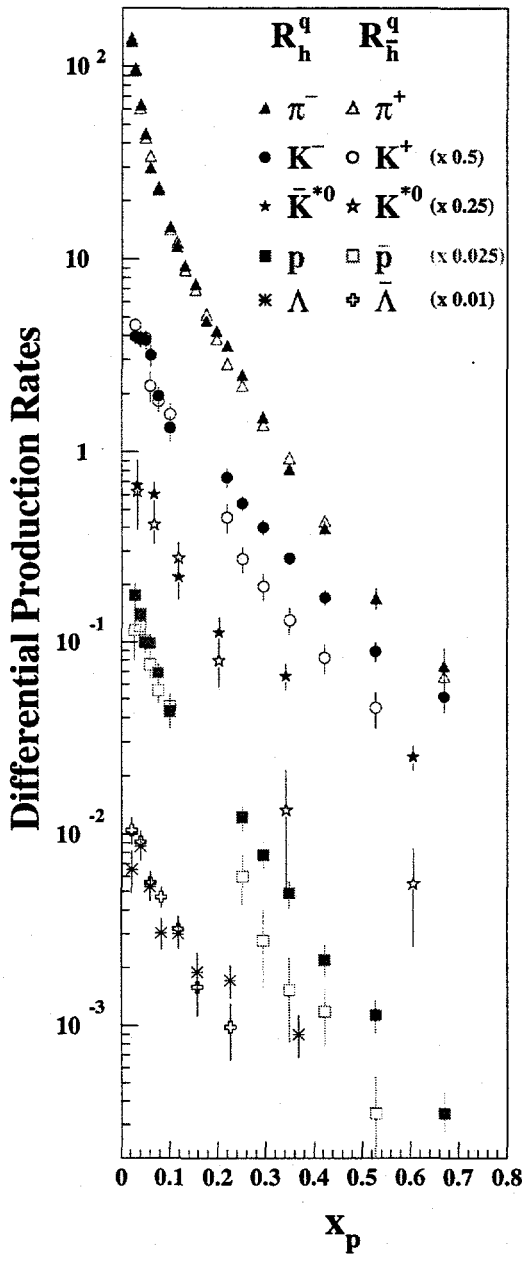

Figure 7.13: Differential production rates of particle and anti-particle in quark jets versus $x_p = p/p_{beam}$.

background from the inclusive fit and to adjust their normalisations to obtain a good fit to the total sample. Once the normalisations are known, the simultaneous fit only adjusts for normalised differences in signal and background between the "enhanced" and the "depleted" sample. The background normalised difference is allowed to float due to the statistical difference in the numbers of events that form the background. However, this quantity deviates from zero only by 5-8%. The signal normalised difference, however, increases with momentum as shown in figure 7.14 (e), indicating the onset the of "leading particle" effect.

The d and the s quarks have the same decay widths from the Z^0, thus there are equal numbers of d and the s flavor events produced.

Assuming the production mechanism at high momentum to be dominated by the "leading particle" effect, the production of K^{*0} in the "enhanced" and "depleted" samples is depicted in figure 7.12. For the *depleted* sample the d quark (or antiquark) pulls an s antiquark (or quark) from the QCD vacuum, and reciprocally, for the *enhanced* the s pulls a $\bar{d}$. The number of $d\bar{d}$ and $s\bar{s}$ events being the same, the difference in the two samples arises only from string fragmentation probabilities to s versus d, the ratio of the two being the "strangeness suppression", an important parameter of all fragmentation models [79]. Studies of this parameter have been performed at the Z^0 mass [80] as well as at higher energies [82]. A summary of these measurements can be found in [81], the world average being $\gamma_s = 0.290 \pm 0.015$. As

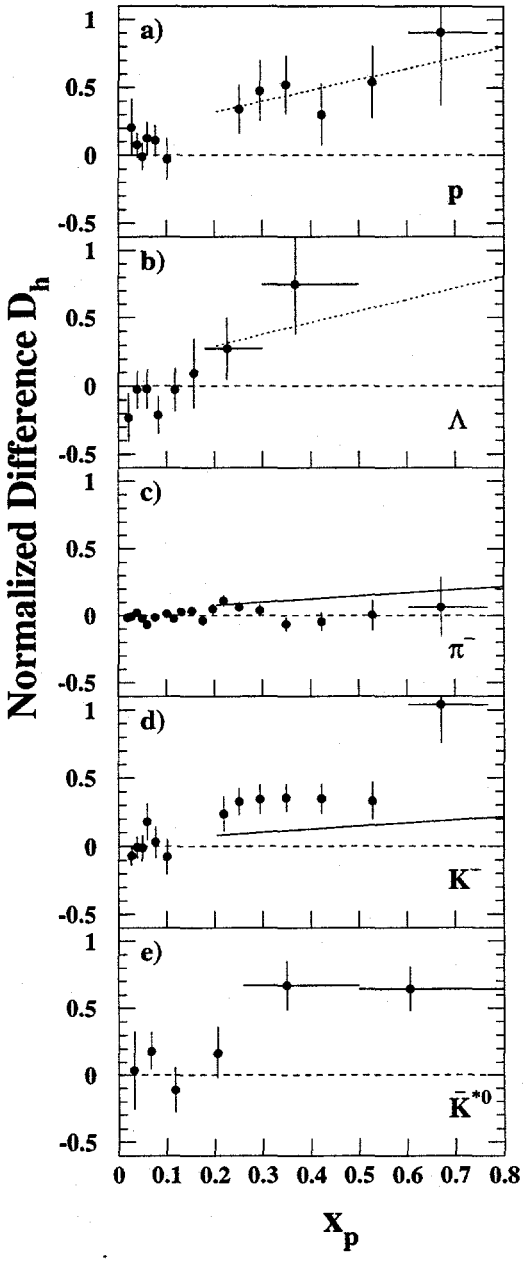

Figure 7.14: Normalised differences of particle production rates in quark and anti-quark jets versus $x_p = p/p_{beam}$ at SLD. The K^{*0} is in plot (e).

pointed out in Chapter 6, most measurements assume a model to unfold the inclusive production rate ratios of strange to non-strange particles. The model systematic errors are usually not considered as these involve convoluted computations.

The problems with the traditional measurements are:

- the use of two distinct particles. The particles, usually mesons, have different structure and in the case of the vector mesons - the ϕ to K^{*0} ratio - different spin alignments to which are associated different transverse momenta with respect to the breaking string. This affects the production rates and skews the γ_s measurement.

- the use of an inclusive rate ratio. This induces a dependence on the model's fragmentation function for the two particles over the broad momentum region implied.

- the inclusion of low momenta regions. Whereas at high momenta the structure of the hadron becomes negligible with respect to the string breaking mechanism, at low momenta the model used has a considerably larger impact on the result.

In this analysis the final state is the same particle for both of the compared samples and the production is studied only at high momentum. The normalised differences are then unfolded for heavy flavor contamination, quark-tag purity and fragmentation contamination, table 7.3 listing the momentum dependent normalised difference throughout the unfolding procedure.

Table 7.3: The normalised difference at various stages in the unfolding procedure: removal of b, c and u quark contaminations, quark-tag unfolding and removal of fragmentation contamination.

bin [Gev/c]	D_h raw	D_h after b, c, u	D_h after q-tag	D_h after fragm.
0.8-2.2	0.015±0.112	0.000±0.113	-0.001±0.222	0.000±0.223
2.2-4.0	0.076±0.056	0.081±0.057	0.159±0.112	0.169±0.112
4.0-6.8	-0.032±0.065	-0.031±0.066	-0.061±0.130	-0.010±0.131
6.8-12.0	0.091±0.069	0.080±0.070	0.157±0.137	0.216±0.134
12.0-22.0	0.287±0.067	0.297±0.067	0.581±0.132	0.627±0.121
22.0-45.0	0.295±0.073	0.314±0.073	0.616±0.144	0.640±0.137

The contamination unfolding uses the following relation:

$$D_h{}' = D_h + \frac{x(1 - D_h^2)}{1 + xD_h} \tag{7.7}$$

where x is a quantity denoting the type of contamination the unfolding refers to. In the case of the b, c and u quarks:

$$x = \frac{c_d - c_e}{2 - c_e - c_d} \tag{7.8}$$

where c_e and c_d are the percent contamination from the respective source of the "enhanced" and respectively the "depleted" sample. For the b quark x is very small and negative. For the c quark it is slightly larger, but still negative, while for the u

quark it is positive and relatively large.

For fragmentation:

$$x = \frac{A_e - A_d}{2 + A_e - A_d} \tag{7.9}$$

where A_e and A_d are the analysing powers in the "enhanced" and the "depleted" sample, $A = (leading - nonleading)/(leading + nonleading)$, and refer to the validity of the "leading particle" assumption. For the "enhanced" sample, the analysing power is that for the s quark and at high momentum reaches into the range of 0.60-0.80 (90% purity), while for the "depleted" sample, it is the d quark analysing power, on the order of 0.40-0.65 (80% purity) at high momentum. This shows that it is more difficult to produce a high momentum "non-leading" K^{*0} in $s\bar{s}$ events than in $d\bar{d}$ events. Again, this relates to the masses of the two quarks.

The quark-jet tag purity unfolding is simpler:

$$D_h{}' = \frac{D_h}{2p - 1} \tag{7.10}$$

where p is the quark-jet tag purity ($75.5 \pm 1.0\%$ for $d\bar{d}$ and $s\bar{s}$ events).

The two highest momentum bins were used to extract the strangeness suppression parameter. Table 7.4 lists the values for γ_s for these bins throughout the unfolding procedure.

The combined value for the two high momentum bins is: $\gamma_s = 0.225 \pm 0.068 \pm$

Table 7.4: Strangeness suppression parameter γ_s at various stages in the unfolding procedure. The uncertainties refer to a ± 25 % error in the Monte Carlo predicted contaminations.

unfolding	12-22 GeV/c	uncertainty	22-45 GeV/c	uncertainty
raw	0.2801 ± 0.1081	0.00000	0.2665 ± 0.1163	0.00000
$b\bar{b}$	0.2803 ± 0.1081	0.00005	0.2665 ± 0.1163	0.00010
$c\bar{c}$	0.3020 ± 0.1130	0.00610	0.2701 ± 0.1175	0.00110
$u\bar{u}$	0.2648 ± 0.1056	0.00750	0.2373 ± 0.1113	0.00840
fragm.	0.2291 ± 0.0914	0.00650	0.2198 ± 0.1023	0.00570

$0.011(model)$, the error being statistics dominated. The result, though in agreement with other methods at the level of 1σ, suggests a somewhat stronger strangeness suppression than seen in inclusive production rate ratios. It should be noted that measurements for γ_s have been reported ranging from $0.17 \pm 0.02 \pm 0.01$ in K^+p collisions at 250 GeV/c [82] up to 0.55 ± 0.05 in pp collisions at 45 and 62 GeV [83].

The Monte Carlo predictions also show a softer strangeness suppression than observed in the data. JETSET 7.4 gives a value of $\gamma_s = 0.314 \pm 0.020$ for this measurement, while HERWIG 5.8 gives $\gamma_s = 0.257 \pm 0.012$ in closer agreement with the data described above. It is to be noted however that JETSET is the model that implements γ_s at the string/quark level, for HERWIG the strangeness suppression occurs only as a function of the hadron mass. It is thus JETSET that will benefit mostly in tuning from this measurement.

Compared to the ϕ/K^{*0}-measurements in light flavor events, described in this dis-

sertation, this model free result shows a stronger strangeness suppression, although the statistical error precludes a definitive conclusion. Since the measurement is statistics dominated, the larger data sample that the SLD experiment should collect in the 1997-98 run could be used to improve the accuracy.

Chapter 8

Summary of Results

This dissertation presented a measurement of production rates of ϕ and K^{*0} strange vector mesons in the 150,000 hadronic Z^0 decays collected by the SLC Large Detector (SLD) in the 1993-1995 run periods. The two particles were reconstructed using the SLD Čerenkov Ring Imaging Device (CRID), one of a new generation of devices that have been developed over the past 20 years for efficient particle identification over a wide momentum range. Without this particle identification system the K^{*0} rate for instance, would be subject to a 40% backgrounds related uncertainty. As with many first-generation devices, a large amount of work was necessary in order to achieve successful particle identification results. This included design, prototyping, engineering effort, as well as calibration, alignment and understanding the identification performance characteristics. The author was involved with part of the End Cap CRID calibration and with the geometrical alignments of the Barrel

and the End Cap CRID sub-systems. The result of this large collective effort is that the SLD CRID presently achieves excellent particle identification performance over a momentum range from 0.3 GeV/c to 25 GeV/c.

The two analyses study inclusive as well as momentum dependent production rates in the individual flavor, as well as in the flavor inclusive samples, with the aim of better understanding the hadronisation process. The results are compared to Z^0 fragmentation models such as HERWIG and JETSET and with MLLA/LPHD parton shower predictions.

For the flavor inclusive analysis, the fragmentation models are in agreement with the data for various regions in momentum. For instance, HERWIG describes well the K^{*0} data in the intermediate momentum region (figure 6.12), while JETSET is in good agreement with the ϕ data in the same momentum range (figure 6.11). More elaborate modeling is required however for both programs and the measurements described in this dissertation provide the necessary data to do so. It is to be noted that the heavier the particle, the more likely it is to have originated directly in fragmentation. Thus the ϕ and the K^{*0} mesons (with masses on the order of 1 GeV/c^2) carry more significant information about hadronisation than light mesons. This is very useful for fragmentation models like JETSET and HERWIG that can use this data to tune the parton shower formation algorithm. The MLLA/LPHD predictions are also in good agreement with the data, indicating that the fundamentals of the perturbative

mechanism for shower formation are correctly understood.

To further explore this aspect the measurement was repeated in three event flavor samples, enriched in light flavor events (84%), charm events (33%) and beauty events (89%). The data revealed new and interesting aspects such as a softer cut-off with momentum of the production rates in beauty flavor events. This indicates more next-to-leading ϕ and K^{*0} than anticipated in JETSET. Also, the ratios of rates in beauty events with respect to light flavor events were found too small in JETSET with respect to the data for the intermediate momentum region, which could indicate again more particle production from fragmentation than expected.

The results of the flavor inclusive analysis are consistent with those from similar experiments. In the intermediate momentum region however, experiments using dE/dx particle ID systems seem to observe a higher K^{*0} production than Čerenkov Imaging experiments, although with relatively high errors. This leads to a somewhat higher inclusive rate observed. The K^{*0} rate presented in this dissertation is in very good agreement with the $K^{*\pm}$ rate (ALEPH [84]), as expected due to the small effect of the Coulomb interaction in hadronisation. This is an independent confirmation that the Čerenkov Imaging system at SLD is well understood.

The flavor dependent analysis is a first measurement of ϕ and K^{*0} rates in light, charm and beauty flavor events.

Also a first measurement is the production of K^{*0} in quark and anti-quark jets.

8. Summary of Results

This analysis showed direct evidence for the "leading particle" effect and allowed a model independent measurement of the strangeness suppression parameter γ_s, which is an important quantity of all fragmentation models [79]. This measurement, $\gamma_s = 0.225 \pm 0.068 \pm 0.011(model)$, indicates a slightly higher strangeness suppression than observed indirectly in inclusive production rate ratios of mesons. With the 1997-98 SLD run this measurement is expected to improve by a factor of about 2.0 in statistical power and provide a very good knowledge of this quantity.

Bibliography

[1] P. Clarke, *RAL-90-055* (1990).

[2] A. Lath, Ph.D Dissertation, Mass. Institute of Technology (1994), *SLAC Report 454.*

[3] B. W. Lynn and C. Verzegnassi, *Phys. Rev.* **D35** (1987) 3326.

[4] SLD Collaboration: K. Abe *et al.*, *Phys. Rev. Lett.*, **73** (1994) 25,
SLD Collaboration: K. Abe *et al*, *SLAC-PUB-7291* (1996).

[5] M. Hildreth, Ph.D Dissertation, Stanford University (1995), *SLAC Report 458*,
SLD Collaboration: K. Abe *et al.*, *Phys. Rev.* **D53** (1996) 2271.

[6] D. C. Williams, Ph.D Dissertation, Mass. Institute of Technology (1994), *SLAC Report 445*,
SLD Collaboration: K. Abe *et al.*, *Phys. Rev. Lett.* **74** (1995) 2895.

[7] A. Blondel, B. W. Lynn, F. M. Renard, and C. Verzegnazzi, *Nucl. Phys.* **B304** (1988) 438.

[8] M. Gell-mann, *Phys. Lett.* **8** (1964), 214.

G. Zweig, *CERN 8409/TH* (1964).

[9] M. Y. Han and Y. Nambu, *Phys. Rev.* **139B** (1965) 1006.

[10] E. Bloom *et al.*, *Phys. Rev. Lett.* **23** (1969) 930.

M. Breidenbach *et al.*, *Phys. Rev. Lett.*, **23** (1969) 935.

[11] H. Fritzsch, M. Gell-Mann and H. Leutwyler, *Phys. Lett.* **B47** (1973) 365,

D. J. Gross and F. Wilczek , *Phys. Rev. Lett.* **30** (1973) 1343,

H. Politzer, *Phys. Rev. Lett.* **30** (1973) 1346.

[12] See e.g. F. Halzen and A. Martin *Quarks and Leptons: An Introductory Course in Modern Particle Physics* J. Wiley and Sons, (1984).

[13] G. Hansen *et al.*, *Phys. Rev. Lett.* **35** (1975) 1609.

[14] SLD Collaboration: K. Abe *et al*, *Phys. Rev.* **D51** (1995) 962.

[15] J. Lauber, Ph.D Dissertation, University of Colorado (1993), *SLAC Report 413*,

SLD Collaboration: K. Abe. *et al.*, *Phys. Rev. Lett.* **71** (1993) 2528.

[16] TASSO Collaboartion: R. Brandelik *et al.*, *Phys. Lett.* **B86** (1979) 243.

[17] T. Sjostrand, *Comp. Phys. Comm.* **39** (1986), 347.

[18] J. Ellis, M. K. Galliard,G. C. Ross, *Nucl. Phys.* **B111** (1976) 253.

[19] A. Ali *et al.*, *Nucl. Phys.* **B167** (1980) 229.

[20] K. J. F. Gaemers, J. A. M. Vermaseren, *Z. Physik* **C7** (1980) 81.

[21] G. Altarelli and G. Parisi, *Nucl. Phys.* **B126** (1977), 298.

[22] R. D. Field and R. P. Feynmann, *Nucl. Phys.* **B136** (1992), 1.

[23] F. E. Page and S. D. Protopopescu, in *Physics of the Superconducting Supercollider-1986* (1987) 320.

[24] X. Artru and G. Mennessier *Nucl. Phys.* **B70** (1974) 93.

[25] B. Anderson *et al.*, *Z. Phys.* **C1** (1979) 105.

[26] B. Anderson *et al.*, *Phys. Reports* **97** (1983) 33.

[27] B. Foster (ed.), *Electron-Positron Annihilation Physics*, 1990.

[28] T. Sjöstrand, *Comp. Phys. Comm.* **82** (1994) 74.

[29] T. Sjostrand, M. Bengtsson, *Comp. Phys. Commun.* **43** (1987) 3.

[30] G. Marchesini, B. R. Webber, *Nucl. Phys.* **B310** (1988) 453.

[31] Ya. I. Azimov, Yu. L. Dokshitzer, V. A. Khoze, and S. I. Troyan, *Zeit. Phys.* **C27** (1985) 65.

[32] N. C. Brummer, *NIKHEF-H/94-09* (1994).

[33] Yu. L. Dokshitzer, V. S. Fadin, and V. A. Khoze, *Zeit. Phys.* **C18** (1983) 37.

Ya. I. Azimov, Yu. L. Dokshitzer, V. A. Khoze, and S. I. Troyan,

Zeit. Phys. **C31** (1987) 213.

Yu. L. Dokshitzer, V. A. Khoze, A. H. Mueller and S. I. Troyan,

Basics of Perturbative QCD Editions Frontieres, (1991).

Yu. L. Dokshitzer, V. A. Khoze, and S. I. Troyan, *Z. Phys.* **C55** (1992) 107.

[34] A summary of these measurements may be found in N. Brummer,

Ph.D. Dissertation, Leiden, *NIKHEF-H* RX-1473 (1994).

[35] DELPHI Collaboration: P. Abreu *et al.*, CERN-PPE-95/28 (1995).

[36] D. Dupen, *SLAC-62*, (1966).

[37] M. Swartz, *SLAC-PUB-4656* (1988).

[38] SLD Collaboration: K. Abe *et al.*, *Phys. Rev. Lett.*, **70** (1993) 2515.

[39] SLD Collaboration: K. Abe *et al.*, *Phys. Rev. Lett.*, **73** (1995) 24.

[40] SLD Collaboration: K. Abe *et al.*, *SLAC-PUB-95-7000* (1995).

[41] SLD Collaboration: G. Agnew *et al.*, *SLD Design Report* SLAC-0273 (1984).

[42] K. Pitts, Ph.D Dissertation, University of Oregon (1994), *SLAC Report 446.*

[43] The Particle Data Group, *Phys. Rev.* **D54**, Part I (1996).

[44] M. Strauss, *SLAC-PUB-6686* (1994).

[45] M. Hildreth *et al.*, *SLAC-PUB-6656* (1994).

[46] SLD Collaboration: K. Abe *et al.*, *Nucl. Inst. and Meth.* **A328** (1993) 472.

[47] P. N. Burrows *et al.*, *SLD Note 229* (1993).

[48] P.A. Čerenkov, *Izvestya, AN, SSSR, Seriya Fiz., OMEN* (1937).

[49] I.M. Frank and I.G. Tamm, *Doklady Akad. Nauk., SSSR* **14**(3) (1937).

[50] S. Willocq *et al.*, *SLAC-6693*, (1995).

[51] G. Poelz *et al.*, *Nucl. Instr. and Meth.* **195** (1982) 491,

C. Arnault *et al.*, *LAL-* **79**/44 (1979) 21.

[52] T. Pavel, Ph.D Dissertation, Stanford University, *SLAC-R-491* (1996).

[53] RTZERO code, *SLD production version CRID section* (1994).

[54] *IEEE Trans. Nucl. Sci.* **42** (1995) 518.

[55] R. Brun *et al.*, *CERN DD/EE/84-1* (1987).

[56] P. N. Burrows, *Z. Phys.* **C41** (1988) 375.

[57] OPAL Collaboration: M. Z. Akrawy *et al.*, *Z. Phys.* **C55** (1990) 505.

[58] P. N. Burrows and H. Masuda, *SLD Physics Note 36* (1995).

[59] C. Peterson *et al.*, *Phys. rev.* **D27** (1983) 105.

[60] SLD Collaboration: K. Abe *et al.*, *Phys. Rev.* **D53** (1996) 1023.

[61] K. Hayes, in *Proceedings of the Third MarkII Workshop on SLC Physics*, SLAC-315 (1987).

[62] Mark II Collaboration: R. G. Jacobsen *et al.*, *Phys. Rev. Lett.* **67** (1991) 3347.

[63] R. G. Jacobsen, Ph.D. Dissertation, Stanford University (1991), *SLAC Report 381.*

[64] H. A. Neal, Jr. II, Ph.D Dissertation, Stanford University (1995), *SLAC Report 473.*

[65] DELPHI Collaboration: P. Abreu *et al.*, *Phys. Lett.* **B298**, (1992) 236.

[66] G. D. Lafferty, *Z. Phys.* **C60** (1993) 659.

[67] MINUIT code, *CERN D506 - Version 92.1* (1992).

[68] DELPHI Collaboration: P. Abreu *et al.*, *CERN-PPE/96-77* (1996).

[69] SLD Physics Note 58, (1997).

[70] SLD Collaboration: K. Abe *et al.*, *Phys. Lett.* **B371** (1996) 149.

[71] SLD Collaboration: K. Abe, *et al.*, *Phys. Rev. Lett.* **72** (1994).

[72] OPAL Collaboration: M. Z. Akrawy *et al.*, *Z. Phys.* **C68** (1995) 1

[73] G. Bocquet *et al*, *CERN-PPE/95-170* (1995)

[74] ALEPH Collaboration: D. Buskulic *et al.*, *Z. Phys.* **C69** (1996) 379,
OPAL Collaboration: M. Z. Akrawy *et al.*, *Z. Phys.* **C68** (1995) 1,
DELPHI Collaboration: P. Abreu *et al.*, *CERN-PPE/96-77* (1996).

[75] SLD Collaboration: K. Abe *et al*, *SLAC-PUB-7395*, January 1997,
(accepted by Phys. Rev. Lett.).

[76] ALEPH Collaboration: D. Buskulic *et al.*, *Z. Phys.* **C69** (1996) 379.

[77] G. D. Lafferty, *Phys. Lett.* **B353**(4) (1995) 541.

[78] K.G. Baird, Ph.D Dissertation, Rutgers University (1995),
SLAC-R-483.

[79] T. Sjöstrand, *Comp. Phys. Comm.* **82** (1994) 279.

[80] W. Hoffman, Ann. Rev. *Nucl. Part. Sci.* **38** (1988) 279.

[81] J. L. Bailly et al., *Phys. Lett.* **B195** (1987) 609.

[82] M. Adamaus et al., *Phys. Lett.* **B198** (1987) 427.

[83] A. Breakstone et al., *Phys. Lett.* **B135** (1984) 510.

[84] ALEPH Collaboration: R. Barate *et al.*, CERN-PPE-96/186 (1996).